

Deciphering cellular heterogeneity of
cardiomyocytes and muscle stem cells during
pathology and ageing

INAUGURAL-DISSERTATION
for the degree of Doctor rerum naturalium
(Dr. rer. nat.)

by
Michail Yekelchyk

submitted to the
Faculty of Biology and Chemistry
Justus-Liebig-University
Giessen, Germany

prepared in the
Department of Cardiac Remodeling
Max Planck Institute for Heart and Lung Research
Bad Nauheim, Germany

Bad Nauheim, 2021

PREFACE

First Reviewer: Prof. Dr. Dr. Thomas Braun

Max Planck Institute for Heart and Lung Research, Bad Nauheim, Germany

Second Reviewer: Prof. Dr. Norbert Weissmann

Justus-Liebig-University, Giessen, Germany

First Examiner: Prof. Dr. Albrecht Bindereif

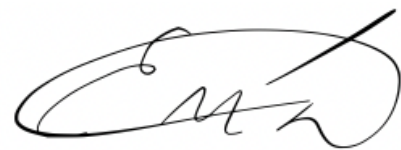
Justus-Liebig-University, Giessen, Germany

Second Examiner: Prof. Dr. Alexander Goesmann

Justus-Liebig-University, Giessen, Germany

Declaration

I declare that I have completed this dissertation single-handedly without the unauthorized help of a second party and only with the assistance acknowledged therein. I have appropriately acknowledged and cited all text passages that are derived verbatim from or are based on the content of published work of others, and all information relating to verbal communications. I consent to the use of an anti-plagiarism software to check my thesis. I have abided by the principles of good scientific conduct laid down in the charter of the Justus Liebig University Giessen "Satzung der Justus-Liebig-Universität Gießen zur Sicherung guter wissenschaftlicher Praxis" in carrying out the investigations described in the dissertation.



Michail Yekelchyk

Parts of this dissertation were published:

Yekelchyk M., Guenther S., Preussner J., Braun T., „Mono- and multi-nucleated ventricular cardiomyocytes constitute a transcriptionally homogeneous cell population”, *Bas. Res. Cardiol.*, **2019**

INDEX

1.	INTRODUCTION	7
1.1.	Approaching cellular heterogeneity	7
1.2.	Heterogeneity of stem cells	11
1.3.	Mammalian ageing and its hallmarks	14
1.4.	Heart physiology and anatomy in brief	16
1.4.1.	Cardiac remodeling and regeneration	19
1.5.	Skeletal muscle physiology and anatomy in brief	22
1.5.1.	Muscle regeneration and the role of muscle stem cells	24
1.6.	Aims of dissertation.....	26
2.	MATERIALS AND METHODS.....	27
2.1.	Animal experimentation.....	27
2.1.1.	Proposals for animal experiments.....	27
2.1.2.	Maintenance of mice.....	27
2.1.3.	Sacrificing the mice.....	27
2.1.4.	Transverse aortic constriction.....	27
2.1.5.	Magnetic resonance tomography	27
2.1.6.	Cardiotoxin regeneration assay.....	28
2.1.7.	<i>Tibialis Anterior</i> muscle isolation.....	28
2.1.8.	Diaphragm isolation.....	28
2.1.9.	Application of Galanin peptide.....	28
2.1.10.	Cre-lox (inducible) system.....	28
2.1.11.	TetO-tTA/rtTA (inducible) system	29
2.1.12.	List of used mouse strains.....	29
2.2.	Molecular biology.....	30
2.2.1.	Isolation of genomic DNA from mouse tail biopsies.....	30
2.2.2.	Genotyping	30
2.2.3.	Isolation of RNA.....	31
2.2.4.	Measurement of RNA and DNA concentrations.....	31
2.2.5.	DNA and RNA size distribution analysis by capillary gel electrophoresis.....	31
2.2.6.	Quantitative reverse transcription PCR (qRT-PCR)	32
2.2.7.	RNA sequencing library preparation (RNA-seq)	33
2.2.8.	Assay for transposase-accessible chromatin library prep. (ATAC-seq)	34
2.2.9.	Single-cell RNA sequencing (scRNA-seq).....	36
2.2.10.	Single-cell ATAC sequencing (scATAC-seq).....	38
2.3.	Biochemistry.....	39
2.3.1.	Protein isolation from adherent cells	39
2.3.2.	Measurement of protein concentration	39
2.3.3.	SDS polyacrylamide gel electrophoresis	40
2.3.4.	Western blot analysis	40
2.4.	Histology	40
2.4.1.	Cryo-sectioning.....	40
2.4.2.	Hematoxylin & Eosin staining.....	41
2.4.3.	Masson's Trichrome staining	41
2.4.4.	Immunofluorescence.....	41
2.4.5.	Whole mount staining	43
2.4.6.	Fluorescence microscopy.....	43
2.4.7.	Confocal microscopy.....	43
2.5.	Cell biology	43
2.5.1.	Isolation of adult cardiomyocytes	43
2.5.2.	Isolation of <i>flexor Digitorum Profundus</i> (FDP) muscle fibers	44
2.5.3.	Fluorescent-activated cell sorting (FACS).....	44
2.5.4.	Isolation and culture of muscle stem cells (MuSCs) and primary myoblasts	44
2.5.5.	Determination of myoblast proliferation and differentiation	46

2.5.6.	Live imaging of cultured cells with IncuCyte	46
2.5.7.	Viral transductions and shRNA-induced knock-down.....	47
2.6.	Bioinformatics	48
2.6.1.	Next generation sequencing (NGS)	48
2.6.2.	Demultiplexing of sequencing reads, quality assessment and trimming.....	49
2.6.3.	Mapping of sequencing reads to reference genome or transcriptome.....	50
2.6.4.	Sequencing read count, normalization and log-fold-change calculation.....	50
2.6.5.	Statistical tests (p-value, false discovery rate (FDR)).....	50
2.6.6.	Gene set enrichment analysis (GSEA).....	51
2.6.7.	Handling of single-cell datasets.....	51
2.6.8.	Dimensional reduction and clustering in single-cell datasets	52
2.6.9.	Calculation of differential expression/accessibility in single-cell datasets	52
2.6.10.	Analysis of microscopic images and particle analysis.....	52
2.6.11.	List of used R packages	52
3.	RESULTS	53
3.1.	Mono- and multi-nucleated ventricular cardiomyocytes constitute a transcriptionally homogeneous cell population	53
3.1.1.	Image-based quality control of single cardiomyocytes is necessary to avoid artificial cell clustering.....	53
3.1.2.	Mono- and multinucleated cardiomyocytes have similar expression patterns	56
3.1.3.	Cardiac hypertrophy induces transcriptional heterogeneity in cardiomyocytes.....	60
3.1.4.	Hypoxic responses drive cardiomyocytes heterogeneity in hypertrophic hearts	63
3.1.5.	HIF1 α stabilization inversely correlates with vascularization in hypertrophic hearts	66
3.2.	The neuropeptide Galanin restores the regenerative capacity of the aged muscle	68
3.2.1.	Ageing has a distinct transcriptional signature in murine quiescent muscle stem cells	68
3.2.2.	A <i>Gal^{pos}</i> subpopulation of quiescent muscle stem cells is lost during ageing.....	71
3.2.3.	Ageing alters chromatin accessibility in quiescent muscle stem cells	75
3.2.4.	I.p. Galanin injections induce transcriptional, epigenetic and metabolic changes in the qMuSCs.....	80
3.2.5.	Galanin partially rejuvenates the transcriptome of aged quiescent muscle stem cells.....	82
3.2.6.	Galanin is required for the proliferation of primary myoblasts	84
3.2.7.	Galanin is required for muscle regeneration and its absence results in muscle fibrosis	86
3.2.8.	Galanin is required for neuromuscular junction formation, regeneration and maintenance.....	88
3.2.9.	The transcriptional profile of Gal KO quiescent MuSCs recapitulates natural ageing	90
3.2.10.	<i>Gal</i> cKO in MuSC causes impaired muscle regeneration but leaved muscle re-innervation intact	92
3.3.	Annexin A3 marks a defective subpopulation of aged muscle stem cells	94
3.3.1.	An <i>Anxa3^{pos}</i> subpopulation of quiescent muscle stem cells emerges during ageing.....	94
3.3.2.	<i>Anxa3</i> mRNA knock-down partially rescues the proliferation defect of aged myoblasts	96
3.3.3.	Overexpression of <i>Anxa3</i> attenuates the proliferation rate of young primary myoblasts	97
3.3.4.	<i>Anxa3</i> overexpression disrupts muscle regeneration and induces muscle fibrosis.....	99
3.3.5.	<i>Anxa3</i> OE induces transcriptional changes characteristic for disruption of MuSCs homeostasis	102
3.3.6.	<i>Anxa3</i> OE does not recapitulate natural ageing at the transcriptional level	105
3.3.7.	Myoblasts, overexpressing <i>Anxa3</i> , do not induce apoptosis in fibro-adipogenic progenitor cells	107
4.	DISCUSSION	113
4.1.	Mono- and multinucleated ventricular cardiomyocytes constitute a transcriptionally homogeneous cell population	113
4.2.	The neuropeptide Galanin restores the regenerative capacity of aged muscles	119
4.3.	Annexin A3 marks a defective subpopulation of aged muscle stem cells	123
5.	LIST OF ABBREVIATIONS	127
6.	REFERENCES	128
7.	ACKNOWLEDGEMENTS	141

ABSTRACT

Cellular heterogeneity is present on genomic, epigenomic, transcriptomic, proteomic and metabolomic levels. Single-cell approaches have revolutionized the detection of rare and subtle cellular subpopulations and are applicable to the majority of organs and tissues, including cardiac and skeletal muscles. Despite active research, many aspects of muscle heterogeneity remain unresolved. Examples for the latter, investigated in the current dissertation, are the evaluation of heterogeneity among cardiac muscle cells (CM) in basal vs. hypertrophic conditions, as well as juvenile vs. aged skeletal muscle stem cell (MuSCs) pool.

In case of healthy adult cardiomyocytes wide ranging homogeneity was found with only minor transcriptional differences between cells of different nuclearity. When homeostasis was disturbed by traverse aortic constriction, which led to cardiac hypertrophy, a notable transcriptional heterogeneity among cardiomyocytes developed. Furthermore, cardiomyocytes located in poorly vascularized zones of the hypertrophic myocardium showed transcriptional signatures characteristic for hypoxic responses. In contrast to cardiomyocytes, strong cellular heterogeneity was found among quiescent MuSCs already at early age (2 month), which further changed with ageing (24 month). In particular, a subpopulation of quiescent MuSCs, defined by expression of the *Gal* gene, decreased, while a subpopulation expressing the *Anxa3* gene emerged with age. Based on these findings, lack of Galanin and the induction of Annexin A3 were hypothesized to be of functional significance in the context of age-related reduction of muscle regeneration capacity. Systemic supplementation of Galanin peptide was applied to aged mice to restore juvenile levels of the neuropeptide. Intriguingly, application of Galanin partially rejuvenated the transcriptional profile of aged quiescent MuSCs. On the other hand, overexpression of *Anxa3* gene in quiescent MuSCs abolished muscle regeneration and induced extensive muscle fibrosis in young mice, resembling conditions in aged muscles. Thus, *Gal* and *Anxa3* are potential crucial factors, important for muscle regeneration in ageing animals.

In conclusion, this work shows that cellular heterogeneity is not detectable among cardiomyocytes of different nuclearity, but appears when cardiomyocytes adapt to hypoxic conditions. Heterogeneity is, however, occurring in MuSCs upon ageing. The work presented in this thesis lays the groundwork to investigate whether the observed transcriptional and epigenetic heterogeneity is of functional relevance for organ homeostasis and pathological reactions in disease.

ABSTRAKT

Zelluläre Heterogenität existiert auf genomischer, epigenomischer, transkriptomischer, proteomischer und metabolomischer Ebene. Einzelzellansätze haben die Erkennung seltener zellulärer Subpopulationen revolutioniert und sind auf die meisten Organe und Gewebe anwendbar, einschließlich Herz- und Skelettmuskel. Trotz aktiver Forschung bleiben viele Aspekte der Muskelheterogenität ungelöst. Beispiele dafür sind die Bewertung der Heterogenität zwischen Herzmuskelzellen unter basalen und hypertrophen Bedingungen sowie der Pool von juvenilen und gealterten Muskelstammzellen. Die vorliegende Dissertation trägt zur Beantwortung dieser offenen Fragen bei.

Im Rahmen der Arbeit wurde bei gesunden erwachsenen Kardiomyozyten eine weitreichende Homogenität mit nur geringen Transkriptionsunterschieden zwischen Zellen unterschiedlicher Nuklearität gefunden. In Reaktion auf eine durch Aortenverengung gestörte und zu Herzhypertrophie führenden Homöostase, entwickelte sich jedoch eine bemerkenswerte Transkriptionsheterogenität unter den Kardiomyozyten. Darüber hinaus zeigten Kardiomyozyten in schlecht vaskularisierten Zonen des hypertrophen Myokards Transkriptionssignaturen, die für hypoxische Reaktionen charakteristisch sind. Im Gegensatz zu Kardiomyozyten wurde bei ruhenden Muskelstammzellen bereits früh (2 Monate) eine starke zelluläre Heterogenität festgestellt, die mit zunehmendem Alter (24 Monate) weiter evolvierte. Insbesondere verkleinerte sich eine Subpopulation ruhender MuSCs, die sich durch die Expression des *Gal*-Gens auszeichnet, während eine andere, für die Expression des *Anxa3*-Gens kennzeichnend ist, mit zunehmendem Alter erst auftrat. Basierend auf diesen Befunden wurde angenommen, dass der Mangel an Galanin und die Induktion von Annexin A3 im Zusammenhang mit der altersbedingten Verringerung der Muskelregenerationskapazität von funktioneller Bedeutung sind. Um dies weiter zu erhärten wurde Galanin gealterten Mäusen systemisch als Protein verabreicht, mit dem Ziel sein Niveau die juvenilen Mäuse anzupassen. Interessanterweise verjüngte die Anwendung von Galanin das Transkriptionsprofil gealterter ruhender MuSCs teilweise. Im Gegensatz dazu interferierte eine Überexpression des *Anxa3*-Gens in ruhenden MuSCs mit der Muskelregeneration und induzierte in jungen Mäusen eine ausgedehnte Muskelfibrose, was dem Phänotyp gealterter Muskeln ähnelt. Diese Ergebnisse lassen den Schluss zu, dass *Gal* und *Anxa3* für die Muskelregeneration bei alternden Tieren wichtig sind.

Zusammenfassend zeigt diese Arbeit, dass zelluläre Heterogenität bei Kardiomyozyten unterschiedlicher Nuklearität auf der Transkriptebene nicht nachweisbar ist, sich aber einstellt, wenn sich Kardiomyozyten an hypoxische Bedingungen anpassen. Heterogenität in MuSCs nimmt dagegen mit zunehmendem Alter zu. Die in dieser Dissertation vorgestellten Arbeiten bilden die Grundlage für weiterführende Studien, bezüglich der möglichen funktionellen Relevanz der beobachteten transkriptionellen und epigenetischen Heterogenität für die Organhomöostase generell, sowie im Kontext pathologischer Mechanismen.

1. INTRODUCTION

1.1. Approaching cellular heterogeneity

Heterogeneity is an essential property of life and present at all levels and scales of observation. On the global level it is represented by the wide spectrum of organisms in the planetary flora and fauna, their populations and hierarchies. On an individual level it is reflected in anatomic variety. Microscopically, heterogeneity is present within cell populations, differentiation state, as well as cell cycle stage of individual cells. Biological variation is present even among organelles within individual cells, and reflected in their transcriptomes and underlying differences in their genomes and epigenomes ¹. Such vast and multilevel combinatorial palette provides an incredible capacity for adaptation of biological life.

A first level of heterogeneity is genomic. Genomes of different species display considerable difference, although many genes are evolutionary conserved ². Yet even within the same species, genomes are also not fully identical between individuals. Various mutations and variants, both inherited and acquired, yield unique individual genomes ³. Furthermore, diseases (for example, genomic integration of HIV ⁴ or mutations in cancer ⁵) as well as genotoxic exposure (such as impaired DNA repair upon exposure to radiation ⁶) may alter the genome of individual cells, leading to acquisition of genomic heterogeneity among the cells even of the same organism.

A second layer of heterogeneity manifests in the transcription of genes regulated by the epigenetic landscape and transcription factors ⁷. The epigenetic landscape defines chromatin accessibility, as only open heterochromatin is efficiently transcribed. Chromatin landscape is characterized by epigenetic marks, which include histone modifications (methylation, acetylation, biotinylation and others) and DNA modifications (like methylation, hydroxymethylation, acetylation and others) ⁸. Epigenetic marks are highly dynamic, and therefore serve to acquire heterogeneity upon extrinsic or intrinsic stimuli.

Additionally, transcribed pre-mRNA undergoes many further modification, including (differential) splicing, which cause various splicing forms of the same gene, RNA methylation and other epi-transcriptomic modifications ⁹. As a consequence, these multilayered processes result in heterogeneity among mRNA molecules, which are suitable for translation into proteins. Moreover, translation into proteins is also regulated by miRNA and lncRNA, as well as by the amount and activity of ribosomes ¹⁰. On top of that, translated proteins undergo post-translational modifications, which

may include assembly into protein complexes, cleavage of signaling elements, protein phosphorylation, acetylation, ubiquitination and many others ¹¹.

Altogether cells possess an incredibly complex and versatile system of regulation, supporting acquisition of cellular heterogeneity, and ultimately adaptation towards dynamic environments.

Genetically heterogeneous cells (for example due to mutations or variants), are not necessary transcriptionally heterogeneous ¹². It happens, for example, when DNA mutations or variants are located in areas of genome not transcribed in the current cell type. Further, transcriptional heterogeneity does not necessary advance to proteomic heterogeneity, for example, due to various RNA degradation mechanisms and nuances of RNA processing or properties and abundance of ribosomes ¹³. Finally, proteomic heterogeneity does not necessary lead to phenotypic differences among cells for various reasons, for example, absence of respective ligand or receptor ¹⁴. These examples render it apparent that methods used to study heterogeneity must be level-specific and no universal method exists to study cellular heterogeneity.

The most common way to assess differences between cells and tissues is histological analysis ¹⁵. Cells or tissues are chemically treated to visualize different cell types with visible dyes. This method is also the oldest, which basics were established by Nobel Laureate Paul Ehrlich in 1877 ¹⁶. Different chemical dyes stain specific organelles and cellular compartments, which are later assessed microscopically. One of the most popular histological methods, Hematoxylin and Eosin staining, colors nuclei in dark blue (hematoxylin) and cytoplasm in light pink (eosin) ¹⁷. Other popular chemical stainings include Masson's Trichrome staining (staining fibrotic tissue bright blue, nuclei dark blue and cytoplasm dark red) ¹⁸, Oil Red staining (colors adipocytes in red) ¹⁹, Nicotinamide adenine dinucleotide staining (rendering the mitochondria network dark blue) ²⁰ and many others. However, chemical stains provide only a handful of colors to distinguish the basic cell types and organelles.

The advent of immunostaining drastically enhanced histological analysis. Discovered in the immune system, antibody-antigen specificity allowed a sensitive method to visualize the presence of proteins in cells and tissues ²¹. In comparison to chemical stains, immunostaining provides a much higher variety of antibodies against various epitopes, which is only limited by the availability of fluorophores or conjugates. Briefly, an organism's immune system (commonly used are rabbits, mice, goats, donkeys or monkeys) is exposed to recombinant protein or a compound of interest. As

a result, the animal's immune system produces specific antibodies to detect (and ultimately eliminate) the original protein or compound. The antibody may then be used to detect the original protein or compound in other species. Due to structural conservation and to the benefit of reagent utility, many antibodies show species cross-reactivity²². To amplify the signal, it is common to employ a two-step immunostaining, combining primary and secondary antibodies. In this scenario, the secondary antibody is species-specific and detects the primary antibody. It usually carries a fluorophore and its signal may be detected by fluorescence microscopy. Due to the relative simplicity and a broad library of existing antibodies, immunostaining is widely used to decipher the cellular heterogeneity of tissues and cell cultures.

Later, the fluorescent in-situ hybridization (FISH) method was developed to directly measure the distribution of RNA molecules in the sample. Similarly to immunostaining, this method allows spatial microscopic evaluation of expression, albeit on the RNA, not the protein level²³. Sequence-specific RNA probes labeled with fluorophores are hybridizing to complementary RNA molecules in cells or tissues. The fluorescence signal is subsequently detected by microscope. This method is very sensitive and therefore widely used to investigate rare and subtle cellular fractions.

All microscopic methods (chemical staining, immunostaining, FISH, etc.) share, however, common caveats. First of all, such methods suffer from the low number of spectrally distinguishable fluorophores, therefore limiting simultaneous assessment of numerous targets. Depending on the microscope, it is difficult to clearly distinguish more than a handful of different fluorophores in the same sample, therefore restricting the analysis to only few proteins / RNA molecules. Secondly, depending on the optical system of the microscope, the magnification is limited and do not allow precise microscopy of compartments, which are smaller than organelles. Finally, researchers are limited by the availability of commercial reagents. Altogether, this sets limitations of the microscopical evaluation of cellular heterogeneity.

All methods presented so far are of a more or less targeted, implying pre-hoc knowledge of marker proteins or genes and their relation to different cell types or subtypes. In many cases, however, such markers are unknown, exemplifying the need for high-throughput unsupervised methods to decipher heterogeneity²⁴. Until recently, such approaches did not exist, but driven by rapid development of next generation sequencing (NGS) techniques, the last decade witnessed the arrival of powerful tools serving that purpose²⁵. Robust chemistry, advanced enzymes, constantly increasing

computational capacity and sophisticated bioinformatic analysis, all contributed to the advent of single-cell genomic, transcriptomic and epigenetic assays (Fig. 1).

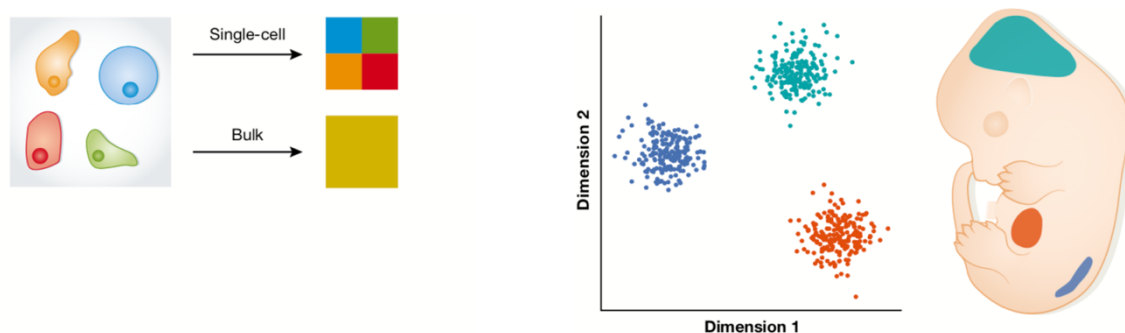


Figure 1. The concept of resolving cellular heterogeneity using scRNA-seq ²⁸

Starting in 2009 from manual picking of cells and separating them into single tubes for library preparation, single-cell techniques now allow omics with associated cell morphology information (e.g. Takara ICELL8) ²⁶, massive droplet-based arrays (e.g. Chromium 10X) ²⁷ or even multi-omics approaches, gathering two separate datasets from the same cells ^{28,29}. Multi-omics approaches are particularly fruitful: it is now possible to combine single-cell transcriptomics with chromatin accessibility or DNA methylation analysis ³⁰, as well as use cell-surface antibody-bound barcodes to define cell types ³¹. Single-cell techniques revolutionized the discovery of small and rare cell populations. Where it was previously necessary to know specific cell markers to separate cell types for bulk NGS analysis (for example by fluorescent-activated cell sorting (FACS) or magnet-activated cell sorting with specific antibodies), now scientists can use whole tissues, organs or biopsies with minimum sample loss and without any enrichment bias without the risk of losing populations during isolation or due to low sensitivity of antibodies. Current studies go so far as to even use whole organisms for single-cell analysis, resulting in unprecedentedly high resolution of cellular anatomy ^{32,33}.

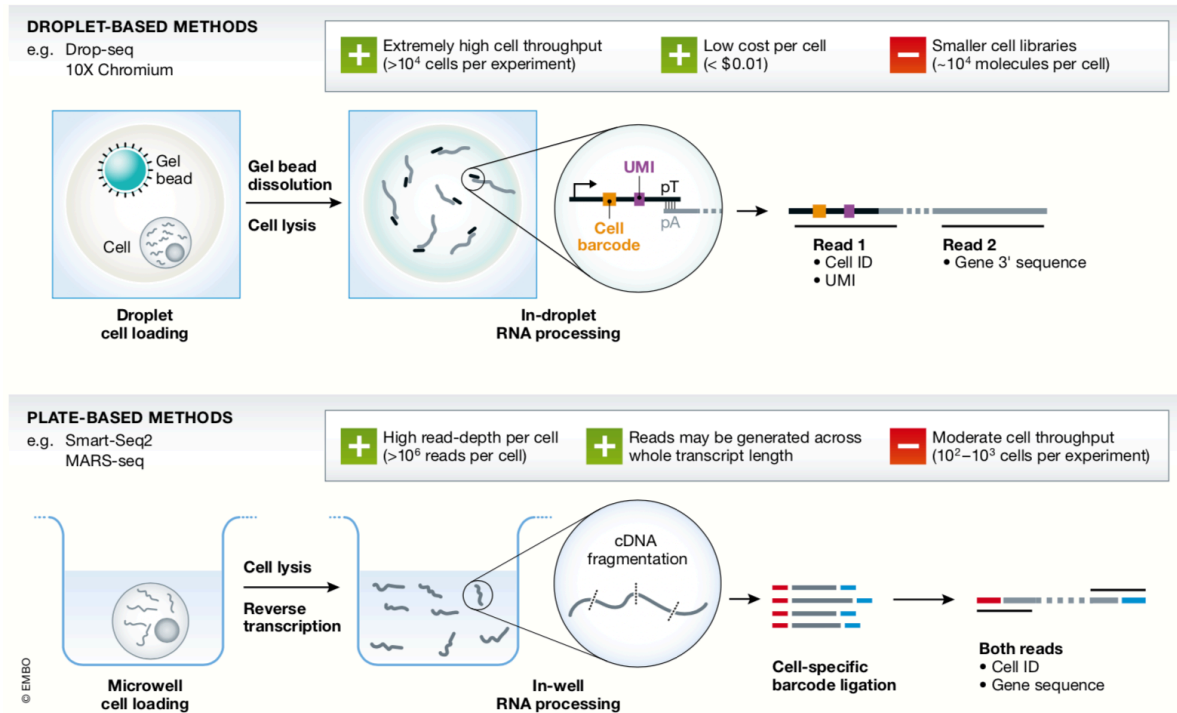


Figure 2. Overview of a scRNA-seq library preparation for Drop-seq (upper panel) and Plate-seq (lower panel) ²⁸

Single-cell techniques have plenty of advantages, but also have a list of caveats (Fig. 2). Firstly, high complexity of single-cell datasets and absence of standardized quality criteria may lead to grave misinterpretations of datasets (see chapter 3.1.1). Secondly, due to the inherent scarceness of input material, which limits the efficiency of library preparations, single-cell assays are less sensitive than bulk approaches ²⁶. Finally, due to massive parallelization of analysis (as compared to bulk analysis) all single-cell approaches are considerably more expensive than bulk ones and require deep sequencing, which altogether leads to increased experiment costs. However, steadily advancing NGS technology and constantly decreasing price per sequenced base suggests that single-cell studies will get even more attractive with time.

1.2. Heterogeneity of stem cells

Stem cells are characterized by their capacity to differentiate into various cell types, as well as to self-renew. There are two major types of stem cells in mammals: embryonic stem cells (ESC) and adult stem cells (ASC). ESC are isolated from the inner cell mass of blastocysts during the early development of an embryo, while ASC are tissue-specific and are found in fully developed adult organisms. In contrast to ESC, which give rise to the full complement of cell types in the organism, ASC are

restricted progeny of respective tissue- or organ-specific cell types ³⁴. During the development of organism, the differentiation capacity of stem cells decreases (Fig. 3). Initially, the zygote gives rise to totipotent cells, which harbor the highest differentiation potential, generating the embryo proper and extra-embryonic tissue. One step further, pluripotent cells form that give rise to all cell types of the organism, except the primitive endoderm. In contrast to totipotent stem cells, pluripotent cells do not give rise to placenta (trophectoderm). Subsequently, the formation of three germ layers restrict pluripotent stem cells into multipotent ectodermal, endodermal and mesodermal stem cells, respectively. Multipotent stem cells, which include ASC, give rise to somatic cells. The process of differentiation is orchestrated by acquisition of lineage-specific and attenuation of pluripotency-associated expression patterns ³⁵. Differentiation is accompanied by changes in the epigenetic landscape: the chromatin becomes increasingly condensed, and primarily lineage-specific gene regions remain accessible ³⁶. Not only chromatin accessibility, but also epigenetic marks are changing during cellular differentiation. Particularly, DNA methylation is tightly correlated with the differentiation process, restricting transcription to cell type specific genes ^{37,38}.

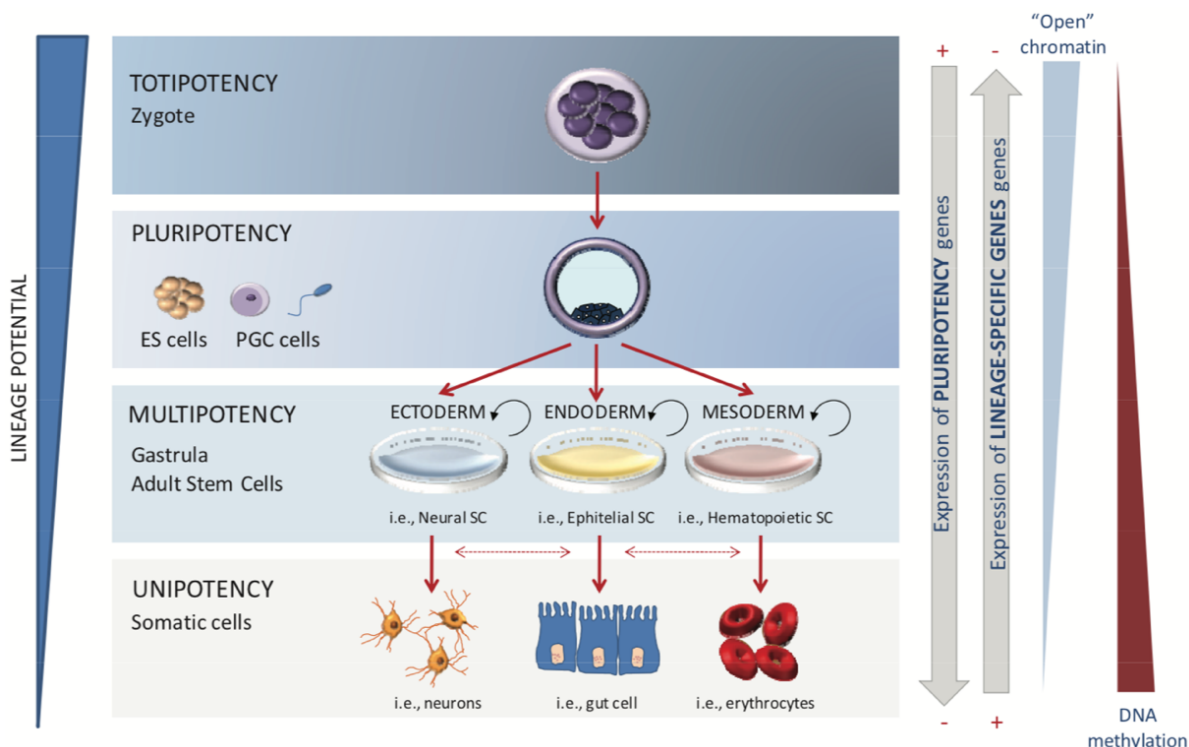


Figure 3. Lineage restriction of human developmental potency ³⁷

Several fully developed tissues and organs harbor ASC, and many stem cell populations were reported to have intrinsic heterogeneity ³⁹ (Table 1).

Table 1: Major types of adult mammalian stem cells and heterogeneity among them

Type	Function	Heterogeneity	Ref.
Hematopoietic stem cells	Formation of the blood cells during hematopoiesis	Short- and long-term repopulating stem cells are phenotypically and functionally distinct; Heterogeneity is based on the lineage bias (Lineage-balanced, Myeloid-, Lymphoid-, Megakaryocyte-biased stem cells)	40
Mammary stem cells	Formation of the mammary gland during puberty and gestation	Heterogeneous based on distinctive molecular markers and context-dependent functions (Basal-restricted stem cell, multipotent cycling stem cell, multipotent quiescent stem cell; Luminal-restricted stem cell, Luminal ER- stem cell (estrogen receptor negative), Luminal ER+ stem cell (estrogen receptor positive))	41
Intestinal stem cells	Formation of the surface cells of small and large intestines	Heterogeneous based on regional differences in crypt size, proliferative index and the distribution of proliferative cells along the crypt axis; Heterogeneity based on transcriptional profile	42
Mesenchymal stem cells	Differentiate into osteoblasts, chondroblasts, adipocytes, neuroectodermal cells and hepatocytes	Heterogeneous based on expression of pluripotent stem cells markers (such as Oct4, Nanog, Sox2, ABCG2); differences based on the tissue (Bone marrow, Wharton's jelly, umbilical cord blood, Adipose tissue, Molar cells, Amniotic fluid)	43
Endothelial stem cells	Differentiate into endothelial cells, which line blood vessels	Heterogeneous based on expression of cell surface markers (CD34, CD133, KDR)	44
Neural stem cells	De-novo neurogenesis	Stem cells of the ventricular-subventricular zone are anatomically and transcriptionally different; Heterogeneous in relation to pre- and post-natal quiescence and activation processes. Hippocampal neural stem cells are heterogeneous based on morphology, metabolism and response to stimuli	45,46
Spermatogonial stem cells	Maintenance of the spermatogonial population	Heterogeneity based on morphological features, which are also transcriptionally distinct (A_s , A_{pr} and A_{ai})	47

Muscle stem cells	Give rise to the muscle fibers and essential for the muscle regeneration	Heterogeneous based on quiescence level (quiescent / activated), activity of metabolism, asymmetric division, speed of proliferation; Differences are orchestrated by specific signaling cascades, as well as underlying transcriptional and epigenetic deviations)	48
Pulmonary stem cells	Regenerate the epithelium of lung alveoli	Heterogeneous based on the target cell type of surface airway epithelium in the trachea and bronchi; Differences between Basal (Neuroendocrine, Brush, Ionocyte, Pre-ciliated cells), Secretory (Club-like, Goblet, Multiciliated cells) and Alveolar (Alveolar epithelial progenitors and alveolar type 2 cells) cell lineages	49
Sweat gland stem cells	Formation of the sweat glands	Heterogeneous based on stem cell potency and corresponding physiological roles	50
Vocal fold mucosa stem cells	Formation of the vocal fold	The cell pool is divided into cobblestone-like cells, vocal fold stellate cell-like cells and fibroblast-like spindle cells; The heterogeneity could be caused by mechanical regulation (tension during phonation)	51
Stem cells in the ovary	Renewal of the follicles in the ovary	Heterogeneous based on quiescence state: quiescent “very small embryonic-like stem cells” (VSELs) and activated ovarian stem cells (OSC)	52

It has been assumed that the intrinsic heterogeneity of ASC populations is crucial for tissue and organ homeostasis. However, many properties of ASC subpopulations are unknown, and high-throughput analyses are required to decipher their functions.

1.3. Mammalian ageing and its hallmarks

Ageing represents an accumulation of changes in organisms, acquired over the lifespan. In humans, such changes may be separated into changes in the physical, psychological and social domain, and only physical aspects will be assessed in this thesis.

The causes of ageing are still primarily unknown and only a handful of clues are available. The effect of ageing is ubiquitous – it affects all organs, tissues and cells in mammalian organism ⁵³. As a rule, these effects are negative and examples are an increased probability of diseases acquisition ⁵⁴, decreased fertility with complete loss in menopause (in females) ⁵⁵, sarcopenia in muscles ⁵⁶, atherosclerosis of vessels ⁵⁷,

dementia and development of cognitive impairment of the brain ⁵⁸. The age-induced impairment of organismic functions is so broad and pleiotropic, so inseparable from human tradition and history, that it is considered a normal and inevitable part of biological life ⁵⁹. However in the modern ageing society, more and more scientists consider ageing a long-ongoing multisymptomatic disease, and it may therefore not without merit to search for a cure ⁶⁰.

The modern view on ageing defines 9 distinct hallmarks of ageing (when restricting scope to mammals) ⁶¹:

- 1) **Genomic instability.** Organismal DNA undergoes changes throughout life, primarily by accumulation of mutations ⁶².
- 2) **Telomere attrition.** Telomeres are repetitive regions at the termini of eukaryotic chromosomes, which have protective function against DNA damage and prevent fusion with neighboring chromosomes. Telomeres are shortened during cell mitosis, and convey the capacity of 50-70 cell divisions (so called Hayflick limit ⁶³). When exceeding this limit, cell undergoes senescence. Restorative maintenance of telomers is achieved by telomerase, an enzyme that is present in embryonic stem cells, male sperm cells, epidermal cells, activated T cells, B cell lymphocytes, certain ASC and cancer cells, but not in the majority of somatic cells. Transgenic overexpression of Telomerase immortalizes otherwise mortal cells (i.e. they never reach senescence), increasing, however, the risk of malignancies.
- 3) **Epigenetic alterations.** Ageing dramatically changes the cellular epigenetic landscape ⁶⁴. This includes changes in chromatin accessibility, DNA methylation patterns and various epigenetic marks.
- 4) **Loss of proteostasis.** Proteostasis is a generic term to define protein biogenesis, folding, trafficking and subsequent degradation. Ageing considerably attenuates these processes ⁶⁵.
- 5) **Deregulated nutrient sensing.** Anabolic signaling is proposed to be an accelerating factor of ageing, while decrease of nutrient signaling is associated with delayed onset of ageing ⁶⁶.
- 6) **Mitochondrial dysfunction.** Ageing is clearly associated with decreased functions of mitochondria ⁶⁷. However, it has not been formally shown yet that improved mitochondrial function slows the ageing process.
- 7) **Cellular senescence.** Senescence is commonly characterized as an irreversible cell cycle arrest, accompanied with drastic functional decrease ⁶⁸.

Originally associated with cells beyond the Hayflick limit, it is now also used to describe aged cells, which exhaust their normal functionality (for example, regenerative capacity) independent of the number of divisions they have undergone. Some authors speculate that senescence is a compensatory response to accumulated cellular damage, which may be beneficial *per se*, but become harmful when senescent cells prevail in or dominate cell populations.

8) **Stem cell exhaustion.** Decline of the regenerative potential is one of the most profound hallmarks of ageing ⁶⁹. It affects the majority of ASC, including the immune system ⁴⁰, forebrain ⁴⁵, bone ⁴³ and muscle ⁷⁰.

9) **Altered intercellular communication.** Ageing alters cell-to-cell communication and severely affects the autocrine and paracrine signaling in the niche ⁷¹.

Collectively, ageing has pleiotropic effects on the organism, which may be crudely dissected into separate phenotypes. Tackling them all may result in organismic rejuvenation. For example, there is a clear correlation between healthy lifestyle and longevity. Caloric restriction, physical exercise and avoidance of chronic stress have profound beneficial effects on the length of mammalian life.

1.4. Heart physiology and anatomy in brief

The heart is a muscular organ whose primary task is to pump blood through the cardiovascular system ⁷². To achieve that, the mammalian heart is built of 2 atria and 2 ventricles, connected to the vasculature by veins (vena cava superior and pulmonary veins) and arteries (Aorta and pulmonary artery). In addition, a system of heart valves ensures one-way flow of blood from the left and right atria to left and right ventricles, respectively (Fig. 4). The contractile cycle of the heart consists of diastole and systole: in a first step ventricles are relaxed and filled with blood (through the mitral and tricuspid valves). In the subsequent second step the heart contracts (atria first, followed by ventricles) and pushes the blood into the circulation (through the aortic and pulmonary valves). In turn, the contraction of the heart muscle (myocardium) is regulated by an autonomous system of pacemaker cells, concentrated in the sinoatrial node. Pacemaker cells are connected to the myocardium through the Bundle of His and Purkinje fibers. In general, the heart rate and the cardiac output are regulated by oxygen demand of the organism and may vary in accordance to physical activity and other factors.

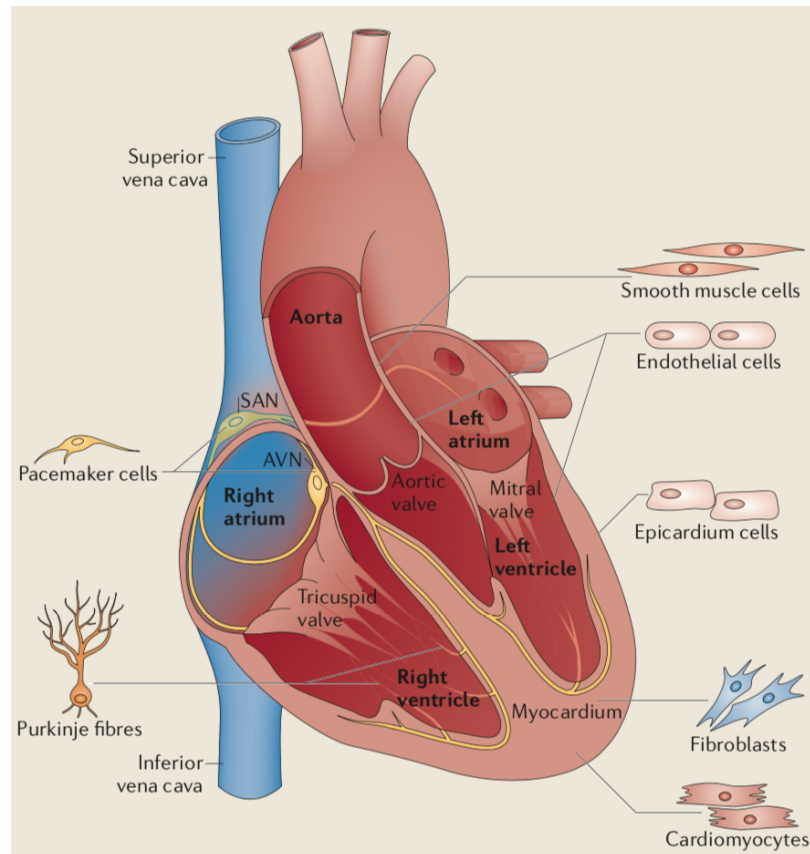


Figure 4. Schematic anatomy of the human heart and its resident cell types ⁷³

The mammalian heart wall consists from 3 layers ⁷⁴: endocardium (inner wall), myocardium (musculature) and epicardium (outer wall) (Fig. 5). The endocardium, which lines the heart valves and chambers, consists of a simple squamous epithelium. It continues into the endothelium of veins and arteries. Endocardium and myocardium are connected by a thin layer of connective tissue. The myocardium is a striated muscle layer, therefore responsible for involuntary heart contraction. Notably, the pattern of muscle fibers in the heart represents a set of complex swirls across the ventricles and atria. Cardiac muscle contractility relies on cardiomyocytes (approx. 20% of all myocardial cells) and the pacemaker cells (approx. 1% of all cardiomyocytes). At last, the pericardium forms a sack, surrounding the heart. It consists of the fibrous membrane (outer surface) and double serous membrane (inner surface). The serous membrane secretes a lubricant (pericardial fluid). Therefore, the main functions of the pericardium are structural (stabilization of heart in the chest and movement lubrication) and barrier (protection from infection).

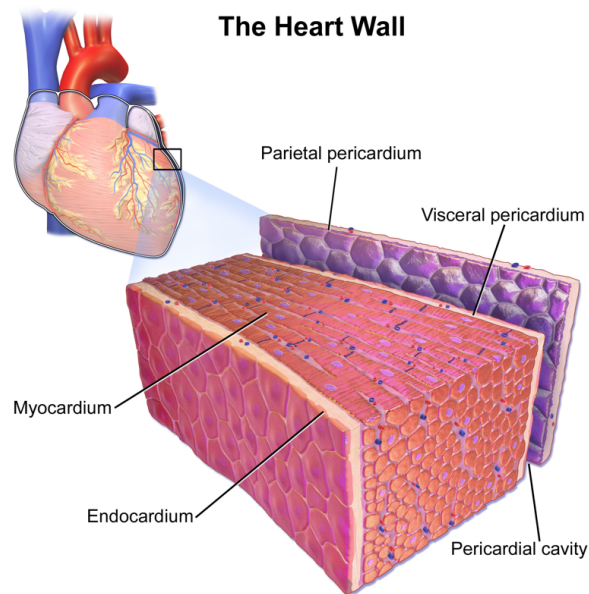


Figure 5. Layers of the human heart wall ⁷⁵

Coronary vasculature is responsible for the supply of oxygen and nutrients to the heart, as well as for the removal of metabolic waste (Fig. 6). In essence, the coronary vasculature comprises veins, arteries and lymphatic vessels. The blood supply for coronary arteries comes directly from the aorta and divides into the left main and the right coronary artery. The left main coronary artery further divides into the left anterior descending and left circumflex arteries. The coronary arteries continue to branch into smaller arteries. The vein system is represented by the coronary sinus vein, which receives blood from the great cardiac vein, the posterior cardiac vein, the middle cardiac vein as well as small cardiac veins. The blood from the anterior cardiac vein is fed directly back into the right atrium.

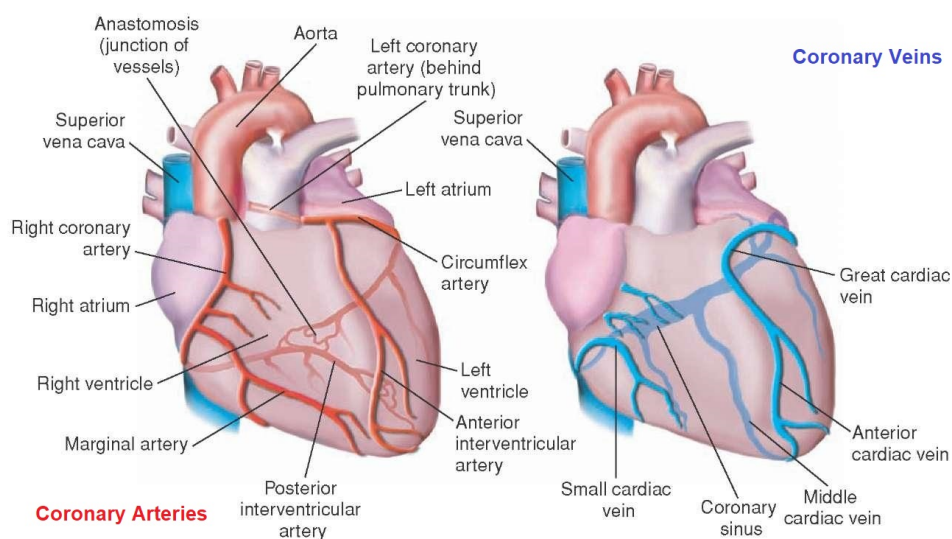


Figure 6. Coronary circulation of the human heart ⁷⁵

1.4.1. Cardiac remodeling and regeneration

Cardiac remodeling summarizes changes in heart size, shape, structure and function. Remodeling may be triggered by a physiological process (like exercise) or pathological malfunction (injury or disease) ⁷⁶. The major causes of remodeling include acute myocardial infarction, increased blood pressure or blood volume, damage to heart valves and others. The most prominently studied instances of cardiac remodeling include dilated, hypertrophic and restrictive cardiomyopathies (Fig. 7) ⁷⁷.

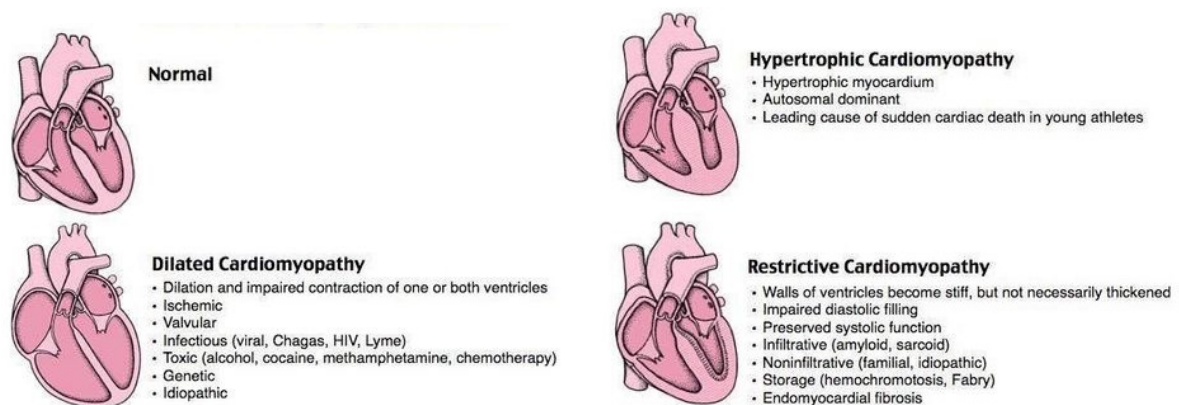


Figure 7. Major types of cardiomyopathies ⁷⁷

The myocardium, the primary layer of the heart, is involved in cardiac remodeling. The classical example of cardiac remodeling are the consequences of acute myocardial infarction (Fig. 8) ⁷⁸. Infarction refers to tissue necrosis, induced by insufficient blood supply. Essentially, primary causes of the myocardial infarction are blocked cardiac arteries.

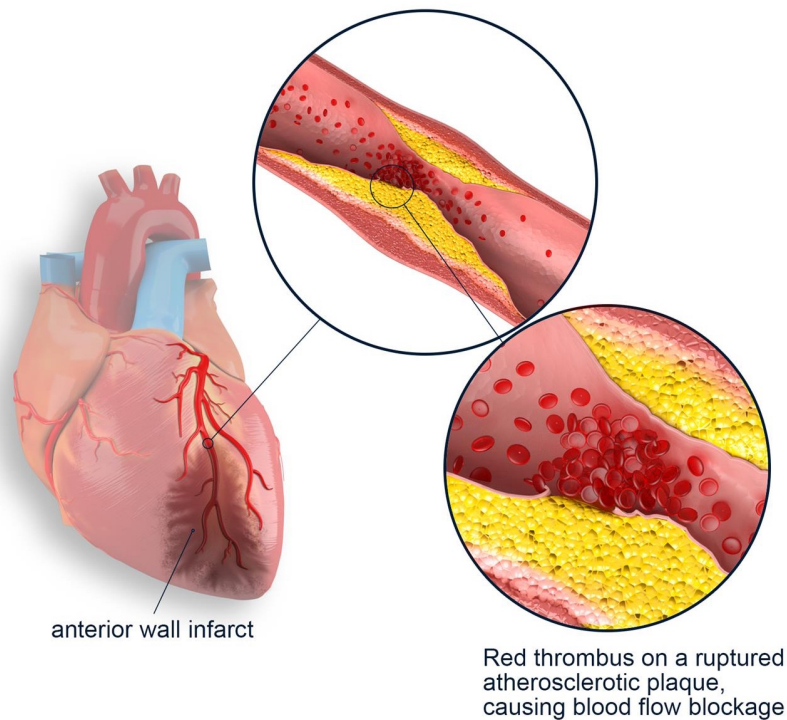


Figure 8. Myocardial infarction in a nutshell ⁷⁵

Impaired blood flow results in a shortage of oxygen, which eventually leads to myocardial damage via ischemic cascade. This process generally associated with a lack of oxygen-dependent ATP production in cardiomyocytes mitochondria. As a consequence, affected cardiomyocytes undergo either necrosis, apoptosis or autophagy ⁷⁹. Subsequently, this activates the immune system, leading to a massive inflammatory response. Dead cardiomyocytes are eventually removed by neutrophils and macrophages. As a result, cardiomyocytes, which survive infarction, undergo spatial, morphological and metabolic remodeling ⁸⁰. Finally, fibroblasts are being activated and repopulate the infarcted region, resulting in fibrosis. In contrast to skeletal muscle, the adult mammalian heart is unable to regenerate and instead forms a patch of scar tissue. Scarring maintains the function of a damaged heart to a certain extent, but the global condition of the heart continues to decline over time ⁸¹.

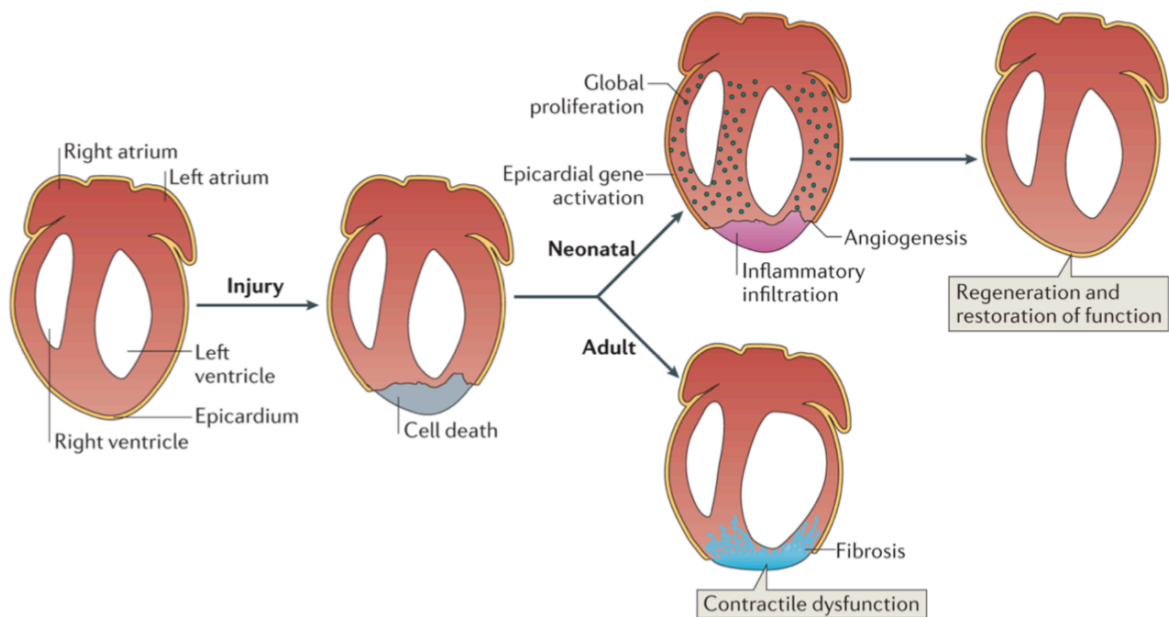


Figure 9. Mammalian hearts lose their regeneration capacity within one week after birth ⁷³

Interestingly, the mammalian heart can regenerate during the first 7 days after birth (Fig. 9) ⁷³. Neonatal cardiomyocytes retain a proliferation potential and may therefore regenerate injured heart area. However, neonatal cardiomyocytes undergo maturation into adult cardiomyocytes and enter a state of cell cycle arrest. This arrest underlies the absence of myocardial regeneration in the adult mammalian heart. The inability of adult cardiomyocytes to proliferate is claimed to be a protective mechanism against unwanted proliferation ⁷³. It is important to mention, that a slow turnover of cardiomyocytes was detected throughout the human life. Cardiomyocytes are replaced with an estimated yearly rate of 5% at the age of 15 and of 0.5% at the age of 60. The underlying mechanisms of this turnover remain unclear ⁸².

Most of the cardiomyocytes are comparatively large and rod-shaped, with average lengths around 100 μm and diameters between 10 and 25 μm (Fig. 10). Upon hypertrophy, cardiomyocytes produce additional sarcomeres, which lead to increased cross-sectional area. Notably, cardiomyocytes may have different number of nuclei and different nuclei ploidy. For example, in mice the majority of cardiomyocytes are binucleated (approx. 90%) with a small percentage of mononucleated and multinucleated cells (approx. 10%) ⁸³. Furthermore, around 10% of binucleated cardiomyocytes nuclei have 4n ploidy.

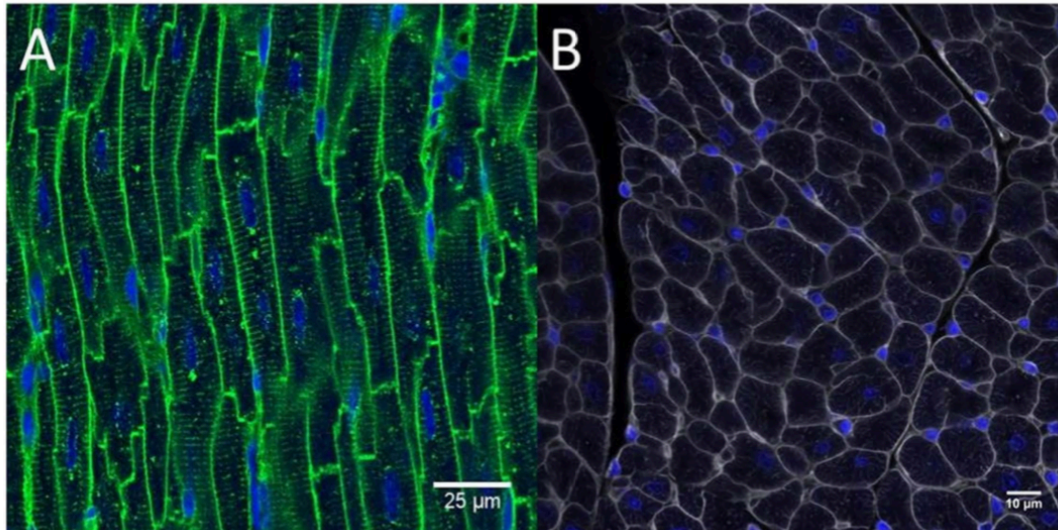


Figure 10. Cardiomyocytes in sections parallel (A) and perpendicular (B) to fiber direction. DAPI appears in blue, WGA-AF488 appears in green (A) and gray (B) ⁸³

The reason for multinucleation remains unclear and it is also unknown whether cardiomyocytes with distinct numbers of nuclei or different size are functionally or transcriptionally divergent.

1.5. Skeletal muscle physiology and anatomy in brief

Skeletal muscles are required for voluntary movements ⁸⁴. Muscles contain fascicles, which bundle different types of muscle fibers. Muscle fibers represent the individual contractile units due to the high content of sarcomeres, composed of actin and myosin proteins, which are separated by Z discs. Sliding of actin on the myosin filament results in shortening of the sarcomere, causing contraction of muscles (Fig. 11).

Myofibers have a tight internal organization. Most of the cytoplasm is occupied by myofilaments and thus referred to as sarcoplasm. Typically, myofibers have multiple nuclei, which appear flattened and are located close to the cellular membrane. In contrast, mitochondria are located between the myofibrils. Myofibrils are surrounded by sarcoplasmic reticulum, whose main purpose is to store (and release) calcium. Notably, enlarged areas of sarcoplasmic reticulum are referred to as terminal cisternae. Connected they form transverse tubules (T-tubules). As a result, T-tubules are transmitting the activating action potential and eventually cause skeletal muscle contraction.

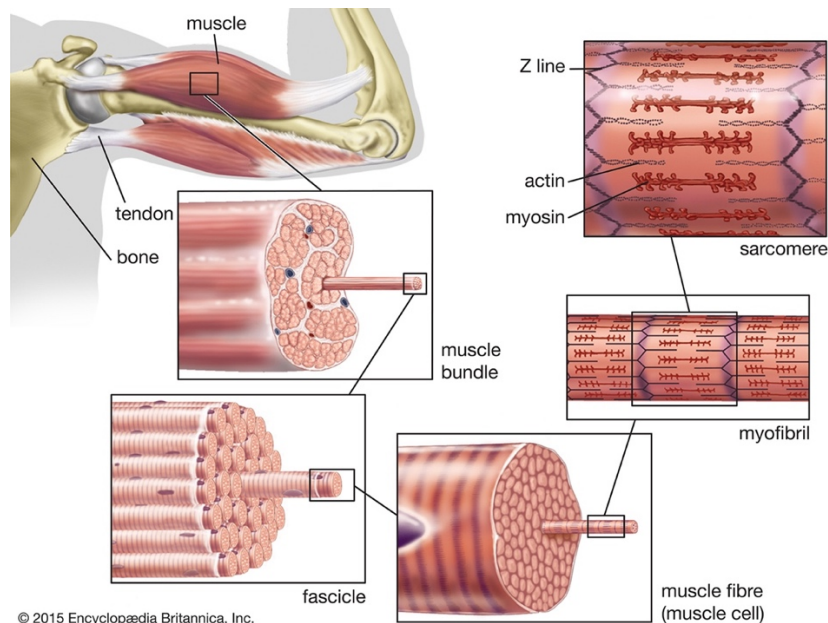


Figure 11. Skeletal muscle structure

Skeletal muscles are innervated by somatic nerves, 60% of which are motor neurons and 40% are sensory neurons (Fig. 12)⁸⁵. A single motor neuron innervates a group of muscle fibers (5-10 fibers), which is referred to as a motor unit. Each myofiber has one neuromuscular junction (NMJ), a chemical synapse, to which the motor neuron connects. In order to transmit a signal, presynaptic terminals of motor neurons release acetylcholine, which binds to nicotinic acetylcholine receptors in the NMJ. In contrast, sensory neurons are primarily twisted around muscle spindles, and sense mechanical tension. Typically, muscle spindles are formed by 6-13 small muscle fibers, which are called intrafusal muscles. Muscle spindles stimulate sensory neurons upon elongation.

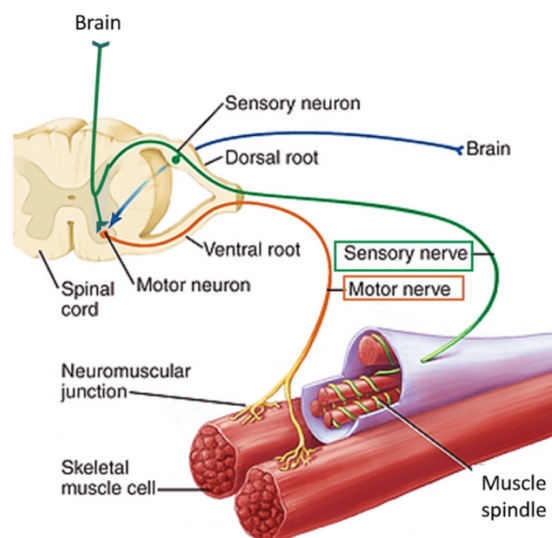


Figure 12. Innervation of the skeletal muscle

1.5.1. Muscle regeneration and the role of muscle stem cells

Skeletal muscle has a remarkable life-long regeneration capacity. The process of muscle regeneration requires a sophisticated interplay of various cell types, orchestrated by complex spatial and temporal signaling pathways (Fig. 13). Muscle stem cells (MuSCs, also called satellite cells) are essential for muscle regeneration^{86,87}. Typically, these cells are located under the basal lamina of muscle fibers, and in absence of muscle injury are mostly preserved in a quiescent state. Quiescent MuSCs express the *Pax7* transcription factor, which following activation of MuSCs may trigger *Myf5* and *MyoD* transcription factor activity. Muscle injury activates MuSCs, therefore triggering extensive proliferation. Through asymmetric cell division, however, a small fraction of activated cells is reserved for self-renewal and later returns to quiescence.

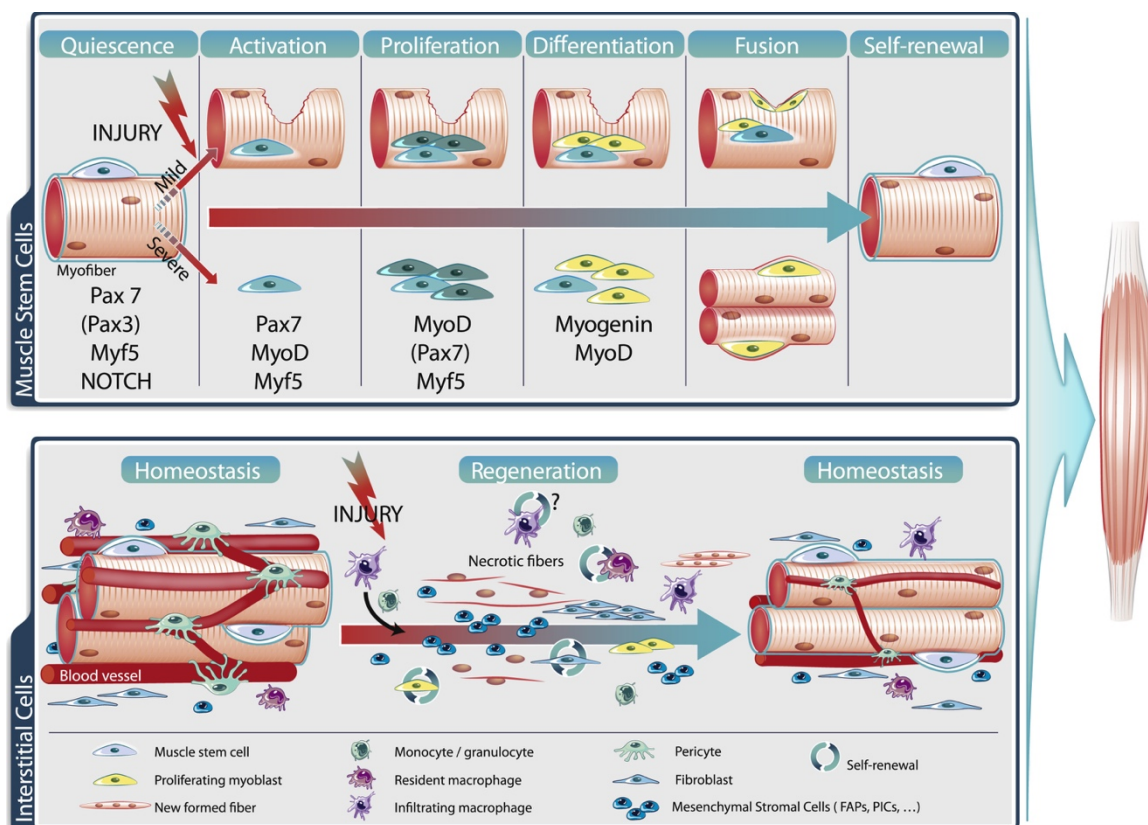


Figure 13. Overview of the skeletal muscle regeneration process⁸⁸

At the initial stage of muscle regeneration (1-2 days after injury), fibro-adipogenic progenitor cells (FAPs) secrete inflammatory cytokines, which attract neutrophils, monocytes and other immune cells. They remove damaged necrotic muscle fibers and establish room for formation of new muscle fibers⁸⁹. Within a few days FAPs proliferate, secrete extracellular matrix (ECM) components (mainly

collagens) and transform into myofibroblasts. Myofibroblasts replace necrotic muscle fibers, providing a scaffold for newly forming myofibers. Activated MuSCs transition into myoblasts, and after sufficient proliferation, start to express *Mrf4* and *MyoG* transcription factors, which are required for differentiation and eventually cell fusion into muscle fibers. At later stages of muscle regeneration, myofibroblasts undergo apoptosis and are replaced by newly formed muscle fibers. Skeletal muscle regeneration also requires vascularization and re-innervation of newly formed fibers. MuSCs, reserved for self-renewal, repopulate the stem cell pool to basal level and return to quiescence.

It is known that both MuSC numbers and regenerative potential decrease with age in mammals ⁷⁰. The gradual decrease of MuSCs number in aged organisms is connected with disturbed regulation of quiescence ⁹⁰. Additionally, impairment of asymmetric cell division reduces the ratio of MuSCs that return to quiescence ⁹¹. Functionally, MuSCs in aged individuals exhibit decreased capacity to regenerate muscle – they have lower proliferation rates and are prone to precocious differentiation ⁹². The mechanisms of MuSCs ageing are still unclear, although few hallmarks were identified (Fig. 14). Among them is accumulation of DNA damage ⁹³. It originates from exposure to ultraviolet and ionizing radiation, chemical damage, reactive oxygen species and others. DNA repair mechanisms are also attenuated with age, which may contribute to accumulating damage ⁹⁴. Furthermore, ageing induces alterations in the chromatin landscape, which primarily include chromatin accessibility, DNA methylation and histone modifications ³⁷. Histone modifications, including methylation, phosphorylation, ubiquitination, acetylation and others have major effects on initiation or suppression of gene expression. It has been shown that ageing induces acquisition of suppressing histone marks (like *H3K27me3*) and loss of certain enhancer marks (like *H3K4me3*). Such alterations have a dramatic effect on the cellular transcriptome and overall cell viability and behavior ⁹⁵.

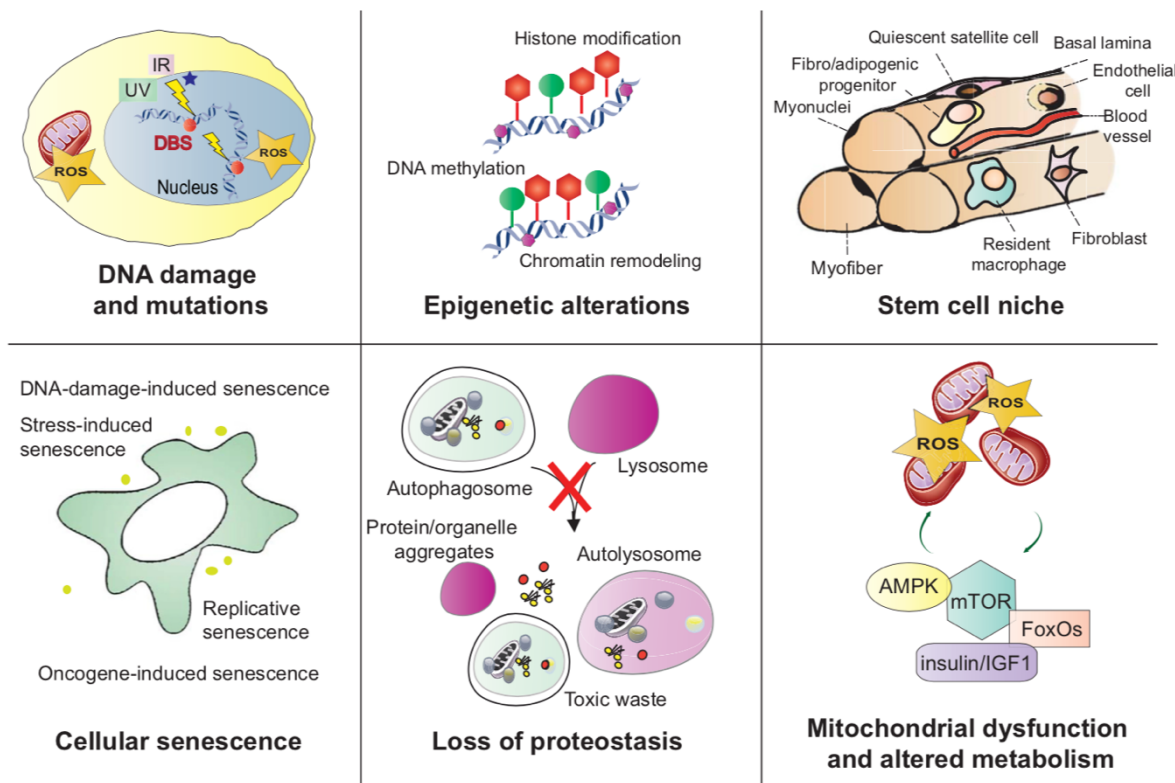


Figure 14. Hallmarks of ageing in the muscle stem cells ⁹⁰

Moreover, the MuSC niche undergoes drastic changes with age ⁷⁰. Disturbance of the MuSC niche drives change or even loss of proper regulatory networks. Involved signaling pathways include Notch, mTOR, TGF β , JAK/STAT, NF- κ B, MAPK/ERK, Sprouty and others ^{96,97}. Altered niche signaling affects MuSCs quiescence, activation, decreases myoblast proliferation and limits muscular regeneration in general ⁹⁸. Not only signaling within niche, but also circulating factors influence the state of MuSCs. Strikingly, exposure to juvenile circulation (in heterochronic symbiosis) restores muscle regeneration capacity in aged mice ⁹², which suggests that young animals own certain circulating factors exerting positive effect on MuSCs that are lost during ageing ⁹⁹.

1.6. Aims of dissertation

The dissertation had 2 major aims:

- 1) Deciphering cellular heterogeneity within cardiomyocytes, focusing on transcriptional differences between mono- and multi-nucleated cardiomyocytes in healthy and hypertrophic hearts.
- 2) Deciphering cellular heterogeneity within muscle stem cells and its impact on muscle regeneration in young and aged mice.

2. MATERIALS AND METHODS

2.1. Animal experimentation

2.1.1. Proposals for animal experiments

All animal experiments were planned and performed in accordance with German animal protection laws and EU ethical guidelines (Directive 2010/63/EU). All animal experiments were approved by the local governmental animal protection authority (*Regierungspräsidium Darmstadt*). The first chapter of *Results* is covered by the TVA license (*Tierversuchsantrag*) B2/1208 and the second and third chapters are covered by TVA license B2/1211.

2.1.2. Maintenance of mice

All mice were kept under strictly hygienic conditions in a separate animal facility. Animal cages were filled with sterile wood chips and paper tissues. Every cage had hanging water bottle and food container. All cages were connected to the air filtration system and cages were opened only under the laminar hood. Animal caretakers and scientists communicate via special internal software, called CAT system (*Computer administriertes Tierhaus*, provided by the Max-Planck-Institute Göttingen, Germany).

2.1.3. Sacrificing the mice

Mice were anesthetized through inhalation of 2% Isoflurane. Sacrificing was performed by cervical dislocation.

2.1.4. Transverse aortic constriction

Six-month-old C57Bl6 male mice were used for the transverse aortic constriction (TAC). TAC was accomplished using 26-gauge needles to partially ligate the proximal aorta resulting in an acute left-ventricular pressure overload. Pressure overload inside the left ventricle resulted in heart hypertrophy.

2.1.5. Magnetic resonance tomography

Magnetic resonance tomography (MRI) was performed before TAC operation and after on a 7.0 Brucker Pharmascan. Mice were anesthetized by Isoflurane (1.5-2%) and kept on a thermostat (37°C). MRI data was analyzed using Qmass digital imaging software (Medis).

2.1.6. Cardiotoxin regeneration assay

Cardiotoxin (CTX) injury assay is a well-established method to evaluate the efficiency of muscle regeneration. Mice were anesthetized by i.p. injection of 120 mg/KBW (kg-body-weight) Ketamine and 16 mg/KBW Xylazine. The fur from the *Tibialis Anterior* (TA) muscle was removed and the skin was disinfected with 80% ethanol. Muscle injury was induced by a local injection of 30µl of 0,1 mg/ml Cardiotoxin into the TA muscle. The mice received postoperative painkillers: Buprenorphine s.c. (0,1 mg/KBW right after operation) and 2,5 mg/100 ml Tramadol in drinking water for the next 5 days.

2.1.7. *Tibialis Anterior* muscle isolation

After sacrificing a mouse, the skin from the hindlimbs was removed. The upper fascia, covering the TA muscle, was cut and removed. The distal tendon of the TA muscle was cut with a scalpel. The TA muscle was pulled up with forceps and cut at the highest possible proximal position.

2.1.8. Diaphragm isolation

After sacrificing a mouse, skin from the chest was removed. The chest section of ribs was cut and removed. The heart and lungs were cut and removed. The diaphragm was rinsed with PBS and cut in the circular manner from the chest cavity. The diaphragm was transferred to a Petri dish with PBS and the leftovers of aorta and vena cava were removed.

2.1.9. Application of Galanin peptide

The Galanin peptide (40 µg/KBW) was injected i.p. daily.

2.1.10. Cre-lox (inducible) system

The Cre-lox is a transgenic technology, widely used in genetically modified animal models. The Cre recombinase enzyme is catalyzing the recombination of DNA at positions, delimited by LoxP sites. Therefore, the LoxP sites are introduced flanking to genomic sites of interest (e.g. exons or promoters of target genes) and DNA fragment between them is deleted. The Cre-lox system is widely used to generate knock-out, overexpression, exon-skipping and other genetic alterations *in vivo*. Usually the Cre-recombinase sequence is expressed under promoters of genes, which are

either ubiquitously expressed (to get a global recombination, for example *Rosa26^{Cre}*), or only expressed in the specific cell types (like *Pax7^{Cre}* for MuSCs, *LysM^{Cre}* for macrophages, *HSA^{Cre}* for skeletal muscle, *Nes^{Cre}* for neurons, etc.). Altogether, a Cre-lox recombination allows restriction of the genetic alteration to a specific cell type. Moreover, a Cre-recombinase could be either constitutively active or only be activated by injection(s) of Tamoxifen or other activators, which allows an induction of recombination in a spatiotemporal manner.

2.1.11. TetO-tTA/rtTA (inducible) system

The TetO-tTA/rtTA system allows regulation of the gene expression with a tetracycline or its derivatives (like doxycycline). There are 2 types of the system: Tet-On and Tet-Off. They enable turning on or turning off the expression of a target gene, respectively. Particularly, in the Tet-Off system, a tetracycline transactivator (tTA) protein binds to the TetO operator sequence (which is inserted before the target gene promoter) in **absence** of doxycycline. As a result, expression of the target gene is increased. Alternatively, the Tet-On system allows binding of a reverse tetracycline transactivator (rtTA) only in **presence** of doxycycline. The TetO-tTA/rtTA system allows flexible and precisely timed modulation of gene expression. Such, while the Cre-lox recombination is irreversible after exposure to Tamoxifen, the TetO-tTA/rtTA effect can be reversibly induced by supplement/removal of doxycycline.

2.1.12. List of used mouse strains

Table 2 lists mouse strains, which were used in the current dissertation.

Table 2. List of used mouse strains

No	Strain	Formal name	Function	Ref.
1	<i>Pax7:zsGreen</i>	<i>Pax7^{zsGreen}</i>	Expression of <i>zsGreen</i> fluorescent tag under <i>Pax7</i> promoter allows FACS of MuSCs.	100
2	<i>Gal KO</i>	<i>Pax7^{zsGreen} & Gal^{-/-}</i>	Germline knock-out of <i>Gal</i> gene with <i>zsGreen</i> MuSCs tag	101
3	<i>Gal TG OE</i>	<i>Pax7^{zsGreen} & Gal^{tetO} & tg^{rtTA}</i>	Germline overexpression of <i>Gal</i> gene with <i>zsGreen</i> MuSCs tag	102
4	<i>Anxa3 OE</i>	<i>Pax7^{zsGreen} & Pax7^{CreERT2} & Rosa26:<i>Anxa3</i>^{loxP}</i>	Overexpression of <i>Anxa3</i> gene in quiescent MuSCs, labeled with <i>zsGreen</i> tag	103
5	<i>Anxa3 OE</i>	<i>Pax7^{zsGreen} & Pax7^{CreERT2} & Rosa26:<i>Anxa3</i>^{Tomato}</i>	Overexpression of <i>Anxa3</i> gene in quiescent MuSCs, labeled with <i>zsGreen</i> tag, progeny is additionally labeled with Tomato mark	103
6	<i>Gal cKO</i>	<i>Pax7^{zsGreen} & Pax7^{CreERT2} & Gal^{loxP/loxP}</i>	MuSCs-specific inducible knock-out of <i>Gal</i> gene with <i>zsGreen</i> MuSCs tag	-

2.2. Molecular biology

2.2.1. Isolation of genomic DNA from mouse tail biopsies

Mouse tail biopsies were digested at 55°C overnight in 500 µl of TENS Buffer. The buffer composition: 50 mM Tris-HCl pH 8.0; 100 mM EDTA pH 8.0; 100 mM NaCl; 1% SDS; 200 µg/ml Proteinase K (freshly added before digestion). Genomic DNA was precipitated by 500 µl Isopropanol. The mixture was centrifugated for 10 min at 16k g and the pellet washed with 700 µl of 70% Ethanol. 300 µl of nuclease-free water was used for elution.

2.2.2. Genotyping

Genotyping was performed by a PCR amplification of the specific loci with the visualization on a gel electrophoresis. A thermostable 2X Taq PCR master-mix (containing PCR buffer and DNA polymerase) was used for the reactions (Vazyme, China). Per reaction, 8 µl of the PCR master-mix was mixed with 10 µl of nuclease-free water, 0.2 µl of each 100µM genotyping PCR primer and 1 µl of genomic DNA. The PCR program was adjusted based on the annealing temperature of every PCR primer combination. However, the template PCR program included 95°C denaturation for 5 minutes, followed by 30-35 cycles of denaturation (95°C), annealing (see Table 3) and extension (72°C). The PCR products were visualized on the 2% agarose gel (with addition of 35µl/L Ethidium Bromide).

Table 3: Genotyping primer combinations

Name	Sequence (5' -> 3')	Ann. temp., °C
Pax7:zsGreen (fw)	CTG CAT GTA CCA CGA GTC CA	57
Pax7:zsGreen (rev)	GTC AGC TGC CAC TTC TGG TT	
Gal KO (fw)	GCC TGC AGA CTG CGA TGG TA	60
Gal KO (rev)	GAC TGT GGG TGA TCC TCT CC	
Gel KO (neo)	CGC AGC GCA TCG CCT TCT AT	
Gal TG OE (Gal_fw)	GCC TGC AGA CTG CGA TGG TA	60
Gal TG OE (Gal_tetO)	TTT TGA CCT CCA TAG AAG ACA CC	
Gal TG OE (tg_tTA_fw)	GAC TGT GGG TGA TCC TCT CC	
Gal TG OE (tg_tTA_rev)	GAG TAT GGT GCC TAT CTA ACA TCT	
Pax7 CreERT2 (wt fw)	GTG TCT CCA AGA TTC TGT GC	58
Pax7 CreERT2 (fw)	ACT AGG CTC CAC TCT GTC CTT C	
Pax7 CreERT2 (rev)	GCA GAT GTA GGG ACA TTC CAG TG	
Rosa26_Anxa3 (fw)	CTT GCT CTC CCA AAG TCG CTC TGA G	57
Rosa26_Anxa3 (rev)	CTG CTT GGT ACT GCT TGA CAA TCA GCT G	

Gal cKO (i2)	GTC CCT GAA GCT GCT GAA GGT AG	60
Gal cKO (i3)	GTG AAT GGT GGT ATG AGG TCA GG	
Gal cKO (rev)	GGC ACA TGG CTG AAT ATC GAC GG	
Rosa Tomato (fw)	AAA GTC GCT CTG AGT TGT TAT	57
Rosa Tomato (rev)	GGA GCG GGA GAA ATG GAT ATG	
Rosa Tomato (spliAC)	CAT CAA GGA AAC CCT GGA CTA CTG	

2.2.3. Isolation of RNA

The isolation of RNA from cells and tissues was performed using QIAzol miRNEasy kit (Qiagen, USA) according to the manufacturer's protocol. Briefly, 700 μ l of the QIAzol lysis reagent was added to each sample. Addition of Chloroform afterwards allowed the separation of proteins and other residuals from the RNA. Samples were centrifuged, and the upper aqueous phase, containing RNA, was separated from the rest. 625 μ l (1.5x of the aqueous phase) of 99,9% Ethanol was added to the samples. Further, the samples were loaded on the Rneasy MinElute (Qiagen, USA) RNA purification columns and centrifuged. Such, RNA got bound to the membranes of columns. To remove the residual genomic DNA from the samples, the membranes were treated with a DNase enzyme according to the manufacturer's instructions (Qiagen, USA). After several washes with the ethanol-based buffers, RNA samples were eluted in 14 μ l of nuclease-free water. Final RNA concentration was determined by the HS RNA Qubit (Thermo, USA). The RNA integrity was evaluated by capillary gel electrophoresis (Fragment Analyzer, Agilent, USA).

2.2.4. Measurement of RNA and DNA concentrations

The concentrations were measured by the Qubit HS RNA and DNA kits according to the manufacturer's instructions (Thermo, USA). In brief, the measurement master-mix was prepared by mixing buffers and fluorescent dyes. To measure the sample concentration, 1 μ l of sample was added to 199 μ l of the master-mix. The fluorescent signal was measured by the Qubit device and initial sample concentration was interpolated based on empty (0 ng/ μ l) and positive (10 ng/ μ l) controls.

2.2.5. DNA and RNA size distribution analysis by capillary gel electrophoresis

The size distribution of isolated RNA molecules, as well as sequencing libraries (DNA) was evaluated using capillary gel electrophoresis. Both LabChip Touch 24 (Perkin Elmer, USA) and Fragment Analyzer (Agilent, USA) were used for this

purpose, depending on the number of samples to test (Fragment analyzer have the capacity to run more samples in one run). In brief, the nucleic acids, diluted in the TE buffer (Tris pH 8.0, Qiagen, USA) were loaded on the source plate. The gel and fluorescent dye (supplied in the kits) were premixed and loaded on the microcapillary chip (LabChip) or connected via pipes with the microcapillary array (Fragment Analyzer). By applying an electric current to the system, nucleic acids were floating through the gel with speed, inversely proportional to their size. Fluorescent dye allowed to monitor the amounts of fragments at the detection position of the system at every moment of the measurement. This results in an intensity curve, representing the size distribution of RNA or DNA molecules in the sample. To evaluate RNA integrity, ribosomal integrity factor (RIN) was calculated, using manufacturers software. In a nutshell, RIN is a proportion between intensities of 28S and 18S ribosomal RNA peaks.

2.2.6. Quantitative reverse transcription PCR (qRT-PCR)

The PrimeScript RT Master Mix (Takara Bio Inc, Japan) was used for reverse transcription of RNA into cDNA. Briefly, a 5X master-mix, containing reverse transcription buffer and reverse transcriptase, was added to RNA sample and incubated for 15 min at 37°C. The RT master-mix contained both poly-A and random octamers RT primers, which results in a synthesis of the whole transcriptome cDNA. The enzyme was then heat-inactivated by an incubation at 85°C for 5 sec. The acquired cDNA was used for qPCR. 2 µl of the cDNA-containing mixture was added to the 2X SYBR™ Green PCR master-mix (Thermo, USA) and 0.2µl of each 100µM transcript-specific primer. The SYBR™ PCR master-mix contained a fluorescence dye which intercalated with the double-stranded DNA during PCR elongation step. This allows to measure the PCR product concentration based on the intensity of a fluorescent signal. The PCR product is increasing at every PCR cycle, and *Ct* is proportional to the initial amount of cDNA molecules in the sample. Therefore, based on the number of cycles necessary to reach the plateau in amplification (the situation, when additional PCR cycles do not increase the SYBR™ fluorescence due to used up PCR reagents in the tube), we can evaluate the initial amount of RNA transcripts in the sample. The qPCR was performed on the MIC qPCR thermocycler (BMS, Australia). The template PCR program included 95°C denaturation for 5 minutes, followed by 40-45 cycles of denaturation (95°C), annealing (see Table 4) and extension (72°C). The relative expression of transcript was normalized to the expression of *Gapdh* gene.

Table 4: qRT-PCR primer combinations

Name	Sequence (5' -> 3')	Ann. temp., °C
Gapdh (fw)	CAG CAA GGA CAC TGA GCA AGA GAG	59
Gapdh (rev)	ATT CAA GAG AGT AGG GAG GGC TCC	
Gal (fw)	TGC AGG AAA GGA GAC CAG GAA G	
Gal (rev)	GCC TCT TTA CGG TGC AAG AAA CTG	
GalR1 (fw)	CAT TCG CAA AGA TTC ACA CCT GAG	
GalR1 (rev)	GTT TGT TTC TGT GTC TGG TCC ACT	
GalR2 (fw)	ACA GGT ATC TGG CCA TCC GCT AC	
GalR2 (rev)	ACT GGC GGT AGT AGC TCA GGT AGG	
GalR3 (fw)	TAC ACG CTG GAT GCC TGG CTC TTT	
GalR3 (rev)	GTA CCT GTC CAC GGA GAC AGC AG	
Anxa3 (fw)	CAT GGT GGC TCT TGT TAC TG	
Anxa3 (rev)	CAT CTG CCT GCT TGA CCT	
Esr1 (fw)	GCG CAG CTG TCT CCT TTC CT	
Esr1 (rev)	CGG TTC TTG TCA ATG GTG CA	

2.2.7. RNA sequencing library preparation (RNA-seq)

Isolated total RNA was used as an input for RNA-seq library preparation, using SMARTer™ Stranded Total RNA-seq Kit v2 (Pico input, Mammalian) (Takara, Japan), according to the manufacturer's instructions (Fig. 15). Briefly, RNA was denatured and fragmented at 95°C for 1-4 minutes, depending on the RIN factor. Then fragmented RNA was reverse-transcribed into cDNA using random octamers primers, resulting in generation of the whole transcriptome cDNA. Unique barcoded adapters were incorporated to both 3' and 5' ends of every cDNA fragment during an initial PCR amplification (5 cycles). Using LNA-based technology, the cDNA, complementary to ribosomal RNA, was depleted from the library. Final PCR was performed for 12-15 cycles, depending on the input amount of RNA (1-10 ng of total RNA usually). The libraries were purified and size selected (300-700 bp) using SPRI beads (Magbio, USA). The library concentration was measured by the DNA HS Qubit kit. The size distribution of the library was evaluated by capillary gel electrophoresis (PerkinElmer Lab Chip 3K DNA or Agilent Fragment Analyzer DNA HS).

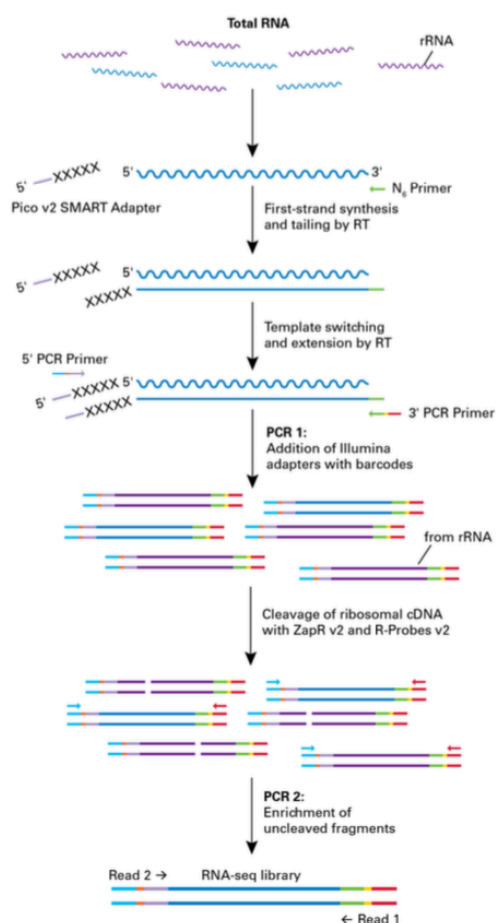


Figure 15. The workflow diagram for the SMARTer™ Stranded Total RNA-seq kit v2

2.2.8. Assay for transposase-accessible chromatin library prep. (ATAC-seq)

Primary cells were used as input for ATAC-seq library preparation (Fig. 16). Briefly, cells in suspension were centrifuged for 5min 600g (or higher, according to cell type) at 4°C to form cell pellets. Then cell pellets were mixed with the Tagmentation mix and incubated for 30 mins at 37°C at thermo-shaker. The Tagmentation mix was composed of 12.5µl 4X THS buffer, 5µl 0.1% Digitonin detergent (Promega, USA), 30µl nuclease-free water and 2.5 µl TDE1 transposase (Nextera™ DNA kit, Illumina, USA). The 4X THS Tagmentation buffer was composed of 132 mM Tris-acetate (pH 7.8), 264 mM Potassium acetate, 40 mM Magnesium acetate, 64% v/v Dimethylformamide (DMF). After Tagmentation, DNA fragments were purified using MinElute PCR purification columns (Qiagen, USA). 250 µl of PB buffer (binding & lysis buffer) was added to each sample and the whole mixture was loaded on the purification column. The column was washed 2 times with 500 µl of PE buffer (ethanol-based washing buffer) and the DNA was eluted in 10 µl of nuclease-free water.

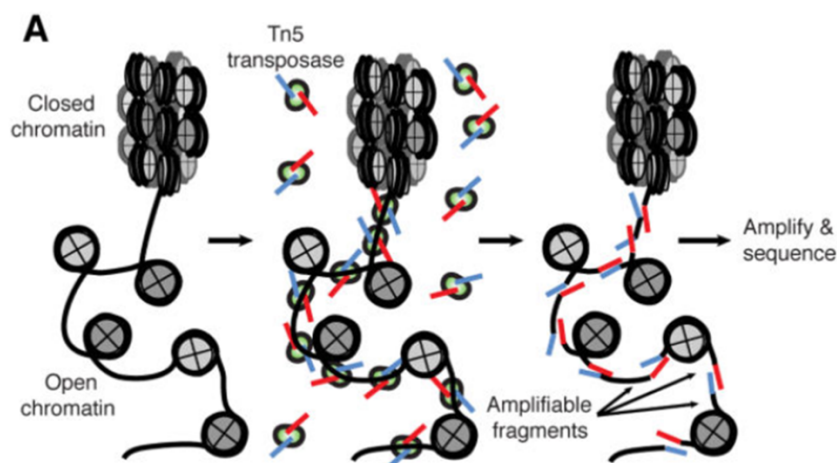


Figure 16. The ATAC-seq principle ¹⁰⁴.

A modified Tn5 transposase inserts Illumina-compatible adapters to 3' and 5' of cut DNA fragments at the positions of open chromatin. Therefore, the eluted DNA fragments were immediately ready for a PCR using i5 and i7 Nextera™ indexing barcodes (Illumina, USA). The eluted DNA was mixed with 25 µl of NEBNext High-Fidelity 2X PCR master-mix (NEB, USA), 1 µl of each i5 and i7 10 mM Nextera™ barcodes (Illumina, USA) and 13 µl of nuclease-free water. The initial PCR was performed with the following program: 5 min 72°C, 30 sec 98°C; 5 cycles: 10 sec 98°C, 30 sec 63°C, 1 min 72°C. Because of the unmeasurably low concentration of the initial tagged fragments, it is not possible to equalize the input amount among samples for the PCR. Therefore, after the initial PCR (5 cycles), 5 µl of the mixture was separated for a side-qPCR to evaluate the amount of cycles needed to reach the amplification plateau. 7,5 µl of SYBR™ Green 2X Mastermix (Thermo, USA) and 2,5 µl of nuclease-free water were added to 5 µl of the side reaction. The qPCR was performed as described in 2.2.6 and the number of additional cycles was determined for every sample (the number of qPCR cycles related to a middle of the amplification curve). For each of the initial samples the second PCR (with the same program) was performed with a number of cycles, defined by the side-qPCR. The libraries were cleaned and size-selected (200-1000 bp) with SPRI beads (Magbio, USA). The libraries concentrations were measured by the DNA HS Qubit kit. The size distribution of libraries was evaluated by capillary gel electrophoresis (PerkinElmer Lab Chip 3K DNA or Agilent Fragment Analyzer DNA HS).

2.2.9. Single-cell RNA sequencing (scRNA-seq)

The single-cell RNA sequencing was performed on a SMARTer™ ICELL8 system (Takara Bio, Japan) according to the manufacturer's instructions (3' DE kit). Basically, the machine consists of two major parts: the liquid handler and the imaging system (Fig. 17).

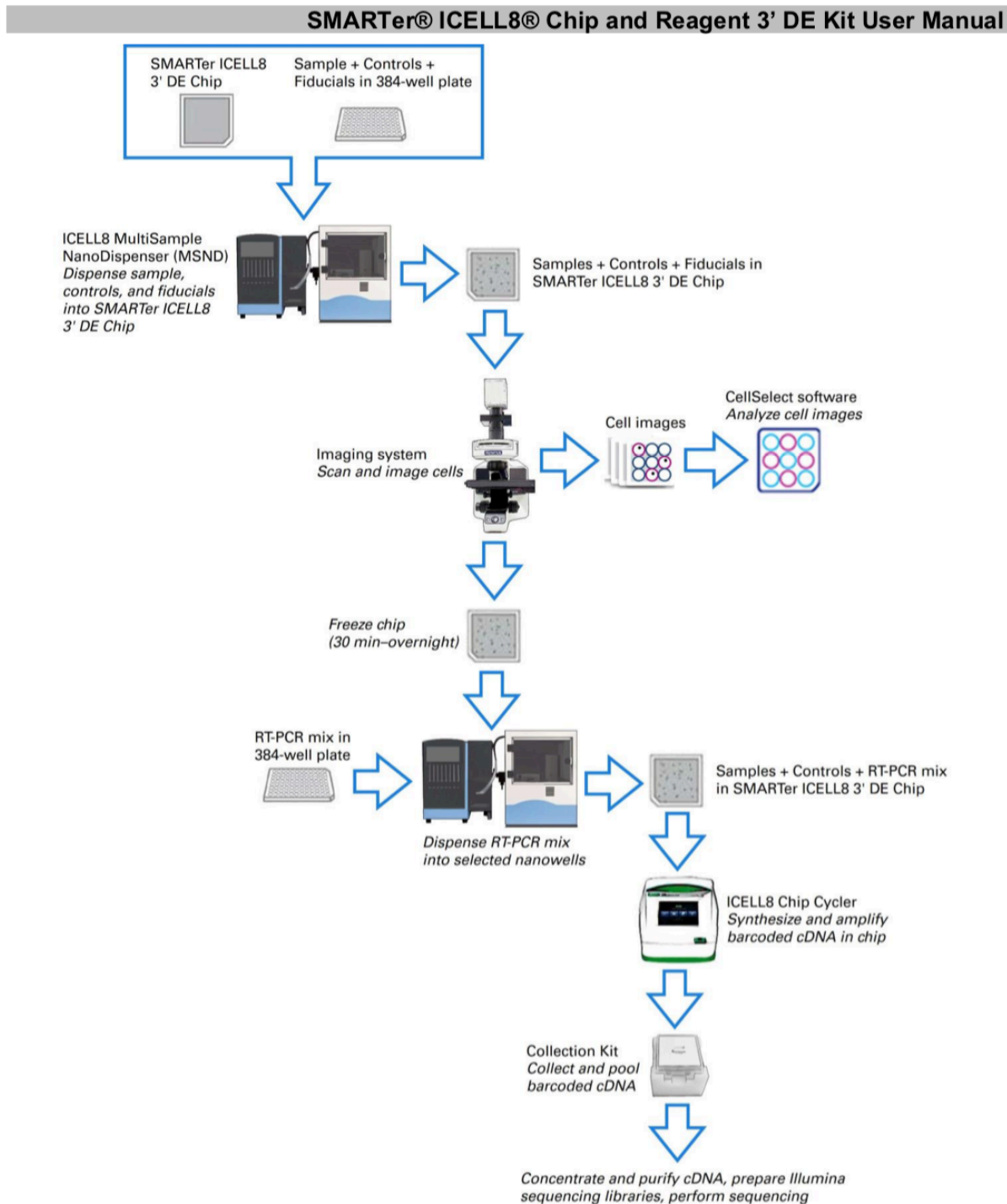


Figure 17. The workflow diagram for the SMARTer™ ICELL8 Chip and Reagent 3' DE kit

The cell suspension was stained with Hoechst live stain nuclear dye (Thermo, USA) and was loaded on the source well plate and placed inside the liquid handler. The liquid handler aspirated the cell suspension using eight large-bore nozzles and dispensed it over the microwell chip (50 nl of the cell suspension was dispensed in every well). The microwell metal chip has 5184 (72x72) wells of approx. 150 nl volume. The separation into single cells is based on the Poisson distribution of a limited dilution: approximately 1/3 of the microwells were empty, 1/3 had multiple cells inside and 1/3 harbored single cells. Then the chip was sealed with a transparent seal and moved to the imaging system. The imaging was performed in a reflection mode using Hoechst channel to visualize the cell nuclei and Texas Red channel to visualize the marker wells (located in the microchip corners), which are required for a correct triangulation. After the imaging, chip was frozen at -80°C for a long-term storage. Using the CellSelect™ software (Takara Bio Inc, USA), only the wells containing single cells inside were selected for the further procedures.

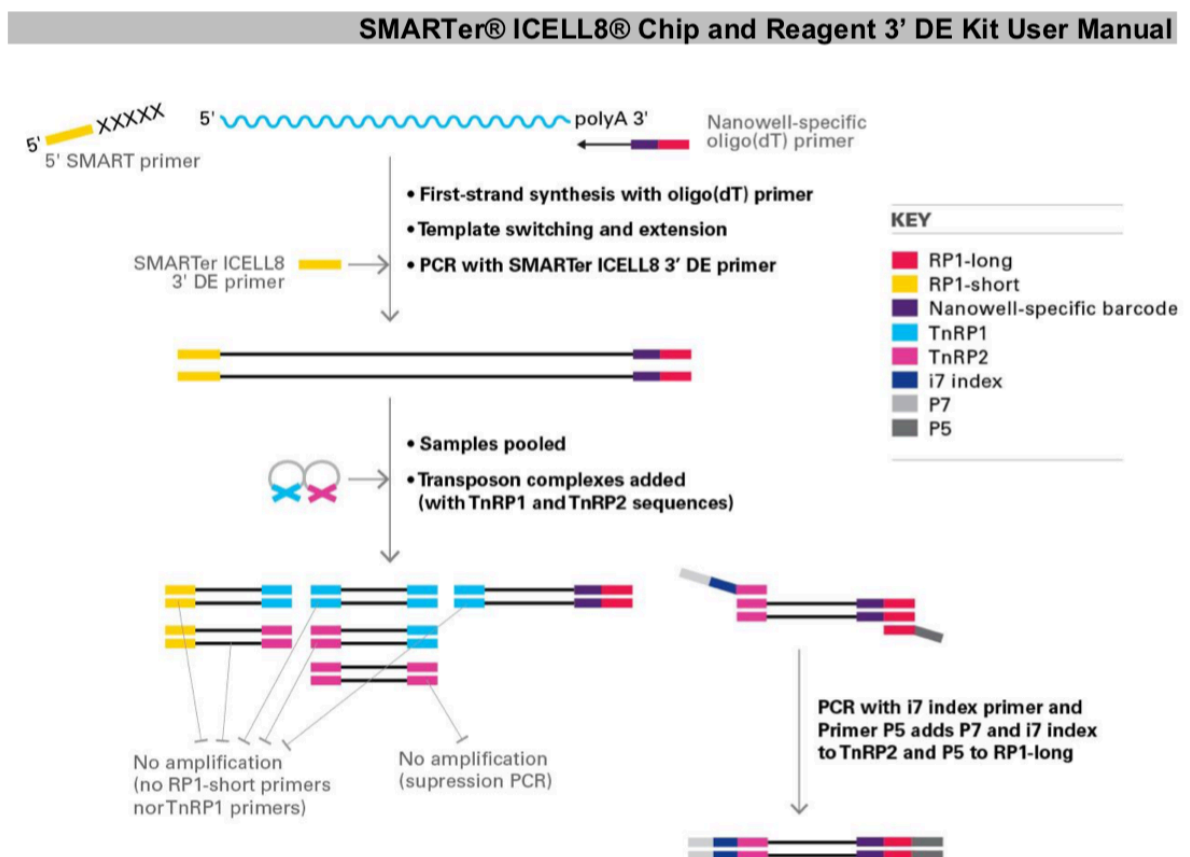


Figure 18. The cDNA synthesis and library preparation with SMARTer™ Chip and Reagent 3' DE kit

Every microwell in the chip contained pre-filled unique 10bp poly(dT)-tailed barcode, which allowed to demultiplex the library after sequencing (Fig. 18). The RT

solution, which contained buffers and enzymes for lysis, reverse transcription and cDNA pre-amplification, was dispensed in the selected wells (the wells with single cells). The chip was sealed and incubated in a chip-adapted PCR machine with a program, provided by the manufacturer (briefly, 1.5h at 42⁰C for reverse transcription, 24 cycles of: 10 sec 98⁰C, 30 sec 65⁰C, 3 min 68⁰C for cDNA preamplification). After thermocycling, the chip was placed (with wells down) in a special holder in order to pool all the cDNA molecules from the wells into one tube by centrifugation. The pooled mixture was cleaned by a DNA Clean & Concentrator column (Zymo, USA) and additionally by SPRI beads (Magbio, USA). The cleaned solution contained cDNA from the single-cells mRNAs. To make the sequencing library, Nextera™ XT kit (Illumina, USA) was used. Briefly, 10 µl of Tagmentation buffer and 5 µl of the Amplicon Tagment Mix (Tn5 transposase) was mixed with 5 µl of the diluted cDNA (1 ng total) and incubated for 5 min at 55⁰C. This step fragmented the cDNA and introduced Illumina-compatible adapters to the ends of DNA fragments. After quenching the reaction with a Neutralization buffer (supplied in the kit), the PCR reagents were added to the mixture: 15 µl of Nextera PCR Mastermix (NPM), 5 µl of i7 index primer and 5 µl of ICELL8 Nextera P5 primer. The PCR was performed with a following program: 3 min 72⁰C, 30 sec 95⁰C, 12 cycles: 10 sec 95⁰C, 30 sec 55⁰C, 30 sec 72⁰C. The libraries were cleaned and size-selected (300-600bp) with SPRI beads (Magbio, USA). The libraries concentrations were measured by the DNA HS Qubit kit. The libraries size distribution was evaluated by capillary gel electrophoresis (PerkinElmer Lab Chip 3K DNA or Agilent Fragment Analyzer DNA HS).

2.2.10. Single-cell ATAC sequencing (scATAC-seq)

The scATAC-seq protocol allows a massive parallel chromatin accessibility screening of hundreds of cells (Fig. 19). The protocol was developed by Sarah Teichmann's group¹⁰⁵.

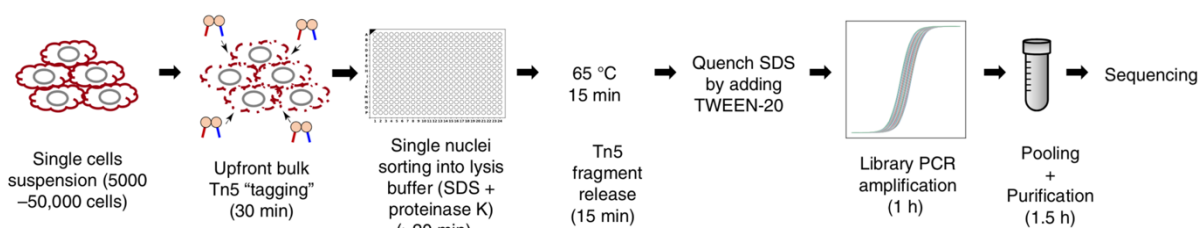


Figure 19. The workflow diagram for the scATAC-seq library preparation¹⁰⁵

As in the bulk ATAC-seq protocol, the cells were first centrifuged, and the pellets were resolved in a Tagmentation mix (see 2.2.8 for details). After Tagmentation, cut DNA fragments are retained into nucleus. This feature allowed FAC-sorting of the treated nuclei on 96/384 well plates in a single-nucleus mode. The wells were pre-filled with an SDS-Proteinase K cocktail, which lysed the nuclei and released the tagmented fragments (65°C 15 min). After the fragments release, SDS was quenched by Tween-20. The NEBNext High Fidelity 2X PCR Mastermix (NEB, USA), as well as both i5 and i7 Nextera™ XT indexing barcodes (forming a unique combination) were added to each well. The PCR program was performed according to 2.2.8. After the PCR, samples from all wells were pooled into one tube. The mixture was cleaned by a MinElute PCR purification column (Qiagen, USA). The libraries were additionally cleaned and size-selected (200-1000 bp) by SPRI beads (Magbio, USA). The libraries concentrations were measured by the DNA HS Qubit kit. The size distribution of libraries was evaluated by capillary gel electrophoresis (PerkinElmer Lab Chip 3K DNA or Agilent Fragment Analyzer DNA HS).

2.3. Biochemistry

2.3.1. Protein isolation from adherent cells

The SDS protein buffer was added to wells with cultured cells. The cell lysate was transferred into a tube. The protein solution was sonicated and subsequently centrifugated for 10 min at 14k g to remove the debris and insoluble compounds. The supernatant was used for further experiments.

2.3.2. Measurement of protein concentration

The DC kit (BioRad, USA) was used for a protein concentration measurement. It is a colorimetric assay, similar to the conventional Lowry assay. It is based on the reaction of proteins with an alkaline copper tartrate solution and Folin reagent. Depending on the protein concentration, the color of the solution varies between transparent and blue. The concentration was determined via absorption measurement at 750 nm wavelength, referring to a standard curve. The standard curve was generated with known concentrations of the bovine serum albumin (BSA).

2.3.3. SDS polyacrylamide gel electrophoresis

The isolated proteins were mixed with LDS 4x NuPAGE sample buffer (Invitrogen, USA) and denatured at 95°C for 5 minutes and subsequently transferred to ice. The 4-12% polyacrylamide NuPAGE gels (Invitrogen, USA) were used. The samples (including a ladder) were loaded on the gel wells and run with the following program: 80V for 15 min and 150V until the first ladder band was reaching the end of the gel.

2.3.4. Western blot analysis

The SDS PAGE separation of proteins was followed by a wet protein transfer onto a nitrocellulose membrane. The transfer was performed at 50V for 2h in the Xcell II Blot Module (Invitrogen, USA) in a transfer buffer (12.5 mM Glycine, 12.5 mM Bis-Tris, 0.8 mM EDTA, 20% Methanol). To ensure the optimal transfer, blotting membranes were stained with a RedAlert stain (Millipore, USA). For the antibody staining, membranes were blocked for 1h with 5% skim milk powder (Sigma, Germany) in TBST (20 mM Tris, 140 mM NaCl, 0.1% v/v Tween 20). Then the membranes were incubated in the same blocking solution, but with an addition of a primary antibody (see Table 5) overnight on a shaker at 4°C. After washing the membrane with TBST (3 times; 1h each), the membrane was incubated with a secondary antibody (coupled to horse-radish-peroxidase (HRP)). The reaction between antigen and antibody was detected by the Super-Signal Femto-enhanced chemiluminescence kit (Pierce, UK) on the VersaDoc 3000 Imaging system (BioRad, USA).

Table 5. Antibodies used for the western blot analysis

Name	Dilution	IgG	Manufacturer
V5-tag	1:10 000	rabbit	Ab9116, Abcam, UK
Tubulin	1:1000	mouse	T 6074, Sigma, Germany
Anti-rabbit HRP	1:10 000	goat	31460 Pierce, UK
Anti-mouse HRP	1:10 000	goat	1858413, Pierce, UK

2.4. Histology

2.4.1. Cryo-sectioning

The histological analysis of tissues was performed on cryosections. The mouse hearts were embedded in a Tissue-Tek O.C.T. Polyfreeze (Sakura, Japan) and frozen in the liquid nitrogen. The *Tibialis anterior* muscles were frozen in a precooled (in the liquid nitrogen) isopentane to avoid freezing artifacts. Frozen tissues were stored at -

80°C until sectioning. To make sections, cryostat-microtome was used (Leica, Germany). The cryostat temperature was set to -25°C. The cryosections were cut with a thickness of 10 µm and transferred to the SuperFrost microscope slides (Thermo, USA) and stored at -20°C for short term until further usage.

2.4.2. Hematoxylin & Eosin staining

The Hematoxylin & Eosin staining (H&E) is a classical histological staining ¹⁷. The microscopic slides with sections were equilibrated in ddH₂O for 2 mins and stained with Hematoxylin for 12 mins. The slides were washed in a running tap water for 10 mins. The slides were dipped in 70% Ethanol-HCl (200ml 70% Ethanol + 2ml 37% HCl) 5 times and then washed in running tap water for 7 minutes. The slides were stained with Eosin for 12 mins. The slides were dipped consecutively in 70%, 80%, 90% and incubated for 10 mins in 100% Ethanol. The slides were incubated in Xylol for 11 mins. Finally, the slides were air dried and mounted with a synthetic resin Entellan (Sigma, Germany).

2.4.3. Masson's Trichrome staining

The trichrome staining visualizes collagen-rich fibrotic muscle tissues with blue color ¹⁸. The microscopic slides with sections were air-dried and then rinsed in ddH₂O for 2 mins. The slides were mordanted in a preheated Bouin's Solution at 56°C for 15 mins in a tightly closed container. The slides were washed under the running tap water for 20 mins. The slides were stained in Hematoxylin for 12 mis and then rinsed with a running tap water for 5 mins. The slides were incubated in Biebrich Scarlet-Acid Fuchsin solution for 5 mins and then rinsed in ddH₂O. Then the slides were incubated in Phosphotungstic / Phosphomolybdic acid / ddH₂O solution (1:1:2) for 5 mins. The slides were incubated in Anillin Blue solution for 5 mins. The slides were transferred into 1% Acetic acid for 2 mins and then rinsed in ddH₂O. The slides were dehydrated in 96% (2 sec), 100% (2 min) and again in 100% (2 min) Ethanol. The slides were incubated two times in Xylol (2 x 10 mins). Finally, the slides were air dried and mounted with a synthetic resin Entellan (Sigma, Germany).

2.4.4. Immunofluorescence

The spatial protein expression was determined by immunofluorescence. The microscopic slides, tubes with isolated FDP muscle fibers or cell culture wells were

fixed with 4% paraformaldehyde (PFA) for 15 mins at RT. Then the samples were washed 3 times with PBS (5 mins each). The samples were blocked with a blocking solution (1% BSA and 0.3% Triton in PBS) for 1h at RT. Then the samples were incubated overnight at 4°C in a blocking solution with addition of a primary antibody in the desired dilution (see Table 6). Afterwards the samples were washed with PBS 3 times (5 mins each). Then the samples were incubated for 1h with a secondary antibody in the desired dilution in PBS. The samples were washed with PBS 1 time (5 mins) and the nuclei were counterstained with DAPI (5 min, 0.5 µg/ml) and then washed 3 times with PBS (5 min each). Finally, the samples were mounted with Mowiol 4-88 (Sigma, Germany).

Table 6. The list of used antibodies for immunofluorescence.

Name	Dilution	IgG	Manufacturer
Pax7	1:1000	mouse	MAB1675, R&D, USA
MyoG	1:500	mouse	ab1835, Abcam, UK
V5-tag	1:1000	rabbit	ab9116, Abcam, UK
Galanin	1:500	goat	PA5-19206, Thermo, USA
Galanin receptor 1	1:500	rabbit	SAB4501089, Sigma, Germany
Galanin receptor 2	1:500	rabbit	ab203072, Abcam, UK
Galanin receptor 3	1:500	rabbit	TA317570, OriGene, USA
Active (cleaved) caspase 3	1:500	rabbit	ab2302, Abcam, UK
Laminin	1:1000	rabbit	L9393, Sigma, Germany
Embryonic MHC	1:100	mouse	F1.652, Hybridoma Bank, USA
Neurofilament-H	1:300	mouse	801711, BioLegend, USA
Annexin A3	1:500	rabbit	PA541314, Thermo, USA
HIF-1	1:300	rabbit	NB100-479SS, Novus Bio, USA
PCM1	1:300	mouse	Sc-398365, Santa Cruz, USA
CD31	1:500	goat	AF3628, R&D, USA
Activated Pol II (Ser5p)	1:500	rabbit	Ab5095, Abcam, UK
Wheat Germ Agglutinin (WGA)	1:500	goat	AS-2024, Vector Laboratories, USA
Anti-mouse Alexa fluor 488	1:1000	goat	A11001, Invitrogen, USA
Anti-mouse Alexa fluor 594	1:1000	goat	A11005, Invitrogen, USA
Anti-rabbit Alexa fluor 488	1:1000	goat	A11070, Invitrogen, USA
Anti-rabbit Alexa fluor 594	1:1000	goat	A11012, Invitrogen, USA
Anti-goat Alexa fluor 594	1:1000	chicken	A21468, Invitrogen, USA
CD31 FITC conj.	1:500	rat	11-0311-82, Thermo, USA
CD45 Alexa fluor 488 conj.	1:500	rat	103121, BioLegend, USA
Itga7 Alexa fluor 647 conj.	1:4000	rat	FAB3518R, RnDSsystems, USA
Sca-1 PE-Cy7 conj.	1:3000	rat	25-5981082, Thermo, USA
Apoptosis staining kit	1:200	-	Ab176749, Abcam, UK

2.4.5. Whole mount staining

The *Tibialis Anterior* muscles and diaphragms, isolated according to 2.1.7 and 2.1.8, were used for the whole mount staining. The freshly isolated muscles were fixed for 1h at RT in 4% PFA and then overnight at 4°C in 1% PFA. Then the muscles were washed 3 times with PBS (15 mins each) and then with 100 mM glycine in PBS (15 min). The muscles were permeabilized for 1h at RT in 0.5% Triton X-100 in PBS and blocked for 4h at RT in 3% BSA, 5% FCS and 0.5% Triton X-100 in PBS. The muscles were incubated overnight at 4°C with a primary antibody (see Table 6) in a blocking solution. Then the muscles were washed 3 times with PBS at RT, 1h each. Afterwards, the muscles were incubated overnight at 4°C with a secondary antibody. After three washes with PBS (1h each), the TA muscles were kept in PBS, while the diaphragms were placed on slides and flat-mounted with Mowiol 4-88.

2.4.6. Fluorescence microscopy

The fluorescence microscopy was performed on Zeiss Axio Imager Z1 Upright Trinocular (Zeiss, Germany). The following channels were used (excitation / emission): 358 nm / 461 nm (blue color), 488 nm / 525 nm (green color), 532 nm / 554 nm (yellow color), 594 nm / 617 nm (red color). The objectives in a range of 5x-40x (air) and 63x (oil) were used. The manufacturer's software was used for imaging (Zeiss Zen, Zeiss, Germany).

2.4.7. Confocal microscopy

The confocal microscopy was performed on Leica SP8 (Leica, Germany). The following channels were used (excitation / emission): 358 nm / 461 nm (blue color), 488 nm / 525 nm (green color), 594 nm / 617 nm (red color). 20x and 63x objectives were used. The manufacturer's software was used for imaging and analysis of the 3D stacks (LAS-X, Leica, Germany).

2.5. Cell biology

2.5.1. Isolation of adult cardiomyocytes

The following protocol was used for isolation of adult rod-shaped murine cardiomyocytes. A cannula was inserted into the aorta of an isolated heart. The heart was fixed on the perfusion system, where it was perfused with 20 ml of calcium-free buffer (113 mM NaCl, 4.7 mM KCl, 0.6 mM KH₂PO₄, 0.6 mM Na₂HPO₄, 1.2 mM

MgSO₄·7H₂O, 12 mM NaHCO₃, 10 mM KHCO₃, 10 mM HEPES, 30 mM Taurin, 10 mM 2,3-Butanedioneminoxime, 5.5 mM glucose). Then the heart was perfused with 20 ml of the enzyme buffer (Calcium free buffer + 0.25 mg/ml Liberase DH, 0.14 mg/ml Trypsin, 12.5 μM CaCl₂). This resulted in a heart swelling. When it turned pale, it was removed from the perfusion system. The ventricles were chopped into small pieces and incubated in the stop buffer 1 (enzyme buffer + 10% FCS, 12.5 μM CaCl₂). The resuspended cells were transferred to 50 ml falcons with a wide-bore pipette. The falcons were centrifugated for 1 min at 300g and the supernatants were discarded. The pellets were resuspended in the stop buffer 2 (enzyme buffer + 5% FCS, 12.5 μM CaCl₂). The cell mixtures were filtered through 500 μm cell strainers. These cell mixtures were immediately used for the following experiments.

2.5.2. Isolation of *flexor Digitorum Profundus* (FDP) muscle fibers

To isolate the FDP muscle fibers, mouse feet were cut from the sacrificed mice. The feet were fixed on a surgical table and the skin was removed from the paw. The tendons were detached from the paw and removed. The FDP muscles were cut from both distal and proximal sides and rinsed with PBS. Then the muscles were incubated in 0.2% Collagenase P (Sigma, Germany) in DMEM with 1% penicillin-streptomycin for 2h at 37°C. Then the fibers were washed 3 times with PBS with 1% FCS and transferred to a Petri dish. The debris was removed with 20μl pipette (nerves, cell aggregates, etc.). Finally, the FDP fibers were transferred to a tube with PBS. Isolated FDP fibers were used for further experiments.

2.5.3. Fluorescent-activated cell sorting (FACS)

The FACS is commonly used for separating certain cell populations from the cell suspensions, based on the cell size, shape and fluorescent tags. The BD FACSAria III (BD, USA) with 100 μm nozzle was used. The following channels were used (excitation / emission): 358 nm / 461 nm (blue color), 488 nm / 525 nm (green color), 594 nm / 617 nm (red color).

2.5.4. Isolation and culture of muscle stem cells (MuSCs) and primary myoblasts

The following protocol was used for the isolation of muscle stem cells (MuSCs) from the *Pax7:zsGreen* mice. The *Pax7* is a marker of MuSCs and *Pax7:zsGreen* mice

expresses a transgenic *Pax7* promoter with an attached sequence of the *zsGreen* fluorescent tag⁸⁷. Therefore, the MuSCs express green fluorescence signal.

The *Pax7:zsGreen* mice were sacrificed and all exterior skeletal muscles were collected (lower limb muscles, upper limb muscles, breast muscles, back muscles) and placed in a 50 ml falcon with isolation media (DMEM (Sigma, Germany) + 2% penicillin-streptomycin). Then muscles were chopped into a fine slurry on the tissue chopper (McIlwain, USA). 18ml of isolation media and 2 ml of Dispase (Corning, USA) were added to the muscle slurry in 50 ml falcons. The falcons were incubated on water bath for 30 mins with regular shaking. Afterwards the cell mixture was thoroughly pipetted using 24 ml syringe (without attached needle). Then 2 ml of 0.5% Collagenase type II (Worthington, USA) was added to the falcons. The falcons were incubated on water bath for 30 mins with regular shaking. Afterwards the cell mixture was thoroughly pipetted using 24 ml syringe. Then the tube was filled up to 50 ml volume with FCS media (DMEM + 1% penicillin-streptomycin + 10% FCS) to inactivate the enzymes. The cell mixture was consecutively filtered through 100µm, 70µm and 40µm cell strainers and centrifugated at 1200g for 10 mins. The pellet was resuspended in 5 ml of cell-sorting buffer (PBS + 1% FCS + 10mM EDTA) and loaded on top of the Percoll (Sigma, Germany) sugar gradient. The Percoll sugar gradient was prepared from 90% Percoll (9 parts of Percoll and 1 part of 10X PBS). 90% Percoll was diluted with PBS to make 70% Percoll and with FCS media to make 30% Percoll. 3 ml of 70% Percoll was slowly injected with a syringe needle under the 5 ml of 30% Percoll in a 15 ml falcon tube. The Percoll tubes with samples were centrifugated for 20 min at 1200g with the lowest settings of acceleration and deceleration to avoid mixture of the phases. After centrifugation, a cloud of cells, enriched for the MuSCs, was visible on the border between 30% and 70% Percoll. 2 ml of media from this interface was collected by 1ml pipette and filtered through 40 µm cell strainer. This final mixture was stained with DAPI to discriminate alive (DAPI-neg) and dead (DAPI-pos) cells. The final mixture was used for FACS. The gating strategy included thresholds on forward and side scatters, the sorted cells were also DAPI-negative and *zsGreen*-positive. The isolation of MuSCs from one *Pax7:zsGreen* mouse resulted in 90-150k of cells. The isolated cells were either used for other experiments (DNA/RNA isolation, ATAC-seq, etc.) or were cultured.

To culture MuSCs, the cells were resuspended in a culturing media (DMEM/GlutaMAX (Gibco, USA) + 1% penicillin-streptomycin + 20% FCS). The media

with cells, containing 12-15k cells per 1 ml, was aliquoted among the wells of the 24-well plate. The cells were cultured at 37°C and 5% CO₂ until desired timepoint.

2.5.5. Determination of myoblast proliferation and differentiation

The proliferation rate of cells in culture could be directly assessed by the measurement of DNA synthesis. In the proliferating cells, which undergo DNA synthesis, EdU (Invitrogen, USA) could be incorporated into DNA instead of deoxythymidine. The Click™ reaction allowed detection of the incorporated EdU. It was catalyzed by copper, where alkaline (EdU) and azide (Alexa Fluor dye) reacted covalently. The EdU labelling and detection was done according to the manufacturer's protocol.

At the desired timepoint of cell culture, EdU was added to the wells to reach the final concentration of 10 µM. 2h afterwards all media was removed from the wells, cells were rinsed with PBS and fixed with 4% PFA for 15 mins. Then the cells were washed 3 times with PBS. Then the cells were permeabilized with 0.5% Triton-X100 (15 mins) and incubated for 30 mins with a reaction mix from the EdU kit (Alexa fluor 594 conjugate). The cells were then washed 3 times with PBS and counter-stained with DAPI. Afterwards the EdU-positive nuclei could be detected by red fluorescence under the microscope.

To evaluate the differentiation commitment of myoblasts, immunofluorescence staining for Myogenin was performed. Myogenin is a marker of myoblasts, which finished proliferation and committed towards differentiation¹⁰⁶. The immunostaining was achieved according to 2.4.5. The secondary antibody had Alexa fluor 488 tag, therefore it was possible to evaluate both proliferation (EdU, in red) and differentiation (Myogenin, in green) on the same myoblasts culture well.

2.5.6. Live imaging of cultured cells with IncuCyte

To evaluate the dynamics of cell proliferation and differentiation, IncuCyte live imaging station (Fig. 20) (Sartorius, Germany) was used according to the manufacturer's instructions.



Figure 20. The IncuCyte live imaging station with an open tray for the well plates

Briefly, the well plate with cultured cells was loaded into the IncuCyte station, which itself was placed into a cell culture incubator (37°C and 5% CO₂). Every hour the imaging of cultured cells was performed in 1-3 channels: brightfield and/or green fluorescence (488nm excitation) and/or red fluorescence (594nm excitation). The imaging was performed over the whole course of cell culture experiment. The images were stored and analyzed by the manufacturer's software. The software also provided a tool to evaluate the cell confluence and colocalization of the fluorescent signals.

2.5.7. Viral transductions and shRNA-induced knock-down

The retroviral transduction was used to knock-down the Annexin A3 protein expression in the myoblasts. The work was done in the S2 safety-approved cell culture facility. The shRNA against *Anxa3* mRNA was obtained from the RNAi Consortium shRNA library (id: TRCN0000110725, target sequence: GCACTCTAAAGTGCAAGCAAA, 3'UTR region of *Anxa3* transcript). The shRNA-containing plasmid was packed into the retrovirus in HEK cells. After 2 days, the culturing media from the HEK cells was collected, filtered through 0.2 µm filter and was added to the proliferating myoblasts. Virally packed GFP plasmid was used as a positive control. After 1 day of exposure to the viral media, it was removed, cells were washed with PBS and fresh media was added to the wells. Upon successful transduction, the control cells were expressing fluorescent GFP tag and shRNA-treated cells decreased the expression of Annexin A3 protein (confirmed by the Western blot). Similar strategy was used to overexpress *Anxa3* mRNA sequence in the myoblasts.

2.6. Bioinformatics

2.6.1. Next generation sequencing (NGS)

The sequencing was performed on a NextSeq500 sequencer (Illumina, USA). V3 high capacity flow-cells were used. The signal detection of the NextSeq500 system relies on a two-colour technology (green and red). The sequencing was performed according to the manufacturer's protocol.

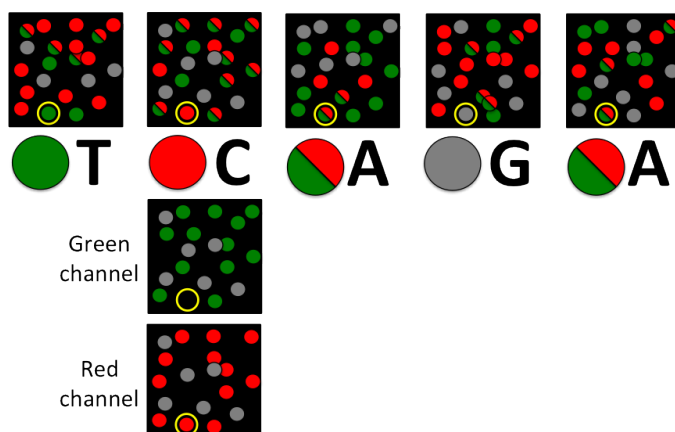


Figure 21. The principle of base-calling in the NextSeq500 2-color sequencer

In brief, uniquely barcoded sequencing libraries were first denaturized with 0.2M NaOH and then re-naturized with 0.2M TRIS pH8.0. Then the libraries were mixed together with a final concentration of 20 pM in 1.3ml volume with HT1 buffer (provided by the manufacturer). The whole mixture was then loaded into the input well of the high75 sequencing cartridge and loaded into the NextSeq500 machine. The NextSeq500 allows sequencing with various read-length parameters. It allows to set length of the read 1 and 2, as well as length of the Index read 1 and 2. Different library types require different parameters (see Table 7).

Table 7. Sequencing parameters for different library types.

Library type	Read 1	Read 2	Index read 1	Index read 2
RNA-seq	75	0	8	8
ATAC-seq	38	38	8	8
scRNA-seq Takara ICELL8	11	80	0	0
scRNA-seq 10X Chromium	26	58	8	0
scATAC-seq plate-based	38	38	8	8
scATAC-seq 10X Chromium	34	34	8	16

The first step of sequencing is clustering. The library is pumped into the flow-cell, which has adapters, attached to its surface (complimentary to 3' and 5' ends of the library fragments). Every bound DNA fragment is undergoing several rounds of the clonal expansion, which creates clusters of clonal copies around it. At the end of the clonal expansion, all library molecules in clusters are single-stranded. Afterwards the flow-cell is flushed with the nucleotides, which have 4 types of labels (no tag, green tag, red tag, green and red tags). If this nucleotide is complimentary to the first nucleotide of the template, it binds and stops further prolongation. Then all residual nucleotides are washed out and the flow-cell is imaged in 2 channels (green and red). Which type of nucleotide was incorporated is detected by the emitted fluorescent signal. This operation is repeated in total 91-92 times (for high75 cartridge, depends on the read length parameters). After the sequencing run, clusters are detected on the images and bases are called. The NextSeq500 software has strict QC criteria regarding cluster detection and base calling. The acquired sequencing reads are stored in a *fastq* format, which is used for further analysis.

2.6.2. Demultiplexing of sequencing reads, quality assessment and trimming

Since all libraries had unique indexed barcode from 3' or 3' and 5' ends, it was possible to demultiplex the reads, derived from different libraries (samples). The *Bcl2fastq* (Illumina, USA) script was used for demultiplexing. Briefly, this script searches for supplied sample index combinations across all index reads and filters them into the respective separate *fastq* files. Every base in NextSeq500 is called with a certain confidence. This confidence represents the probability of falsely called base per total number of bases. Such, there are four major types of confidence: 10 (1 error in 10 bases), 20 (1 error in 100 bases), 30 (1 error in 1000 bases) and 40 (1 error in 10000 bases). Usually all bases with confidence <30 are discarded. Therefore, only bases which are called with confidence 30 and 40 are used for the analysis. The confidence is highest at the beginning of the read and decreases to the end of the read due to increased background fluorescence. This implies, that discarding low confidence bases usually means trimming the sequencing reads at point, when the base confidence decreases below 30. The reads, which passed QC and were trimmed, were written in new *fastq* files and used for further analysis.

2.6.3. Mapping of sequencing reads to reference genome or transcriptome

Mapping is a procedure of finding the position of sequencing read on the reference genome or transcriptome. The filtered *fastq* files were mapped to the reference using STAR ¹⁰⁷. As a result of mapping, every sequencing read is being associated to a specific location on the genome (or transcriptome), while reads, which were not fitting, are discarded. The mapping rate refers to a percentage of reads which were successfully mapped to the reference. The mapping rate depends on a method of the library preparation, species and quality of the initial sample. It is also possible to run Basic Local Alignment Search Tool to determine nucleic acids of which species were also present in the initial sample. Usually the mapping rate of 70-90% is considered to be good. Often a small percentage (<5%) of reads could be mapped to the different species: bacteria (for example from the cell culture contamination), human (contamination from the researcher) and others due to the sequence similarities.

2.6.4. Sequencing read count, normalization and log-fold-change calculation

To evaluate the expression of a gene (RNA-seq) or chromatin accessibility (ATAC-seq), the reads at the certain regions need to be annotated and counted. In the RNA-seq a read is associated with a gene, if the read overlaps with the gene exons. In the ATAC-seq a read is associated with a gene, if it is overlapping with the gene body, gene promoter, upstream region (up to 5kb upstream) and known gene enhancer regions. Such reads are being counted for every gene and written into a matrix, containing genes/transcripts on Y axis and samples on X axis with counts in the matrix cells. This matrix is often called Count table. To normalize the reads, library size normalization was used. In specific cases (like single-cell sequencing) further normalization methods are mentioned additionally. The library size normalization uses sequencing depth (total number of sequencing reads per sample) as a factor for counts normalization. This method is commonly used in the bulk RNA and ATAC sequencing experiments ¹⁰⁸. To evaluate the differential expression or differential accessibility of genes between conditions (which contain multiple replicates), the DESeq2 method was used ¹⁰⁹.

2.6.5. Statistical tests (p-value, false discovery rate (FDR))

The statistical tests in the NGS experiment are primarily used to evaluate the significance of the differential expression/accessibility. In many cases, statistical

significance is to be determined between 2 conditions, while each of them has multiple replicates. The most common statistical test is the two-sided Student's t-test. However, due to multiple testing in the sequencing datasets, the FDR is preferred (for example, Benjamini-Hochberg or Bonferroni methods) ¹¹⁰. Since sequencing analysis compares expression/accessibility of thousands of genes, an appropriate correction of p-value is needed. It is required to correct for an increased rate of *type I errors* due to conduction of multiple simultaneous comparisons ¹¹¹. (*Type I error* represents the rejection of a true null hypothesis while *type II error* means non-rejection of a false null hypothesis.) Both the p-value and FDR calculations were performed using internal algorithms of R programming language.

2.6.6. Gene set enrichment analysis (GSEA)

The GSEA is used for coarse evaluation of cell types, tissues or processes, associated with a certain subset of genes. The GSEA is commonly used to find out if any particular terms are enriched in the differentially expressed/accessible (DE/A) genes. The GSEA analysis was performed using KOBAS pipeline ¹¹². It uses Ensembl gene id's as input and performs GSEA by comparing the given set of genes to known databases. The used databases are: Gene Ontology (GO), BioCyc, KEGG, PANTHER, Reactome.

2.6.7. Handling of single-cell datasets

The single-cell analysis, starting from the Count tables, was performed in R. In brief, the single-cell dataset was composed of three major matrixes: Count table, feature table and phenotype table. The Count table (MxN matrix) contained genes on Y axis and single cells on X axis, while the matrix cells contained counts. The feature matrix (N rows) contained information about genes, present in the Count table. This information included Ensembl gene id, gene name, description, etc. The phenotype matrix (M rows) contained information about single cells, present in the Count table. This information included sequencing performance (number of reads, mapping rate, percentage of duplicates, percentage of dropouts, percentage of mitochondrial reads, etc.), cell type (defined during the analysis) and other cell-related parameters. Usually these three matrixes aggregated into one single-cell R object. There are multiple packages for the single-cell analysis, providing computational tools for single-cell objects. In this dissertation the *Scater* package was primarily used. Since the first part of the results was published, the respective dataset was deposited in the European Nucleotide Archive (<https://www.ebi.ac.uk/ena>) under accession number PRJEB29049.

2.6.8. Dimensional reduction and clustering in single-cell datasets

The dimensional reduction is used in sequencing analysis to visualize multidimensional data in two-dimensional space. It uses the Count table to perform linear or non-linear matrix transformation to find the dimensions of highest differences between cells. The most common algorithms to perform dimensional reduction are principle component analysis (PCA), t-distributed stochastic embedding (t-SNE) and uniform manifold approximation and projection (UMAP) ¹¹³. Cells, appearing close to each other after dimensional reduction, form cell clusters.

2.6.9. Calculation of differential expression/accessibility in single-cell datasets

The MAST method was used to calculate the single-cell DE/A genes ¹¹⁴. First, to define the cell cluster identity, DE/A should be calculated between the given cell cluster and all other cells. The resulting list of top genes should contain the marker genes for a respective cell population. After the definition of all cell clusters in the dataset, DE/A analysis is run between the particular clusters, or between global conditions, if single-cell experiment includes multiple runs (for example, control single-cell dataset and treatment single-cell dataset).

2.6.10. Analysis of microscopic images and particle analysis

The Fiji / ImageJ software was used for microscopic images analysis. The consecutive analysis of multiple images was performed using Macro programming. In brief, the software was used to generate pseudo-colored images and montages from the fluorescence microscopy, image stacks, 3D models for confocal microscopy, measure the particle number and size on the fluorescent microscopic images. The colocalization analysis was performed using JaCOP plugin. The measurement of particles size and their number was done by the Particle Analyzer plugin.

2.6.11. List of used R packages

The following R packages were used: for single-cell analysis: *Scater* (v.1.18.6), *SingleCellExperiment* (v.1.12.0), *MAST* (v.1.16.0), *Seurat* (v.4.0.1), *Signac* (v.1.1.1), *umap* (v.0.2.7.0), *destiny* (v.3.4.0); for data visualization: *viridis* (v.0.6.0), *RcolorBrewer* (v.1.1-2), *gplots* (v.3.1.1), *ggplot2* (v.3.3.3), *ggrepel* (v.0.9.1); for data handling: *readr* (v.1.4.0), *readxl* (v.1.3.1), *tidyr* (v.1.1.3), *data.table* (v.1.14.0), *plyr* (v.1.8.6), *car* (v.3.0-10), *devtools* (v.2.4.0); for gene references: *EnsDb.Mmusculus.v79* (v.2.99.0).

3. RESULTS

3.1. Mono- and multi-nucleated ventricular cardiomyocytes constitute a transcriptionally homogeneous cell population

3.1.1. Image-based quality control of single cardiomyocytes is necessary to avoid artificial cell clustering

The role of multinucleation in adult mammalian cardiomyocytes is still unclear. Furthermore, it is not known whether a subpopulation of cardiomyocytes exists, presumably consisting of mononucleated cardiomyocytes, that is superior to others for renewal of the myocardium and heart regeneration. To investigate differences between individual cardiomyocytes, as well as putative heterogeneity among them, a transcriptomic analysis on single-cell level is required. To date, neither droplet-based, nor microfluidic scRNA-seq protocols allow the analysis of intact cardiomyocytes. To overcome this limitation, the ICELL8 platform (Takara Bio Inc, USA), which uses a large-bore nozzle dispenser to distribute single cells into 5184 microwells was employed in this work (Fig. 22A). In brief, the ICELL8 technique is based on the dispersion of a diluted cell suspension into the microwell chip, with subsequent microscopic imaging and library preparation in the wells, harboring single cells. Due to the high physical density of cardiomyocytes, the standard protocol had to be modified to enable adequate loading of microwells according to the Poisson distribution (Fig. 22B, C). Modifications were: separation of the loading process into three consecutive steps with gentle mixing of the cardiomyocytes suspension between the steps to avoid sedimentation. For “standard” cells this effect is negligible, but cardiomyocytes show an increased rate due to the high cellular weight. Additionally, the input cell concentration was reduced from 1 to 0.2 cell per single-well dispersion volume (50 nl) to reduce the chance of loading multiple cells into one well. The cell yield was between 450 and 750 intact cardiomyocytes per chip, which is lower than the maximum possible yield (approx. 1800 cells per chip), but still lies within an acceptable range. High fragility, as well as low concentration of cardiomyocytes were assumed to be the reasons for suboptimal loading.

An initial analysis of scRNA-seq data (586 single cardiomyocytes) revealed two separate clusters of cells by PCA as well as t-SNE dimensional reduction plots (Fig. 22D, E). However, the strongest difference between the clusters was driven by the absolute number of detected genes per cell and thus was presumably not linked to different biological properties. Since the ICELL8 protocol included an imaging step, the

correlation between the microscopic appearance of cardiomyocytes, their transcriptomes and the clusters from dimension reduction were analyzed. Notably, all cardiomyocytes from the PCA Cluster 1 had low numbers of detected transcripts, were morphologically small, showing a not rod-shaped morphology, and had unclear cellular silhouettes (most likely originating from Cell Tracker dye leakage) (Fig. 22F). Such observations implied that such cardiomyocytes had acquired cellular damage and underwent partial RNA degradation. Such changes may have decreased the efficiency of scRNA-seq library preparation and thus the number of detected genes. This finding demonstrates the importance of image-based quality assessment in the ICELL8 protocol. As a result, the experimental design was amended to exclude damaged cells from the further analysis.

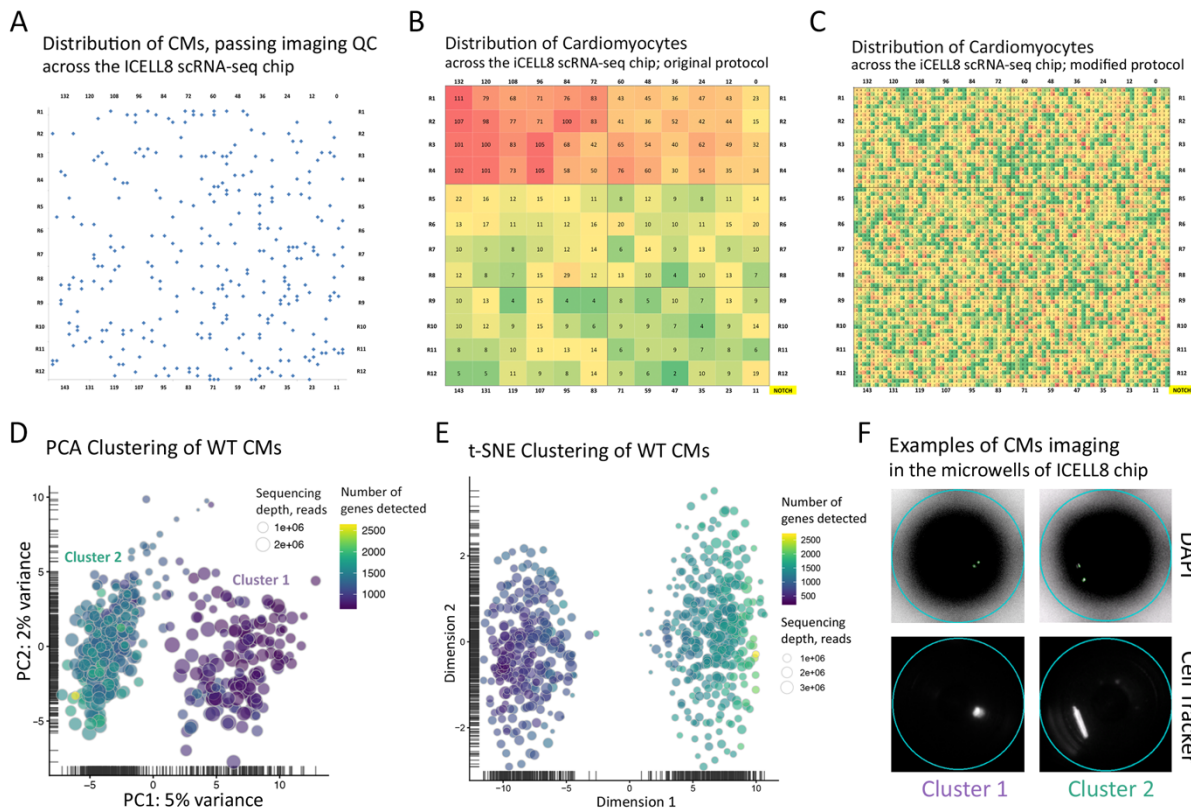


Figure 22. Image-based quality control of single cardiomyocytes for scRNA-seq is necessary to avoid artificial cell clustering. (A) Distribution of cardiomyocytes, which passed quality criteria, across the microwell ICELL8 chip. (B) The unmodified dispensing protocol resulted in non-equal distribution of cardiomyocytes across the chip due to the size and density of cardiomyocytes; colors show the of cells in the groups of wells. (C) The adjusted dispensing protocol evenly distributes cells on the chip; colors show the number of cardiomyocytes in the wells. (D) PCA dimensional reduction illustrates the separation of cardiomyocytes into two clusters. (E) t-SNE dimensional reduction illustrates the separation of cardiomyocytes into two clusters. (F) Microphotographs of cardiomyocytes in Cluster 1 and 2 (DAPI and Cell Tracker (Texas Red); 2 channel reflection mode; before library preparation). QC reveals that cardiomyocytes in Cluster 1 are damaged.

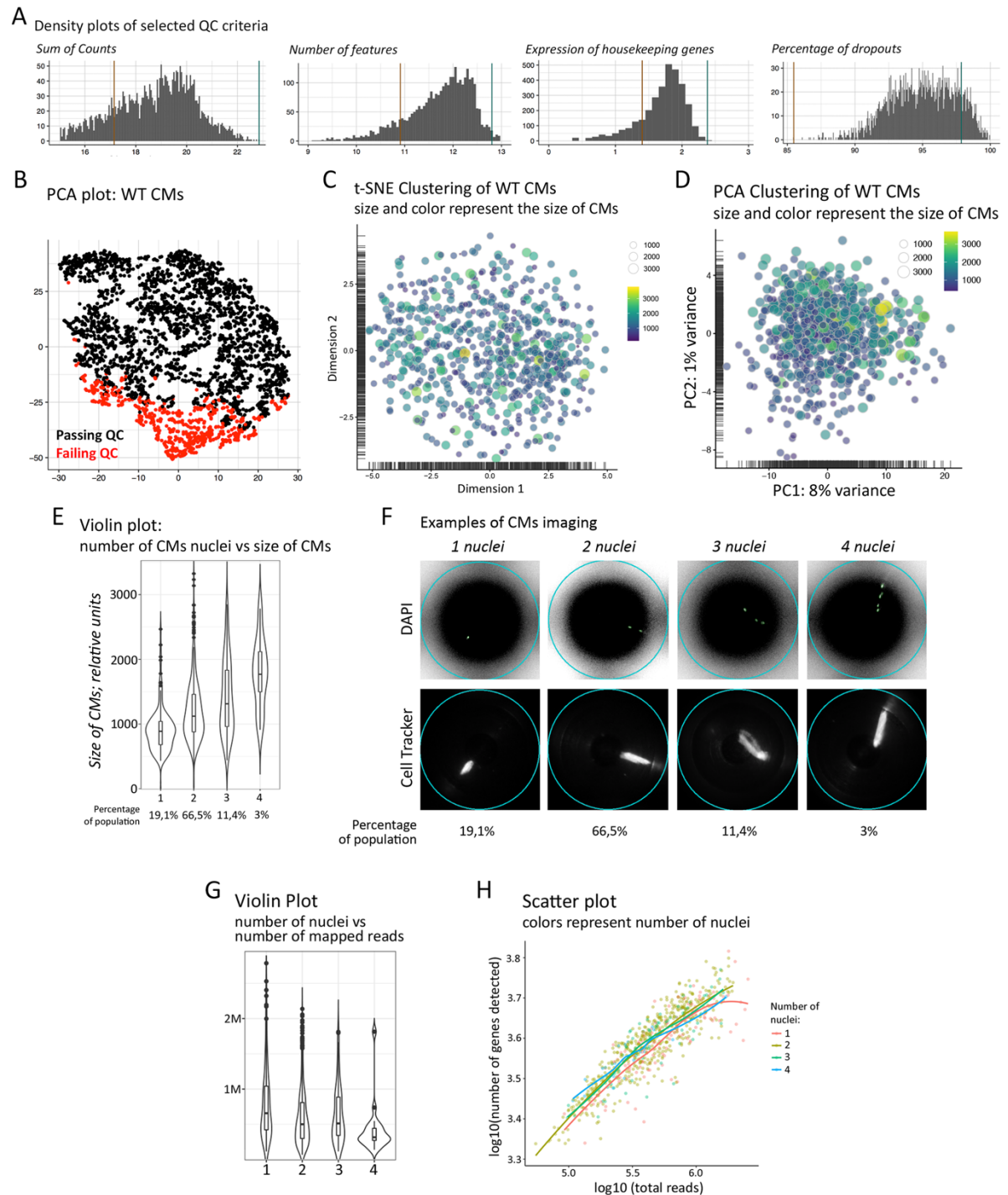


Figure 23. Quality control for the scRNA-seq. (A) Density plots illustrate filters for certain QC criteria. (B) PCA dimensional reduction illustrate cell clustering based on QC criteria. (C) PCA dimensional reduction of intact rod-shaped cardiomyocytes. (D) t-SNE dimensional reduction of rod-shaped intact cardiomyocytes. (E) Violin plot shows correlation between number of nuclei and size of cardiomyocytes. (F) Exemplary microphotographs of cardiomyocytes with different nuclearity (DAPI and Cell Tracker (Texas Red); 2 channel reflection mode; before library preparation). (G) Violin plots illustrate the absence of correlation between number of nuclei and mapped reads per single cell. (H) Scatter plot show linear correlation between the number of detected genes and total reads (log10), as well as the stochastic distribution of cell nuclearity in the scatter plot.

Due to the technical heterogeneity in the first ICELL8 microwell chip, resulting in the removal of more than 200 cardiomyocytes from the Cluster 1 the overall analysis became underpowered. To increase the number of single-cells in the analysis, as well as to exclude artificial clustering by selecting only perfectly shaped cardiomyocytes, an additional ICELL8 microwell chip was loaded with adult murine cardiomyocytes. Aside of image-based selection of cells, additional sequencing quality assessment was performed on the total number of features (number of detected genes), dropouts, mitochondrial transcripts, non-unique alignments and expression of cardiomyocyte marker genes (Fig. 23A). As a result, 715 cells out of 2767 loaded wells contained intact and single rod-shaped cardiomyocyte by microscopic inspection and were used for analysis (Fig. 23B). Library preparation was performed in all selected wells, including cell lysis, reverse transcription, unique indexing, cDNA pre-amplification, as well as library construction based on Tn5 transposase fragmentation of full-length cDNA. On average, each cell was characterized by 0.6M sequencing reads corresponding to 3.8k detected genes. Since the number of healthy rod-shaped cardiomyocytes on the second chip (715 cells) was much higher than on the first one (200 cells) and in order to avoid massive batch correction between chips, only the second ICELL8 chip was used for the final analysis.

PCA dimensional reduction showed only a moderate level of heterogeneity (8% and 1% variance at first and second principle components, respectively) across healthy adult murine cardiomyocytes, which was insufficient to drive formation of distinct clusters. The PCA analysis, which is a linear dimensional reduction, was supplemented with t-SNE analysis, which is a non-linear dimensional reduction. However, neither PCA nor t-SNE analysis revealed any profound cellular clusters. Strikingly, cardiomyocyte size did not correlate with PCA or t-SNE clustering (Fig. 23C, D). Taken together the data suggests that strict image-based quality control is needed to avoid technical artifacts, which might arise from inclusion of damaged cells. Furthermore, the data show that adult rod-shaped cardiomyocytes are highly homogeneous independent of their size and do not cluster into distinct subpopulations.

3.1.2. Mono- and multinucleated cardiomyocytes have similar expression patterns

The scRNA-seq dataset, which included 715 single cells, was analyzed in order to compare mono- and multinucleated cells. Cardiomyocytes with multiple numbers of nuclei are larger than their mononucleated counterparts⁸³. Our data confirmed this

observation (Fig. 23E, F): in-well images of cardiomyocytes show clear positive correlation between the size of the cell (Cell-Tracker-positive area) and number of nuclei (nuclear stain). Correspondingly, the demultiplexing results (sequencing reads were separated between the single cells based on the unique well barcodes) indicated that cardiomyocytes of different nuclearity had comparable numbers of mapped sequencing reads, which indicated that comparable sequencing depths were reached across the cells (Fig. 23G, H). As shown by the PCA analysis of 715 single cardiomyocytes (Fig. 23C, D), no transcriptional heterogeneity was observed based on the cell size, which suggests, that cardiomyocyte nuclearity only marginally influences the transcriptome. To further investigate this issue, the nuclearity of each cardiomyocyte was assessed based on staining nuclei and used as a factor for in silico separation of all cells into groups of mono-, bi- and multinucleated cells.

Differential expression analysis was performed between designated groups of mono-, bi- and multinucleated cardiomyocytes. This resulted only in a small number of differentially expressed genes (DEG; FDR<5%) (Fig. 24A, B). The DEGs included four mitochondrial transcripts (mt-Nd4l, mt-Nd2, mt-Nd1, mt-Co3), as well as the transcripts of *Tpt1*, *Slc25a4*, *Rrad*, *Macrod1*, *Hes1*, *Fth1*, *Egr1*, *Cyr61*, *Cox8a*, *Btg2*, *Atf3* genes. Interestingly, the *Hes1* and *Egr1* genes are known to be involved in cellular response to hypoxia^{115,116}. Both of them were slightly downregulated in cardiomyocytes with a single nucleus. Log-fold-changes (LFCs) of differentially expressed genes were, however, low and did not lead to formation of distinct clusters in PCA nor t-SNE plots (Fig. 24C, D; Fig. 26A). Additionally, gene set enrichment analysis (GSEA) identified no statistically significant terms that were up- or downregulated in any of the groups. The principle of GSEA (2.6.6) is to annotate differentially expressed genes to the certain terms (categories, ontologies, processes or compartments) and then summarize the results to see whether some terms are significantly enriched in DEGs. The absence of significant terms in the list of DEGs between mono- and multinucleated cardiomyocytes suggest that DEGs represented a disconnected set of transcriptionally altered genes, which do not share common biological functions. Taken together, these results indicate that nuclearity has no major effect on the composition of the cardiomyocyte transcriptome.

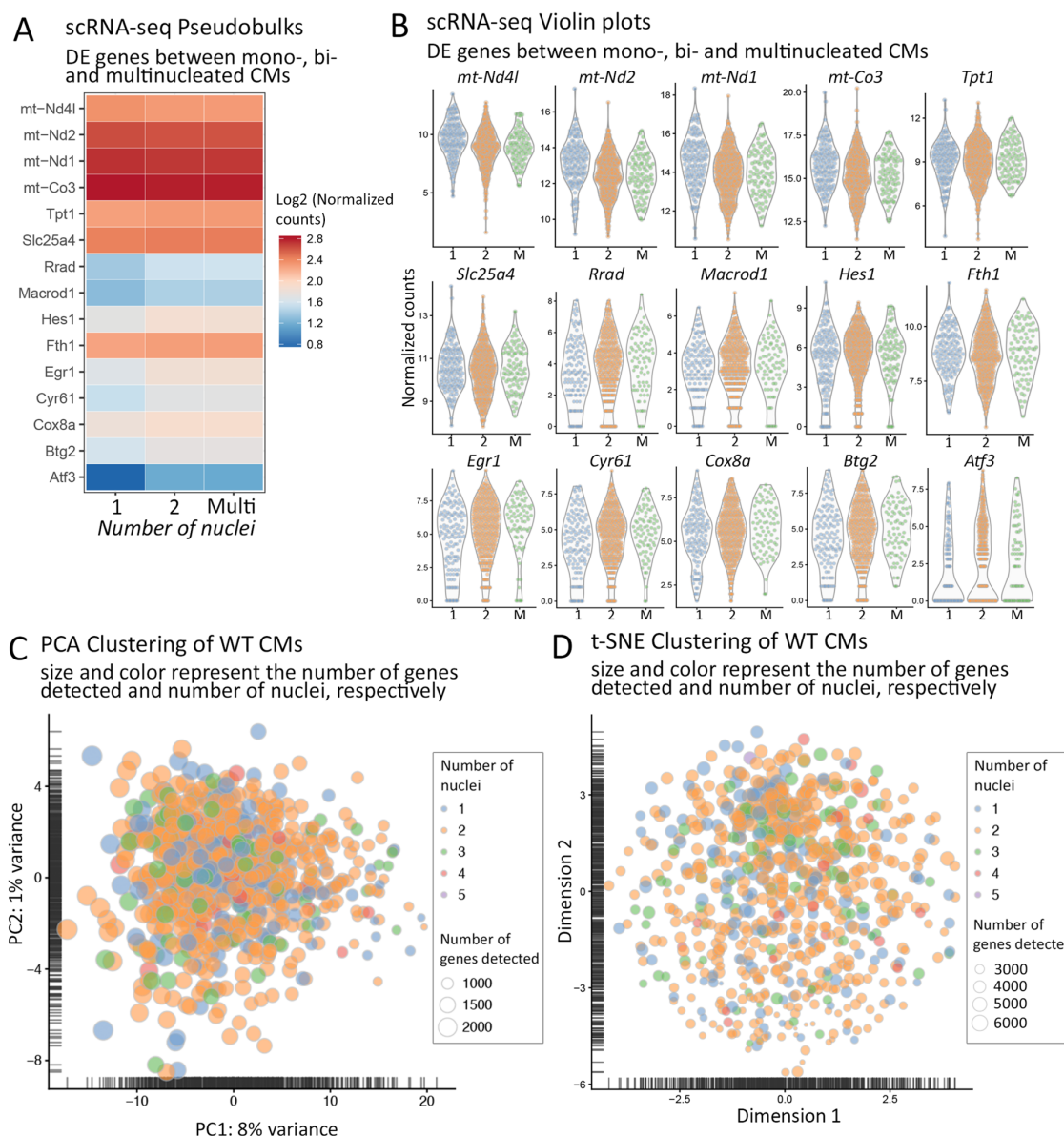


Figure 24. Mono- and multinucleated cardiomyocytes have similar expression patterns. (A) Heatmap of differentially expressed genes in mono-/bi- and mono-/multi-nucleated cardiomyocytes (pseudobulk visualization; FDR < 5%). (B) Violin plots of differentially expressed genes in mono-/bi- and mono-/multi-nucleated cardiomyocytes (single-cell visualization; FDR < 5%). “Normalized counts” are size-factor normalized counts (see Methods) (C, D) Cardiomyocyte nuclearity do not induce cluster formation in PCA and t-SNE dimensional reduction plots.

Surprisingly, the total number of reads per cardiomyocyte was not different between mono- and binucleated cardiomyocytes. This number correlates to the initial mRNA content¹¹⁷ of single cells, suggesting that increased cardiomyocyte nuclearity does not lead to a proportional increase in the number of transcripts (Fig. 25B).

Although the intact rod-shaped cardiomyocytes were transcriptionally homogeneous and did not form clusters on PCA or t-SNE dimensional reductions, an additional analysis of expression of cell cycle genes was performed to estimate putative differences between cardiomyocytes of different nuclearity. Surprisingly, a

small number of cell cycle stimulatory genes was detected in cardiomyocytes, which is uncommon for post-mitotic cells ¹¹⁸ (Fig. 25C). Such genes included *Ccni*, *Ccnl2*, *Ccnk*, *Ccnd3*, *Ccnh*, *Ccny*, *Ccnd2*, *Ccnl1*, *Ccna2*, *Cdk4*, *Ccng1*. In addition, several inhibitory cell cycle-related genes such as *Cdkn2d*, *Cdk2ap1*, *Inca1*, *Cdkn1b* were detected. Transcripts of the individual cell cycle genes were, however, randomly distributed across the dataset and no single cardiomyocyte expressed a larger set of stimulatory or inhibitory cell cycle genes. Furthermore, no correlation between nuclearity and expression of cell cycle genes was observed (Fig. 25D).

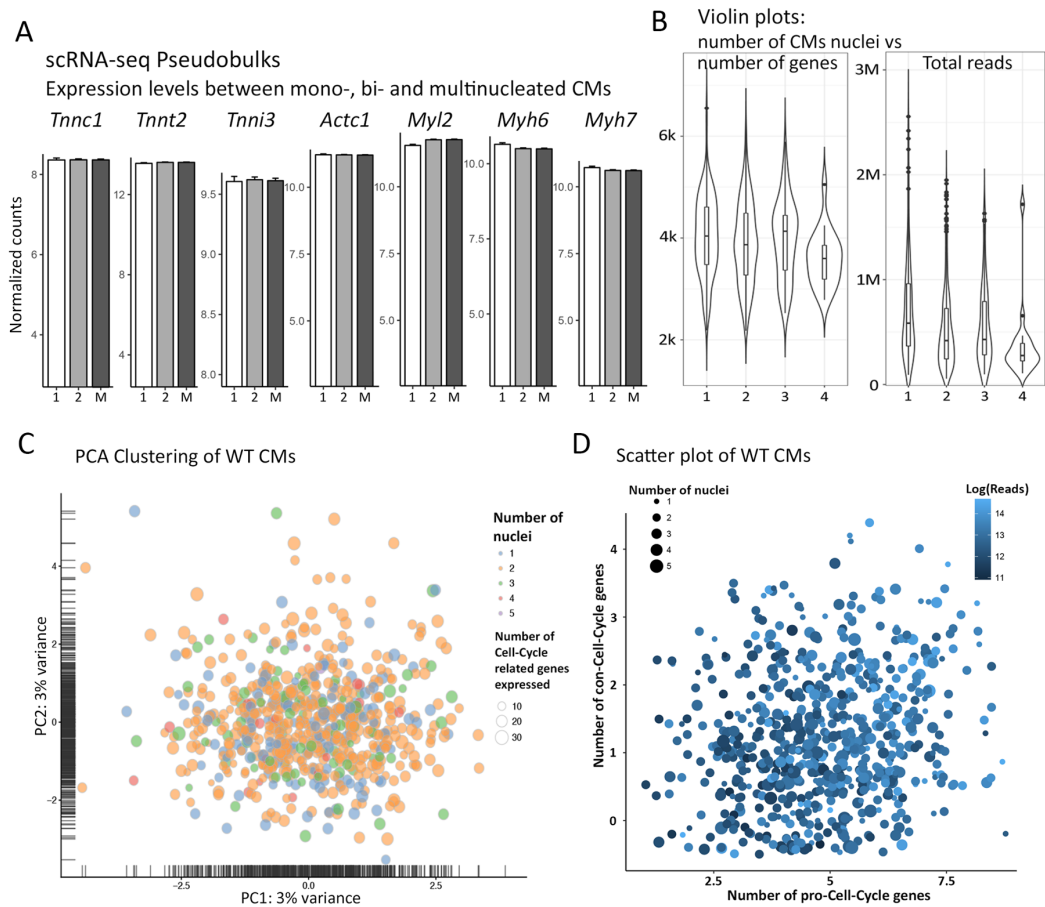


Figure 25. Mono- and multinucleated cardiomyocytes randomly express a limited set of cell-cycle genes. (A) Pseudobulk bar plots show equal expression of cardiac marker genes in mono- and multinucleated cardiomyocytes. “Normalized counts” are size-factor normalized counts (see Methods). **(B)** Violin plots show no correlations between number of nuclei and number of detected genes or number of nuclei and total reads per single cell. **(C)** No clustering was found based on nuclearity (color) and number of cell cycle genes expressed (presence of Cyclins, CDKs, Inhibitors illustrated as size of data points) in PCA dimensional reduction plots. **(D)** Scatter plot illustrates no clustering based on cell cycle genes expression (cyclins, CDKs) and cell cycle inhibiting genes (Inhibitors of Cyclins and CDKs), total reads (color) and nuclearity (size). For proper visualization the number of genes was kept discrete but data points were moved on both axes with a random number in the range of (-0.5, 0.5).

3.1.3. Cardiac hypertrophy induces transcriptional heterogeneity in cardiomyocytes

Since no heterogeneity was observed under basal conditions, the next step was to investigate the single cell transcriptome under non-steady-state conditions. For that purpose, a pathological condition was chosen, i.e. cardiac hypertrophy. The single cell analysis was repeated using cardiomyocytes isolated from mice that underwent transverse aortic constriction (TAC to induce cardiac hypertrophy due to left ventricle blood pressure overload)¹¹⁹. WT animals of the same biological background and age were employed to avoid potential confounding effects.

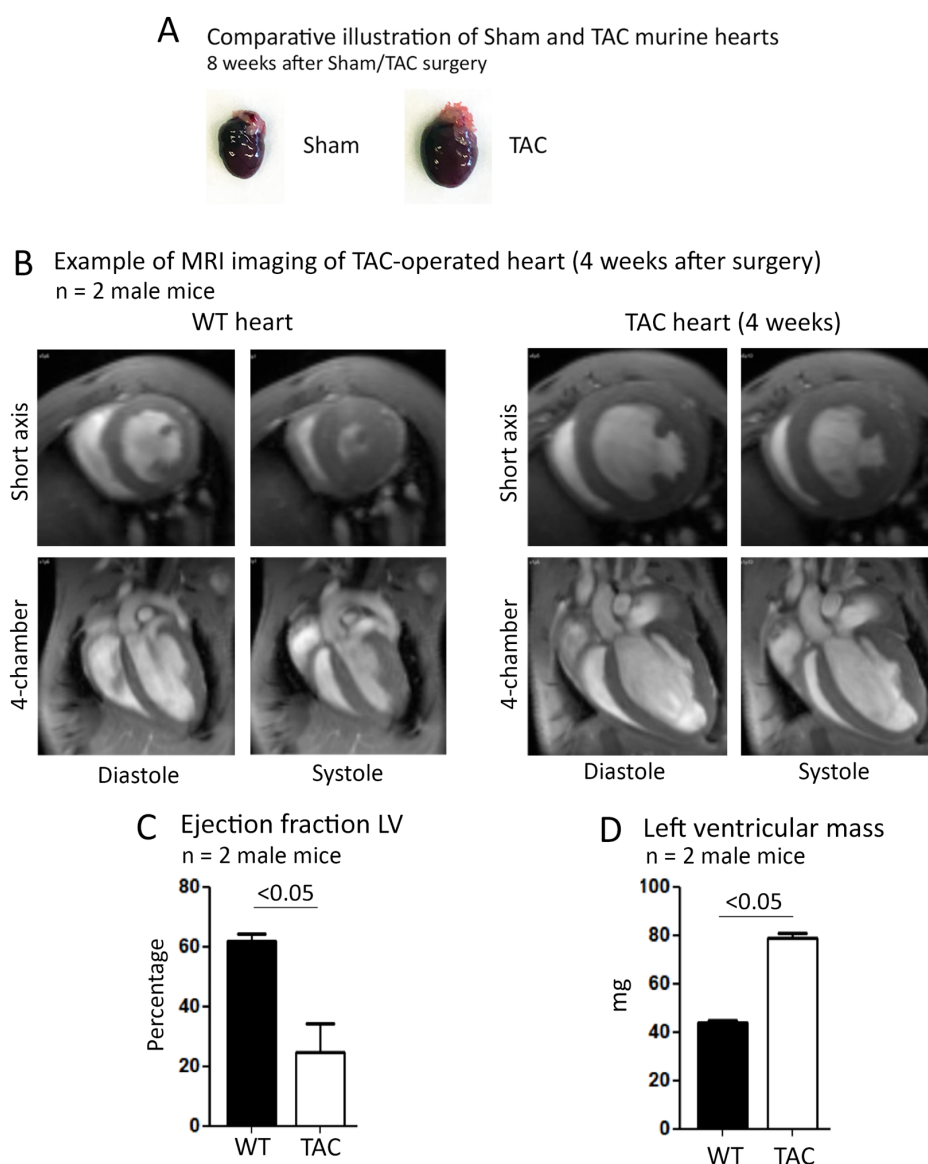


Figure 26. Effects of TAC on cardiac hypertrophy and heart function. (A) Photographs of isolated mouse hearts 8 weeks after transaortic constriction (TAC) and sham operation. (B-D) Left ventricular mass and ejection fraction, measured by magnetic resonance imaging (MRI) of mouse hearts 4 weeks after sham (WT) and TAC operations. TAC surgery leads to profound cardiac hypertrophy. The illustrations in (B) represent short axis (top) and 4-chamber (bottom) views of sham and TAC hearts in systole and diastole (n=2, Student's t-test).

Cardiomyocytes, isolated from hypertrophic hearts 2 month after TAC, were subjected to the ICELL8 platform to generate TAC scRNA-seq dataset. 1/8 of the wells were loaded with cardiomyocytes from untreated WT animals as a control. Additionally, the WT cardiomyocytes were used as reference to merge the initial WT single-cell dataset with the TAC dataset and to remove technical batch-effect. In the TAC scRNA-seq experiment, 236 TAC cardiomyocytes and 40 WT cardiomyocytes were obtained. Altogether, the merged dataset contained 236 TAC and 755 WT cardiomyocytes. TAC-derived cardiomyocytes were transcriptionally clearly different from WT cells, as shown on the PCA and t-SNE plots (Fig. 26A-D; Fig. 27A, B).

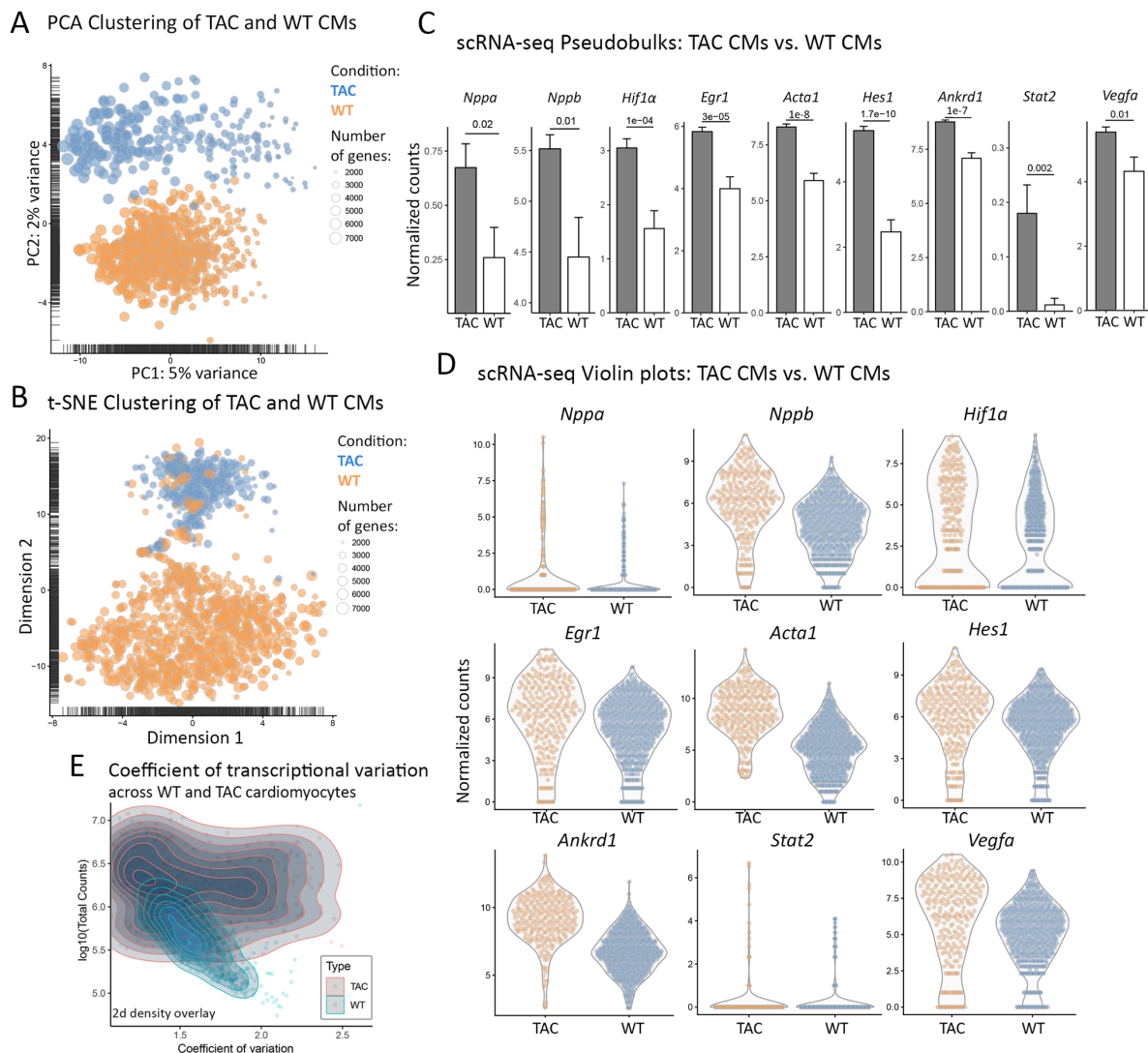


Figure 27. Homogeneity of cardiomyocytes is lost after an induction of hypertrophy. (A, B) PCA and t-SNE dimensional reduction illustrate transcriptional differences between healthy and hypertrophic cardiomyocytes. TAC: N=4 mice; Sham: n= 4 mice. 2 TAC-operated mice were used to generate TAC scRNA-seq dataset (C, D) Pseudobulk bar plots and violin plots illustrate differential expression of hypoxia-related genes in healthy and hypertrophic cardiomyocytes. “Normalized counts” are size-factor normalized counts (see Methods) (Student’s t-test) (E) Scatter plot illustrates an increase of transcriptional variation upon TAC-induced cardiac hypertrophy.

Bioinformatical analysis revealed that expression of cardiac marker genes remained constant in healthy and hypertrophic cardiomyocytes. 184 genes were significantly differentially expressed (FDR < 5%) between TAC and WT cardiomyocytes by scRNA-seq. The differences were also clearly visible on PCA and t-SNE dimensional reduction plots. The first and second principal components (PCA analysis) represented 5% and 2% of the total variance, respectively. An overlap, representing cardiomyocytes from both WT and TAC groups, was observed by both techniques, which may indicate that not all cardiomyocytes respond equally to hypertrophic heart remodeling.

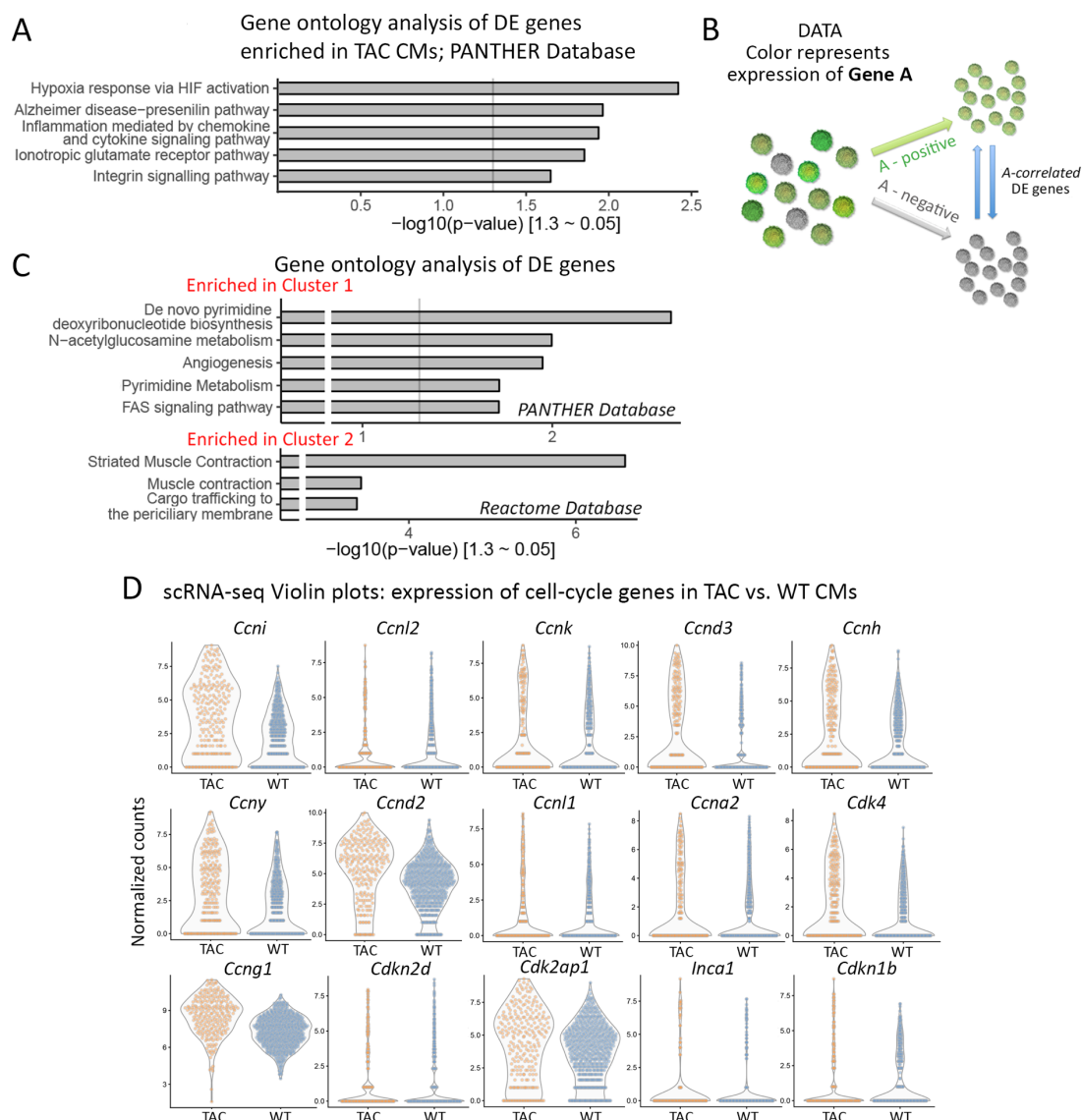


Figure 28. Homogeneity of cardiomyocytes is lost after an induction of hypertrophy. (A) Enriched GSEA terms of differentially expressed genes in cardiomyocytes isolated from WT and TAC hearts (Panther database). **(B)** Scheme showing separation of gene-related groups for single-cell interactome analysis. **(C)** Enriched GSEA terms of differentially expressed genes in Cluster 1 and Cluster 2 cardiomyocytes from TAC hearts (PANTHER and Reactome database). **(D)** Violin plots show expression of cell cycle-related genes in WT and TAC cardiomyocytes. “Normalized counts” are size-factor normalized counts (see 2.6.6. of methods).

Notably, DEGs that separated WT and TAC groups of cardiomyocytes included genes, typically elevated upon hypertrophy and hypoxia: *Nppa*, *Nppb*, *Hif1 α* , *Egr1*, *Acta1*, *Hes1*, *Ankrd1* (Fig. 27C, D). Furthermore, cardiomyocytes in the TAC group were enriched for the “Hypoxia response via HIF-activation” GO term ($p < 0.05$), as well as for various signaling pathways and inflammatory terms (Fig. 28A).

Cell-associated coefficients of transcriptional variation were calculated for WT and TAC cardiomyocytes. To calculate this coefficient, a standard deviation of expression of all genes was calculated for each cell and normalized to total expression counts. These coefficients were visualized against the number of sequenced reads (Fig. 27E). As a result of cardiac hypertrophy, transcriptional variation dramatically increased. Furthermore, single-cell interactome analysis was performed. In brief, “base-genes”, that were expressed in less than 80% of cardiomyocytes and showed at least 10% of mean expression levels (2617 genes in total) were selected. Base-gene-positive ($> 0.7 \times$ mean expression) and negative ($< 0.7 \times$ mean expression) groups, containing at least ten cells each, were subjected to differential gene expression analysis using the MAST approach resulting in a list, which relates the 2617 base-genes to differentially expressed genes. Only differentially expressed genes with fold change > 2 and FDR < 0.01 were used for further analysis. Base-genes together with genes showing a statistically significant correlation formed an interactome map visualized in circular plots. Genes showing significant co-expression (excluding base-gene self-pairs) were connected by lines. The single-cell interactome analysis verified a dramatic increase of gene-gene co-expressions in TAC vs WT conditions (236 pairs for WT and 716 pairs for TAC) (Fig. 28B; Fig. 29A). Altogether the results indicate that cardiomyocytes acquire elevated transcriptional activity upon cardiac hypertrophy.

3.1.4. Hypoxic responses drive cardiomyocytes heterogeneity in hypertrophic hearts

Among TAC cardiomyocytes, two partially connected clusters of cardiomyocytes were found, in which the separation correlated to expression of *Hif1 α* (Fig. 29B), the master regulator of hypoxic response¹²⁰. K-means ($k=2$) clustering was performed to strictly separate the clusters (Fig. 29C)¹²¹. Analysis of differentially expressed genes between these clusters revealed that virtually all of them were up-regulated in cardiomyocytes from cluster 1 (*Hif1 α ^{high}*), suggesting that these cardiomyocytes are more transcriptionally active compared to cluster 2. Notably, the

differentially expressed genes, up-regulated in the cardiomyocytes from the first cluster were enriched for the GO term “Angiogenesis”, while cardiomyocytes from the second cluster were enriched for “Striated muscle contraction” (FDR<0.05) (Fig. 28C) by GSEA. The impact of *Hif1 α* on the expression pattern of TAC-derived hypertrophic cardiomyocytes was analyzed next. To this end, cardiomyocytes, with an expression level of *Hif1 α* exceeding 70% of the mean expression level across the dataset were considered to be *Hif1 α* positive. Approx. 41% of TAC cardiomyocytes fell into that category. Both groups had statistically undistinguishable expression of cardiac marker genes *Tnni3*, *Tnnt2*, *Myh6* and *Myh7* (Fig. 30A). However, global comparison led to the identification of more than 2000 DEGs between *Hif1 α* ⁺ and *Hif1 α* ⁻ TAC cardiomyocytes (FDR<0.01) (Fig. 30B), and most of the DEGs were up-regulated in *Hif1 α* ⁺ group. Among these, *Hif1 α* ⁺ TAC cardiomyocytes showed higher expression of *Egln2* (*Phd1*)¹²² and *Vegfa*¹²³. Simultaneous increase of *Egln2* and *Vegfa* expressions was found and visualized on pseudobulk (Fig. 29E) and single-cell levels (Fig. 29D, F). Additionally, *Hif1 α* ⁺ TAC cardiomyocytes as compared to their *Hif1 α* ⁻ counterparts, overexpressed *Ldha*, *Pgk1*, *Pfkl*, *Hk2* (Fig. 29E, F), which are known downstream targets of the *Hif1 α* transcription factor.

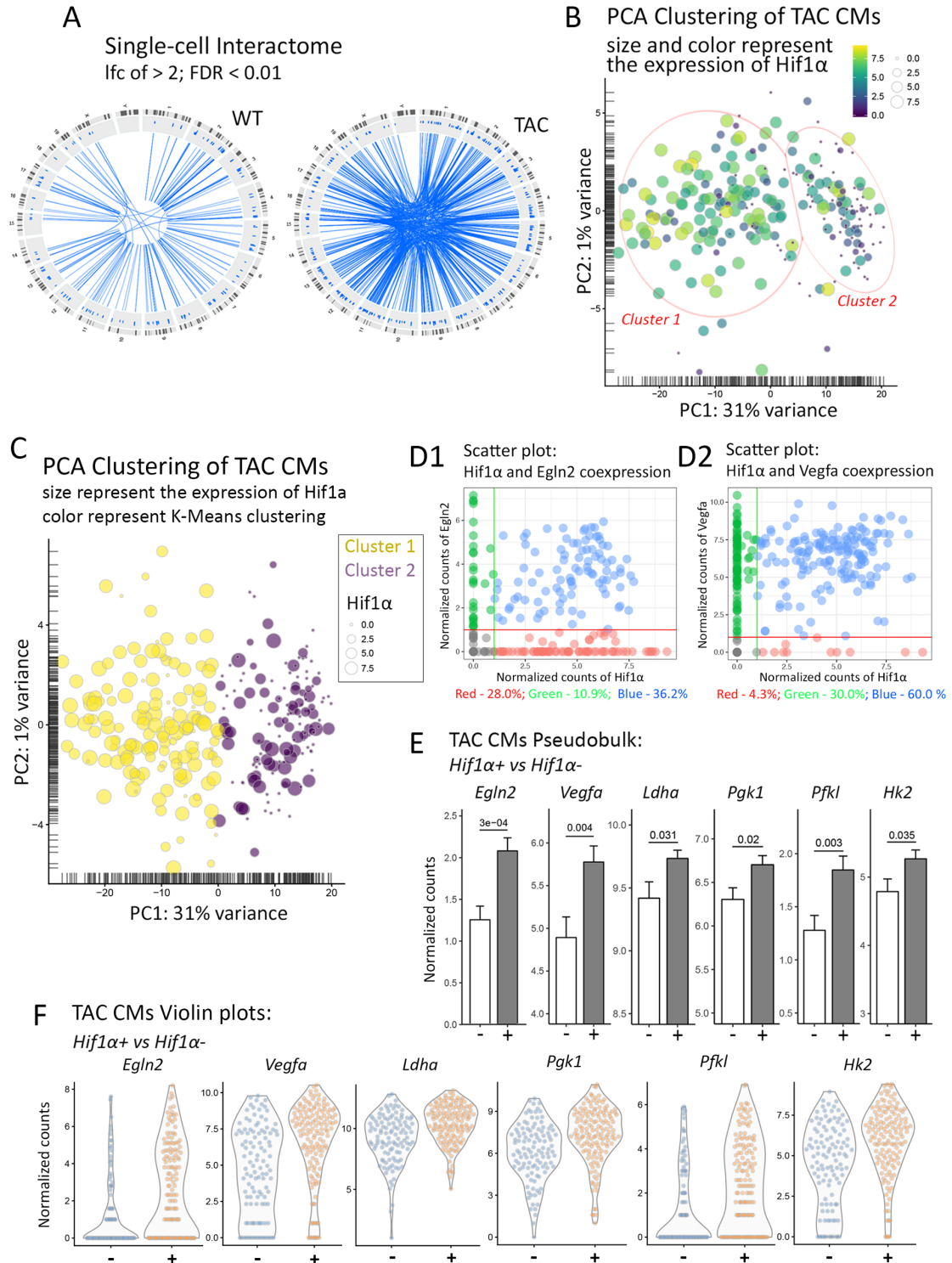


Figure 29. Hypoxic responses drive cardiomyocytes heterogeneity in hypertrophic hearts. (A) Single-cell interactome analysis shows elevated of gene co-expressions during TAC-induced cardiac hypertrophy. Genes with significant co-expression (excluding Base-Genes self-pairs), were connected by lines. TAC: N=10 mice; Sham: n= 4 mice. **(B, C)** PCA dimensional reduction plots of TAC-derived hypertrophic cardiomyocytes form two cell clusters based on *Hif1α* expression. Red ellipses in panel B refer to arbitrary visualization. The formal clustering by K-means is shown in panel C. **(D)** Scatter plots illustrating co-expression of *Hif1α* and *Egln2* (D1) and *Hif1α* and *Vegfa* (D2) with single-cell resolution. Percentages of cardiomyocytes in respective clusters are written below the plots. **(E, F)** Pseudobulk bar plots and violin plots illustrate differential expression of certain genes in *Hif1α*⁺ and *Hif1α*⁻ cardiomyocytes (Student's t-test). "Normalized counts" are size-factor normalized counts.

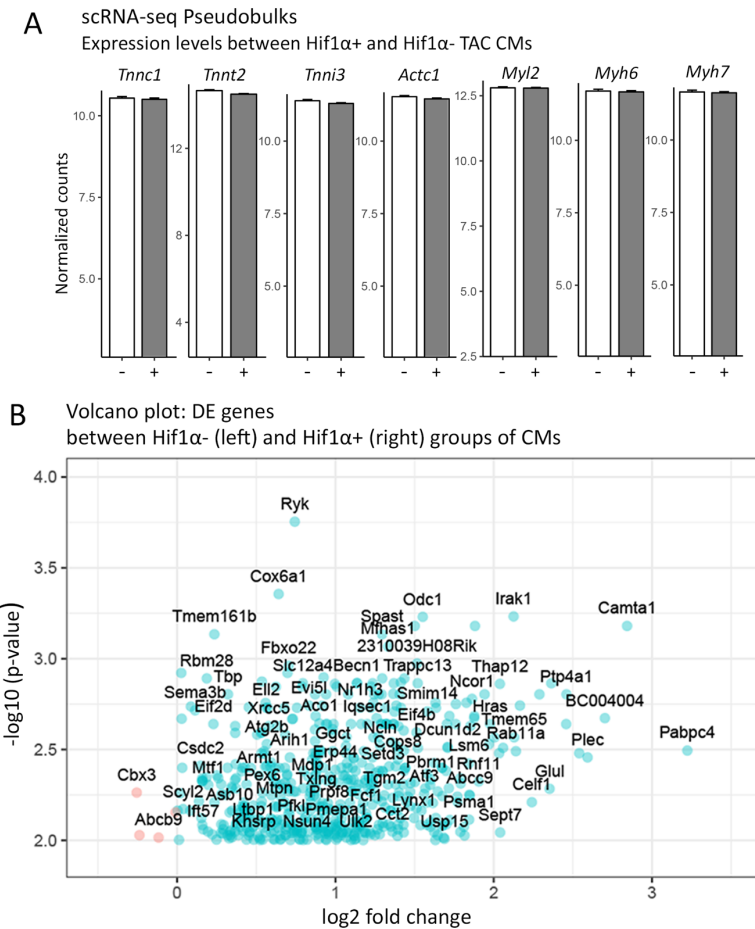


Figure 30. Hypoxic responses drive cardiomyocytes heterogeneity in hypertrophic hearts. (A) Pseudobulk bar plots illustrate statistically equal expression of cardiac marker genes in *Hif1α*⁺ and *Hif1α*⁻ cardiomyocytes. “Normalized counts” are size-factor normalized counts (see Methods) (B) Volcano plot illustrates differentially expressed genes in *Hif1α*⁺ and *Hif1α*⁻ cardiomyocytes.

3.1.5. HIF1α stabilization inversely correlates with vascularization in hypertrophic hearts

The analysis of single cell transcriptomic data revealed that heterogeneity among TAC cardiomyocytes was primarily associated with response to hypoxia. The lack of oxygen in hypertrophic myocardium, which triggered hypoxia responses, might be induced by insufficient vessel growth. To test this hypothesis, hypoxic cells were identified by immunostaining against *Hif1α* and vascularization was assessed by immunostaining against CD31 (endothelial marker). As expected, control hearts (sham operation) showed absence of *Hif1α* expression, and the vascular network was well-organized with wide and long blood vessels (Fig. 31A1). In contrast, hypertrophic hearts had areas with patches of *Hif1α*⁺ nuclei (Fig. 31C). Additionally, the blood vessels in hypertrophic hearts were smaller and had no obvious interconnections (Fig. 31A2, 31A3).

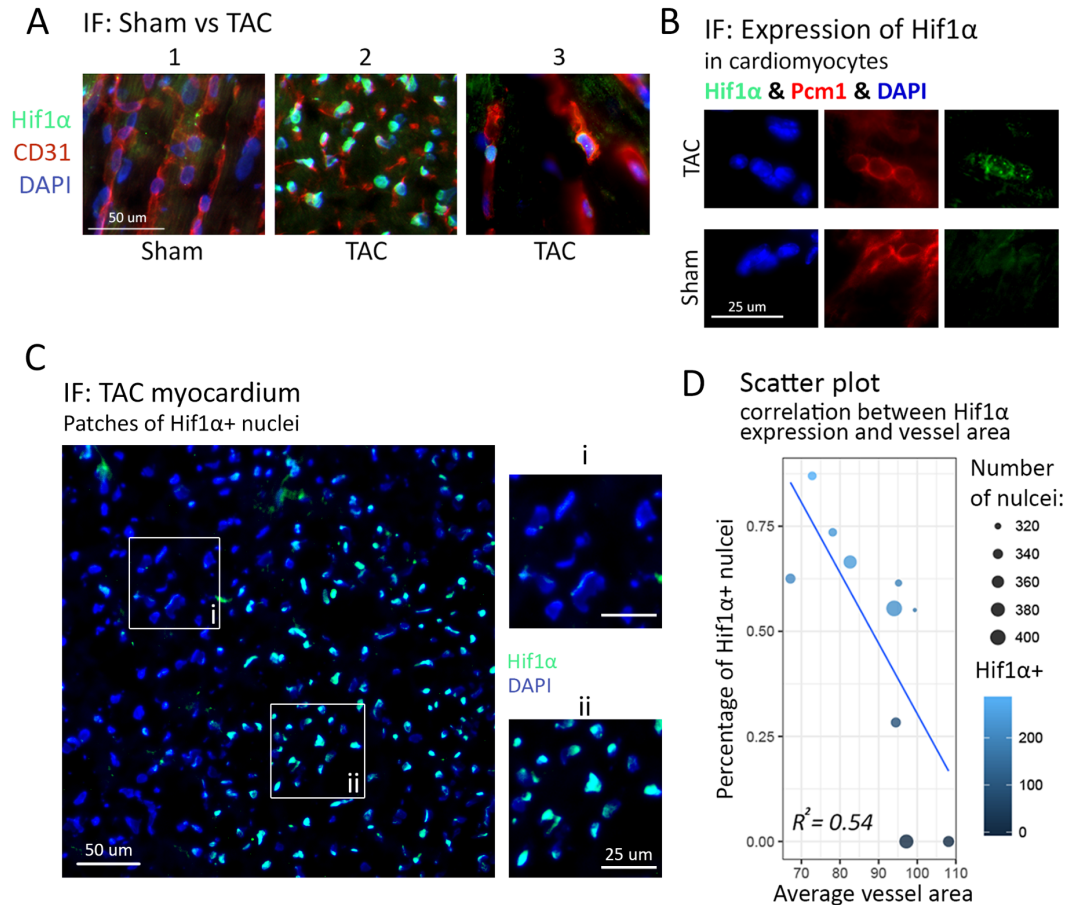


Figure 31. HIF1 α stabilization in cardiomyocytes inversely correlates with the distance to blood vessels in the hypertrophic hearts. (A) Immunofluorescent staining for *Hif1 α* and CD31 under different conditions: (1) Sham; (2, 3) TAC. TAC: N=10 mice; Sham: n= 4 mice. (B) Immunofluorescent staining for *Hif1 α* and *Pcm1*. (C) “Patchy” pattern of *Hif1 α* expression (D) Scatter plot illustrates an inverse correlation of *Hif1 α* expression and average vessel area (square μm) in the proximity ($R^2=0.54$).

To evaluate *Hif1 α* expression in cardiomyocytes, sections from hypertrophic hearts were co-stained for *Hif1 α* and PCM1 (cardiomyocyte nuclei marker)⁸². Co-staining revealed hypoxic cardiomyocytes with nuclei positive for *Hif1 α* (Fig. 31B). The average area of blood vessels (CD31⁺ area) was counted, and a clear inverse correlation ($R^2=0.54$) was found with a number of *Hif1 α* ⁺ nuclei in the area (Fig. 31D). Taken together, these data confirm that *Hif1 α* ⁺ cells are preferentially located in areas of myocardium, which lack proper vascularization.

3.2. The neuropeptide Galanin restores the regenerative capacity of the aged muscle

3.2.1. Ageing has a distinct transcriptional signature in murine quiescent muscle stem cells

The efficiency of muscle regeneration is decreasing with age (see 1.3.4.), and pathological changes in the muscle stem cells (MuSCs) pool are suggested to be the primary reason of such regenerative decline. To investigate changes and decipher the cellular heterogeneity among juvenile and aged MuSCs, Takara ICELL8 scRNA-seq was applied. Two divergent timepoints were selected for comparison: mice aged 2 month (named as young) and 24 months (named as old). To allow a fast and stringent isolation of MuSCs via FACS, the *Pax7:zsGreen* mouse model was used. Since expression of the *Pax7* transcription factor is a marker of MuSCs^{86,87}, all cells that emit green fluorescence in FACS after isolation from muscles were considered to be MuSC. Freshly isolated quiescent MuSCs (qMuSCs) from four young and four old mice were used to generate a single-cell dataset, which underwent the same quality assessment as described in 3.1. The final dataset consisted of 2830 single cells (1783 cells for old and 1047 cells for young time points). scRNA-seq yielded an average of 0.52M reads corresponding to 3391 detected genes per cell.

The UMAP dimensional reduction¹¹³ was performed to evaluate the global transcriptional differences between young and aged MuSCs. The reduction revealed moderate heterogeneity within the dataset and a large overlap between clusters of young and old MuSCs (Fig. 32A). Aged MuSCs, however, were characterized by higher transcriptional variation (Fig. 32B, C), which recapitulates recent results from Hernando-Herraez et. al¹²⁴. The differential expression analysis (using DESeq2) between young and aged MuSCs resulted in a list of 467 DEGs (Fig. 32D). Of these, 324 genes were up-regulated in young MuSCs, and 143 genes were up-regulated in old cells (Fig. 32D). Within this set, GSEA (FDR<5%) revealed up-regulation of the following terms in young MuSCs: “Aerobic respiration” (BioCyc database); “Cell division” and “ATP Synthesis” (GO database); “Oxidative phosphorylation” and “Ribosome” (KEGG database); “DNA replication” (PANTHER database). Old MuSCs were enriched for “Positive regulation of cell differentiation” and “Negative regulation of neuron projection development” (GO database). These findings recapitulate the known phenotypes of ageing: decreased cell proliferation, attenuated metabolism and a disturbed balance between proliferation and differentiation⁹⁰.

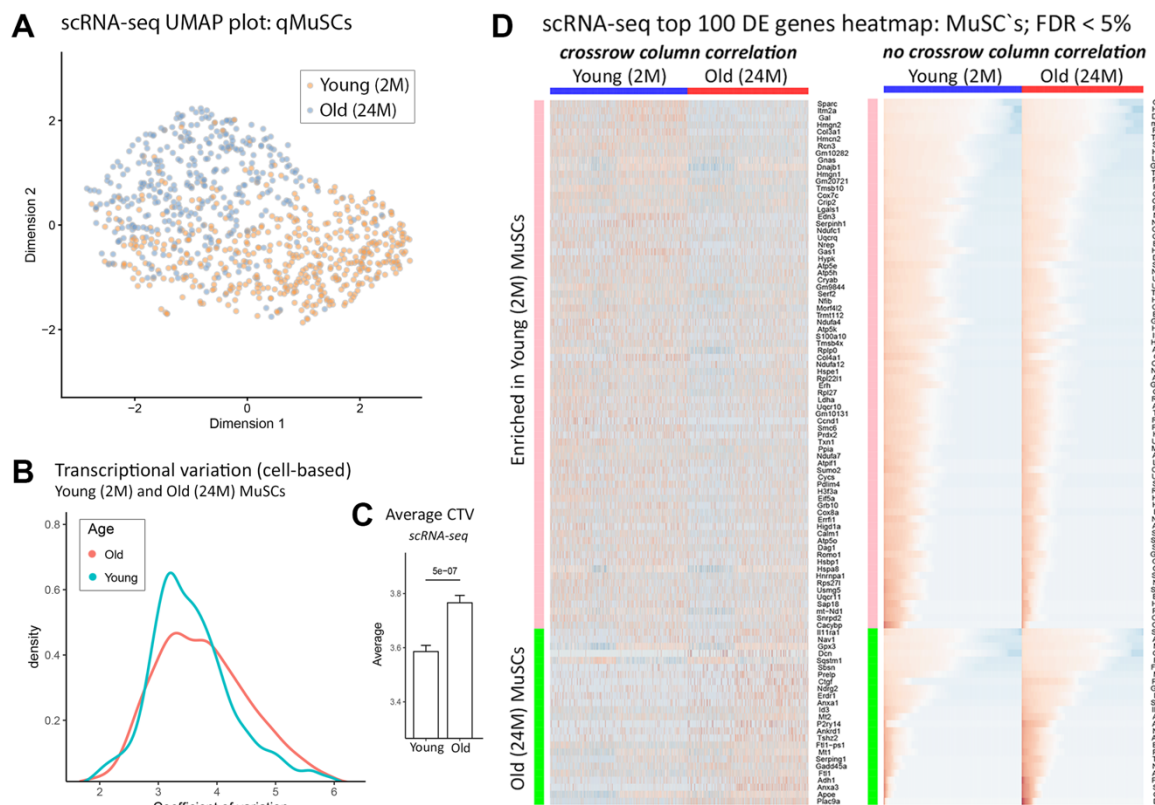


Figure 32. Ageing creates a distinct transcriptional signature in murine qMuSCs. (A) UMAP dimensional reduction shows overlapping clusters of young and old quiescent MuSCs. (B),(C) A density plot and a barplot show an increase of transcriptional variation among quiescent MuSCs with age. (D) Heatmaps illustrate top 100 differentially expressed genes between young and old quiescent MuSCs.

In terms of highest absolute effect size and differential expression significance, the following genes were identified as genes reflecting aging of MuSC: *Gal*, *Itm2a*, *Sparc* (up-regulated in young MuSCs) and *Anxa3*, *Plac9a/Plac9b/Gm9780* (up-regulated in old MuSCs) (Fig. 33A-C). In the scRNA-seq dataset, 33% of juvenile and 9% of aged MuSCs expressed the *Gal* gene; 49% and 27% expressed the *Itm2a* gene; 47% and 29% expressed the *Sparc* gene; 2% and 22% expressed the *Anxa3* gene; 20% and 44% expressed the *Plac9a/Plac9b/Gm9780* genes respectively. The expression of *Itm2a*¹²⁵ and *Sparc*¹²⁶ were previously described in MuSCs and muscle. However, deletion of these genes in mice did not result in any clear muscular phenotype. *Plac9a/Plac9b/Gm9780*, which represent multiple copies of the same genomic sequence in one locus, were associated with early embryonic development and require further research¹²⁷. Notably, *Plac9a/Plac9b/Gm9780* were recently found to induce cell cycle arrest in human embryonic hepatic cells¹²⁸. This may suggest the involvement of *Plac9* gene family in the dysregulation of proliferation/differentiation balance in old myoblasts.

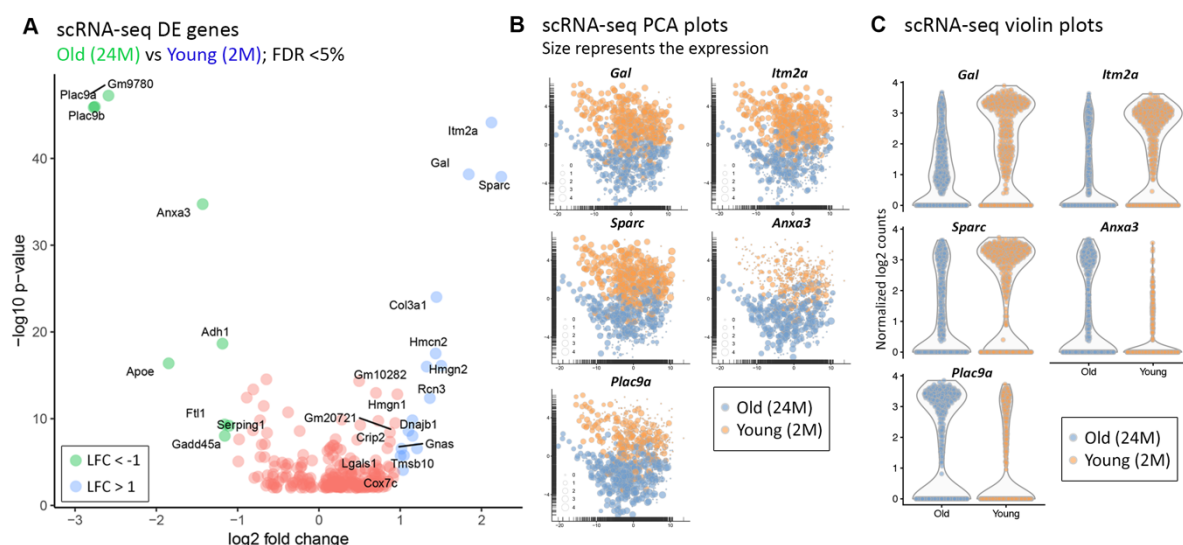


Figure 33. Differentially expressed genes between young and old quiescent MuSCs. (A) Volcano plot illustrate top differentially expressed genes between young and old quiescent MuSCs. **(B)** PCA plots show distribution of selected DE genes. Size of dots represents expression of respective gene. **(C)** Violin plots show expression of selected DE genes in young and old single-cell MuSCs.

Taken together, these data suggest that young and old MuSCs are transcriptionally heterogeneous and have distinct expression signatures. Interestingly, previous studies have not analyzed the role of *Gal*, *Anxa3* and *Plac9* genes in MuSCs. In chapters 3.2 and 3.3 respectively, this thesis focuses on two of them: *Gal* and *Anxa3*.

Galanin is a small neuropeptide, composed of 29 AA in the mouse and 30 AA in humans. It is coded by the *Gal* gene in mice and the *GAL* gene in humans¹²⁹. The Galanin signaling pathway is well conserved across species. Three receptors of Galanin (Fig. 34), named Galanin Receptor 1-3 (*Galr1*, *Galr2*, *Galr3* genes in mouse) are known. The inhibition constants (K_i) of Galanin receptors are remarkably low (K_i = 1 nM, 1.5 nM, 1 nM respectively). Galanin and its receptors are mainly expressed in the nervous system and the brain. In this context, alterations of Galanin signaling were associated with Alzheimer disease, Huntington disease, dementia, depression, anxiety and others¹³⁰. Interestingly, Galanin can promote regeneration of motor neurons. It has been shown that administration of Galanin improves the regeneration of the sciatic nerve, while mice, lacking *Gal* expression, had drastically decreased efficiency of the sciatic nerve regeneration¹³¹. Taken together, this suggests that Galanin and its receptors have a positive effect on nerve maintenance and repair.

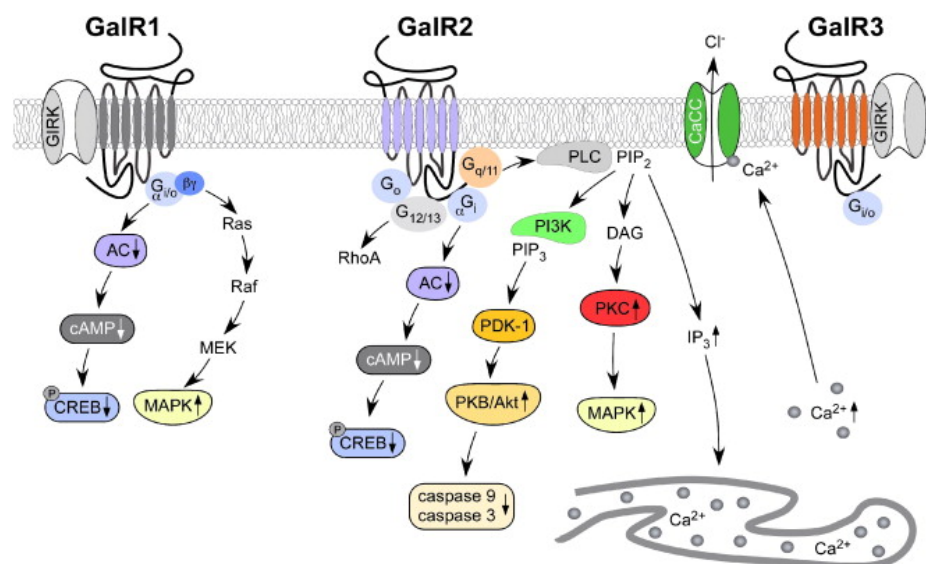


Figure 34. Galanin receptors and their downstream signaling pathways ¹²⁹

Annexin A3 is a secreted protein, which has the capacity to inhibit phospholipases (in particular Phospholipase A2) ¹³². The Annexin protein family is tightly associated with the regulation of apoptosis and progression of cancer. *Anxa3* expression is considered to be a tumor marker ^{133,134}. Overexpression of *Anxa3* increases tumor growth, while downregulation decreases proliferation of tumor cells ^{135,136}.

3.2.2. A *Gal*^{pos} subpopulation of quiescent muscle stem cells is lost during ageing

To evaluate the role of *Gal* in qMuSCs, all young cells from the scRNA-seq dataset were separated *in silico* into *Gal*^{pos} and *Gal*^{neg} groups (346 and 701 cells in groups, respectively) (Fig. 35A, C, D). Differential expression analysis revealed 249 DEGs between the *Gal*^{pos} and *Gal*^{neg} groups. Remarkably, the vast majority of DEGs (248) were up-regulated in the *Gal*^{pos} group (Fig. 35B). These were enriched for the following GSEA terms (FDR<5%): “Aerobic respiration” (BioCyc database), “ATP synthesis coupled proton transport” (GO database), “Ribosome” and “Oxidative phosphorylation” (KEGG database). Strikingly, *Atp5d*, *Atp5e*, *Atp5h*, *Ndufa1*, *Ndufb6*, *Ndufc1*, *Mrps14*, *Mrpl23* transcripts were up-regulated in the young *Gal*^{pos} group (Fig. 36A, B), while expression in the young *Gal*^{neg} group was as low as in old MuSCs. This led to the hypothesis that *Gal*^{neg} young MuSCs are transcriptionally similar compared to old MuSCs. Together with the GSEA analysis, this suggests that loss of *Gal* expression in quiescent MuSCs eradicates a metabolically particularly active subpopulation of MuSCs.

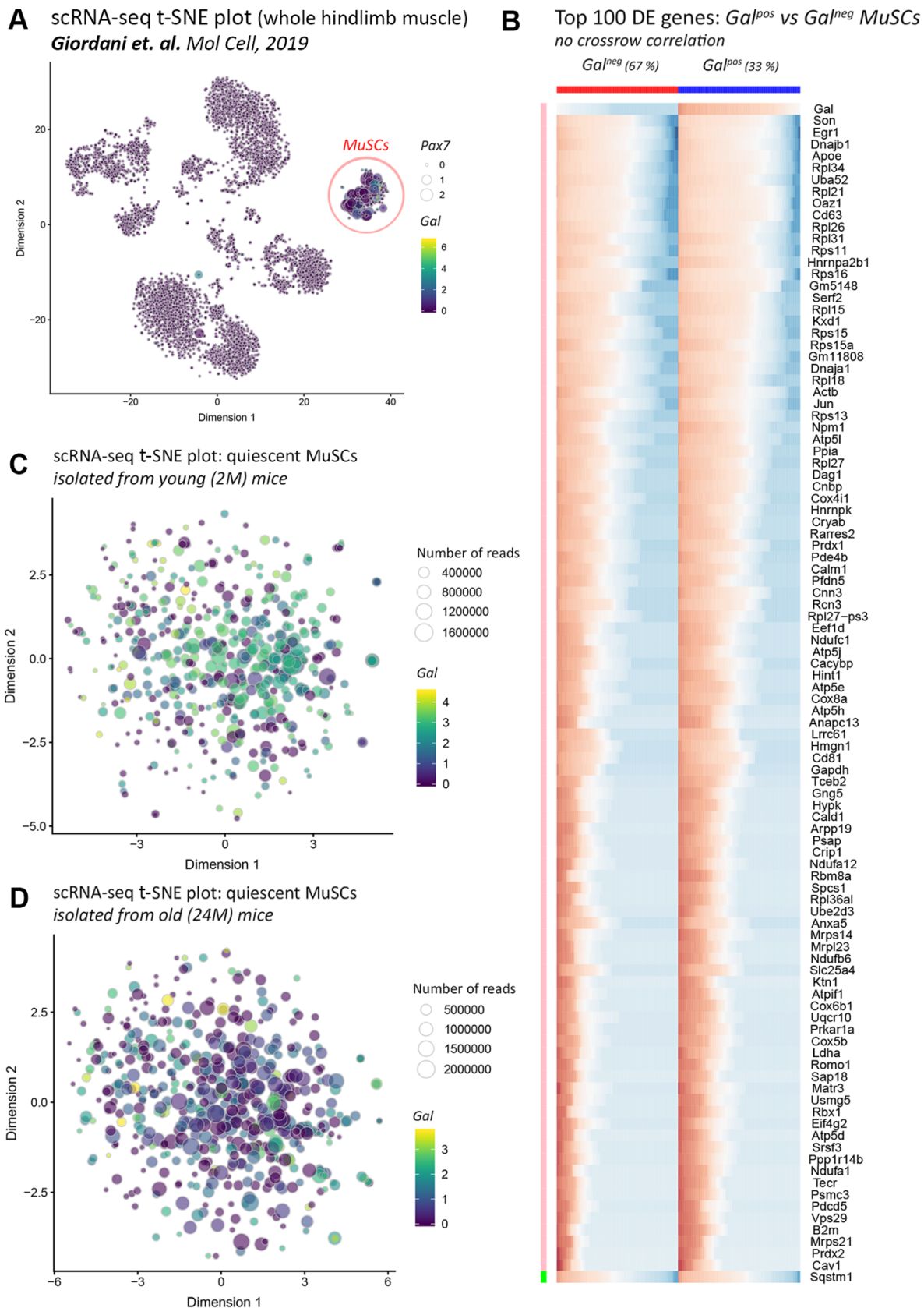
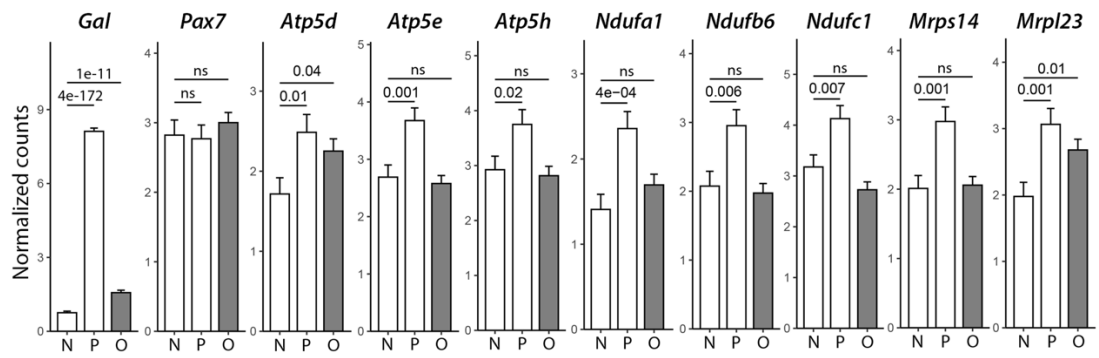


Figure 35. A *Gal*^{pos} subpopulation of quiescent muscle stem cells is lost during ageing. (A) t-SNE dimensional reduction shows exclusive expression of the *Gal* gene in qMuSCs¹³⁷. **(B),(C)** t-SNE plots show decreased proportion of *Gal*^{pos} cells with age. **(D)** Heatmap showing the top 100 DE genes between *Gal*^{pos} and *Gal*^{neg} groups of cells.

A Pseudobulk barplots: Gal^{pos} (P) vs Gal^{neg} (N) vs Old (O) qMuSCs



B Single-cell violin plots: Gal^{pos} (P) vs Gal^{neg} (N) vs Old (O) qMuSCs

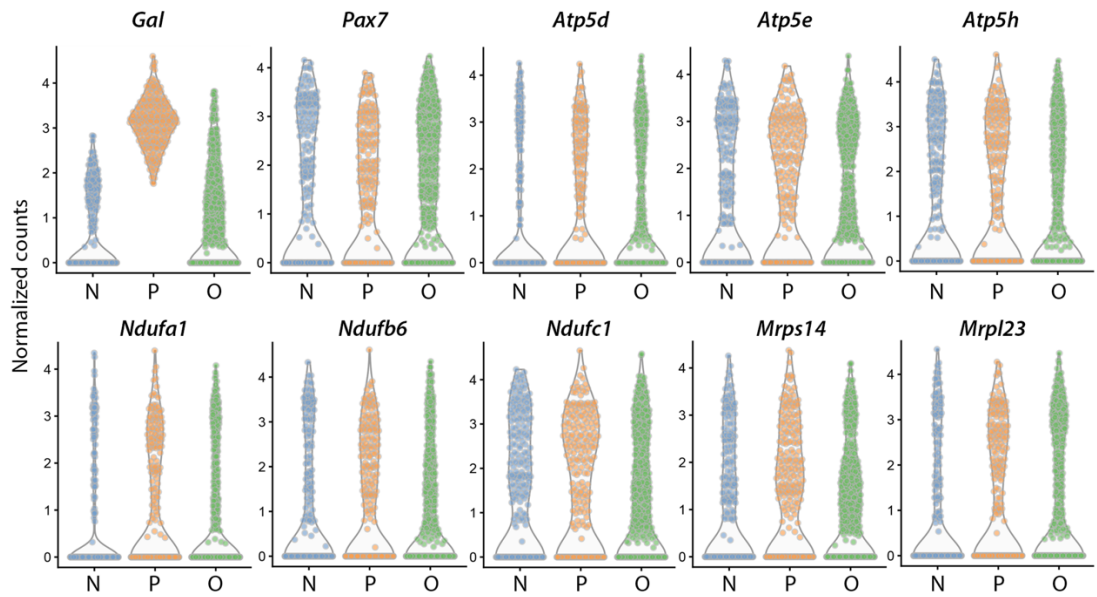


Figure 36. A subpopulation of Gal^{pos} quiescent MuSCs marked by expression of metabolism-relevant genes is lost during ageing. (A),(B) Pseudobulk bar-plots and single-cell violin plots illustrate decreased expression of metabolic genes in Gal^{neg} young qMuSCs and in old qMuSCs (Student's t-test).

Expression of *Gal* in qMuSCs was confirmed by RT-qPCR and compared to *Gal* expression in sciatic nerves, serving as positive control (Fig. 37A). The level of *Gal* expression (normalized to *Gapdh*) was comparable between qMuSCs and sciatic nerves. The binary nature of Galanin protein expression in qMuSCs was further confirmed by immunofluorescence (Fig. 37B). Only a subset of qMuSCs expressed Galanin, corroborating scRNA-seq analysis results.

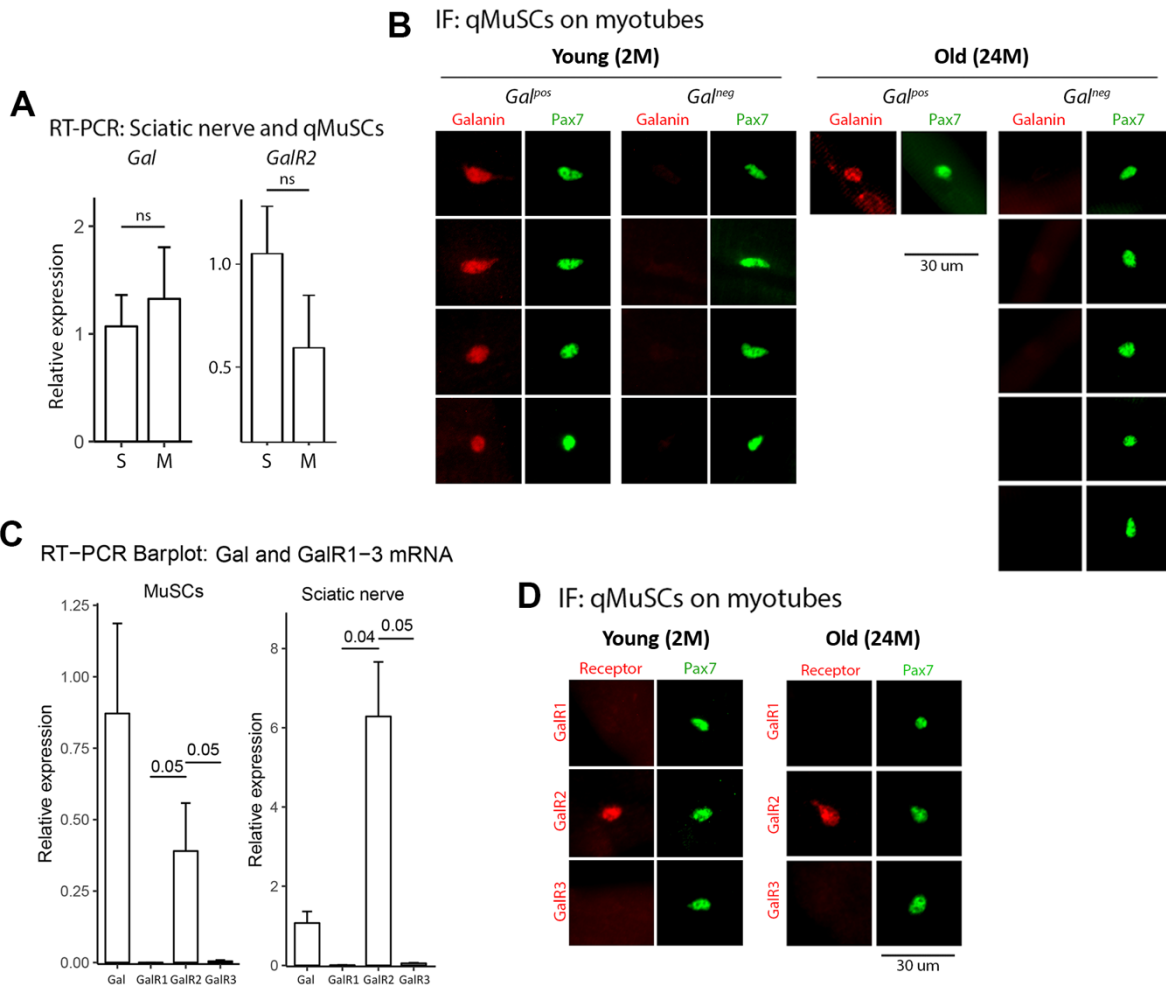


Figure 37. Expression of Galanin and Galanin receptors in quiescent MuSCs. (A) RT-qPCR barplots show expression of *Gal* and *GalR2* in sciatic nerve (S) and in qMuSCs (M) (normalized to *Gapdh*; n=3, Student's t-test). (B) Immunostaining shows examples of Galanin positive and negative young and old qMuSCs. (C) RT-qPCR barplot confirms that *Gal* is expressed in qMuSCs and that *GalR2* is the only Galanin receptor in qMuSCs (normalized to *Gapdh*; n=3, Student's t-test). (D) Immunostaining corroborates the expression of *GalR2* in young and old qMuSCs.

As described above, Galanin binds to three receptors: Galanin receptor 1,2 and 3. The expression of *GalR1*, *GalR2* and *GalR3* was, however, too low to be detected by scRNA-seq. Therefore, RT-qPCR method was used to determine expression levels in pooled qMuSCs using sciatic nerves as a positive control (Fig. 37C). Both qMuSCs and sciatic nerves expressed only *GalR2* ($p < 0.05$). The expression of Galanin receptor proteins in MuSCs was confirmed by immunofluorescence (Fig. 37D), further validating the exclusive expression of Galanin receptor 2 in qMuSCs. The data clearly indicate that Galanin Receptor 2 is the primary Galanin receptor in qMuSCs.

3.2.3. Ageing alters chromatin accessibility in quiescent muscle stem cells

Transcriptional heterogeneity among cells often originates from epigenetic alterations (see 1.1). To evaluate whether such alterations also accompany the age-correlated transcriptional changes observed in qMuSCs, chromatin accessibility was investigated in qMuSCs in the context of ageing using an array-based scATAC-seq method.

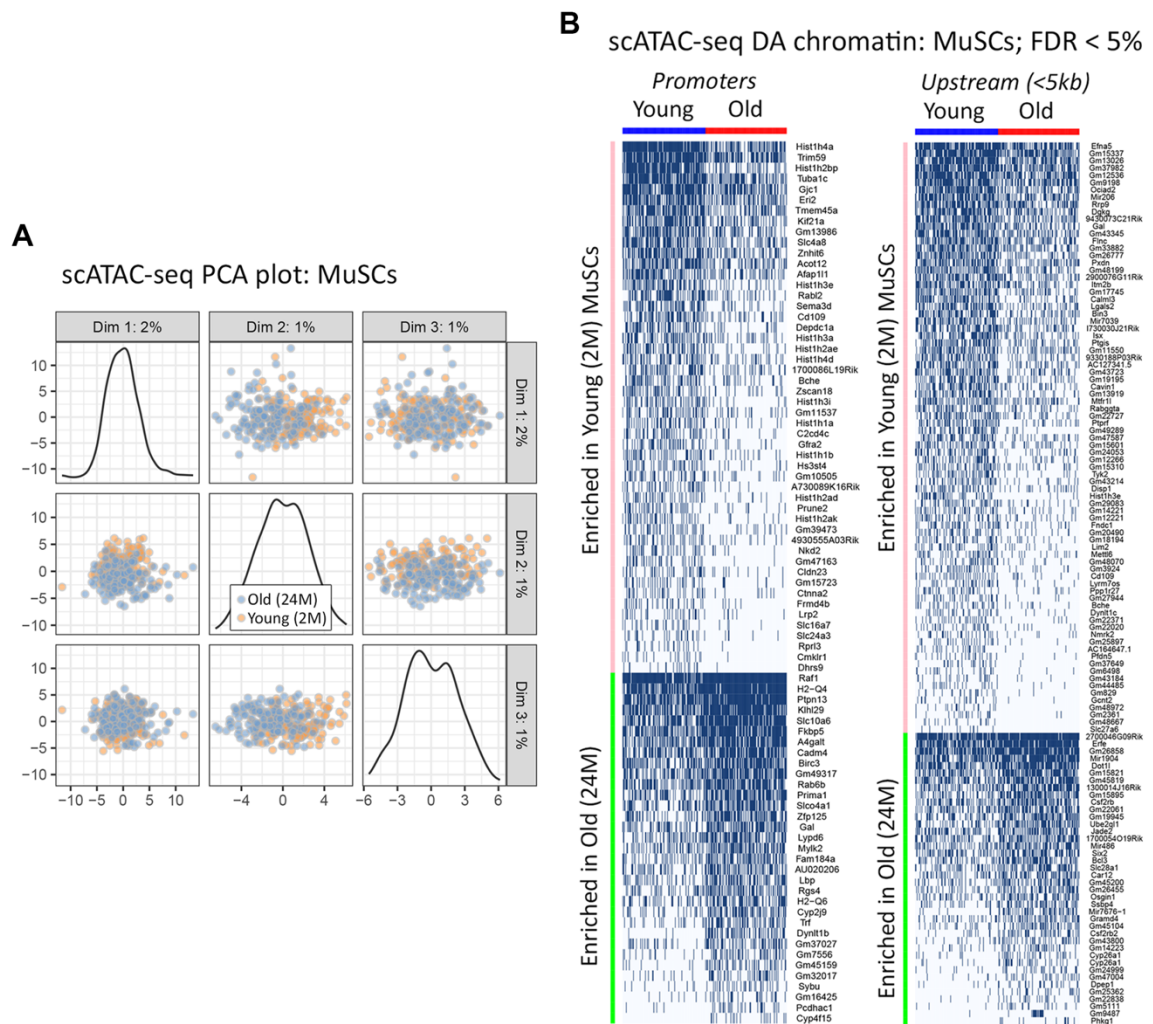


Figure 38. Ageing is accompanied by changes in the chromatin accessibility landscape. (A) PCA dimensional reduction shows overlapping clusters of young and old qMuSCs. **(B)** Binary heatmaps show differentially accessible regions (in promoters and upstream regions, respectively) between young and old quiescent MuSCs.

Similar to the experiments presented above, two timepoints were selected for comparison: mice with 2 and 24 months of age, respectively. Freshly isolated quiescent MuSCs from three young and three old *Pax7:zsGreen* mice were used to generate a single-cell ATAC-seq dataset, composed of 275 single cells in total (136 “old” and 139 “young” cells after QC). Single-cell libraries were sequenced with 2M

reads per cell on average to obtain sufficient data for downstream analysis. The ATAC-seq protocol is designed to reveal the regions of accessible chromatin, represented as peaks, which are formed by enrichment of reads at distinct genomic regions. In total, 70.815 peaks were detected in the dataset across the genome, 26.508 (37,4%) were annotated to genes, because they were located within a +/- 5 kb range from the transcription starting site of a particular gene. Further analysis focused on the peaks located in promoters (11.597 peaks, 43,7% of annotated peaks) and upstream gene regions (5.685 peaks; 21,4% of annotated peaks; 5kb region).

Similar to the scRNA-seq approaches, dimensional reduction methods (like PCA, t-SNE or UMAP) are applicable to scATAC-seq to reveal clusters of single cells with similar chromatin accessibility landscapes. PCA clustering showed a high degree of overlap between young and aged qMuSCs clusters (Fig. 38A). Differential accessibility analysis was performed separately for promoters and upstream regions between young and aged cells. Different from RNA-seq, where gradual changes of gene expression are detected, the chromatin accessibility on the single cell level is determined by the access to the DNA, yielding binary results, either “0 – not accessible” or “1 – accessible”. Binary single-cell data were visualized with volcano plots (Fig. 39A) and heatmaps (Fig. 38B). Juvenile qMuSCs-specific signals were enriched for “Nucleosome assembly” (GO database), “DNA replication” (PANTHER database), and for “DNA Methylation” and “Meiosis”, as well as “Activation of HOX genes in hindbrain development during early embryogenesis” (Reactome database). Significantly differentially accessible chromatin **promoter** regions included the following muscle-related genes: *Tuba1c* (involved in cell division ¹³⁸), *Prune2* (involved in apoptosis ¹³⁹) and *Nkd2* (involved in Wnt signaling ¹⁴⁰) were **up-regulated in young** MuSCs; *Raf1* (MAPK signaling ¹⁴¹) *Birc3* (involved in apoptosis and necroptosis ¹⁴²) and *Rgs4* (MAPK signaling inactivation ¹⁴³) were **up-regulated in old** MuSCs. Significantly differentially regulated chromatin **upstream** regions included the following muscle-related genes: *Mir206* (involved in muscle development ¹⁴⁴), *Flnc* (involved in muscle fiber development ¹⁴⁵), *Calml3* (enhance myosin-10 translation ¹⁴⁶), *Cavin1* (enhances ribosome activity ¹⁴⁷), *Mtfr1l* (involved in aerobic respiration ¹⁴⁸) and *Mettl6* (involved in methylation ¹⁴⁹) were **up-regulated in young** MuSCs and *Gramd4* (involved in apoptosis ¹⁵⁰) were **up-regulated in old** MuSCs.

The overlap between scATAC-seq and scRNA-seq was surprisingly poor: only 14 genes / gene regions (3%) were shared among 466 DEGs (FDR < 0.05) and 474

differentially accessible genes (DAGs) (FDR < 0.05) between young and old MuSCs. The following genes were up-regulated and more accessible in young MuSCs: *App*, *Emp1*, *Tuba1c*, *Hist1h2ad*, *Hist1h2ak*, *Hist1h2ae*; down-regulated and less accessible: *Dnm3*, *Cyp26a1*; down-regulated, but more accessible: *Golim4*, *Ddx3x*, *Hist1h2bp*; up-regulated, but less accessible: *Gal* (*promoter region*), *Pde10a*, *Eif2s3y*. Such disbalance between accessibility and expression may be explained by different modes of transcriptional regulation (for example, transcription factors, methylation, histone modifications, etc.).

The *Gal* gene appeared in both promoter-based and upstream-based lists of differentially accessible regions between young and old qMuSCs (Fig. 39A, B). In light of the findings reported above, it was surprising that the *Gal* **promoter** appeared more accessible in old qMuSCs, while an **upstream** peak was more accessible in young qMuSCs. To explore the biological relevance of these peaks, all cells were separated into groups: *Gal_{promoter}^{open}* vs. *Gal_{promoter}^{closed}* and *Gal_{upstream}^{open}* vs. *Gal_{upstream}^{closed}*. This approach revealed that 49 young cells and 88 old cells had an accessible *Gal* **promoter** region, and 118 young cells and 65 old cells had it closed. The *Gal* **upstream** region was accessible in 93 young cells and 49 old cells, and closed in 74 young cells and 104 old cells.

A differential accessibility analysis revealed 109 regions deregulated between *Gal_{upstream}^{open}* (48 up-regulated) and *Gal_{upstream}^{closed}* groups (61 up-regulated) (Fig. 39C). There were, however, no differentially accessible regions between *Gal_{promoter}^{open}* vs. *Gal_{promoter}^{closed}* groups (excluding *Gal* promoter peak itself). This suggests that a differential accessibility of the *Gal* promoter peak doesn't lead to global changes in the chromatin accessibility of qMuSCs.

The differentially accessible gene regions between *Gal_{upstream}^{open}* and *Gal_{upstream}^{closed}* groups included the following genes: *Kdm6b* (involved in demethylation¹⁵¹), *Frat1* (Wnt pathway¹⁵²), *Col16a1* (collagen gene¹⁵³), *Vgll4* (transcription factor involved in muscle regeneration¹⁵⁴), *Map2k3* (MAPK pathway¹⁵⁵), *Ahnak2* and *Itpkc* and *Trpm8* (calcium signaling¹⁵⁶⁻¹⁵⁸) were in *Gal_{upstream}^{open}*; *Cdkn2d* (cdk inhibitor¹⁵⁹), *Faf1* (regulation of necrosis¹⁶⁰), *Ctdsp1* (negative regulation of G1/S transition¹⁶¹), *Cdh6* and *Cabin1* (involved in chromatin organization^{162,163}), *Isy1* (DNA repair and splicing control¹⁶⁴), *Cenpf* (involved in cell proliferation¹⁶⁵), *Nrbf2* (involved in autophagy¹⁶⁶), *Map3k11* (MAPK pathway¹⁶⁷), *Lama5* (laminin subunit¹⁶⁸), *Inpp4a* (IP3 signaling¹⁶⁹) were in *Gal_{upstream}^{closed}*.

Interestingly, 56% of young MuSCs had an accessible **upstream** region in *Gal* locus, in contrast to 32% of old (Fig. 39D-F). The ratio of age-related decrease in accessibility (56% / 32%) was comparable to the decrease in *Gal* expression (33% / 9%). Taken together, this data suggests that the **upstream** ATAC peak in the *Gal* locus contains a regulatory potential for gene expression.

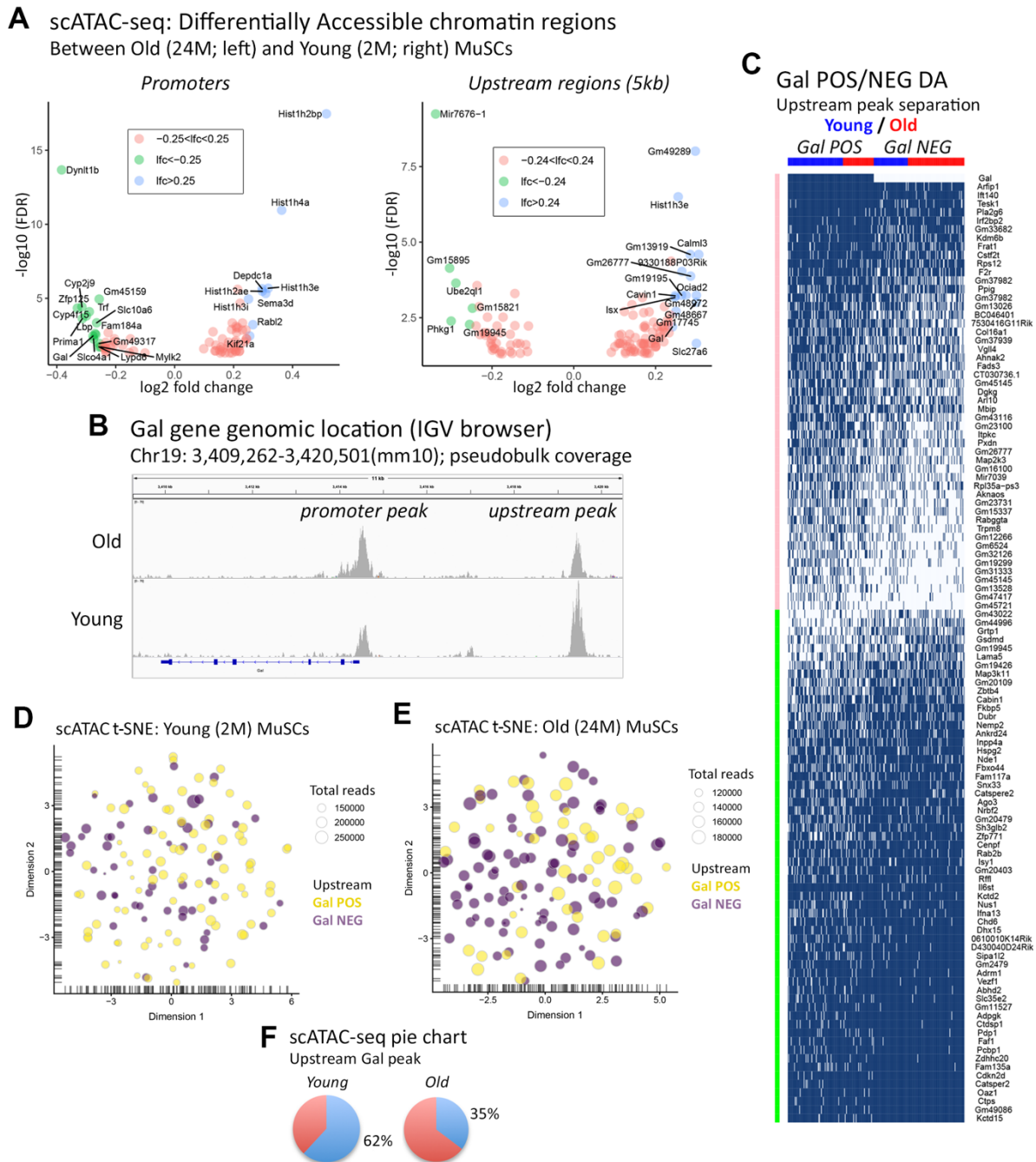


Figure 39. The *Gal* chromatin region is differentially accessible between young and old quiescent MuSCs. (A) Volcano plots illustrate differentially accessible promoters and upstream regions. (B) IGV browser snapshot of merged reads from young and old qMuSCs. (C) Differentially accessible regions between *Gal*^{pos} (*Gal* upstream peak is accessible) and *Gal*^{neg} (*Gal* upstream peak is not accessible) cells. (D),(E) t-SNE plots show distribution of *Gal*^{pos} cells across cell populations in young and old qMuSCs. (F) Pie charts show decrease of proportion of *Gal*^{pos} cells with age.

As described above, analysis of chromatin accessibility in MuSC identified a peak upstream of the *Gal* genes that might regulate *Gal* gene expression. In addition to the chromatin accessibility, *Gal* expression was previously shown to be regulated by DNA methylation of its promoter region, where a CpG island is located¹⁷⁰. However, bulk MeDIP-seq analysis of the differentially methylated regions between young and aged quiescent MuSCs did not reveal any differences in the *Gal* promoter CpG island methylation (data not shown). Another possible regulatory mechanism of *Gal* gene expression might be differential transcription factor binding. The *Gal* gene promoter region harbors binding motifs of various transcription factors (Fig. 40A). In order to be responsible for declining *Gal* expression with age, a putative transcription factor needs to be (i) expressed in quiescent MuSCs; (ii) its binding motif should be present and accessible in the *Gal* promoter; (iii) expression or activity of such a transcription factor should decrease with age. Among the transcription factors, which can bind to the *Gal* promoter, only one fulfills all of these criteria: *Esr1* (estrogen receptor 1) transcription factor (Fig. 40B).

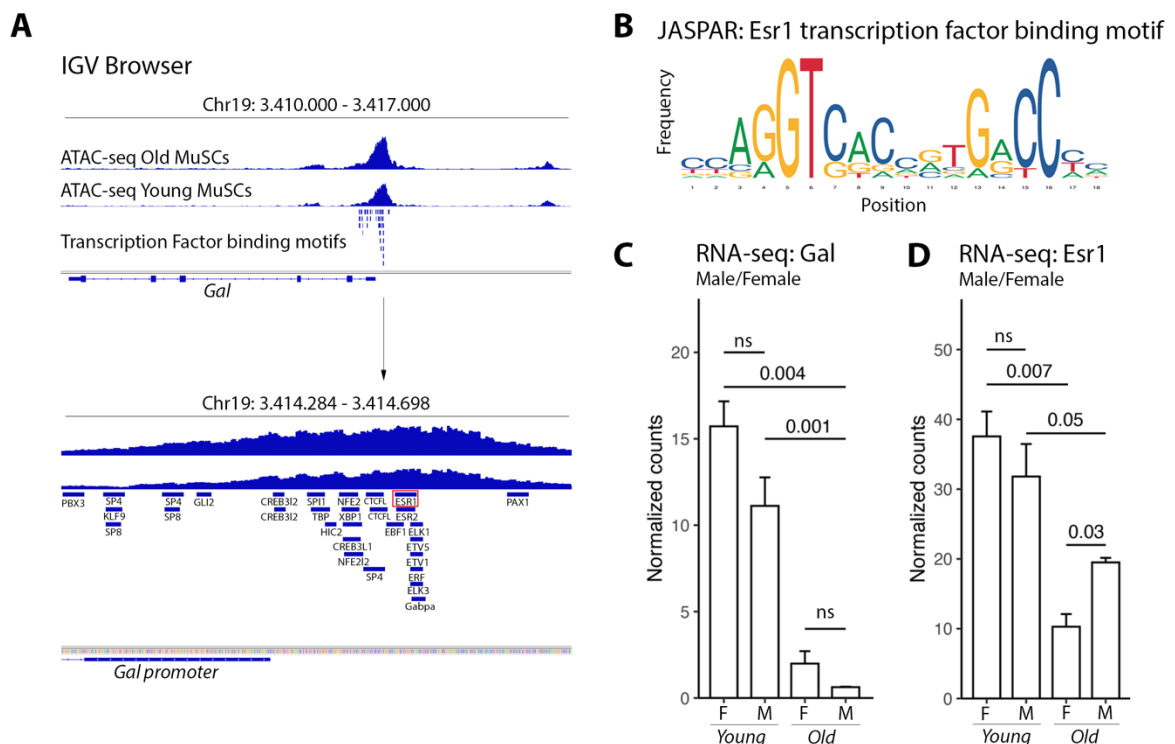


Figure 40. *Gal* promoter region harbors a *Esr1* transcription factor binding motif. (A) IGV browser snapshot shows chromatin accessibility of the *Gal* gene promoter with an overlay map of various transcription factor binding motifs. **(B)** JASPAR *Esr1* transcription factor binding motif. **(C)** Expression of the *Gal* gene decreases with age irrespectively of the mouse sex. **(D)** Expression of the *Esr1* gene decreases with age.

Esr1 is activated by the estrogen hormone. Although estrogen is commonly associated with the female menstrual cycle, it has functions outside of the reproductive system, particularly in the skeletal muscles and in muscle stem cells ¹⁷¹. For example, it's been shown that female mice, which underwent an ovariectomy (an operation, when both ovaries are removed, and therefore Estrogens are not produced anymore), showed increased muscle atrophy and decreased muscle regeneration efficiency ¹⁷². The decreased regeneration efficiency of ovariectomized mice is similar to *Gal* KO animals. In this context it is important to mention, that expression of *Gal* and *Esr1* genes are not sex-specific (Fig. 40C,D). Expression of *Gal* decreases in both male- and female-qMuSCs, as well as *Esr1* gene expression. Therefore, the decrease of *Gal* expression with age might be due to decreased binding of the *Esr1* transcription factor to the *Gal* promoter, which originates from decreased systemic Estrogens abundance with age and/or decreased *Esr1* gene expression ¹⁷³.

To prove this hypothesis, chromatin immunoprecipitation experiments need to be performed with a focus on *Esr1* binding to the promoter of the *Gal* gene, combined with reporter gene assays. It will also be interesting to perform ovariectomies and analyze *Esr1* knock-out strains (qMuSCs-specific) to investigate the resulting consequences on *Gal* gene expression in muscle. Ultimately, the *Esr1* binding site in the *Gal* promoter region might be genetically deleted or altered (with, for example, the CRISPR-Cas9 system) to prevent *Esr1* transcription factor binding.

3.2.4. Intraperitoneal Galanin injections induce transcriptional, epigenetic and metabolic changes in the quiescent muscle stem cells

Galanin is a secreted neuropeptide, and can be easily introduced into the systemic circulation *in vivo*. The next step was to check whether intraperitoneal (i.p.) Galanin injections would alter the state of qMuSCs (transcriptional and/or epigenetic). To this end, two groups (n=2) of *Pax7:zsGreen* mice were formed: young (2 months) with and without Galanin i.p. injections (40 µg/kg/d). Commercially available Galanin (Tocris, Germany) was used for activation of Galanin receptor 2 (K_i = 1.5 nM) ¹⁷⁴. Treatment group received daily Galanin injections for 21 days, followed by FACS-based isolation of qMuSCs and subsequent bulk RNA- and ATAC-sequencing.

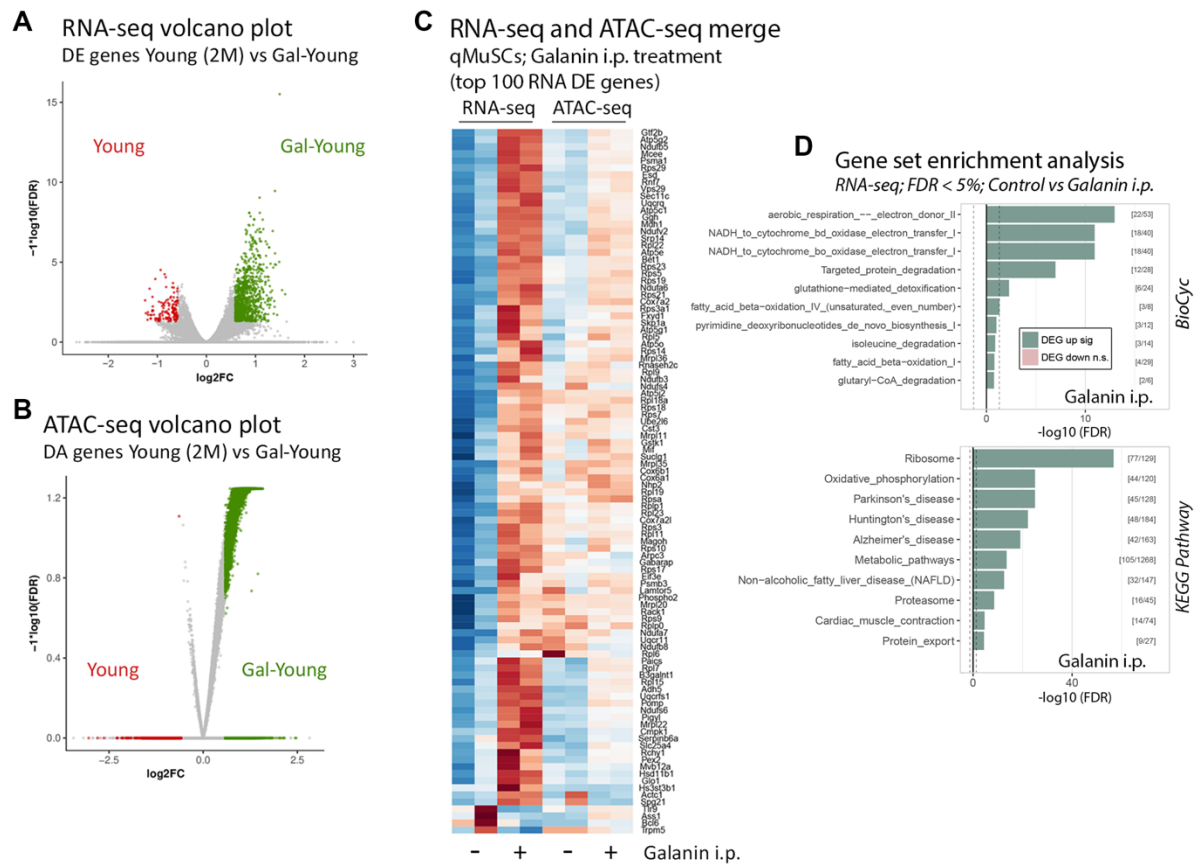


Figure 41. Intraperitoneal Galanin injections induce transcriptional and chromatin accessibility changes in quiescent muscle stem cells. (A),(B) Volcano plots showing the distribution of DE and DA genes and regions between Young (2-month-old) and Gal-Young (Galanin treatment) groups. **(C)** The merged heatmap shows top DE genes between Young and Gal-Young groups and respective chromatin regions. **(D)** GSEA of DE genes between Young and Gal-Young groups (BioCyc and KEGG databases).

Quiescent MuSCs isolated from Galanin-treated mice, showed dramatically increased chromatin accessibility, resulting in increased transcriptional activity (Fig. 41A, B). In total, 1540 regions were differentially accessible between both groups (49 regions were up-regulated in the control and 1491 were up-regulated in the treatment group; FDR<5%), while 875 genes were differentially expressed (101 genes were up-regulated in the control and 774 were up-regulated in the treatment group; FDR<5%). Importantly, differentially accessible regions correlated very well with differentially expressed genes: more accessible genes were also more expressed: 332 transcripts were annotated to the chromatin accessibility regions, 268 (81%) genes were upregulated together with increased chromatin accessibility (Fig. 41C). Overall, the Galanin-treated MuSCs were more transcriptionally active and were enriched for “Aerobic respiration” (BioCyc database), “Ribosome” (GO and KEGG databases), “Oxidative phosphorylation” (KEGG pathway) and “Translation” (Reactome pathway)

by GSEA terms (FDR<5%) (Fig. 41D). The corresponding analysis on the chromatin accessibility level (FDR<5%), showed that the treatment group was enriched for “cAMP biosynthesis” (BioCyc database), “Hippo signaling” and “MAPK signaling” and “Axon guidance” and “Wnt Signaling” (KEGG and PANTHER database), “Gonadotropin-releasing hormone receptor” and “FGF signaling” and “EGF signaling” and “Angiogenesis” (PANTHER database). Taken together, these data suggest that Galanin i.p. supplementation *in vivo* induces transcriptional and epigenetic changes, which may enhance oxidative metabolism in young quiescent MuSCs.

3.2.5. Galanin partially rejuvenates the transcriptome of aged quiescent muscle stem cells

The expression of the *Gal* gene in quiescent MuSCs decreases with age, and this decrease is correlated with distinct transcriptional and epigenetic changes. Therefore, the next step was to test whether a systemic Galanin systemic i.p. application would rescue transcriptional or epigenetic signatures that occur during ageing.

Two groups (n=3) of *Pax7:zsGreen* mice were chosen: old (24 month) with or without 21 day of Galanin i.p. injections (40 µg/kg/d). qMuSCs were isolated by FACS and used for bulk RNA- and ATAC-sequencing. This analysis identified 99 genes as differentially expressed between the control old and treatment old groups (33 genes were up-regulated in the control group and 66 genes were up-regulated in the treatment group) (Fig. 44A). The observed transcriptional changes were, however, different from those seen in the equivalent experiment in young mice reported above. Genes upregulated in the old treatment group did not recapitulate the transcriptional enrichment of genes related to oxidative metabolism, but were instead enriched for the following terms (FDR<5%): “Regulation of intracellular signal transduction” and “Regulation of phosphorylation” (GO database), “Inflammation mediated by chemokine and cytokine signaling pathway” (PANTHER database), “Laminin interactions” and “Axon guidance” (Reactome database). On the chromatin accessibility level, the old treatment group was enriched (FDR<5%) for “cAMP biosynthesis” and “PIP metabolism” (BioCyc database), “Hippo signaling pathway” and “MAPK signaling pathway” and “Axon guidance” and “Wnt signaling” (PANTHER and Reactome databases), “Gonadotropin-releasing hormone receptor pathway” and “FGF signaling pathway” and “EGF signaling pathway” (PANTHER database).

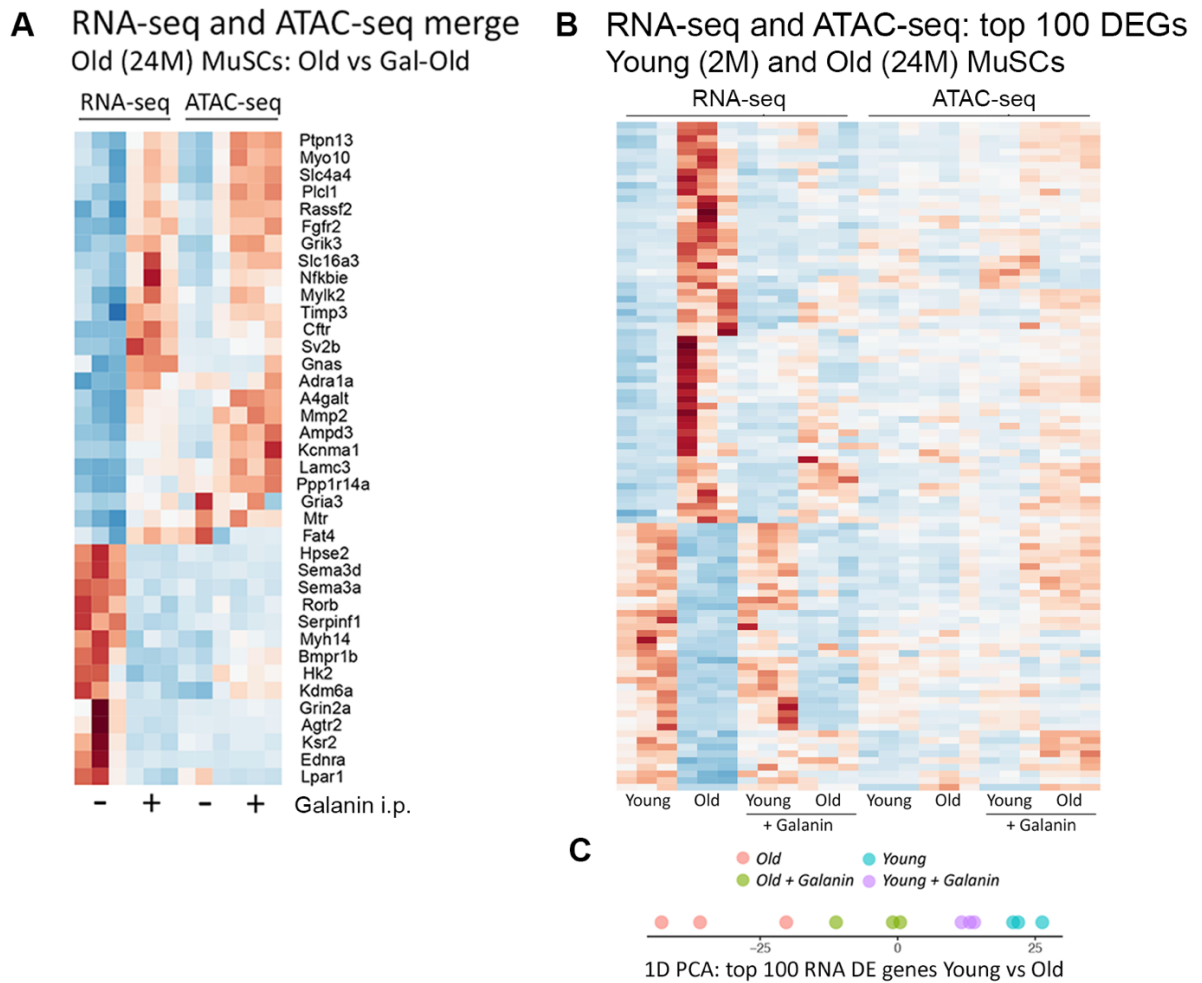


Figure 44. Galanin partially restores the transcriptome profile and alter the chromatin accessibility of aged muscle stem cells. (A) The heatmap shows DE and respective chromatin regions accessibility between Old and Gal-Old (Galanin treatment) groups. (B) The merged heatmap shows partial restoration of Gal-Old transcriptome profile back to Young condition, associated with massive increase in chromatin accessibility. (C) 1D PCA dimensional reduction shows increased similarity of Gal-Old and Young samples.

The expression and accessibility datasets were compared between young, old, young treated and old treated groups. Importantly, treatment with Galanin changed the transcriptional profile of aged quiescent MuSCs towards young qMuSCs, which also correlated to changes in chromatin accessibility (Fig. 44B). More specifically, 44 genes were up-regulated and 31 genes were down-regulated (from top 100 DEGs) from the old back to the juvenile state. For better visualization, PCA one-dimension reduction was performed to demonstrate that the treated group of old mice was transcriptionally closer to the young group, rather than to the control group of old mice (Fig. 44C). These results indicate, that the systemic application of Galanin neuropeptide partially “rejuvenates” the transcriptional profile of aged qMuSCs.

3.2.6. Galanin is required for the proliferation of primary myoblasts

To further investigate the functions of Galanin, additional *in vitro* experiments were performed using genetically modified mice carrying a germline deletion of the *Gal* gene. Young (2 month) and old (24 month) control *Pax7:zsGreen* mice (referred to as WT) and young *Pax7:zsGreen* & *Gal*^{-/-} (referred to as Gal KO) mice were used for the experiments. Freshly isolated quiescent MuSCs were cultured *in vitro*, as described in section 2.5.4 and further analyzed.

While WT myoblasts displayed normal rates of proliferation (based on cell numbers, morphology, as well as EdU incorporation), proliferation of Gal KO myoblasts was severely inhibited (Fig. 45A, C, E). Importantly, the Gal KO cells did not display excessive rates of apoptosis, as evaluated by immunostaining for cleaved caspase 3 (Fig. 45B). Additionally, the relative number of MyoG expressing cells, indicative of the commitment towards myogenic differentiation, was comparable with WT MuSCs (Fig. 45D). After 150h in culture, however, Gal KO cultures were characterized by a dramatically reduced number of cells, compared to WT, indicating that Galanin is necessary for myoblast proliferation. Strikingly, young Gal KO myoblasts behaved similar to the old (24 month) WT myoblasts in culture: both conditions displayed a decreased proliferation rate as well as an altered proliferation/differentiation ratio. Addition of 100nM Galanin to the growth media moderately increased the proliferation rate of young WT myoblasts, which was confirmed by morphometric analysis using the IncuCyte live-imaging system and an EdU incorporation assay (Fig. 45E, F).

Interestingly, myoblasts derived from MuSCs isolated from Galanin-injected (21 day) mice, showed the same increased proliferation, as WT myoblasts, supplied with Galanin in the growth media (Fig. 45G). Surprisingly, addition of Galanin did not normalize the proliferation rate of Gal KO myoblasts. Similarly, the effect of Galanin on old myoblasts was reduced and time-delayed when compared to young myoblasts. In contrast, the expression of *GalR2* appeared unaltered in both old MuSCs and Gal KO cells (data not shown). Taken together, these data indicate, that the ageing phenotype of MuSC cannot be fully rescued by Galanin supplementation *in vitro*, and that *in vitro* supplementation of Galanin does not substitute for the absence of *Gal* in mutant myoblasts. Yet, Galanin supplementation increases the proliferation rate of young myoblasts.

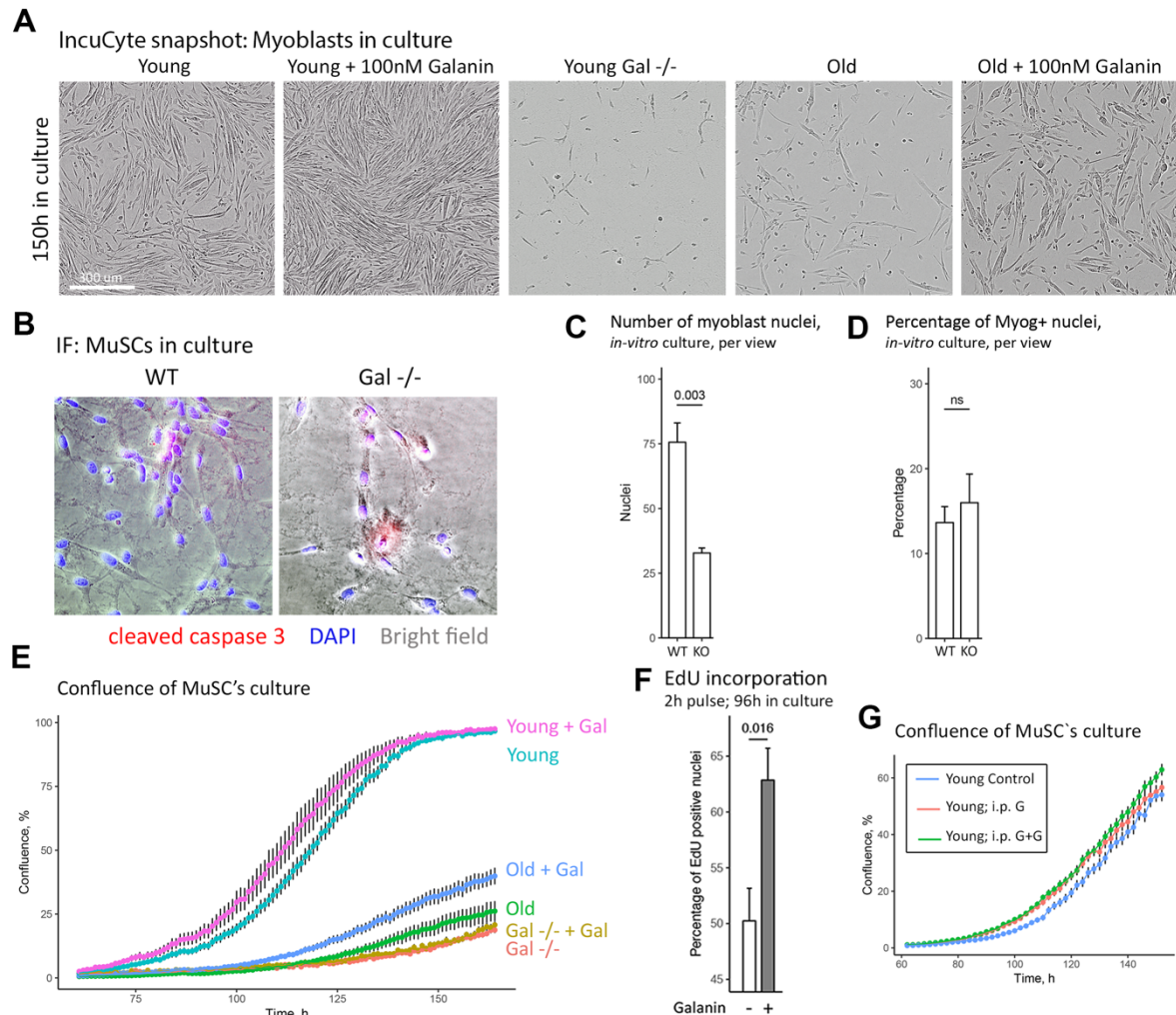


Figure 45. Galanin is required for the proliferation of primary myoblasts. (A) IncuCyte snapshots show endpoint state of primary myoblasts cultures at different conditions. (B) Immunofluorescent analysis of cultured myoblasts shows absence of excessive apoptosis in Gal KO myoblasts. (C) Barplot shows the number of myoblasts nuclei in WT and Gal KO cultures (n=5, Student's t-test). (D) Barplot shows percentage of MyoG-positive myoblasts in WT and Gal KO cultures (n=5, Student's t-test). (E) Confluence plot shows proliferation dynamics of myoblasts cultures. (F) Barplot shows percentage of EdU incorporating myoblasts in control and Galanin-treated groups (n=5, Student's t-test). (G) Confluence plot shows proliferation dynamics in myoblasts cultures.

To analyze whether ageing or *Gal* gene knock-out affects activation of qMuSCs, cultured myoblasts were immunostained for Pax7 and for MyoD at different time-points (1-4 days in culture). MuSCs that were positive only for Pax7 were considered as quiescent, while cells positive for both Pax7 and MyoD were considered as activated. Finally, cells that were only positive for MyoD, were considered as myoblasts. Young WT cells showed normal activation: after 1 day in culture, 89% of MuSCs were activated, followed by 100% activation after 2 days. After 3 and 4 days in culture, 39% and 61% of cells became myoblasts, respectively. Interestingly, both aged and Gal KO showed a delay in activation: after 1 day in culture only 55% and 50% of MuSCs were activated, respectively. Furthermore, after 2 days in culture, 90% of aged and only 57%

of Gal KO cells were activated. Finally, after 3 and 4 days in culture, 41% and 67% of aged cells became myoblasts. Strikingly, even after 3 days in culture, 5% of Gal KO MuSCs remained quiescent while only 45% of Gal KO cells became myoblasts after 4 days in culture (Fig. 46A,B).

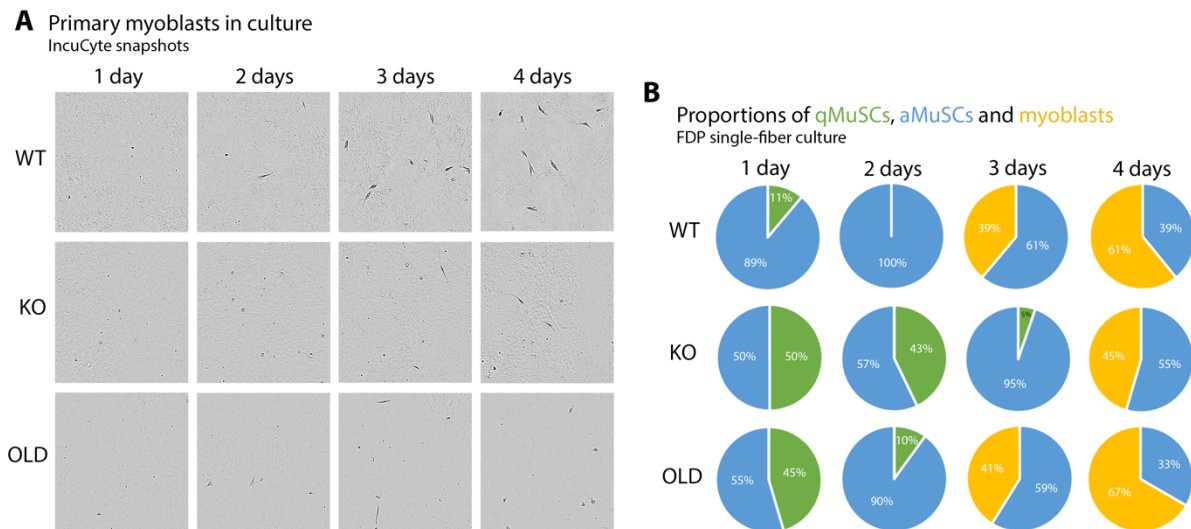


Figure 46. Galanin is required for the activation of MuSC. (A) IncuCyte snapshots show a delayed MuSCs activation in aged and Gal KO cell cultures. (B) Pie charts show proportions between quiescent MuSCs, activated MuSCs and myoblasts in young WT, aged and Gal KO cell cultures.

This data indicates, that both aged and Gal KO MuSCs suffer from delayed activation, suggesting that Galanin is necessary for rapid activation of MuSCs and probably also for successful muscle regeneration.

3.2.7. Galanin is required for muscle regeneration and its absence results in muscle fibrosis

Since proliferation of MuSCs is essential for muscle regeneration after injury, the requirement of Galanin for muscle regeneration was tested by injection of CTX into Gal KO mice *in vivo*. In addition to previously utilized mouse lines, a germline *Gal* overexpressing strain (*Gal_tetO* & *tg_tTA*) was used as well. Six groups (n=5) of mice were employed: young (2 month), young with Galanin treatment (40 µg/kg/d), old (24 month), old with Galanin treatment (40 µg/kg/d), *Gal* ^{-/-} germline knockout (2 month; referred to as Gal KO), and *Gal_tetO* & *tg_tTA* (2 month; referred to as Gal OE). All mice received an injection of the cardiotoxin (CTX) into the Tibialis Anterior (TA) muscle (see section 2.1.6). CTX injection destroys muscle fibers and induces muscle regeneration. Mice were sacrificed at 14 days after CTX injection. Galanin-treatment

groups received daily Galanin i.p. injections for 3 days prior to CTX application and throughout the remainder of the experiment (14 days). The TA muscles of sacrificed mice were collected and frozen. Subsequently, muscles were cryo-sectioned and used for the histological analysis.

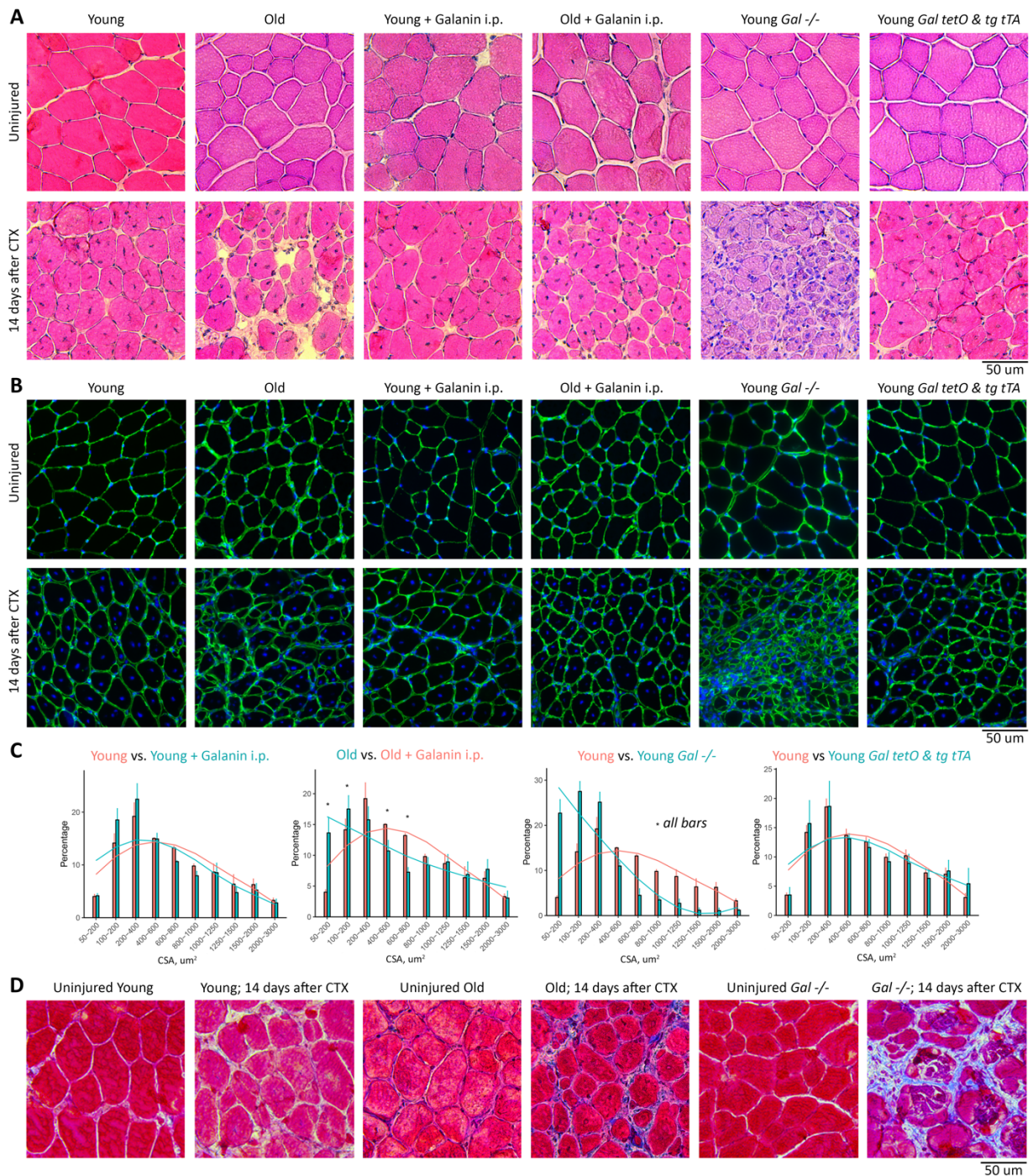


Figure 47. The *Gal* KO mice show impaired muscle regeneration. (A) H&E staining shows regeneration defect in old and *Gal* KO mice. Young refers to 2-month-old and Old refers to 24-month-old. (B) Immunostaining with anti-Laminin antibody shows decreased size of muscle fibers in *Gal* KO mice. (C) Cross-sectional size distribution plots show decreased size of muscle fibers in old and *Gal* KO mice. (D) Masson's trichrome staining highlights muscle fibrosis in *Gal* KO mice.

In a first step, conventional H&E staining of muscle cryosections was performed to evaluate the efficiency of regeneration (Fig. 47A). Successful regeneration (14 days after injury) is primarily marked by full restoration of muscle fibers that reach the same size as uninjured muscle, absence of small underdeveloped fibers and fibrotic areas, as well as centrally localized myo-nuclei as a hallmark of muscle regeneration⁸⁷. All mice, except for the old and Gal KO groups, successfully regenerated the TA muscle within 14 days. In contrast to other groups, the Gal KO mice and, to a lesser extent, old mice, showed strongly impaired TA muscle regeneration (Fig. 47A-C). Anti-laminin immunostaining for the detection of basal lamina of the muscle fibers, additionally revealed thicker laminin-positive areas, surrounding the muscle fibers in Gal KO muscles (Fig. 47B). These observations suggest the development of muscle fibrosis. To confirm this finding, muscle sections were stained according to the Masson's Trichrome protocol. Muscle fibrosis was clearly visible in Gal KO and, to a lesser extent, old mice cryo-sections 14 days after CTX injury (Fig. 47D).

Taken together, these data indicate that Galanin is required for proper muscle regeneration.

3.2.8. Galanin is required for neuromuscular junction formation, regeneration and maintenance

According to the scRNA-seq and RT-qPCR data, only qMuSCs and nerves express *Gal* in the hind-limb skeletal muscles (Fig. 35A). Since it is known that Galanin is important for motor neuron maintenance and regeneration (see 3.2.2), the next step was to investigate whether deletion or overexpression of *Gal* has effects on muscle innervation and re-innervation after injury.

The morphological analysis of the NMJ and innervation was performed using confocal microscopy. Murine diaphragms, isolated from the Young and Old WT, Gal KO and Gal OE mice were stained (whole-mount staining) with anti-Neurofilament (marks neurons) and α -bungarotoxin (BTX, specifically staining NMJs). Image analysis clearly indicated an increased number of denervated NMJs in Old and Gal KO diaphragms, while WT and Gal OE diaphragms were properly innervated (Fig. 48A, B).

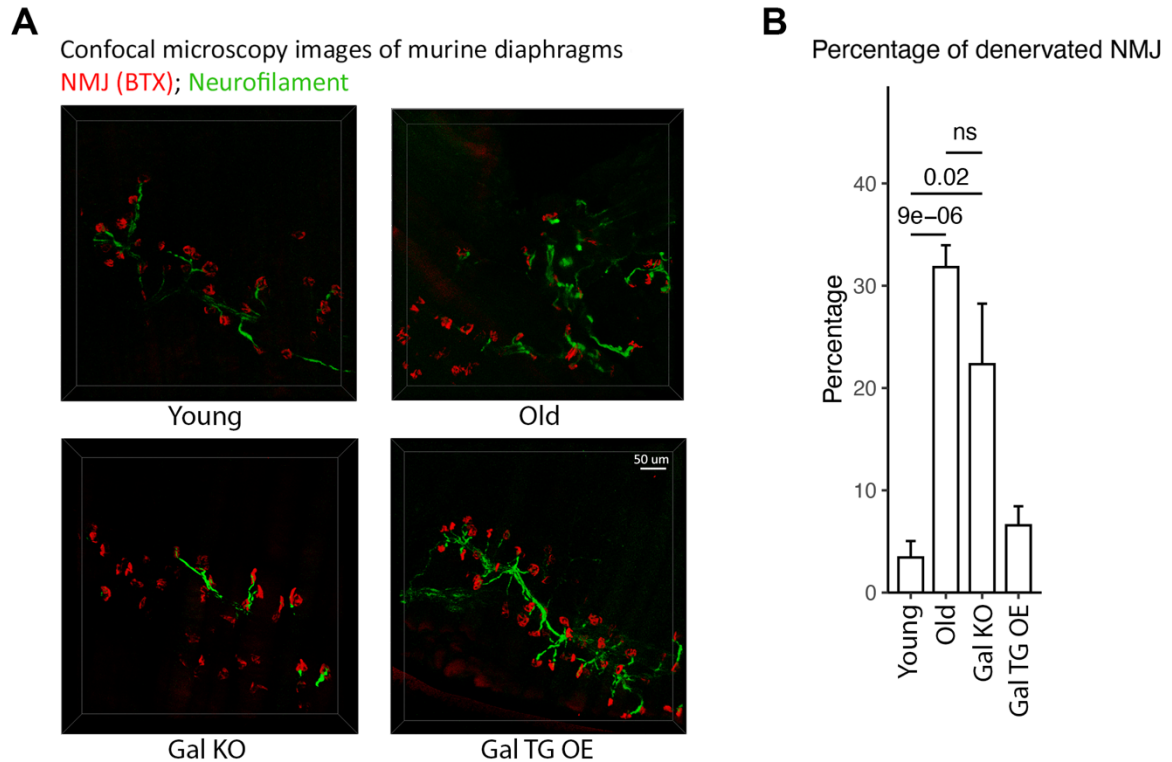


Figure 48. The Gal KO mice have signs of muscle denervation. Confocal images (**A**) and a barplot (**B**) illustrate increased percentage of denervated NMJs in diaphragms, isolated from Old and Gal KO mice. (n=5, Student's t-test)

To enumerate the NMJs and evaluate their morphology upon regeneration, cryo-sections from the CTX injury assay (section 3.2.7) were stained with BTX (Fig. 49A). Cryo-sections of muscles, isolated from young (2 month), old (24 month), young with galanin treatment, old with galanin treatment, Gal KO and Gal OE mice were used for the analysis. The average number of NMJs per section was calculated for each condition and visualized as a barplot (Fig. 49B). Both supplementation of Galanin by injections and by overexpression via the *Gal* transgene, induced a strong increase of the number of NMJs per section. On the other hand, reduced or absent Galanin expression either by age or via knock-out, respectively, induced a decrease in the average number of NMJs per section. Remarkably, overexpression of *Gal* caused not only an increase of NMJs, but also an increase of their size. This phenotype, in comparison to the Galanin treatment groups, was most likely acquired during muscle development, since it was already present prior to muscle injury. Taken together, these data indicate a role for Galanin in the formation, regeneration and maintenance of NMJs.

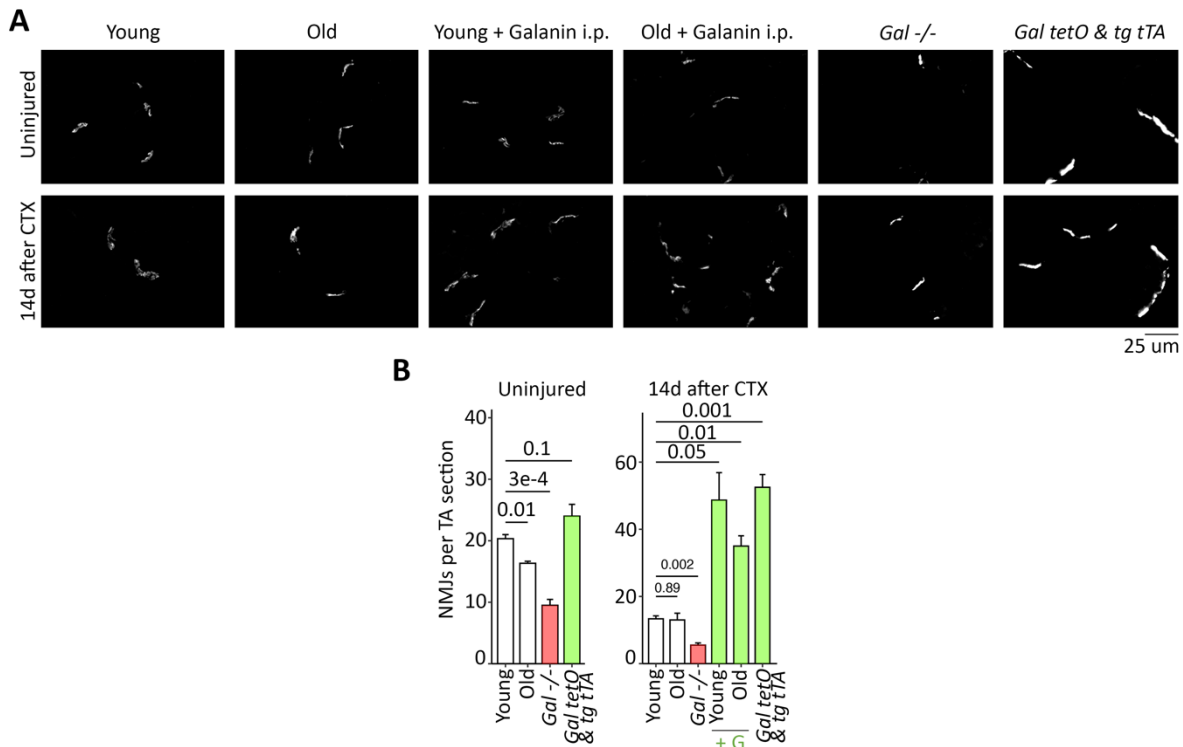


Figure 49. Galanin regulates the number of NMJs in TA muscles. (A) BTX staining shows innervation defect in *Gal*^{-/-} mice. On the other hand, Gal TG OE muscles have increased number and volume of NMJs. Young refers to 2-month-old and Old refers to 24-month-old. (B) Bar-plot shows the correlation of Galanin expression or supplementation and number of NMJs per uninjured and injured TA muscle sections. (n=5, Student's t-test).

3.2.9. The transcriptional profile of Gal KO quiescent MuSCs recapitulates natural ageing

According to the results presented above, Gal KO mice partially recapitulate ageing of MuSCs. Additionally, Gal OE mice showed a phenotype similar to that of mice exposed to Galanin injections. To evaluate the transcriptional similarities between qMuSCs of these groups, respective RNA-seq datasets were merged and reanalyzed. Scatter plots, showing the LFC of first condition on one axis and the LFC of second condition on another axis, were generated for KO/WT and Old/Young pairs (Fig. 50A, B), as well as for OE/WT and Young-Gal/Young pairs (Fig. 50C, D).

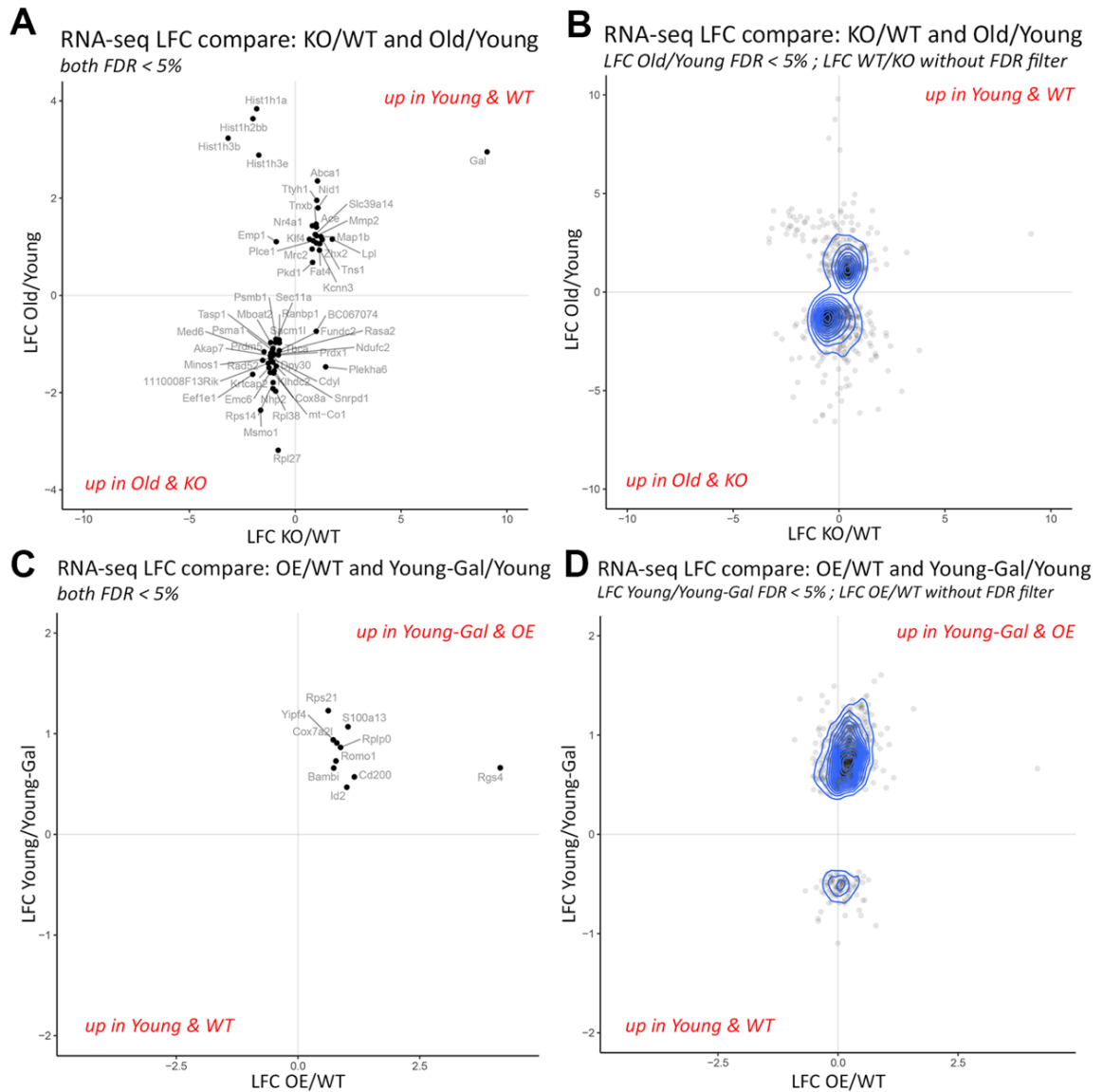


Figure 50. Transcriptional profiles of the Gal KO and Gal OE quiescent MuSCs recapitulate the transcriptional landscape of old and young-with-Galanin-treatment quiescent MuSCs, respectively. (A),(B) The scatter plots illustrate similarities of DE gene sets between WT/Gal KO and Young/Old pairs. **(C),(D)** The scatter plots illustrate similarities of DE gene sets between WT/Gal OE and Young/Young-Gal (Galanin treatment) pairs.

Changes in expression upon ageing and upon knock-out of *Gal* gene were observed to be largely coherent: a gene was considered to be expressed in the same direction, if it was up-regulated in both Gal KO and old conditions, or it was down-regulated in both of them. 660 genes had the same direction of expression changes. 158 genes were upregulated in young and in Gal KO groups, while 101 genes were up-regulated in old and WT conditions. In other words, the transcriptional signatures of ageing and *Gal* knock-out were 72% similar.

On the other hand, 645 genes had the same orientation of expression change when comparing OE/WT and Young-Gal/Young pairs, while 157 genes had the

opposite orientation of expression change, rendering the transcriptional signatures of Galanin i.p. injections and transgenic *Gal* overexpression 80% similar.

Taken together, this analysis suggests that *Gal* knock-out recapitulates aspects of natural ageing, while *Gal* overexpression recapitulates the Galanin i.p. injections and can be used to examine the function of Galanin *in vivo*.

3.2.10. Conditional inactivation of *Gal* in MuSC causes impaired muscle regeneration but leaved muscle re-innervation intact

Since the *Gal* gene is expressed in both qMuSCs and motoneurons, a germline *Gal* KO, which was used in the previous experiments, represent the cumulative result of *Gal* deletion in both cell types. To define a MuSCs-specific phenotype, a conditional *Gal* knock-out mouse strain was acquired from RIKEN BRC (Riken, Japan), in which LoxP-sites are located upstream and downstream of the third exon of the *Gal* gene. After crossing with *Pax7^{CreERT2}* mice, the following strain was obtained: *Gal^{loxP/loxP}* & *Pax7^{CreERT2/+}* (*Gal* cKO). Upon Tamoxifen injection, the third exon of the *Gal* gene is removed by a Cre-recombinase in the *Pax7*-expressing cells, resulting in a defective *Gal* mRNA.

To assess muscle regeneration efficiency, CTX injections were performed into the TA muscles of young WT (n=3) and young *Gal* cKO (after Tamoxifen administration, n=3) mice. Muscles were collected 14 days after the injury and cryo-sectioned. H&E staining was performed, revealing compromised muscle regeneration in *Gal* cKO muscles: 14d after injury muscle fibers were smaller and surrounded by an excessive amount of connective tissue (Fig. 51A). Trichrome staining validated the emergence of muscle fibrosis (Fig. 51B). However, muscle reinnervation was not affected – numbers and morphology of the NMJs were similar to young WT injured and uninjured muscles, respectively (Fig. 51C,D).

Taken together, these results show that removal of Galanin specifically in the MuSCs results in compromised muscle regeneration, but unaltered muscle innervation and re-innervation. This suggests the germline *Gal* KO phenotype results from two different defective processes: a MuSCs-specific (muscle regeneration) and nerve-specific (innervation and re-innervation) defect.

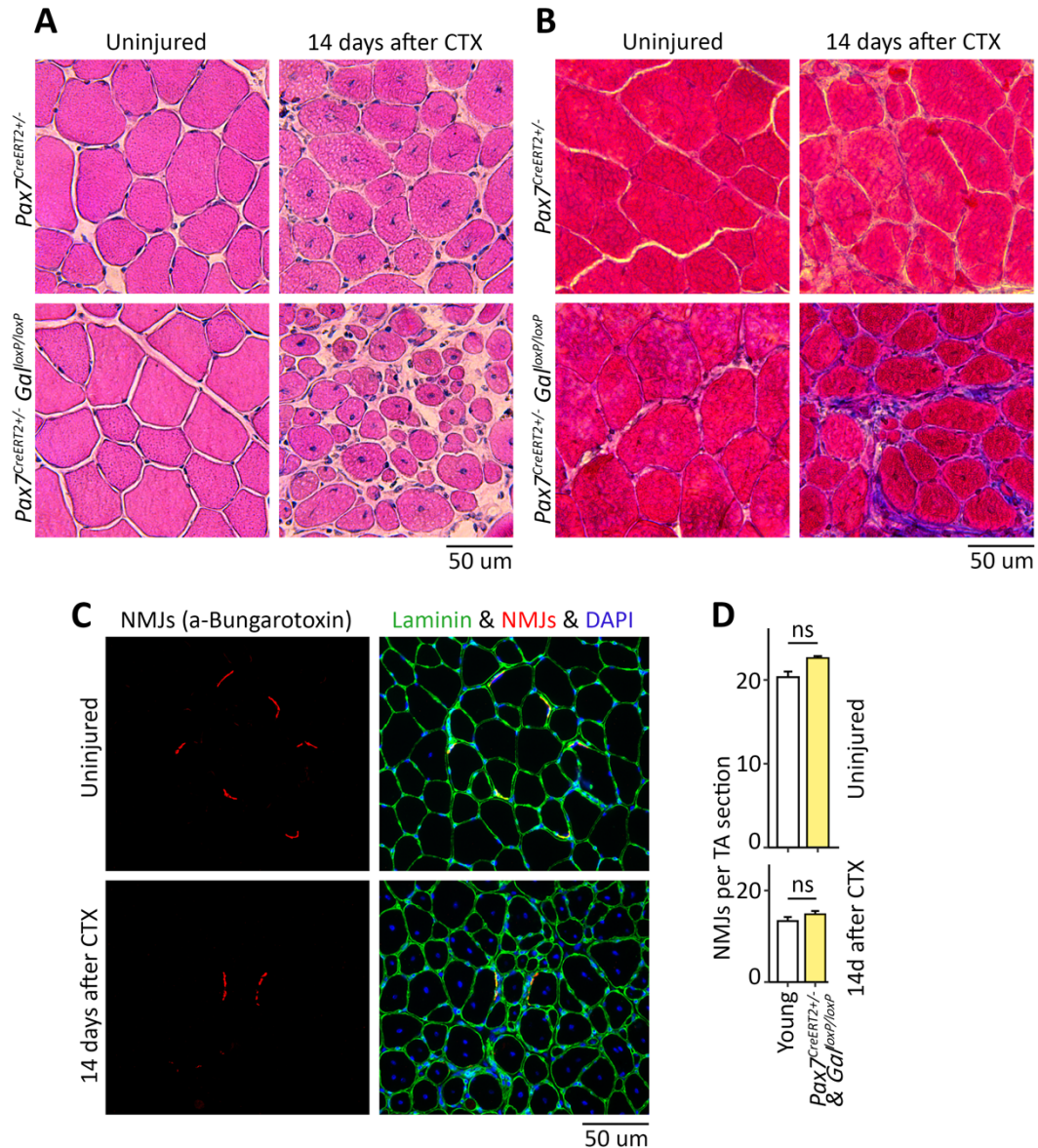


Figure 51. Conditional knock-out of *Gal* in MuSC results in impaired muscle regeneration but intact muscle innervation. (A) H&E staining shows regeneration defect in the *Gal* cKO injured muscles 14d after CTX injection. **(B)** Trichrome staining shows presence of fibrosis in the *Gal* cKO injured muscles 14d after CTX injection. **(C)** BTX staining shows normal amount and morphology of the NMJs in the *Gal* cKO muscles. **(D)** Count of the NMJs per section in the *Gal* cKO condition shows similar numbers to the WT condition.

3.3. Annexin A3 marks a defective subpopulation of aged muscle stem cells

3.3.1. An *Anxa3*^{pos} subpopulation of quiescent muscle stem cells emerges during ageing

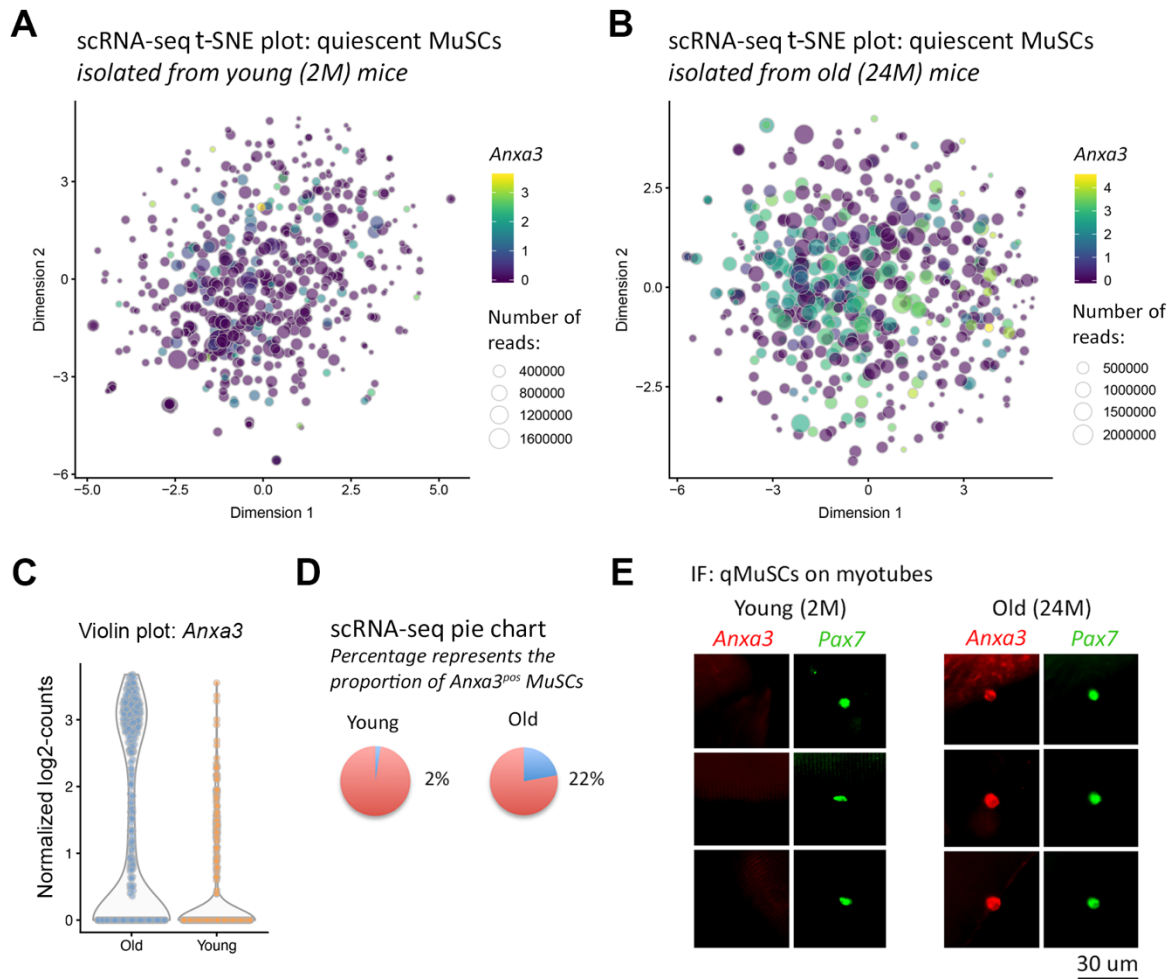


Figure 52. An *Anxa3*^{pos} subpopulation of the quiescent muscle stem cells emerges during ageing. (A),(B) t-SNE dimensional reduction illustrate emergence of *Anxa3*^{pos} group of cells. Expression of *Anxa3* is represented by the size of the dot. (C) Violin plot shows expression of *Anxa3* gene in young and old MuSCs. (D) Pie charts illustrate increase in percentage of *Anxa3*^{pos} qMuSCs with age. (E) Immunostaining shows examples of absence of Annexin A3 expression in young (2-month-old) qMuSCs, but presence in old (24-month-old) qMuSCs.

In initial scRNA-seq analysis of young and aged MuSCs, a fraction of old quiescent MuSCs expressed *Anxa3* (Fig. 52A, B). A cell was counted positive for *Anxa3*, when normalized expression exceeded 5 counts per cell. 22% of quiescent MuSCs expressed this gene in old (24 month) animals, but only 2% in young controls (2 month) (Fig. 52C, D). The finding from scRNA-seq was confirmed by immunofluorescence: only old qMuSCs expressed the Annexin A3 protein (Fig. 52E). To evaluate the transcriptional signature of *Anxa3*^{pos} quiescent MuSCs, all cells from

the scRNA-seq dataset with 24 months of age were separated into *Anxa3*^{pos} (392 cells) and *Anxa3*^{neg} (1.391 cells) groups. 327 genes were differentially expressed between the *Anxa3*^{pos} and *Anxa3*^{neg} qMuSCs (325 genes were up-regulated in the *Anxa3*^{pos} and 2 were up-regulated in the *Anxa3*^{neg} group) (Fig. 53A, B).

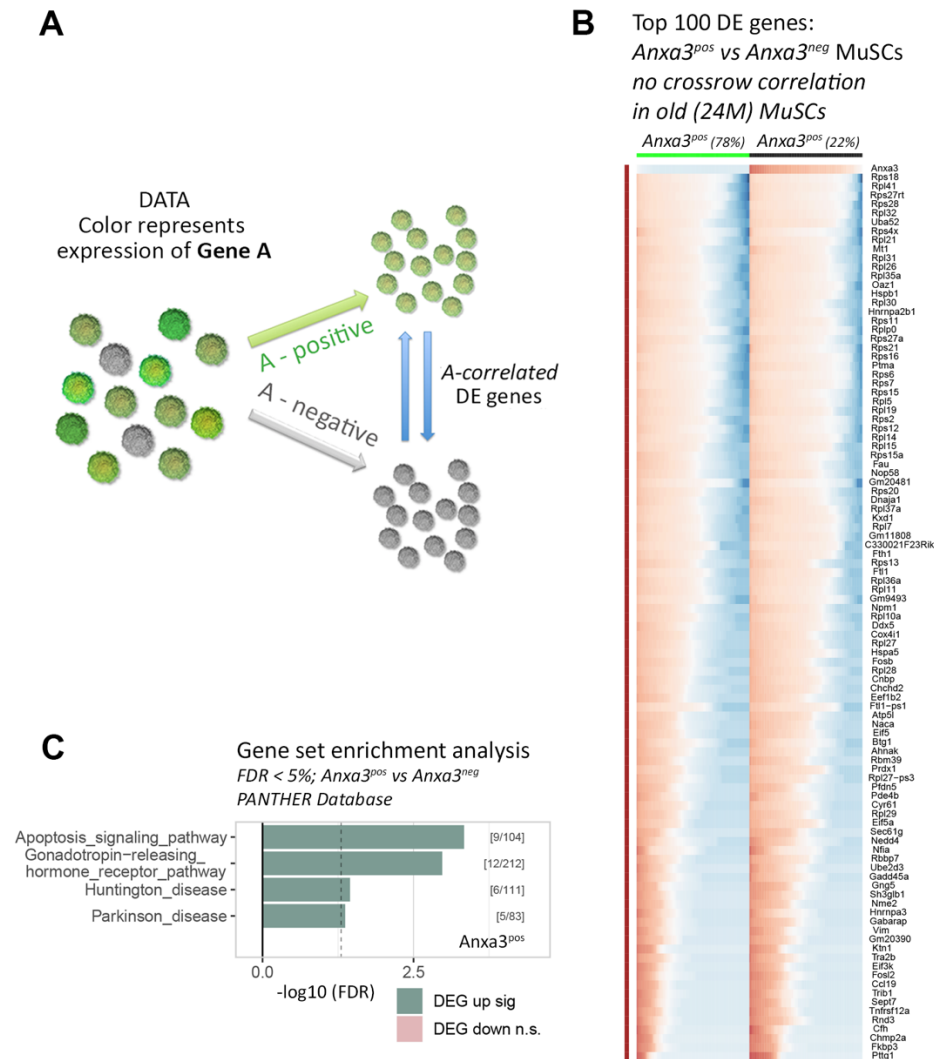


Figure 53. Aged *Anxa3*^{pos} qMuSCs show a distinct transcriptional profile. (A) A concept of in silico separation of single cells into groups based on expression of a certain gene. **(B)** Heatmap illustrating the top 100 DE genes between *Anxa3*^{pos} and *Anxa3*^{neg} aged qMuSCs. **(C)** GSEA of DE genes, PANTHER database.

Genes up-regulated in *Anxa3*^{pos} cells were enriched (GSEA, FDR<5%) for “Apoptosis signaling pathway”, “Gonadotropin-releasing hormone receptor pathway”, “Huntington disease” and “Parkinson disease” (PANTHER database) (Fig. 53C), which raises the possibility that old *Anxa3*-expressing qMuSCs might be defective and marked for apoptosis.

3.3.2. *Anxa3* mRNA knock-down partially rescues the proliferation defect of aged myoblasts

It is known that old primary myoblasts show decreased proliferation and precocious differentiation⁹⁰. This phenotype presumably contributes to attenuated muscle regeneration in old animals^{90,97,175}. To test the role of *Anxa3* *in-vitro*, primary myoblasts, derived from freshly isolated MuSCs of young (2 month) and old (24 month) mice were cultured *in vitro* and assessed for proliferation (confluence and EdU).

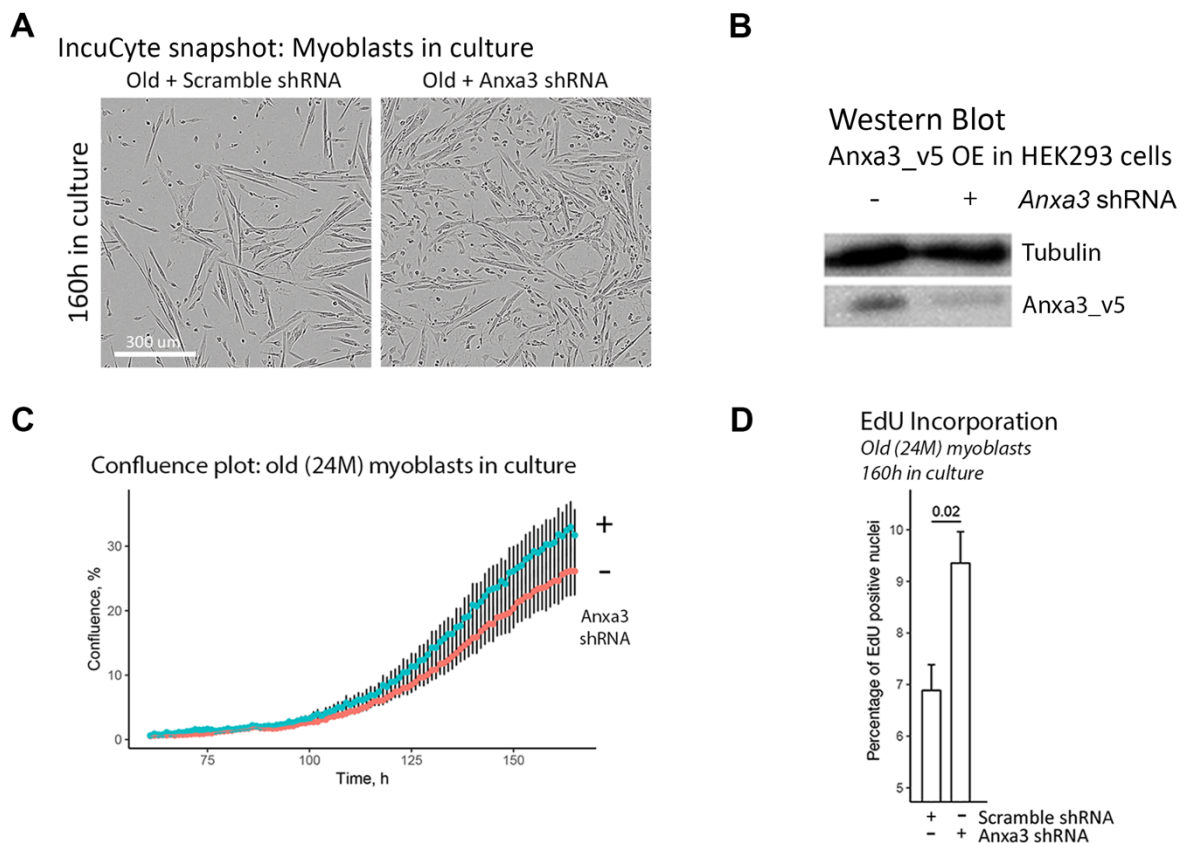


Figure 54. The *Anxa3* mRNA knock-down partially rescues the proliferation defect of aged myoblasts *in vitro* (A) IncuCyte snapshots show the endpoint states of Old and Old *Anxa3* KD myoblasts cultures. (B) Western blot analysis confirms the efficiency of *Anxa3* shRNA. (C) Confluence plot illustrating increased proliferation of old myoblasts upon *Anxa3* KD. (D) Barplot showing increased EdU incorporation upon KD of *Anxa3* (n=5, Student's t-test).

To further investigate the role of *Anxa3*, old primary myoblasts were transfected with a lentivirus, expressing an *Anxa3* shRNA (Fig. 54A) to abolish *Anxa3* expression. The construct was tested in advance for efficacy of RNA interference in HEK293 cells (Fig. 54B). *Anxa3* knock-down resulted in enhanced proliferation of aged primary myoblasts, which was confirmed by the increased confluence in myoblast cultures and increased EdU incorporation (Fig. 54C, D).

Altogether, these results show that old MuSCs show decreased proliferation and precocious commitment towards differentiation, which might contribute to

attenuated regeneration of old muscles *in vivo*. Knock-down of *Anxa3* partially restored the proliferative capacity of aged MuSCs, and therefore might be beneficial for muscle regeneration.

3.3.3. Overexpression of *Anxa3* attenuates the proliferation rate of young primary myoblasts

To validate the previous experiment from the opposite side, young (2 month) primary myoblasts were transduced with a retrovirus carrying a V5-tagged *Anxa3* expression construct. An equivalent GFP expressing construct was used as a control (Fig. 55A). Anti-V5 immunostaining confirmed *Anxa3_V5* expression (Fig. 55B). Overexpression of *Anxa3* in young primary myoblasts led to reduced proliferation and stronger commitment towards differentiation (Fig. 55C). These phenotypes were corroborated by decreased EdU incorporation and an increased percentage of cells expressing MyoG, respectively (Fig. 55D, E).

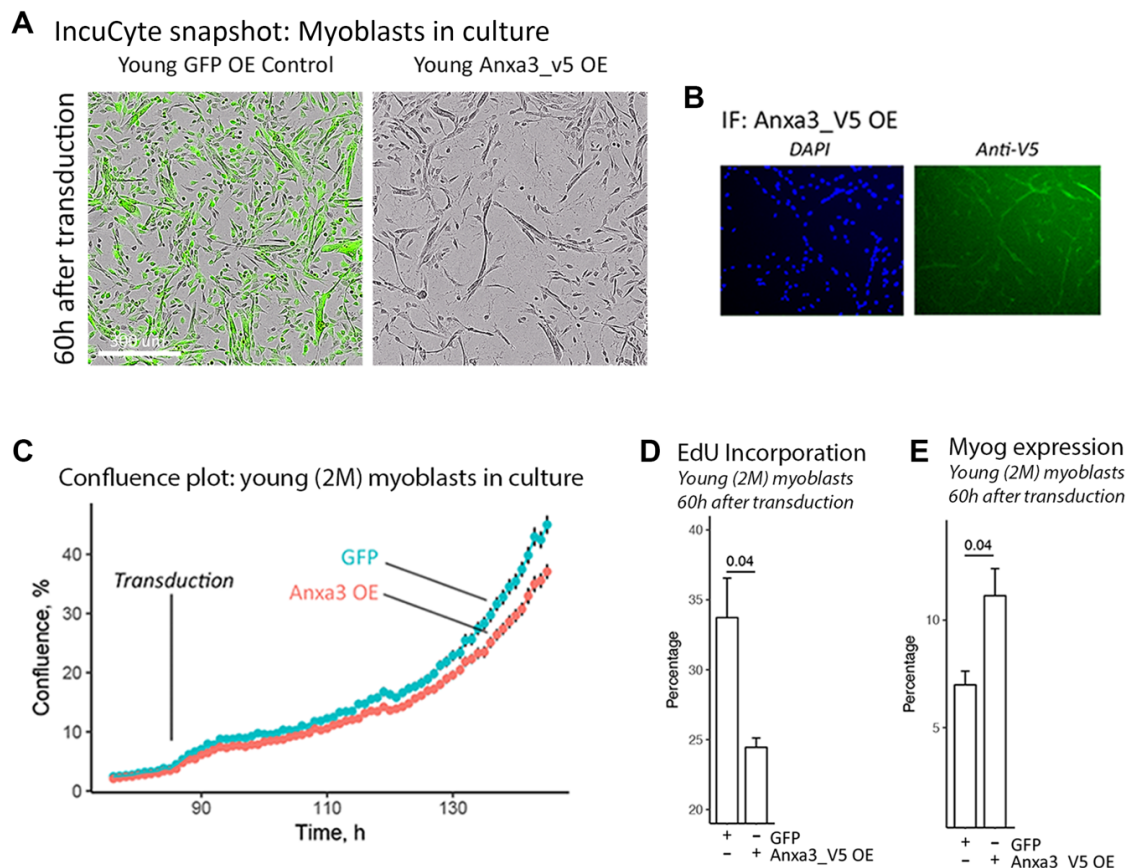


Figure 55. The viral *Anxa3* overexpression attenuates the proliferation rate of the young myoblasts. (A) IncuCyte snapshots show the endpoint states of Young (2-month-old) and Young *Anxa3* OE myoblast cultures. (B) Immunostaining against V5 tag confirms *Anxa3_V5* overexpression. (C) Confluence plot illustrates decreased proliferation of young myoblasts upon *Anxa3* OE. (D) The barplot shows decreased EdU incorporation upon overexpression of *Anxa3*. (E) The barplot shows percentage of MyoG+ myoblasts upon overexpression of *Anxa3* (n=5, Student's t-test).

To investigate the role of *Anxa3* in MuSCs *in vivo*, the following mouse strain was generated: *Pax7:zsGreen* & *Rosa26:Anxa3^{loxP}* & *Pax7:CreERT2* (from here on referred to as *Anxa3* OE). The *Pax7:zsGreen* reporter allowed isolation of qMuSCs via FACS. Mice carrying this transgene were used as controls. As described in 2.1.10, inducible Cre-lox system allows to limit the genetic alteration to a specific cell type, in this case quiescent MuSCs. Upon i.p. injection of Tamoxifen to *Anxa3* OE mice, the *Pax7*-restricted *CreERT2* enzyme recombined the floxed region in the *Rosa26* loci, resulting in a constitutive overexpression of *Anxa3* exclusively in qMuSCs. Quiescent MuSCs were isolated from control and *Anxa3* OE mice and used for *in vitro* culture (Fig. 56A).

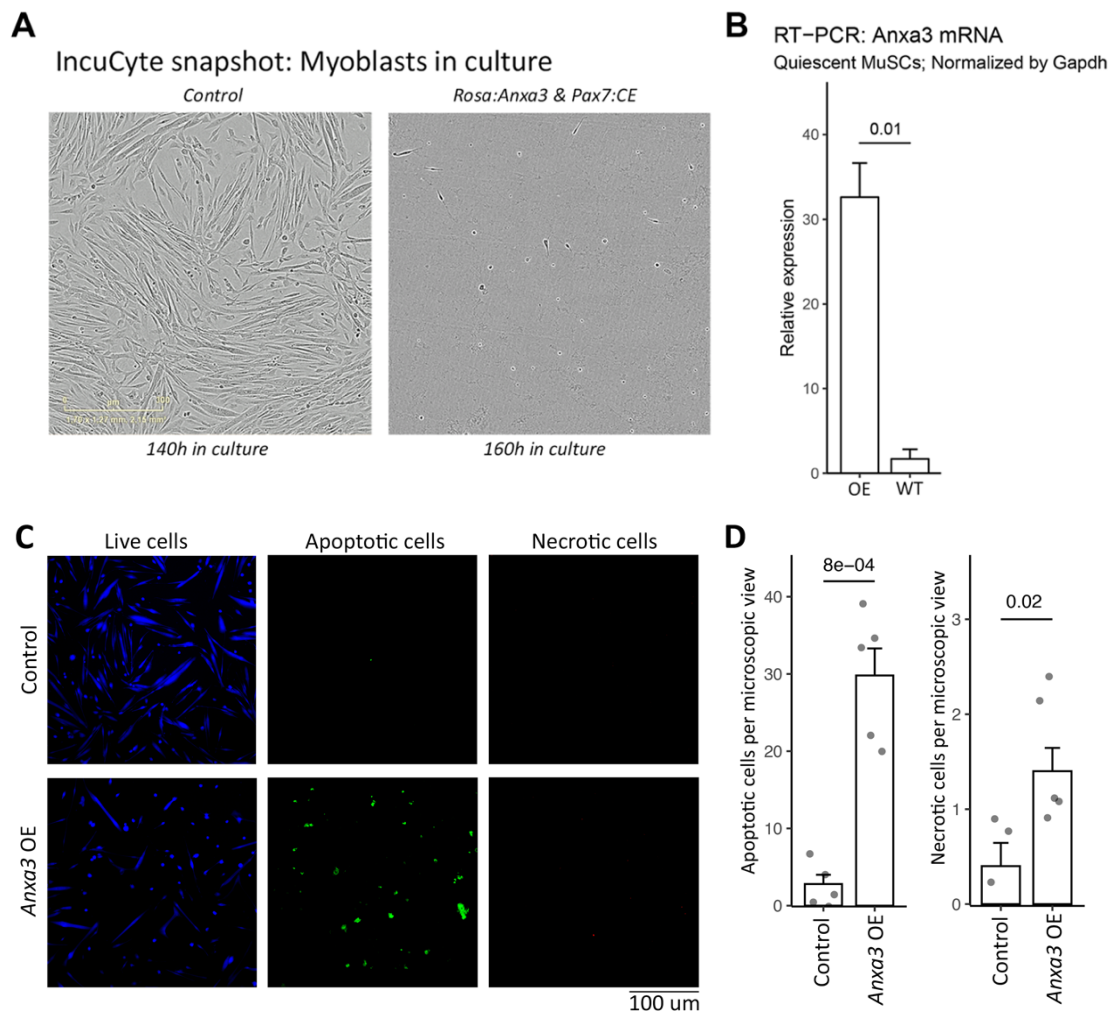


Figure 56. *Anxa3* overexpression reduces proliferation of primary myoblasts *in-vitro*. (A) IncuCyte snapshots show the endpoint states of Young (2-month-old) and Young transgenic *Anxa3* OE myoblasts cultures. (B) RT-qPCR of quiescent MuSCs confirms overexpression of *Anxa3* (n=3, Student's t-test).

Overexpression of *Anxa3* in quiescent MuSCs was validated by RT-qPCR and MuSC from the *Anxa3* OE strain were isolated by FACS and cultured (Fig. 56B). Strikingly, *Anxa3* OE-derived myoblasts showed a severe proliferation defect *in vitro*. The proliferation defect was accompanied by a massive apoptosis (Fig. 56C,D).

In summary, the results suggest that increased expression of *Anxa3* phenocopies several aspects of aging such as impaired cell proliferation and precocious differentiation. In other words, overexpression of *Anxa3* aggravates the condition of geriatric mice by expressing *Anxa3* in all MuSCs. In contrast, only 22% of all qMuSCs are *Anxa3*^{pos} in naturally aged mice (24 month).

3.3.4. *Anxa3* overexpression disrupts muscle regeneration and induces muscle fibrosis

Since *Anxa3* OE myoblasts showed impaired proliferation in culture, the regeneration capacity of the *Anxa3* OE mice was tested *in vivo*. Young *Anxa3* OE mice (2-3 month; n=3) were injected with Tamoxifen, thus inducing *Anxa3* overexpression in qMuSCs. Mice of a control group (n=3) carried a *Pax7:zsGreen* transgene only, where injection of Tamoxifen does not lead to any genetic alterations. All mice received a CTX injection into the TA muscle (see section 2.1.6.). Mice were sacrificed 14 days after CTX injection. Injured TA muscles, as well as matched uninjured controls (opposite limb), were isolated from all animals. Muscles were frozen and subsequently cryo-sectioned. The cryo-sections were stained with H&E, anti-laminin immunofluorescence and Masson's Trichrome staining to examine the efficiency of regeneration, as well as the muscle fiber morphology and presence of fibrosis.

As expected, muscles of control animals successfully regenerated within 14d after injury. As described previously, a successful regeneration (14 days after injury) is indicated by fully restoration of muscle fibers of the same size as uninjured counterparts, absence of small underdeveloped fibers and fibrotic areas, and centrally localized myo-nuclei⁸⁷. In striking contrast to control animals, regeneration was dramatically impaired in *Anxa3* OE mice (Fig. 57A). This was evident from H&E staining showing a drastic decrease in the number of newly forming myofibers. Additionally, the few myofibers newly formed as marked by centralized myo-nuclei were surrounded by a thick layer of connective tissue, harboring numerous mononucleated cells. This finding was further corroborated by anti-laminin immunostaining, showing again thickening of connective tissue and rare regenerating

myofibers and finally confirmation of massive fibrosis by Masson's Trichrome staining (Fig. 57B).

Interestingly, uninjured *Anxa3* OE muscles showed increased Collagen deposition, which resulted in thickening of the ECM (Fig. 57C). To verify that increased expression of *Anxa3* from MuSCs was the reason for ECM accumulation, an additional *Rosa^{Tomato}* allele was crossed into *Anxa3* OE strain. The resulting *Pax7^{CreERT2/+}* & *Rosa^{Tomato/Anxa3}* strain was therefore not only overexpressing *Anxa3* in the qMuSCs after Tamoxifen injection, but also marking recombined cells and their progeny with a fluorescent Tomato marker. Analysis of this strain revealed ECM thickening 2 weeks after Tamoxifen administration. ECM thickening appeared primarily in the proximity of the *Anxa3* overexpressing qMuSCs (Fig. 57D).

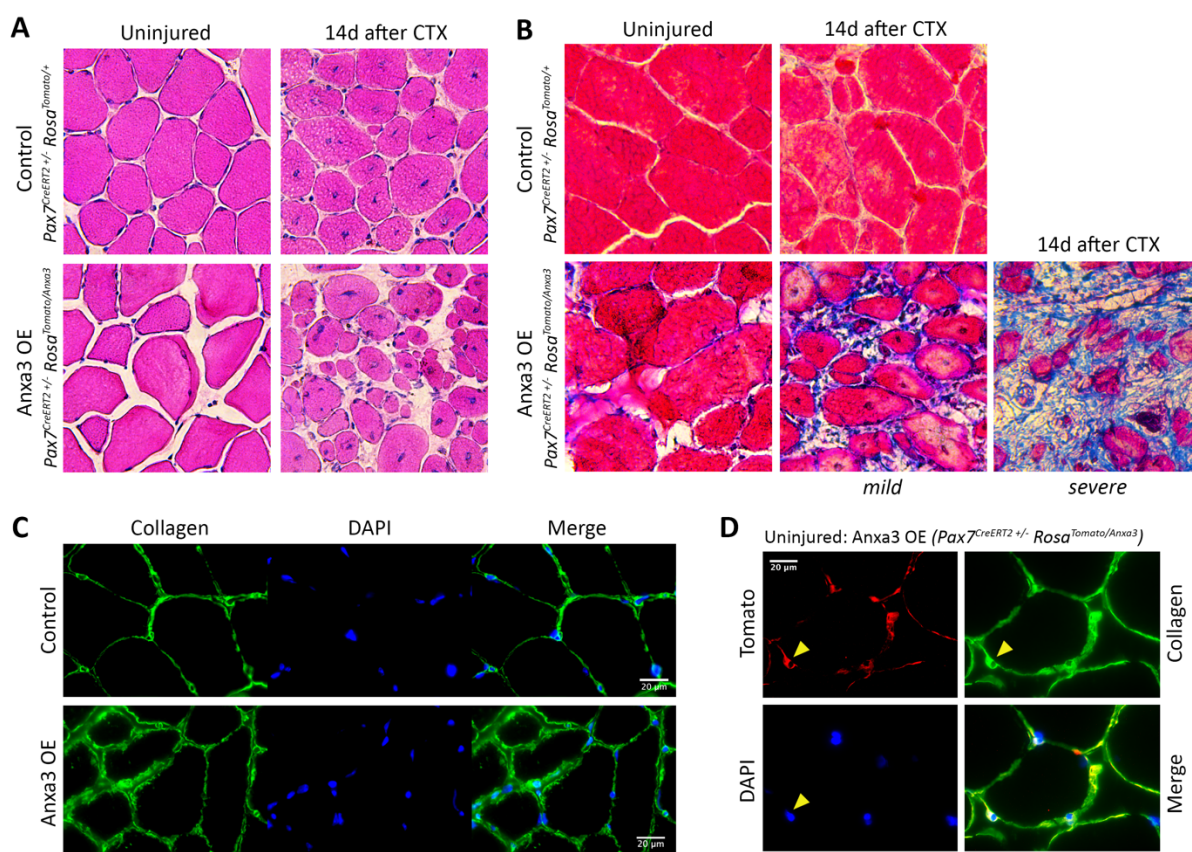


Figure 57. *Anxa3* overexpression disrupts muscle regeneration and induces muscle fibrosis. (A) H&E staining illustrates a proliferation defect in injured TA muscles of qMuSCs-specific *Anxa3* overexpression in mice. Additionally, it shows increased ECM deposition in the uninjured *Anxa3* OE muscles. (B) Masson's trichrome staining reveals massive fibrosis in injured TA muscles of *Anxa3* OE mice. (C) Anti-Collagen immunostaining shows increased Collagen deposition in the uninjured muscles of *Anxa3* OE mice. (D) Anti-Collagen immunostaining and *Pax7*-driven Tomato expression shows increased Collagen deposition in the proximity of *Anxa3* OE quiescent MuSC.

Since increased ECM deposition was observed in uninjured *Anxa3* OE muscles, and caused a massive fibrosis after muscle injury, it seemed likely that fibro-adipogenic progenitor cells (FAPs) are involved. It is known, that excessive proliferation of FAPs and/or their insufficient removal after muscle regeneration leads to muscle fibrosis¹⁷⁶. To investigate whether the numbers of FAPs increase in *Anxa3* OE mice, cryosections of uninjured and injured TA muscles were immunostained for PDGFR α , a marker of FAPs⁹⁷. Immunostaining of *Anxa3* OE sections revealed a slight increase of FAPs number in uninjured TA muscles, and a dramatic increase in the injured muscles 14d after CTX injection, compared to control mice (Fig. 58A, B).

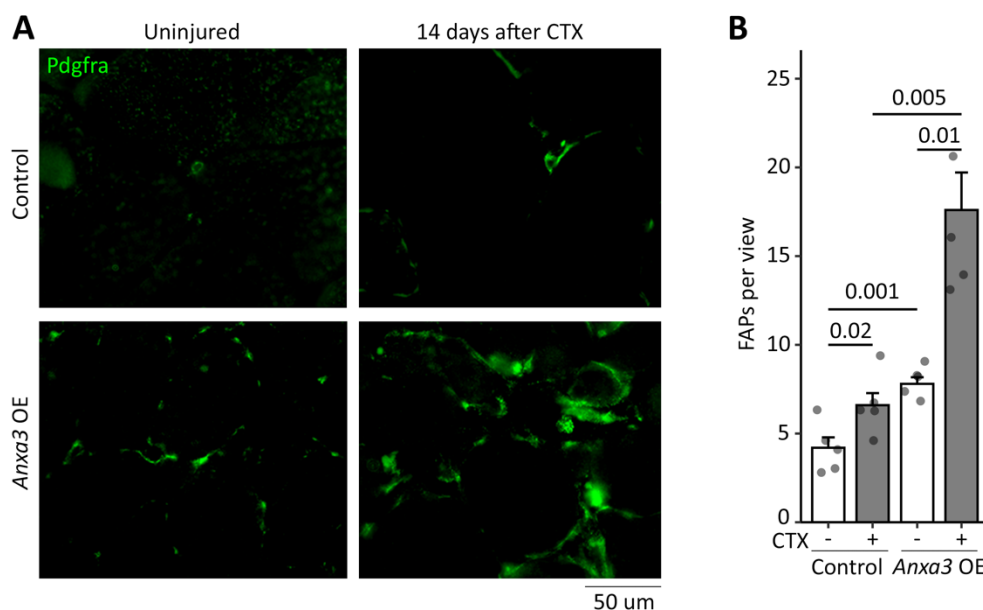


Figure 58. *Anxa3* overexpression increases the number of FAPs. (A) Anti-PDGFR α immunostaining shows increased number of FAPs in the *Anxa3* OE muscles. (B) Counts of FAPs per microscopic image confirms an increase of FAPs numbers upon *Anxa3* overexpression.

Taken together, these results show that *Anxa3* overexpression in qMuSCs prevents successful muscle regeneration and instead induces muscle fibrosis. Furthermore, even without muscle injury, *Anxa3* OE mice showed increased ECM deposition in the direct proximity of *Anxa3* OE qMuSCs. The *Anxa3* overexpression phenotype may therefore be seen as a dramatically aggravated ageing, since similar to aged muscles *Anxa3* OE mice showed a residual capacity of regeneration and aggravated muscle fibrosis.

3.3.5. *Anxa3* overexpression induces transcriptional changes characteristic for disruption of MuSCs homeostasis

To identify the transcriptional signature of *Anxa3* overexpressing MuSC, which are functionally clearly distinct from control cells, an RNA-seq analysis was performed. As described previously, *Pax7:zsGreen* & *Rosa26^{Anxa3/+}* & *Pax7^{CreERT2/+}* (referred as *Anxa3* OE) and *Pax7:zsGreen* (referred as WT) mice were used for this experiment. Mice were injected with Tamoxifen and subjected to qMuSCs isolation 14 days after the last injection. MuSCs were isolated from *Anxa3* OE and WT mice (n=3 each) by FACS and submitted for RNA sequencing.

Comparison of *Anxa3* OE and WT conditions revealed 407 differentially expressed genes (FDR<5%), and 150 of which were **up-regulated in the WT** group, while 257 were **up-regulated in the *Anxa3* OE** group (Fig. 59A). The *Anxa3* gene was clearly up-regulated in the *Anxa3* OE top DEGs, validating the overexpression strategy. By GSEA, genes overexpressed in ***Anxa3* OE** qMuSCs were enriched for the following terms: “Collagen fibril organization” (GO database), “Proteoglycans in cancer” and “AGE-RAGE signaling pathway in diabetic complications” and “Protein digestion and absorption” and “p53 signaling pathway” and “ECM-receptor interaction” (KEGG database), “Integrin signaling pathway” (PANTHER database), “Extracellular matrix organization” and “Degradation of the extracellular matrix” and “Integrin cell surface interactions” (Reactome database). On the other hand, genes with increased expression in **WT** qMuSCs were enriched (FDR<5%) for “AMPK signaling pathway” and “Hippo signaling pathway” and “Insulin signaling pathway” and “Longevity regulating pathway” (KEGG database), “Interleukin signaling pathway” and “Oxidative stress response” (PANTHER database), “Activation of gene expression by SREBF (SREBP)” and “Fatty acid, triacylglycerol and ketone body metabolism” and “Regulation of cholesterol biosynthesis by SREBP (SREBF)” (Reactome database).

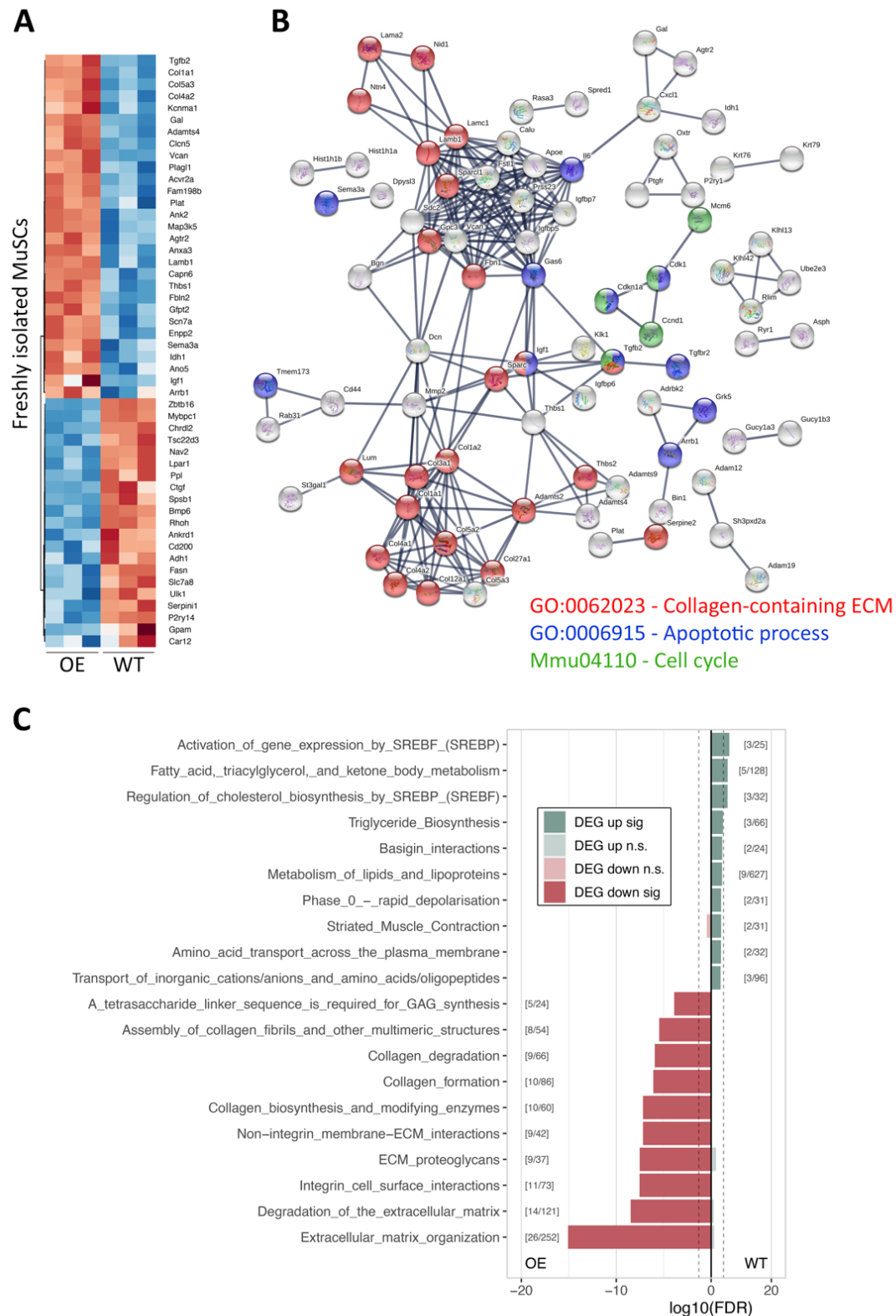


Figure 59. Anxa3 OE quiescent MuSCs have a distinct transcriptional profile. (A) A heatmap shows top DEGs between Anxa3 OE and WT conditions. **(B)** The STRING (*Search Tool for the Retrieval of Interacting Genes/Proteins*) analysis for genes up-regulated in Anxa3 OE quiescent MuSCs shows clusters of collagen, apoptosis and proliferation-related genes. FDR<5%. Color represents GSEA terms (red – GO:0062023 “collagen-containing extracellular matrix”; blue – GO:0006915 “apoptotic process”; green – KEGG Mmu04110 “cell cycle”). **(C)** GSEA analysis of the DEGs between Anxa3 OE and WT conditions shows strong enrichment of the ECM-related terms in Anxa3 OE group of samples.

In particular, expression of collagens (*Col1a2*, *Col5a2*, *Col3a1*, *Col4a1*, *Col27a1*, *Col1a1*, *Col5a3*, *Col4a2*, *Col12a1*) in particular was higher in *Anxa3* OE quiescent MuSC (all significance cutoffs at FDR<5%). Most of these genes are known to promote or accompany fibrosis¹⁷⁷ (Fig. 60). *Ctgf*, which has a direct link to muscle fibrosis through activation of TGFb signaling¹⁷⁸, was, surprisingly, downregulated in *Anxa3* OE cells. In conjunction with this finding, the increased expression of *Tgfb2*, *Tgfb1* and *Tgfb2*, all members of the TGFb family¹⁷⁹ in *Anxa3* OE qMuSCs (Fig. 60) may invite speculation of a *Ctgf*-independent mechanism of initiation of fibrosis.

RNA-seq barplots: WT vs *Anxa3* OE quiescent MuSCs

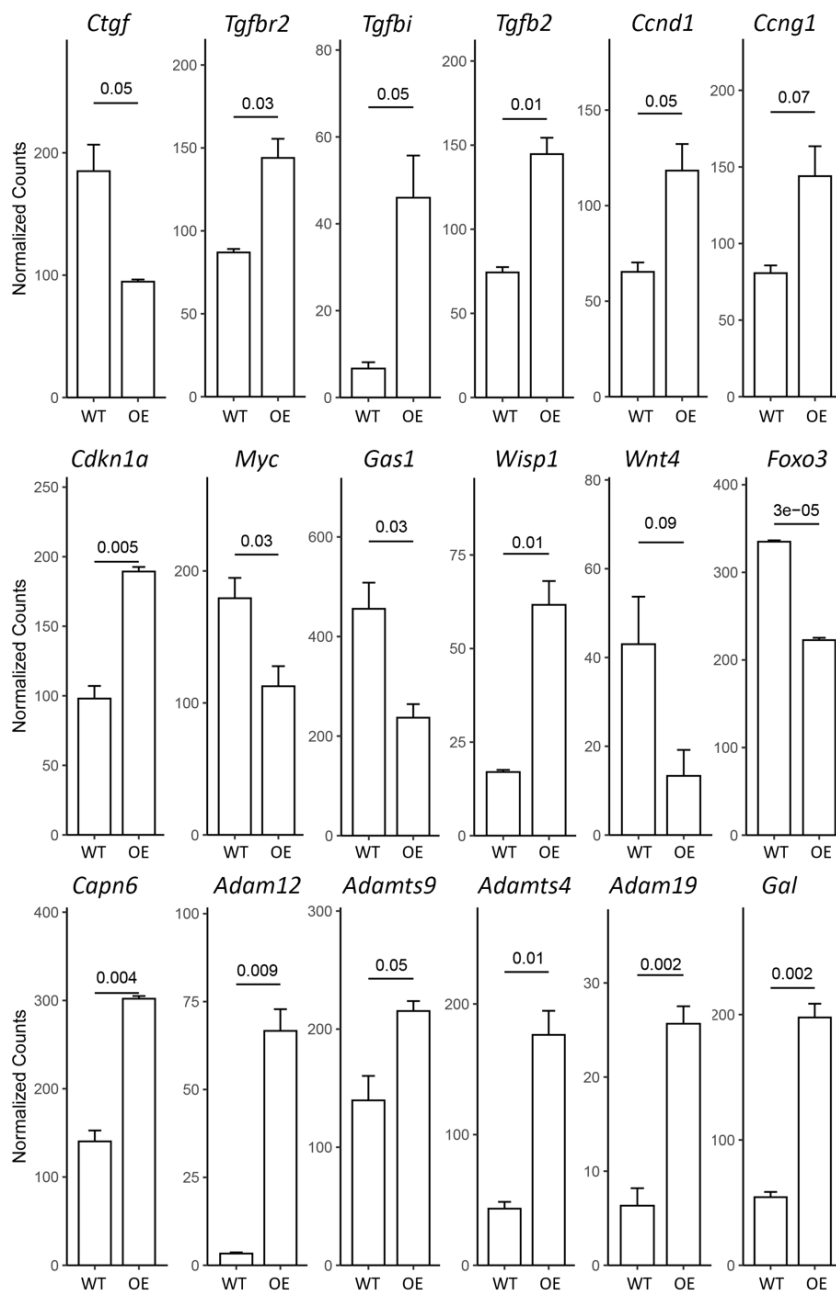


Figure 60. Barplots showing expression levels of select genes in *Anxa3*-overexpressing MuSC. The numbers on top of the bars refer to p-value (n=3, Student's t-test).

Interestingly, genes with increased expression in *Anxa3* OE qMuSCs also comprised *Ccnd1*, *Ccng1*, and *Cdkn1a*¹⁸⁰, two cyclins and a cyclin inhibitor, respectively, while expression of *Myc*¹⁸¹ and *Gas1*¹⁸² was downregulated. This apparent coexistence of pro- and anti-proliferative signals may indicate a disturbance of the cell-cycle machinery, presumably responsible for the proliferative defect in *Anxa3* OE myoblasts (Fig. 60).

Anxa3 OE MuSCs exhibit up-regulation of *Wisp1* expression, which is associated with the fibro-adipogenic progenitors and required for MuSCs expansion and asymmetric division⁹⁷. Additionally, *Anxa3* OE MuSCs showed reduced expression of *Foxo3*, which is required for the maintenance of MuSCs quiescence and self-renewal. *Foxo3* acts through the Notch signaling pathway and is essential for muscle regeneration¹⁸³. Similarly, expression of *Capn6*, which inhibits proper muscle development and regeneration¹⁸⁴, was up-regulated in *Anxa3* OE qMuSCs. The *Anxa3* OE qMuSCs also showed increased expression of *Adam12*, which is known to suppress muscle regeneration and aggravate muscular dystrophy¹⁸⁵. *Adam12* belong to a family of disintegrins and metalloproteases, whose remaining members (*Adamts4*, *Adam19* and *Adamts9*) were also up-regulated. In contrast to the findings for *Gal* above, where expression of *Gal* inversely correlated with the expression of *Anxa3*, *Anxa3* OE MuSCs showed clearly up-regulated expression of *Gal*.

Taken together, the results indicate that *Anxa3* overexpression in quiescent MuSCs induces dramatic transcriptional changes, disrupting MuSCs homeostasis.

3.3.6. *Anxa3* OE does not recapitulate natural ageing at the transcriptional level

In the light of the hypothesis that *Anxa3* overexpression exacerbated ageing, it was evaluated whether *Anxa3* OE recapitulates the transcriptional signature of aged qMuSCs. In order to do that, the RNA-seq dataset of *Anxa3* OE vs WT qMuSCs was compared to the RNA-seq dataset of Young (2 month) vs Old (24 month) qMuSCs, generated in chapter 3.2.1, which shared 103 genes differentially expressed genes (Fig. 61A, B). However, only 37 genes shared the direction of gene expression changes, i.e. were either both up- or down-regulated in *Anxa3* OE and old cells. On the other hand, 40 genes were up-regulated in both young and *Anxa3* OE condition, while 26 were up-regulated in both old and WT groups of cells. This resulted in a similarity of only 36% of transcriptional response between ageing and *Anxa3* overexpressing qMuSCs (Fig. 61C).

3.3.7. Myoblasts, overexpressing *Anxa3*, do not induce apoptosis in fibro-adipogenic progenitor cells

The previous experiments were focusing primarily on the effect of *Anxa3* in MuSCs. However, according to the limb muscles scRNA-seq dataset created by Giordani et. al ¹³⁷, *Anxa3* is expressed in 32% of macrophages, 42% of FAPs and 44% of endothelial cells under normal conditions (Fig. 62A). In total, 25% of all muscle-resident cells had detectable levels of *Anxa3* transcripts. Since the authors used young animals, the cluster of MuSCs did not show any *Anxa3* expression. However, upon RT-qPCR validation of the sorted cell populations (antibody-based FACS), only two cell types showed high expression of *Anxa3* – old MuSCs and FAPs (Fig. 62B). The total percentage of Annexin A3 expression in skeletal muscles was confirmed by immunostaining: approx. 19% of cells on the TA cryosections, probably representing FAPs, had fluorescent signal (Fig. 62C).

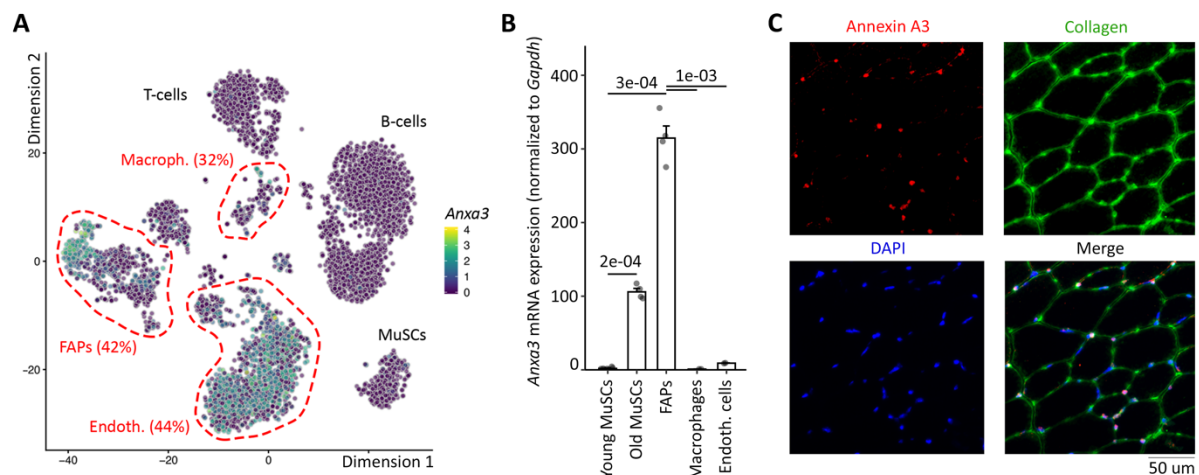


Figure 62. *Anxa3* is expressed in Macrophages, FAPs and Endothelial cells in young muscles (A) t-SNE clustering shows muscle-resident populations of cells. Color overlay indicates expression of *Anxa3*. Cell populations, expressing *Anxa3* are marked with dashed red lines. (B) RT-qPCR of the FAC-sorted cell populations show high expression of *Anxa3* in old MuSCs and FAPs. (C) Immunostaining against Annexin A3 shows that 19% on uninjured WT TA muscles cells express this protein.

Upon muscle regeneration, FAPs provide support for myoblasts. At later stages of regeneration, superfluous FAPs undergo apoptosis ¹⁷⁶. Upon ageing or disease, FAPs can avoid apoptosis and instead form fibrotic structures ⁹⁷. Thus, FAPs are considered to be the most common source of muscle fibrosis. Since Annexin A3 was found in the muscle ECM, and its overexpression induced muscle fibrosis, the next step was to investigate by co-culture experiments, whether MuSCs or myoblasts influence homeostasis of FAPs.

The whole limb muscles of control (*Pax7^{CreERT2/+}* & *Rosa^{+/+}*) and Anxa3 OE (*Pax7^{CreERT2/+}* & *Rosa^{+/Anxa3}*; set of Tamoxifen injections before the isolation) mice were enzymatically digested and purified using Percoll sugar gradient (see 2.5.4). The acquired cell mixtures were cultured on separate cell culture plates. In order to visualize the cell growth, each day one plate was fixed and stored for further analysis.

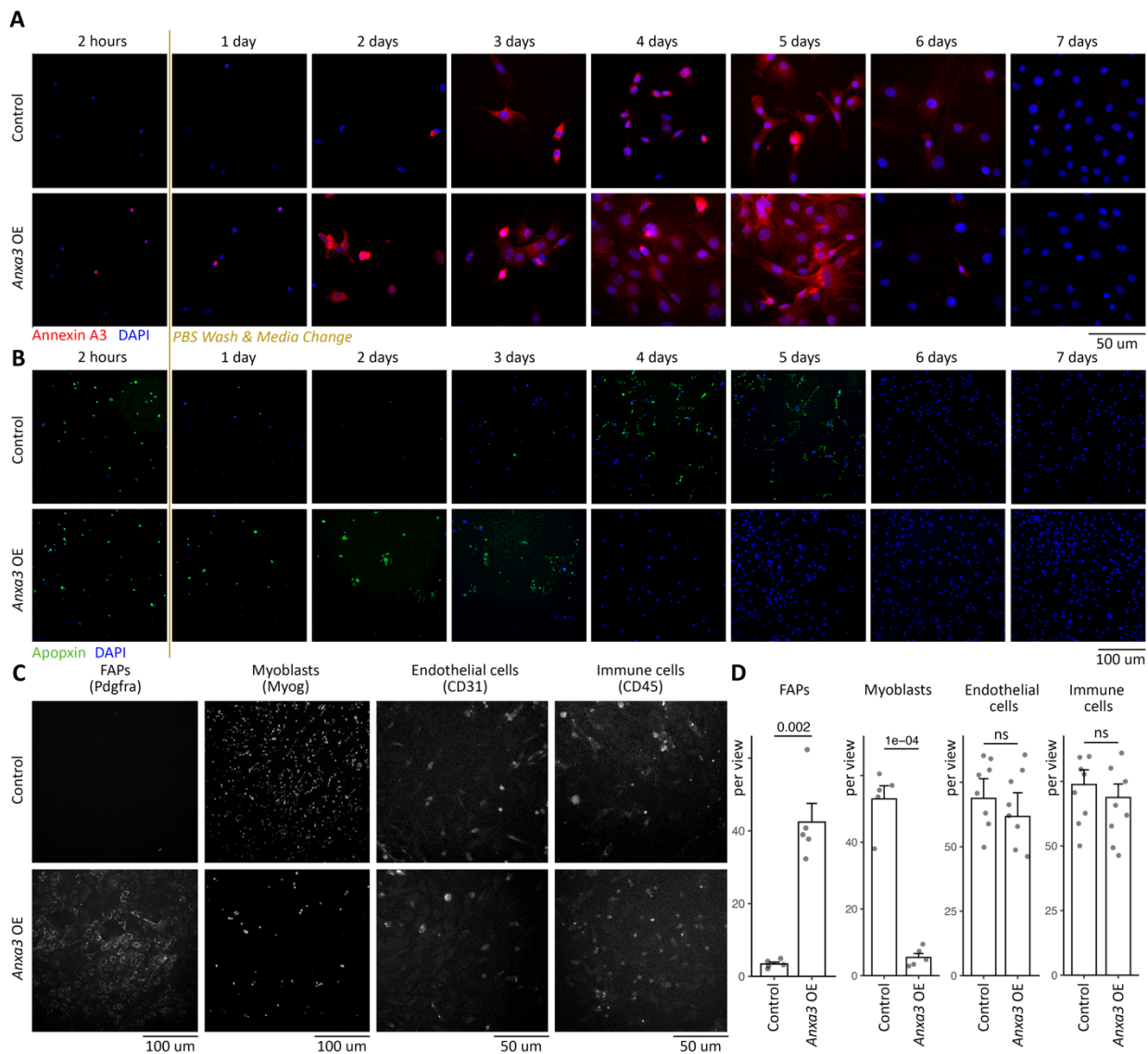


Figure 63. Annexin A3 overexpression shifts apoptosis peak and promotes FAPs proliferation *in vitro*. (A) Immunostaining for Annexin A3 shows that in cell cultures with all muscle-resident cell populations Annexin A3 protein expression peaks between 4 and 5 days in culture for both control and Anxa3 OE samples. (B) Staining for apoptosis shows that Annexin A3 overexpression shifts apoptosis peak in Anxa3 OE cultures from 4-5 days (control) to 2-3 days in culture. (C) Immunostainings show that Anxa3 OE cultures had dramatically increased concentration of FAPs, while diminished concentration of myoblasts, compared to Control cultures. (D) The barplots enumerate cell populations in control and Anxa3 OE cell cultures.

After seven days in culture, all plates were immunostained for Annexin A3 (Fig. 63A). In both control and Anxa3 OE conditions, the Annexin A3 protein expression peaked after 4-5 days and diminished after 6 days in culture. In contrast to control, the Anxa3 OE cell cultures showed continuous expression of the Annexin A3 protein between 1 and 5 days in culture. After staining for apoptosis, it became evident, that in Anxa3 OE cultures, the peak of apoptosis shifted from 4-5 days (control) to 1-3 days (Anxa3 OE) in culture (Fig. 63B). To investigate cell composition of the endpoint cultures (7 days), the respective plates were stained for the PDGFRa (FAPs), Myog (myoblasts), CD31 (endothelial cells) and CD45 (immune cells). The control endpoint cultures did not contain any FAPs, while the concentration of myoblasts was high (Fig. 63C,D). Strikingly, Anxa3 OE cell cultures had strongly increased concentration of FAPs and almost fully diminished population of myoblasts. The concentrations of endothelial and immune cells were not altered between control and Anxa3 OE endpoint cell cultures.

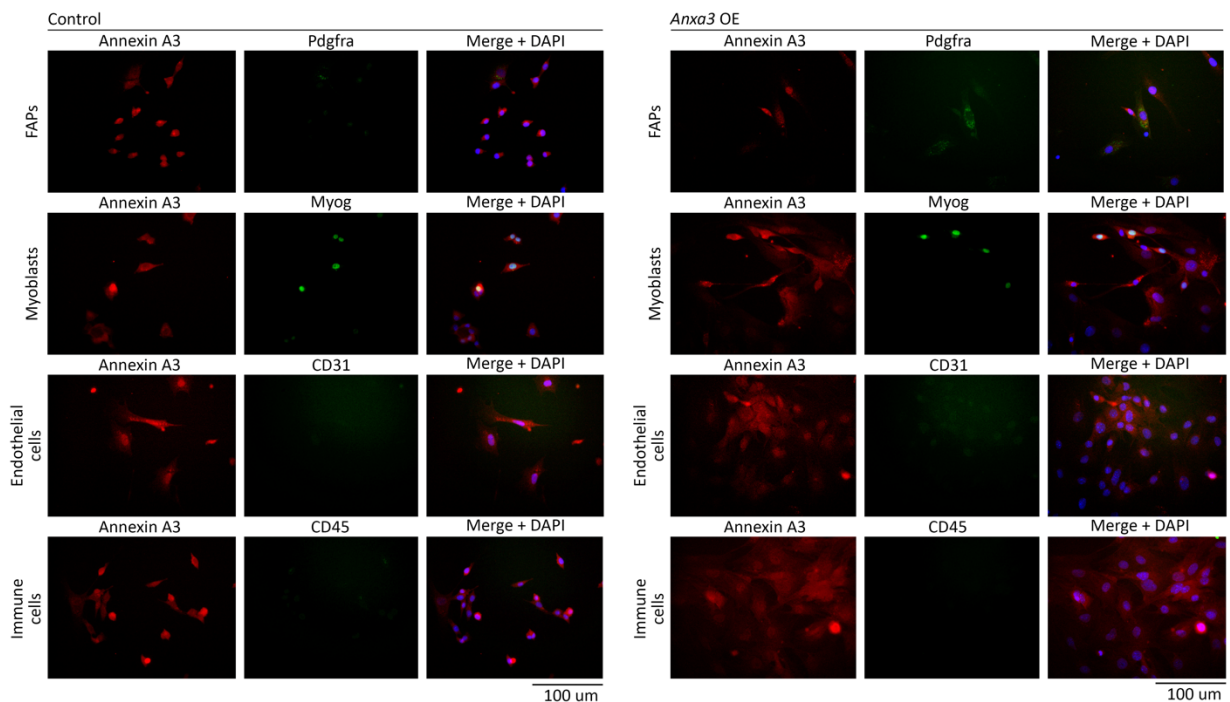


Figure 64. Annexin A3 protein is expressed in FAPs and myoblasts in both control and Anxa3 OE cell cultures.

To investigate, which cell types expressed Annexin A3 protein at its expression peak (4-5 days in culture), the respective plates were co-immunostained for Annexin A3 together with the PDGFRa (FAPs), Myog (myoblasts), CD31 (endothelial cells) and CD45 (immune cells) (Fig. 64). The expression of Annexin A3 protein co-localized with

Myog in both control and Anxa3 OE cultures, confirming its expression in myoblasts. The expression of Annexin A3 also co-localized with PDGFR α in the Anxa3 OE cell cultures, confirming its expression in FAPs. The absence of PDGFR α fluorescent signal in Control cultures proves the absence of FAPs by this culture timepoint.

Since only Myoblasts and FAPs expressed Annexin A3 in cell cultures, the next step was to investigate if these cell types can directly communicate in co-cultures. Muscle cell suspensions were stained with CD31, CD45, Itga7 and Sca-1 antibodies and FAPs were isolated by FACS as CD31⁻ CD45⁻ Itga7⁻ Sca-1⁺ cells¹⁸⁶. In parallel, MuSCs from *Pax7:zsGreen* mice were sorted. MuSCs and FAPs were isolated both from control (*Pax7^{CreERT2/+}* & *Pax7^{zsGreen}*) and Anxa3 OE mice (*Pax7^{CreERT2/+}* & *Pax7^{zsGreen}* & *Rosa^{Anxa3/+}*; set of Tamoxifen injections two weeks before the isolation). The acquired control and Anxa3 OE MuSCs and FAPs were used for cell culture.

FAPs, isolated from Anxa3 OE mice showed moderately higher confluence after four days in culture and higher EdU incorporation, compared to control cells (Fig. 65A-C). In myoblasts & FAPs co-cultures, the wells, which contained Anxa3 OE myoblasts (co-cultures with control and Anxa3 OE FAPs, respectively), had lower confluence, compared to wells with control myoblasts. Such decrease in cell proliferation might reflect a general proliferation defect of Anxa3 OE myoblasts, previously described in 3.3.3. Upon co-cultures of both control and Anxa3 OE FAPs with control myoblasts, many FAPs underwent cell death (Fig. 65B, yellow arrows). Strikingly, no cell death of FAPs was detected in the co-cultures with Anxa3 OE myoblasts (Fig. 65B, green arrows). Upon Annexin A3 immunostaining, it became evident, that both control and Anxa3 OE myoblasts express this protein after four days in culture. Furthermore, its expression was localized in vesicles, which were enlarged upon cellular death. Interestingly, only faint cytoplasmic signals of Annexin A3 were detected in control FAPs. In contrast, FAPs, isolated from Anxa3 OE mice, already showed Annexin A3-positive vesicles in the cytoplasm, indicating that two weeks of Anxa3 overexpression are sufficient to prime FAPs with the Annexin A3-containing vesicles (Fig. 65D,E). Upon co-culture of myoblasts with FAPs, Annexin A3-containing vesicles were found in the cytoplasm of both myoblasts and FAPs. However, only control myoblasts were able to induce apoptosis of FAPs, while co-cultures with Anxa3 OE myoblasts showed no signs of cell death (Fig. 65F).

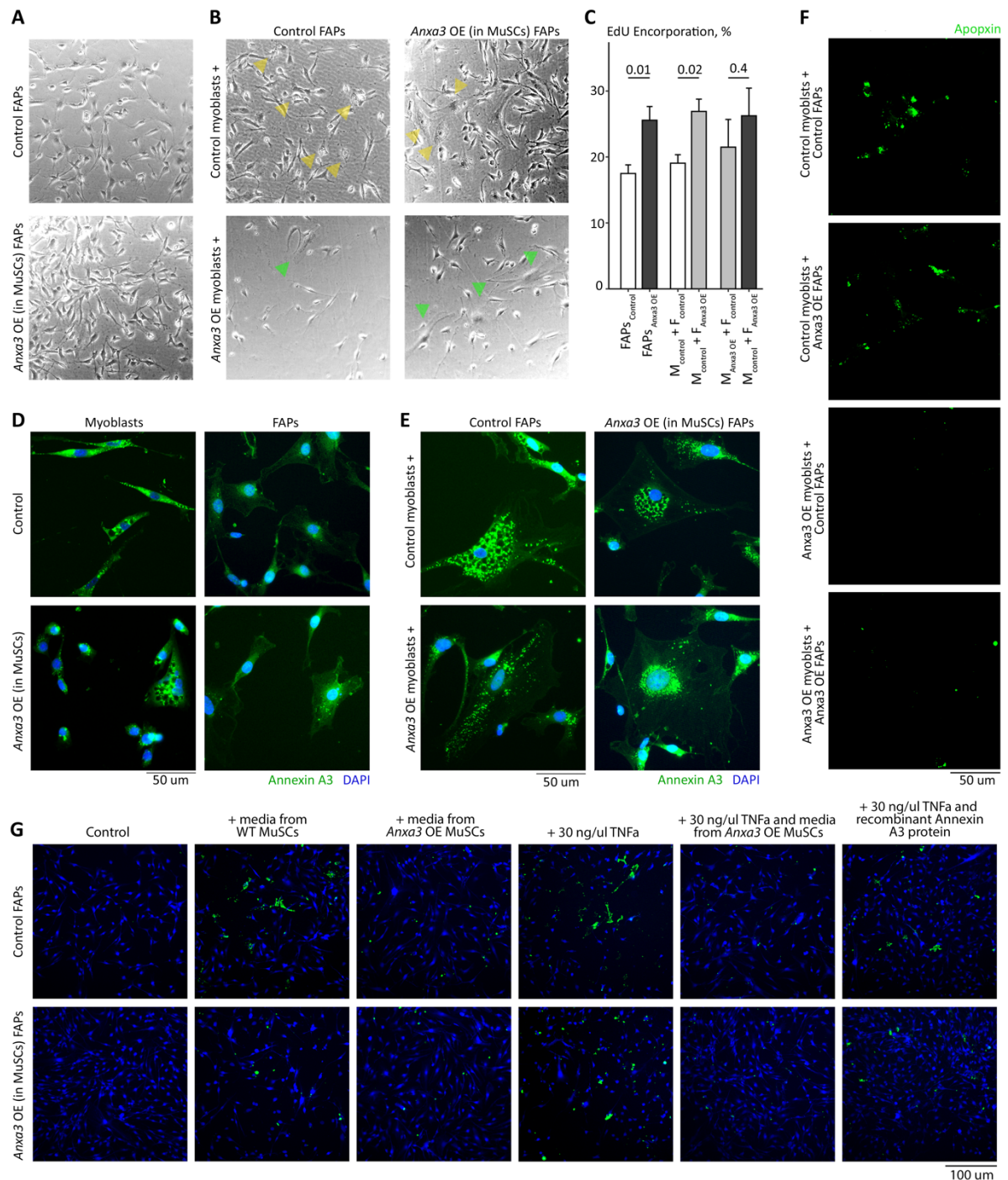


Figure 65. Annexin A3 is involved in signalling between myoblasts and FAPs, preventing apoptosis of FAPs (A) Bright field microscopic images show increased confluence of FAPs, isolated from Anxa3 OE mice. (B) Co-culture images show absence of FAPs apoptosis upon their co-culture with the Anxa3 OE myoblasts. (C) Bar plot shows increased EdU incorporation in FAPs culture from Anxa3 OE mice (D) Immunostaining shows presence of the Annexin A3 protein in the vesicles in myoblasts cytoplasm. (E) Upon co-culture, the Annexin A3-positive vesicles appear in the cytoplasm of FAPs. (F) Anxa3 OE myoblasts fail to induce apoptosis in both control and Anxa3 OE FAPs. (G) A conditioned growth media from the Anxa3 OE myoblasts, in contrast to media from the control myoblasts, fail to induce apoptosis in FAPs. Furthermore, the conditioned growth media from Anxa3 OE myoblasts actively protects FAPs from the TNFa-induced apoptosis. The cultures were exposed to medias and chemicals for 24 hours.

The inability of Anxa3 OE myoblasts to induce apoptosis in FAPs suggests, that the signalling between these cell types is altered upon overexpression of Annexin A3 in MuSCs. To investigate, if MuSCs induce FAPs apoptosis via secreted factors, control and Anxa3 OE MuSCs were cultured for 5 days, and their conditioned growth medias were transferred to separate FAPs cultures (Fig. 65G). An apoptosis staining confirmed, that conditioned media from the control myoblasts was able to induce apoptosis in control FAPs, and, to a lesser extent, in FAPs from Anxa3 OE mice. On contrary, conditioned media from the Anxa3 OE myoblasts was unable to induce apoptosis in neither control nor Anxa3 OE FAPs. An addition of 30 ng/ μ l TNFa (Sigma, Germany) to FAPs was used as a positive control for induction of apoptosis. Strikingly, upon addition of TNFa and Anxa3 OE conditioned media together, almost no apoptosis was present in both control and Anxa3 OE FAPs cell culture. This implies, that Anxa3 OE myoblasts may secrete certain factors, which actively protect FAPs from cell death.

Taken together, these results indicate, that Annexin A3 is involved in cell signalling between MuSCs (and later myoblasts) and FAPs. Annexin A3 overexpression led to (i) moderately increased FAPs proliferation and (ii) the inability of myoblasts to induce FAPs apoptosis. These observations may explain (i) increased Collagen deposition and moderate muscle fibrosis in uninjured Anxa3 OE TA muscles (increased FAPs proliferation because of Annexin A3 signalling); (ii) massive fibrosis upon muscle regeneration in the Anxa3 OE mice (in addition to myoblasts proliferation defect, absence of apoptotic clearance of FAPs leads to massive fibrotic scar).

4. DISCUSSION

The aim of the current dissertation was to gain novel insights into the heterogeneity of different cellular populations in striated muscles at the single cell level. The first chapter explores transcriptional heterogeneity in cardiomyocytes, which were found to be homogeneous in basal conditions, but shift to heterogeneity under pathological conditions. The second and the third chapters describe age-associated transcriptional changes in the heterogeneity of quiescent muscle stem cells. More precisely, the second chapter focuses on the neuropeptide Galanin, which was found to be expressed preferentially in juvenile muscle stem cells, while the third chapter describes the role of Annexin A3, a protein enriched in aged cells. Taken together, these findings emphasize the importance of preserving and maintaining cellular heterogeneity within cardiac and skeletal muscles to secure homeostasis of striated muscles and enable repair functions.

4.1. Mono- and multinucleated ventricular cardiomyocytes constitute a transcriptionally homogeneous cell population

A mammalian heart is composed of various cell populations, and in the last decade, their genetic, epigenetic and transcriptional heterogeneity became a focus of the scientific community ⁷³. Although it is relatively straightforward to assess the heterogeneity of many cell types with modern single-cell approaches, the particular morphology and fragility of cardiomyocytes has hindered investigations at the single-cell level ¹⁸⁷. To shed light on this topic, the first chapter of this dissertation reveals that adult rod-shaped cardiomyocytes represent a homogeneous cell population, at least at the level of resolution provided by the scRNA-seq approach (Fig. 66). For a long time, the differences between cardiomyocytes with various number of nuclei were a subject of speculations. Some authors claimed them to be a byproduct of terminal differentiation of cells, while others hypothesized a superior role of mononuclear cardiomyocytes in terms of heart regeneration ⁷³. The debates regarding the role of cardiomyocyte nuclearity are also connected with hypotheses about cardiac stem cell existence. Long-term experiments indicated a very slow cell turnover of cardiomyocytes ¹⁸⁸. Therefore, some authors speculate that such a turnover might be caused either by division of mononuclear cardiomyocytes, or by differentiation from cardiac stem cells. However, the very existence of cardiac stem cells remains

questionable¹⁸⁹. In terms of cardiomyocytes nuclearity, in this dissertation, mono-, bi- and multinucleated cells were found to be transcriptionally similar. Hypertrophic cardiac remodeling, however, induced profound transcriptional changes in the cardiomyocytes, which gave rise to substantial transcriptional heterogeneity, yet did not correlate with cardiomyocytes nuclearity. This heterogeneity appeared primarily driven by responses to hypoxia and orchestrated by the expression of the transcription factor and hypoxia marker HIF1 α . Its expression inversely correlated with the vascularization of cardiac muscle. Delayed and/or suboptimal vessel growth during heart remodeling may thus be the ultimate origin of the observed transcriptional heterogeneity.

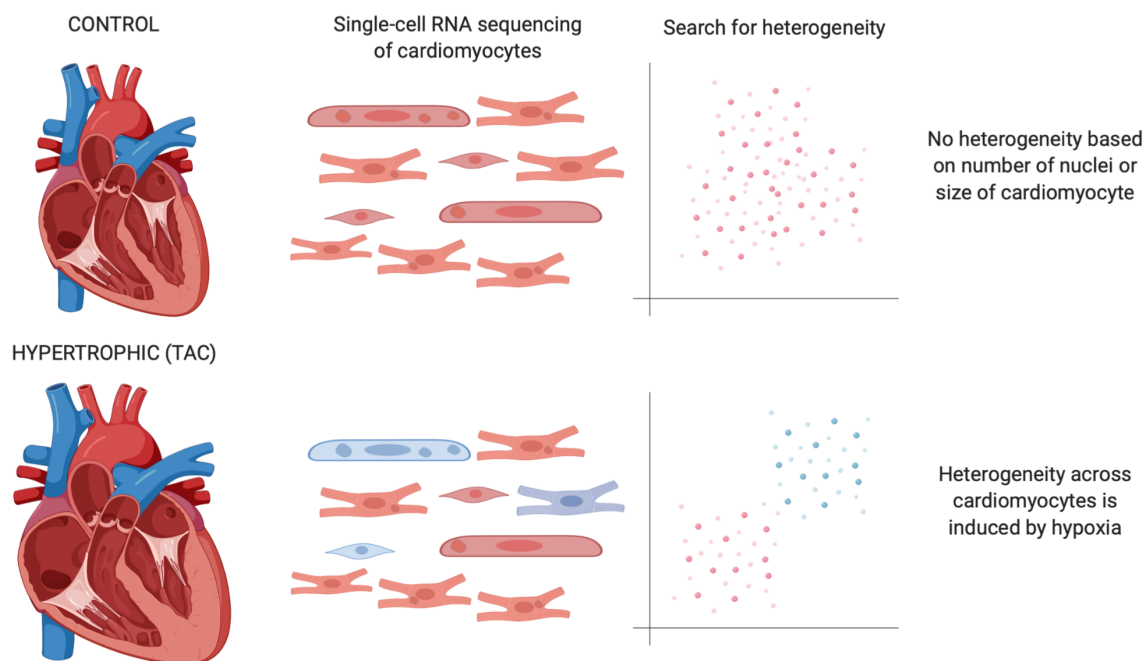


Figure 66. A graphical abstract: Mono- and multinucleated ventricular cardiomyocytes constitute a transcriptionally homogeneous cell population. The cells become heterogeneous upon hypertrophy due to unequal responses to hypoxia. (The figure was created using BioRender application.)

The data might also indicate that transcriptional differences between single rod-shaped adult cardiomyocytes are dominated by the local tissue microenvironment rather than endogenous features (like the number of nuclei or the nuclear ploidy). However, it is entirely possible that cardiomyocytes with different numbers of nuclei are different by other means, which could not be addressed in this work. For example, they might harbor divergent chromatin landscapes or be characterized by proteomic

heterogeneity. Such proteomic heterogeneity might be temporally distinct from transcriptomic one due to slower protein turnover and/or protein processing ¹⁹⁰.

However, the transcriptional homogeneity of cardiomyocytes under basal conditions suggests an alternative hypothesis regarding the role of additional nuclei in these cells. Since the mRNA content appeared comparable between mononucleated and multinucleated cardiomyocytes, it is likely that a subset of nuclei undergo transcriptional silencing. Preliminary data from immunostaining against an activated Pol2 enzyme suggested that binucleated cardiomyocytes comprise one more and one less transcriptionally active nucleus (data not shown). This provocative observation supports the hypothesis of nuclear silencing but clearly requires more detailed investigation to allow solid conclusions for potential functional characteristics.

To investigate the differences between nuclei inside a multinucleated cardiomyocyte (namely intra-cellular heterogeneity), mono and multinucleated cardiomyocytes can be sorted with FACS (for example, using large bore low throughput sorter like the BioSorter from Union Biometrica, Germany). Nuclei may then be isolated from the acquired groups of mono-, bi and multi-nucleated cardiomyocytes and subjected to single cell analysis. Since cellular nuclei are small and round, and imaging quality assessment is not necessary, droplet-based scRNA-seq protocols could be used in such a setting. If intra-cellular heterogeneity exists in multinucleated cardiomyocytes, their nuclei should form separate clusters on dimensional reduction plots, based on their divergent transcriptional activity. In contrast, mononucleated cardiomyocytes should only form one cluster, since they only own a single transcriptionally active nucleus. However, such sub-cellular single-nuclei RNA-seq will not answer the question about mechanisms or reasons of nuclei silencing in multinucleated cardiomyocytes. To understand the reasons, epigenetic screening of these pre-grouped nuclei should be performed. For example, single-nucleus ATAC-seq analysis might uncover decreased chromatin accessibility in silenced nuclei from the multinucleated cardiomyocytes. Yet, the differences between transcriptionally silenced and active nuclei could be also caused by other epigenetic processes.

The bottleneck for a sub-cellular single-nucleus experiment described above would most likely be the sorting of multinucleated cardiomyocytes. Due to their big size and fragility, a special sorting setup needs to be employed. The second problem would be to separate cardiomyocytes based on their nuclearity. An apparently straightforward solution may be to stain the cardiomyocytes with a nuclear dye (e.g. Hoechst for living

cells) and separate the cells of different nuclearity based on the intensity of the nuclear signal, which correlates with the number of present nuclei. However, unlike most other cell types in the organism, some cardiomyocytes show increased ploidy, more than the usual $2N$ ⁸³. This might eventually compromise the sorting strategy, which is only based on the intensity of the nuclear staining. The sorting strategy should therefore include parameters such as size and morphology of the cardiomyocyte, distance between nuclei in the multinucleated cells and others. And finally, large bore sorters have lower throughput than usual sorters. In preliminary experiments ([data not shown](#)), multiple hours were required to obtain only a few hundred of sorted cardiomyocytes, which is not sufficient for the downstream sub-cellular single-nuclei experiments and also rises concerns about the cellular condition (and therefore transcriptome) due to the long time spent in the sorting buffer. An alternative to FACS approach would be manual sorting of cardiomyocytes under the microscope (for example, with mouth pipetting or with IVF-like liquid handlers). The cells should be first isolated from the hearts (with, for example, Langendorf method), stained with nuclei stain and placed in a Petri dish. This method allows precise visual evaluation of cellular morphology, recapitulating imaging quality check in the ICELL8 system, at the expense of a much lower throughput. Ultimately, methods like laser-capture microdissection might be used to isolate nuclei from the cardiomyocytes of different nuclearity. Yet, the common disadvantage of such approaches is low throughput and long handling time, which might result in alterations of cellular transcriptome and epigenome.

Moving away from the normal physiological conditions, many types of pathological cardiac hypertrophy result in decreased capillary density, especially in the subendocardial region. This is a consequence of capillary beds not keeping pace with increasing heart mass, eventually resulting in extended length of the oxygen transport path¹⁹¹. To counter this effect, angiogenesis is enhanced when adaptive cardiac growth occurs. Up-regulation of mTOR signaling and expression of the angiogenic factor VEGF, which is responsive to HIF1 α signaling^{191,192}, is responsible for this phenomenon. Local hypoxia induces expression of *Vegfa* during early stages of cardiomyocyte hypertrophy, promoting local angiogenesis in an attempt to restore normal oxygenation.

Under pathological conditions, expression of HIF1 α is decreased, likely via an increase of p53 expression and MDM2-dependent ubiquitylation, causing proteasomal degradation of HIF1 α . This results in a mismatch between cardiomyocyte expansion

and the density of the supporting capillary network ^{193,194}. Hypoxic responses are thus the most likely main drivers of cardiomyocyte heterogeneity. It is tempting to speculate that not all cardiomyocytes succeed in HIF1 α degradation, even at advanced stages of hypertrophy (8 week after TAC). In contrast, HIF1 α is retained in a subset of cardiomyocytes, located in the hypoxic areas of myocardium. Ultimately, these novel insights into the evolution of heterogeneity in cardiomyocyte responses under pathological conditions may prove to be useful for understanding adaptive cardiac hypertrophy in the context of heart failure ¹⁹⁵.

Rod-shaped cardiomyocytes turned out to be strikingly homogeneous, which is surprising given the diversity in nuclearity. This may suggest that cardiomyocyte polyploidization is a byproduct of terminal differentiation, which prevents unwanted cell proliferation. Multinucleation supports organ growth without deteriorating alterations of cell shape and function. Multinucleation is assumed to support higher metabolic activity, enhance gene expression and higher efficiency of stress responses ^{196,197}. However, virtually no difference was found between mono- and multinucleated cardiomyocytes. Both mono- and multi-nucleated cardiomyocytes randomly expressed a subset of cell-cycle-related genes, arguing against the hypothesis that mononuclear cardiomyocytes are more prone to enter the cell cycle. There was a clear correlation between nuclearity and cardiomyocyte size, but – surprisingly – no correlation with the number of sequencing reads per cell. This implies that increased gene expression is not an inevitable consequence of increased nucleation. Yet, a recent study by Windmueller et al ¹⁹⁸ revealed that mono- and multinucleated cardiomyocytes that are homogeneous in the myocardium of prenatal and adult mice, transiently become transcriptionally distinct within the first week after the mouse birth. P7 mono-nucleated cardiomyocytes, in comparison to multinucleated ones, retained immature pro-cell cycle transcriptome. This observation suggests that multinucleated cardiomyocytes possess higher propensity towards maturation. However, in agreement with the results of the current dissertation, adult cardiomyocytes had only minor transcriptional differences between groups of cardiomyocytes with different nuclearity.

Of course, the present study has limitations and cannot address all aspects of potential heterogeneity within cardiomyocytes. First of all, the analysis was restricted to rod-shaped cardiomyocytes, resulting in exclusion of cardiomyocytes with an unconventional morphology (for example, immature or round-shaped cardiomyocytes ¹⁹⁵). Second, the sensitivity of any scRNA-seq technology is low as compared to bulk

approaches. Only 15-30% of the bulk-detectable transcriptome is represented in scRNA-seq libraries. And finally, the micro-well single-cell approach limits the throughput, although improving quality by offering the possibility for image-based QC. All these limitations might have influenced the detection of heterogeneity. In particular, it is entirely possible, that heterogeneity in rod-shaped cardiomyocytes with the various nuclearity manifests in lowly expressed genes, which are not detected due to the sensitivity limits of current scRNA-seq approaches.

The occurrence of technical artifacts (likely due to cell damage, undergoing cell death or unwanted contamination with cell debris or other cells) highlights the necessity of a strict imaging quality check during scRNA-seq analysis. Most of the current methods for scRNA-seq (for example, droplet-based 10x Chromium or FACS-based plate methods) do not provide imaging quality control, with the exception of the Takara ICELL8 and, to a certain extent, the Fluidigm C1 systems. Even more, it is not yet technically possible to implement imaging quality assessment in the droplet-based methods due to high throughput and droplet generator specifics. Particularly, in the current droplet-based scRNA-seq protocols the cell is being immediately lysed upon encapsulation (to release its RNA). This step should be therefore postponed to allow imaging of the not-yet-lysed cells. The droplet-based methods also allow to perform single-nucleus RNA-seq, when instead of cell suspension, a suspension of cell nuclei from certain tissues are used as an input. This allows single-nucleus analysis of tissues and cells, which otherwise are hard to get cell suspensions of. Additionally, single-nucleus methods do not depend on the initial cell size and morphology. As a drawback, single-nucleus methods represent different transcriptomes (currently transcribed RNAs instead of cytoplasmic RNAs in single-cell). As a conclusion, it is an imperative to choose a scRNA-seq system, which allows image control when working with big and/or fragile cell populations like, for example, cardiomyocytes, nerves or megakaryocytes in order to avoid technical artifacts in the datasets.

Nevertheless, the current study clearly shows that mono- and multinucleated cardiomyocytes have remarkably similar profiles, at least with respect to abundant gene transcripts, and show similar responses to hypertrophy. The current dataset implementing high quality requirements will be a valuable resource for further studies.

4.2. The neuropeptide Galanin restores the regenerative capacity of aged muscles

Growth factor signaling plays an important role in muscle maintenance and regeneration ¹⁹⁹. Low concentrations of signaling molecules and the complexity of signaling networks involved, encumber the investigation of cell-to-cell communication in the skeletal muscle. However, in the last decade, state of the art single-cell transcriptomic analysis started to shed light on the interplay between different cells in the process of muscle regeneration. Motivated by the identification of *Gal* as a gene differentially expressed between young and aged qMuSCs, the second chapter of this dissertation focuses on the role of Galanin neuropeptide in the processes of muscle stem cells ageing and muscle regeneration (Fig. 67).

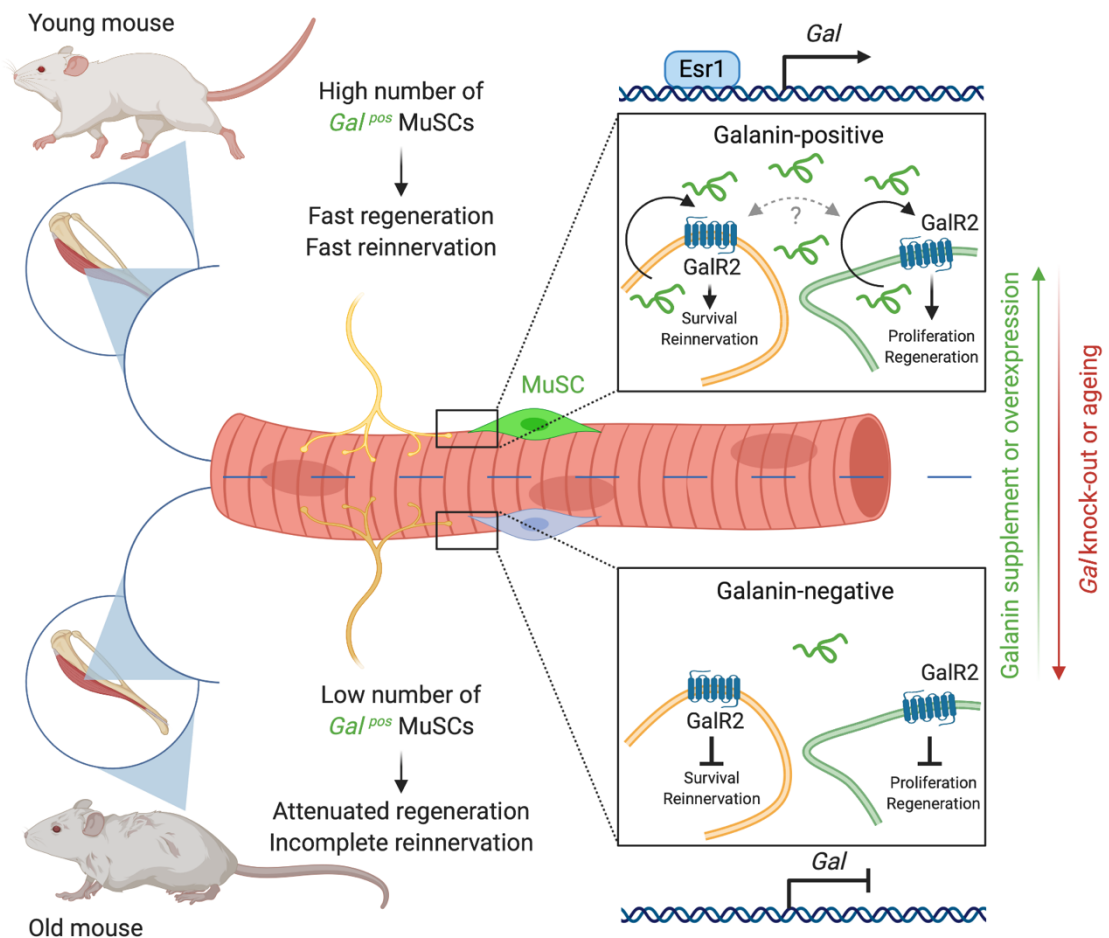


Figure 67. A graphical abstract: The neuropeptide Galanin restores the regenerative capacity of the aged muscles. A number of *Gal^{pos}* qMuSCs decrease with age, which leads to attenuated muscle regeneration and re-innervation upon injury. (The figure was created using BioRender application.)

Galanin was first identified in the neural system. Genetically modified Gal KO mice show decreased efficiency and speed of regeneration of the sciatic nerve after injury, while Gal OE or ectopic Galanin supplementation improved this process ¹³¹. However, Galanin has never been associated with muscles, although whole-muscle scRNA-seq, performed by Giordani et al ¹³⁷, already suggests, that qMuSCs express the *Gal* gene. The study by Giordani et al. was done using the 10x Chromium platform and thus excluded nerve cells due to their big size and fragility. Only fragments of nerves ended up in the single-cell sequencing library, leading to their exclusion *in silico* as debris. In other words, the literature supports Galanin's presence in two cell types of the healthy muscle: neurons and qMuSCs. Although neurons and qMuSCs arise from different germ layers (neurons are derived from the ectoderm and MuSCs from the mesoderm ²⁰⁰) and rely on different mechanisms, both cell types might employ similar signaling pathways to accomplish regeneration. Peripheral neurons regenerate via sprouting ¹⁹⁹ and do not require stem cells. Existing neurons may form new branches, which eventually re-innervate damaged regions of tissue. In contrast, skeletal muscle regeneration mainly relies on stem cells, albeit minor damages of myofibers that do not result in cell death can be repaired without a mandatory contribution from MuSC.

The function of Galanin depends on interactions with corresponding receptors (Galanin receptors 1-3). Both nerves and qMuSCs express Galanin receptor 2, which may imply that similar downstream signaling pathways are used. Galanin receptor 2 is a G-protein coupled-receptor (GPCR), which relies on the $G_{q/11}$, $G_{12/13}$, G_{ai} and G_o proteins for downstream signaling ¹²⁹. It is known, that the GPCR downstream signaling is often multi-vectoral and includes many targets. RhoA ($G_{12/13}$), Adenylyl cyclase (down-regulated by G_{ai}) and Phospholipase C (up-regulated by $G_{q/11}$), have all been reported to be downstream targets of GalR2-associated G-proteins ²⁰¹. Down-regulation of adenylyl cyclase leads to reduced cAMP levels, which in turn reduces activity of the CREB transcription factor. Up-regulation of Phospholipase C increases phosphatidylinositol 4,5-bisphosphate (PIP_2) production, and eventually triggers phosphoinositide 3-kinase (PI3K) and protein kinase C (PKC) activity, which initiate the PKB/Akt and MAPK cascades, respectively. This complex signaling downstream of GalR2 might be the reason of the pleiotropic effects of Galanin in muscle cells.

Galanin signalling might be separated into autocrine (qMuSCs and neurons separately) and paracrine (qMuSCs to nerves and *vice versa*). Autocrine Galanin

signaling in nerves promotes increased nerve regeneration ¹³¹, while enhances activation and proliferation of qMuSCs, thereby stimulating muscle regeneration. It currently remains unclear whether paracrine signaling between MuSCs and neurons based on Galanin exists and is functionally relevant. As shown in the current dissertation, complete absence of Galanin in mice leads to impaired muscle fiber regeneration and prevents subsequent re-innervation. However, a deletion of Galanin specifically in the quiescent MuSCs, resulted only in disturbed muscle regeneration while re-innervation was not affected. This suggests that a re-innervation defect in the germline Gal KO originates only from neurons but not from MuSC. It is, however, still an open question whether absence of Galanin in neurons will affect muscle regeneration. To clarify this question, a neuron-specific *Gal* knock-out has to be generated. In summary, the current model assumes that Galanin in MuSCs is responsible for their efficient activation and proliferation after acute muscle injury, securing successful muscle fiber restoration. On the other hand, Galanin in neurons might be responsible for repair of neurons and muscle re-innervation after injury.

Transgenic overexpression of *Gal* and i.p. injections of Galanin had similar effects on muscle regenerating and transcriptional signatures of quiescent MuSCs, which open exciting perspectives for the therapeutic use of Galanin. Ageing and muscle-affecting conditions (for example, sarcopenia) result in muscle fiber denervation and degeneration of the NMJs ²⁰². Supplementation with Galanin may support re-innervation of affected muscle fibers. However, a muscle regenerative milieu was required to obtain beneficial effects of Galanin supplementation. Galanin was clearly sensed by quiescent MuSCs of old mice after 3 weeks of treatment (as visible by their transcriptional changes), but an increase of NMJs numbers was only found in a combination of CTX injury and Galanin treatment. Treatment-mediated re-innervation may thus require acute pro-regenerative signaling, which is supported by presence of Galanin.

Formation of the NMJs starts with assembly of acetylcholine receptor clusters triggered by the Agrin-MuSK-Dok7 signalling cascade ^{203,204}. However, it remains largely unknown how motoneurons find those acetylcholine receptor clusters on the muscle fibers in order to form NMJs. Hypothetically, Galanin signaling may play a role in either navigation of motoneurons or the maintenance of the NMJs. Liu et al showed that young qMuSCs remain in the proximity of NMJs, while the location of qMuSCs on muscle fibers randomizes with ageing ^{205,206}. This loss of defined location of MuSC

during ageing correlates well with observed extinction of the *Gal^{pos}* qMuSCs subpopulation. Liu et al also showed that MuSCs tend to fuse with muscle fibers and contribute towards the myo-nuclei located under the NMJs. These nuclei are distinct from others in the muscle fiber and provide mRNA encoding NMJ-specific proteins ²⁰⁵. NMJ-associated myo-nuclei numbers decline with age, which contribute to morphological changes of NMJ and denervation. It is possible, that *Gal* expression primes the qMuSCs to contribute towards NMJ-associated myo-nuclei, thus increasing motoneuron survival and preventing NMJ denervation and/or degeneration. To address this correlation, the co-localization of *Gal^{pos}* qMuSCs and NMJs should be investigated using immunofluorescent stainings or by genetic labelling.

The autocrine Galanin signaling in the MuSCs may be connected with the maintenance of cellular quiescence, as expression of the *Gal* gene decreases with the switch from quiescence towards activation and differentiation in MuSC ([data not shown](#)). Mature muscle fibers, finally, do neither express Galanin nor Galanin receptors. Therefore, it is possible, that *Gal* expression selectively primes a subset of quiescent MuSCs and enhances their oxidative metabolism, preparing them for rapid expansion after an injury. Similar concepts were proposed by Rando et al, who discovered “G-alert MuSCs” ^{207,208}, which were claimed to be superior in terms of muscle regeneration. Similarly, Zammit et al discovered “Reserve MuSCs”, which are primed to return to the quiescence ^{209,210}, while other cells proliferate and differentiate into muscle fibers upon injury. Brack et al also showed, that there are two distinct subpopulations of qMuSCs: non-proliferating (label-retaining) and proliferating (non-label-retaining) cells, which renew less and more profoundly, respectively ²¹¹. In general, a complex set of signaling pathways regulates and/or modulates MuSCs quiescence (particularly Notch, MAPK/ERK, Wnt, Hedgehog, *Spry1*, *Staufen1*) ²¹². Many of them are known to be dysregulated with age.

The current study revealed a partial transcriptional rejuvenation of aged qMuSCs, exposed to systemic application of Galanin. Attempts to restore the organismal youth by systemic applications of the certain factors are currently attempted. In particular, muscle functions were improved in aged mice, whose circulation was connected with the blood stream of young mice ²¹³. Such “heterochronic symbionts” prove, that an exposure to juvenile circulating factors rejuvenates aged tissues and cells ^{92,213}. Furthermore, the transplantation of aged qMuSCs to young mice (with own qMuSCs ablated), resulted in efficient engraftment

and muscle regeneration upon injury ²¹⁴. This suggests, that the juvenile niche milieu strongly influences the biological “age” of qMuSCs. Based on the findings in this study, Galanin is a very promising candidate for a circulating juvenile factor.

Taken together, the second chapter of this work reveals the impact of Galanin on muscle regeneration and innervation. It also highlights its potential in the treatment of age-related muscle diseases.

4.3. Annexin A3 marks a defective subpopulation of aged muscle stem cells

In contrast to Galanin, which marks a highly beneficial sub-population of quiescent MuSCs in young mice, the *Anxa3* gene was expressed in a fraction of aged qMuSCs (Fig. 68). Remarkably, young qMuSCs did not express this gene at all. In the literature, *Anxa3* has never been associated with muscle regeneration yet.

All previous research conducted on the *Anxa3* gene, was focused on cancer. In particular, expression of this gene serves as a cancer marker ¹³⁴. Silencing of the *Anxa3* gene was shown to reduce carcinogenesis and decrease the number of metastases ^{135,136}. Furthermore, it was shown that *Anxa3* promotes angiogenesis in a cancer model ²¹⁵. However, mechanistic knowledge about the function of *Anxa3* and especially its role in the skeletal muscle is lacking.

The previously known function of Annexin A3 (and Annexin A1, which belong to the same protein family) is the inhibition of Phospholipase A2, which is involved in lipid metabolism, lipid signaling and receptor-mediated signaling ²¹⁶. The inhibition of Phospholipase A2 by Annexin A3 is likely to increase the metabolic stress and apoptosis and may suppress cell growth and proliferation ²¹⁷. Within this work the phenotype could be recapitulated in myoblasts which expressed the *Anxa3* gene. A possible mechanism of Annexin A3 function might be based on changes in membrane folding. In a recent study, Boye et al showed that addition of Annexin A3 protein caused shrinking of artificial lipid bilayers ²¹⁸. Such mechanical disruption of cellular and/or nuclear membranes might trigger cell death and ultimately disrupt cellular homeostasis. Hypothetically, excessive expression of structural proteins like collagens in the *Anxa3* OE MuSCs, might represent an attempt of cells to withstand the deterioration of the cellular membrane.

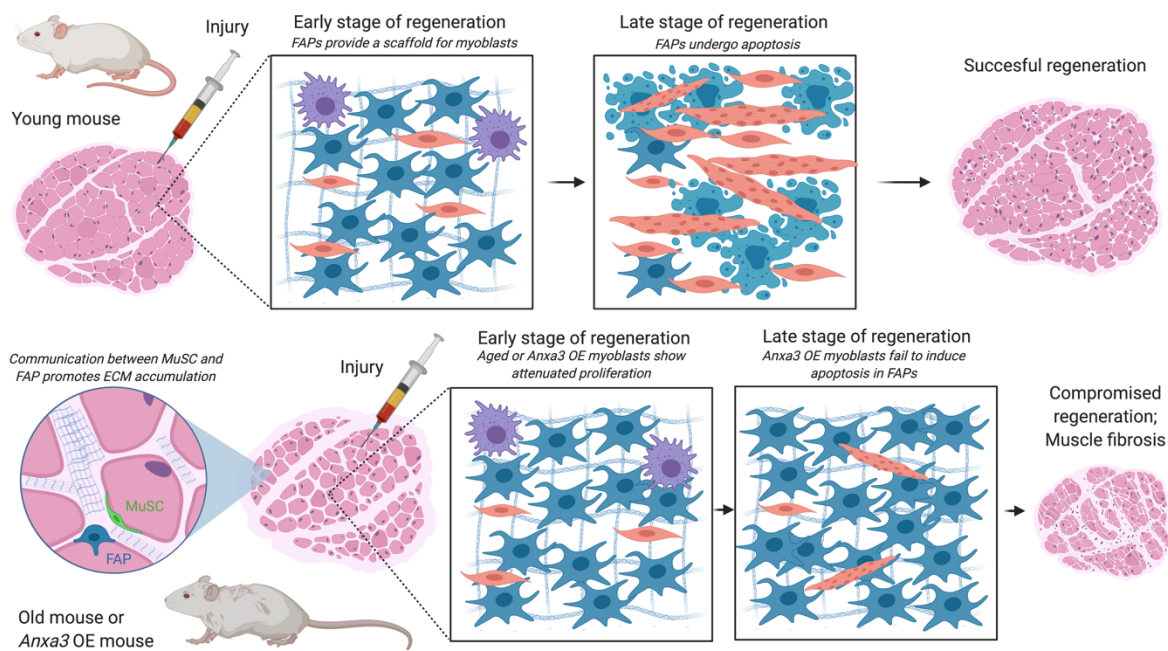


Figure 68. A graphical abstract: Annexin A3 marks a defective subpopulation of aged muscle stem cells. A number of *Anxa3*^{pos} qMuSCs increases with age, which leads to attenuated efficiency of muscle regeneration upon injury, as well as muscle fibrosis. (The figure was created using BioRender application.)

Anxa3 overexpression was found to trigger muscle fibrosis along with excessive expression of genes of the Collagen family. This is interesting since aged muscles are more prone to develop fibrosis, compared to young ones ²¹⁹. Fibrosis as a result of *Anxa3* overexpression may be caused due to increased Collagen expression by a subset of quiescent MuSCs. However, it remains to be clarified, whether the observed fibrosis originates from *Anxa3* OE qMuSCs, or is a byproduct of failed muscle regeneration. It is known, that fibro-adipogenic progenitor cells (FAPs) form a supporting ECM scaffold during early stages of muscle regeneration. These cells eventually differentiate into myofibroblasts and undergo apoptosis when new myofibers have been formed ¹⁷⁶. Should myofibers fail to develop due to MuSCs malfunction, this fibrotic scaffold may be retained.

Previous reports described communication between FAPs and MuSCs ⁹⁷. For example, it's been shown that Wnt signalling induces expression and secretion of Wisp1 by FAPs, which is consecutively sensed by MuSCs. Wisp1 was reported to control expansion and asymmetric division of MuSCs via the Akt pathway ⁹⁷. Strikingly, WISP1 expression decreases with age, therefore diminishing communication between FAPs and MuSCs, which may deteriorate muscle regeneration. So far, the flow of communication was unidirectional (from FAPs to qMuSCs), while the current work

provides evidence for communication in the other direction: from qMuSCs to FAPs. As shown in this dissertation, the concentration of FAPs increased in *Anxa3* OE muscles, giving rise to the hypothesis, that Annexin A3 is a secreted factor that conveys information between MuSCs and FAPs. Unlike Annexin A1, which could be secreted and then sensed by an FPR receptor (Formylpeptide Receptor) ²²⁰, the receptor for Annexin A3 is currently unknown. The *Fpr1* gene, which encodes the FPR receptor, was neither expressed in WT qMuSCs, nor in *Anxa3* OE qMuSCs (data not shown). The hypothesis, that ageing induces FAPs expansion via Annexin A3 signalling (initially secreted from the qMuSCs) and therefore increases ECM deposition, might explain increased muscle fibrosis with age. In this case, pharmaceutically targeting and eliminating *Anxa3*-expressing qMuSCs might not only improve the muscle regeneration, but may also decrease muscle fibrosis.

The next experimental step would be to investigate the communication between MuSCs and FAPs. As shown in this work, FAPs from *Anxa3* overexpressing MuSCs were already primed for increased proliferation. Upon co-culture, it became evident, that *Anxa3* OE myoblasts, in contrast to WT myoblasts, are unable to trigger apoptosis in FAPs. This implies, that myoblasts (or qMuSCs at an earlier time point) communicate with FAPs and fine tune their homeostasis. Such a communication is most likely mediated via vesicles, secreted by myoblasts (or qMuSCs) and sensed by FAPs. Therefore, it is crucial to investigate the differences in the secretome of WT and *Anxa3* OE myoblasts. To define such differences, cells could be shortly placed in culture, followed by analysis of culture supernatants by Mass Spectrometry. Although the results might be very useful for understanding communication between MuSCs and FAPs, there are technical challenges due to the scarceness of input material. Most likely, the concentration of MuSCs-secreted factors is very low, which is a problem for Mass Spectroscopic analysis. ELISA-based dot-assays might be an alternative to Mass Spectrometry, although analysis is limited to a set of known factors.

Annexin A3 might act as a messenger not only between MuSCs and FAPs, but also between MuSCs and endothelial cells. In a cancer model it has been shown, that *Anxa3* promotes angiogenesis ²¹⁵. While sufficient blood supply is *per se* beneficial for muscle homeostasis, an increased vessel area might also be a signature of disturbed vessel alignment ²²¹ or -less likely- be a consequence of ECM thickening. However, it is still not clear whether increased angiogenesis is a direct consequence of Annexin A3 secretion, or represents an indirect effect.

Preussner and Zhong recently showed that defective MuSCs give rise to a muscle rhabdomyosarcoma ¹⁰⁰. Since the rate of tumor development increases with age ²²², acquisition of *Anxa3* expression by a subset of quiescent MuSCs during aging may contribute to increased risk. Although *Anxa3* overexpression prevent cells from proliferating, arguing against a supportive role for tumor development, it is possible that *Anxa3* expressing cells undergo apoptosis or necrosis as a natural response to the cellular malfunction. Yet, if such cells acquired other mutations (for example, p53 mutation), enhanced tumor formation might happen ²²³.

Taken together, the data in the last chapter of this work demonstrates that expression of the *Anxa3* gene in quiescent MuSCs contributes to the deteriorating function of MuSC during ageing. Therefore, silencing of the *Anxa3* gene may attenuate the age-associated decrease in muscle regeneration capacity and enhanced fibrosis. The mechanistic details need to be elucidated by further research. Additional experiments (primarily co-cultures and secretome analysis) need to be performed to explore whether excessive muscle fibrosis is the direct consequence of *Anxa3* overexpression in MuSCs, or whether the phenotype is based on defective MuSCs-FAPs communication.

5. LIST OF ABBREVIATIONS

ASC – Adult Stem Cells
ATAC-seq – assay for Transposase Accessible Chromatin via sequencing
ATP – Adenosine Triphosphate
BSA – Bovine Serum Albumin
BTX – α -Bungarotoxin
cDNA – complementary DNA
CTX – Cardiotoxin
DA – Differential (chromatin) Accessibility
DAPI – 4',6-Diamidino-2-Phenylindole
DE – Differential Expression
DMEM – Dulbecco's Modified Eagle Medium
DNA – Deoxyribonucleic Acid
EDTA – Ethylenediaminetetraacetic Acid
EdU – 5-Ethynyl-2'-deoxyUridine
ESC – Embryonic Stem Cells
FACS – Fluorescence-Activated Cell Sorting
FCS – Fetal Calf Serum
FDP (muscle) – Flexor Digitorum Profundus (muscle)
FDR – False Discovery Rate, also called “adjusted p-value”
FISH – Fluorescent In-Situ Hybridization
GO – Gene Ontology database
GSEA – Gene Set Enrichment Analysis
H&E – Hematoxylin and Eosin
i.p. (injection) – intraperitoneal (injection)
IF – Immunofluorescence
KBW – (injection) per kg of body weight
LFC – Log-Fold-Change
MAST – Model-based Analysis of Single Cell Transcriptomics (R Package)
MeDIP-seq - Methylated DNA immunoprecipitation coupled with next-generation sequencing
MRI – Magnetic Resonance Imaging
mRNA – messenger RNA
MuSCs – Muscle Stem Cells, also called satellite cells
NGS – Next Generation Sequencing
NMJ – Neuromuscular Junction
PBS – Phosphate-Buffered Saline
PCA – Principal Component Analysis
PFA – Paraformaldehyde
QC – Quality Check
qMuSCs – quiescent Muscle Stem Cells
RIN – RNA Integrity Number
RNA – Ribonucleic Acid
RNA-seq – RNA sequencing
(r)tTA – (reverse) tetracycline-controlled Transactivator protein
RT-qPCR – Reverse Transcription quantitative Polymerase Chain Reaction
scATAC-seq – single-cell Assay for Transposase Accessible Chromatin via sequencing
scRNA-seq – single-cell RNA-sequencing
SDS PAGE – Sodium Dodecyl Sulfate Polyacrylamide Gel Electrophoresis
shRNA – short hairpin RNA or small hairpin RNA
STRING - Search Tool for the Retrieval of Interacting Genes/Proteins
t-SNE – t-distributed Stochastic Neighbor Embedding
TA (muscle) – Tibialis Anterior (muscle)
TAC – Traverse Aortic Constriction
TBST – Tris-Buffered Saline with Tween 20
TetO – Tetracyclin responsible element Operator
UMAP – Uniform Manifold Approximation and Projection
WT – wild type

6. REFERENCES

- 1 Komin, N. S., A. How to address cellular heterogeneity by distribution biology. *Current Opinion in Systems Biology* **3** (2017).
- 2 Ellegren, H. Comparative genomics and the study of evolution by natural selection. *Mol Ecol* **17**, 4586-4596, doi:10.1111/j.1365-294X.2008.03954.x (2008).
- 3 Barton, N. H. & Keightley, P. D. Understanding quantitative genetic variation. *Nat Rev Genet* **3**, 11-21, doi:10.1038/nrg700 (2002).
- 4 Ciuffi, A. & Bushman, F. D. Retroviral DNA integration: HIV and the role of LEDGF/p75. *Trends Genet* **22**, 388-395, doi:10.1016/j.tig.2006.05.006 (2006).
- 5 Basu, A. K. DNA Damage, Mutagenesis and Cancer. *Int J Mol Sci* **19**, doi:10.3390/ijms19040970 (2018).
- 6 Grosovsky, A. J. Radiation-induced mutations in unirradiated DNA. *Proc Natl Acad Sci U S A* **96**, 5346-5347, doi:10.1073/pnas.96.10.5346 (1999).
- 7 Das, S. K. Integrating transcriptome and epigenome: putting together the pieces of the type 2 diabetes pathogenesis puzzle. *Diabetes* **63**, 2901-2903, doi:10.2337/db14-0757 (2014).
- 8 Handy, D. E., Castro, R. & Loscalzo, J. Epigenetic modifications: basic mechanisms and role in cardiovascular disease. *Circulation* **123**, 2145-2156, doi:10.1161/CIRCULATIONAHA.110.956839 (2011).
- 9 Karijovich, J., Kantartzis, A. & Yu, Y. T. RNA modifications: a mechanism that modulates gene expression. *Methods Mol Biol* **629**, 1-19, doi:10.1007/978-1-60761-657-3_1 (2010).
- 10 Rodnina, M. V. The ribosome in action: Tuning of translational efficiency and protein folding. *Protein Sci* **25**, 1390-1406, doi:10.1002/pro.2950 (2016).
- 11 Nalivaeva, N. N. & Turner, A. J. Post-translational modifications of proteins: Acetylcholinesterase as a model system. *Proteomics* **1**, 735-747, doi:10.1002/1615-9861(200106)1:6<735::Aid-prot735>3.0.Co;2-8 (2001).
- 12 Fan, J. *et al.* Linking transcriptional and genetic tumor heterogeneity through allele analysis of single-cell RNA-seq data. *Genome Res* **28**, 1217-1227, doi:10.1101/gr.228080.117 (2018).
- 13 Brancini, G. T. P., Ferreira, M. E. S., Rangel, D. E. N. & Braga, G. U. L. Combining Transcriptomics and Proteomics Reveals Potential Post-transcriptional Control of Gene Expression After Light Exposure in *Metarhizium acridum*. *G3 (Bethesda)* **9**, 2951-2961, doi:10.1534/g3.119.400430 (2019).
- 14 Budnik, B., Levy, E., Harmange, G. & Slavov, N. SCoPE-MS: mass spectrometry of single mammalian cells quantifies proteome heterogeneity during cell differentiation. *Genome Biol* **19**, 161, doi:10.1186/s13059-018-1547-5 (2018).
- 15 De Vito, C., Sarker, D., Ross, P., Heaton, N. & Quaglia, A. Histological heterogeneity in primary and metastatic classic combined hepatocellular-cholangiocarcinoma: a case series. *Virchows Arch* **471**, 619-629, doi:10.1007/s00428-017-2196-x (2017).
- 16 Ehrlich, P. Beiträge zur Kenntniss der Anilinfärbungen und ihre Verwendung in der mikroskopischen Technik. *Archiv für Mikroskopische Anatomie* (1877).
- 17 Fischer, A. H., Jacobson, K. A., Rose, J. & Zeller, R. Hematoxylin and eosin staining of tissue and cell sections. *CSH Protoc* **2008**, pdb prot4986, doi:10.1101/pdb.prot4986 (2008).

- 18 Mao, H. *et al.* The use of Masson's trichrome staining, second harmonic imaging and two-photon excited fluorescence of collagen in distinguishing intestinal tuberculosis from Crohn's disease. *Colorectal Dis* **18**, 1172-1178, doi:10.1111/codi.13400 (2016).
- 19 Kinkel, A. D. *et al.* Oil red-O stains non-adipogenic cells: a precautionary note. *Cytotechnology* **46**, 49-56, doi:10.1007/s10616-004-3903-4 (2004).
- 20 Balan, I. S., Fiskum, G. & Kristian, T. Visualization and quantification of NAD(H) in brain sections by a novel histo-enzymatic nitrotetrazolium blue staining technique. *Brain Res* **1316**, 112-119, doi:10.1016/j.brainres.2009.12.042 (2010).
- 21 Matos, L. L., Trufelli, D. C., de Matos, M. G. & da Silva Pinhal, M. A. Immunohistochemistry as an important tool in biomarkers detection and clinical practice. *Biomark Insights* **5**, 9-20, doi:10.4137/bmi.s2185 (2010).
- 22 Ditommaso, S., Giacomuzzi, M., Gentile, M. & Zotti, C. M. Antibody detection and cross-reactivity among species and serogroups of *Legionella* by indirect immunofluorescence test. *J Microbiol Methods* **75**, 350-353, doi:10.1016/j.mimet.2008.06.002 (2008).
- 23 Bayani, J. & Squire, J. A. Fluorescence in situ Hybridization (FISH). *Curr Protoc Cell Biol* **Chapter 22**, Unit 22 24, doi:10.1002/0471143030.cb2204s23 (2004).
- 24 Altschuler, S. J. & Wu, L. F. Cellular heterogeneity: do differences make a difference? *Cell* **141**, 559-563, doi:10.1016/j.cell.2010.04.033 (2010).
- 25 Griffiths, J. A., Scialdone, A. & Marioni, J. C. Using single-cell genomics to understand developmental processes and cell fate decisions. *Mol Syst Biol* **14**, e8046, doi:10.15252/msb.20178046 (2018).
- 26 Goldstein, L. D. *et al.* Massively parallel nanowell-based single-cell gene expression profiling. *BMC Genomics* **18**, 519, doi:10.1186/s12864-017-3893-1 (2017).
- 27 Baran-Gale, J., Chandra, T. & Kirschner, K. Experimental design for single-cell RNA sequencing. *Brief Funct Genomics* **17**, 233-239, doi:10.1093/bfpg/ely035 (2018).
- 28 Reyes, M., Billman, K., Hacohen, N. & Blainey, P. C. Simultaneous profiling of gene expression and chromatin accessibility in single cells. *Adv Biosyst* **3**, doi:10.1002/adbi.201900065 (2019).
- 29 Cao, J. *et al.* Joint profiling of chromatin accessibility and gene expression in thousands of single cells. *Science* **361**, 1380-1385, doi:10.1126/science.aau0730 (2018).
- 30 Clark, S. J. *et al.* scNMT-seq enables joint profiling of chromatin accessibility DNA methylation and transcription in single cells. *Nat Commun* **9**, 781, doi:10.1038/s41467-018-03149-4 (2018).
- 31 Singh, M. *et al.* High-throughput targeted long-read single cell sequencing reveals the clonal and transcriptional landscape of lymphocytes. *Nat Commun* **10**, 3120, doi:10.1038/s41467-019-11049-4 (2019).
- 32 Tabula Muris, C. *et al.* Single-cell transcriptomics of 20 mouse organs creates a Tabula Muris. *Nature* **562**, 367-372, doi:10.1038/s41586-018-0590-4 (2018).
- 33 Regev, A. *et al.* The Human Cell Atlas. *Elife* **6**, doi:10.7554/eLife.27041 (2017).
- 34 Zakrzewski, W., Dobrzynski, M., Szymonowicz, M. & Rybak, Z. Stem cells: past, present, and future. *Stem Cell Res Ther* **10**, 68, doi:10.1186/s13287-019-1165-5 (2019).
- 35 Hailesellasse Sene, K. *et al.* Gene function in early mouse embryonic stem cell differentiation. *BMC Genomics* **8**, 85, doi:10.1186/1471-2164-8-85 (2007).
- 36 Armstrong, L. Epigenetic control of embryonic stem cell differentiation. *Stem Cell Rev Rep* **8**, 67-77, doi:10.1007/s12015-011-9300-4 (2012).

- 37 Berdasco, M. & Esteller, M. DNA methylation in stem cell renewal and multipotency. *Stem Cell Res Ther* **2**, 42, doi:10.1186/scrt83 (2011).
- 38 Sheaffer, K. L. *et al.* DNA methylation is required for the control of stem cell differentiation in the small intestine. *Genes Dev* **28**, 652-664, doi:10.1101/gad.230318.113 (2014).
- 39 Perez-Silos, V., Camacho-Morales, A. & Fuentes-Mera, L. Mesenchymal Stem Cells Subpopulations: Application for Orthopedic Regenerative Medicine. *Stem Cells Int* **2016**, 3187491, doi:10.1155/2016/3187491 (2016).
- 40 Jurecic, R. Hematopoietic Stem Cell Heterogeneity. *Adv Exp Med Biol* **1169**, 195-211, doi:10.1007/978-3-030-24108-7_10 (2019).
- 41 French, R. & Tornillo, G. Heterogeneity of Mammary Stem Cells. *Adv Exp Med Biol* **1169**, 119-140, doi:10.1007/978-3-030-24108-7_7 (2019).
- 42 Moossavi, S. Heterogeneity of the level of activity of Igr5+ intestinal stem cells. *Int J Mol Cell Med* **3**, 216-224 (2014).
- 43 Lyons, F. G. & Mattei, T. A. Sources, Identification, and Clinical Implications of Heterogeneity in Human Umbilical Cord Stem Cells. *Adv Exp Med Biol* **1169**, 243-256, doi:10.1007/978-3-030-24108-7_13 (2019).
- 44 Jung, C., Rafnsson, A., Shemyakin, A., Bohm, F. & Pernow, J. Different subpopulations of endothelial progenitor cells and circulating apoptotic progenitor cells in patients with vascular disease and diabetes. *Int J Cardiol* **143**, 368-372, doi:10.1016/j.ijcard.2009.03.075 (2010).
- 45 Rushing, G. V., Bollig, M. K. & Ihrie, R. A. Heterogeneity of Neural Stem Cells in the Ventricular-Subventricular Zone. *Adv Exp Med Biol* **1169**, 1-30, doi:10.1007/978-3-030-24108-7_1 (2019).
- 46 Tosun, M., Semerci, F. & Maletic-Savatic, M. Heterogeneity of Stem Cells in the Hippocampus. *Adv Exp Med Biol* **1169**, 31-53, doi:10.1007/978-3-030-24108-7_2 (2019).
- 47 Kubota, H. Heterogeneity of Spermatogonial Stem Cells. *Adv Exp Med Biol* **1169**, 225-242, doi:10.1007/978-3-030-24108-7_12 (2019).
- 48 Cho, D. S. & Doles, J. D. Skeletal Muscle Progenitor Cell Heterogeneity. *Adv Exp Med Biol* **1169**, 179-193, doi:10.1007/978-3-030-24108-7_9 (2019).
- 49 Lynch, T. J., Ievlev, V. & Parekh, K. R. Heterogeneity of Pulmonary Stem Cells. *Adv Exp Med Biol* **1169**, 95-117, doi:10.1007/978-3-030-24108-7_6 (2019).
- 50 Brandenburger, M. & Kruse, C. Heterogeneity of Sweat Gland Stem Cells. *Adv Exp Med Biol* **1169**, 55-62, doi:10.1007/978-3-030-24108-7_3 (2019).
- 51 Sato, K. Heterogeneity of Stem Cells in the Human Vocal Fold Mucosa. *Adv Exp Med Biol* **1169**, 63-80, doi:10.1007/978-3-030-24108-7_4 (2019).
- 52 Bhartiya, D., Patel, H. & Sharma, D. Heterogeneity of Stem Cells in the Ovary. *Adv Exp Med Biol* **1169**, 213-223, doi:10.1007/978-3-030-24108-7_11 (2019).
- 53 Robert, L., Labat-Robert, J. & Robert, A. M. Genetic, epigenetic and posttranslational mechanisms of aging. *Biogerontology* **11**, 387-399, doi:10.1007/s10522-010-9262-y (2010).
- 54 Harman, D. The aging process: major risk factor for disease and death. *Proc Natl Acad Sci U S A* **88**, 5360-5363, doi:10.1073/pnas.88.12.5360 (1991).
- 55 Baird, D. T. *et al.* Fertility and ageing. *Hum Reprod Update* **11**, 261-276, doi:10.1093/humupd/dmi006 (2005).

- 56 Marzetti, E., Lees, H. A., Wohlgemuth, S. E. & Leeuwenburgh, C. Sarcopenia of aging: underlying cellular mechanisms and protection by calorie restriction. *Biofactors* **35**, 28-35, doi:10.1002/biof.5 (2009).
- 57 Costopoulos, C., Liew, T. V. & Bennett, M. Ageing and atherosclerosis: Mechanisms and therapeutic options. *Biochem Pharmacol* **75**, 1251-1261, doi:10.1016/j.bcp.2007.10.006 (2008).
- 58 Brayne, C. & Miller, B. Dementia and aging populations-A global priority for contextualized research and health policy. *PLoS Med* **14**, e1002275, doi:10.1371/journal.pmed.1002275 (2017).
- 59 Rattan, S. I. Aging is not a disease: implications for intervention. *Aging Dis* **5**, 196-202, doi:10.14336/AD.2014.0500196 (2014).
- 60 Bulterijs, S., Hull, R. S., Bjork, V. C. & Roy, A. G. It is time to classify biological aging as a disease. *Front Genet* **6**, 205, doi:10.3389/fgene.2015.00205 (2015).
- 61 Lopez-Otin, C., Blasco, M. A., Partridge, L., Serrano, M. & Kroemer, G. The hallmarks of aging. *Cell* **153**, 1194-1217, doi:10.1016/j.cell.2013.05.039 (2013).
- 62 Vijg, J. & Suh, Y. Genome instability and aging. *Annu Rev Physiol* **75**, 645-668, doi:10.1146/annurev-physiol-030212-183715 (2013).
- 63 Shay, J. W. & Wright, W. E. Hayflick, his limit, and cellular ageing. *Nat Rev Mol Cell Biol* **1**, 72-76, doi:10.1038/35036093 (2000).
- 64 Pal, S. & Tyler, J. K. Epigenetics and aging. *Sci Adv* **2**, e1600584, doi:10.1126/sciadv.1600584 (2016).
- 65 Klaips, C. L., Jayaraj, G. G. & Hartl, F. U. Pathways of cellular proteostasis in aging and disease. *J Cell Biol* **217**, 51-63, doi:10.1083/jcb.201709072 (2018).
- 66 Johnson, S. C. Nutrient Sensing, Signaling and Ageing: The Role of IGF-1 and mTOR in Ageing and Age-Related Disease. *Subcell Biochem* **90**, 49-97, doi:10.1007/978-981-13-2835-0_3 (2018).
- 67 Haas, R. H. Mitochondrial Dysfunction in Aging and Diseases of Aging. *Biology (Basel)* **8**, doi:10.3390/biology8020048 (2019).
- 68 van Deursen, J. M. The role of senescent cells in ageing. *Nature* **509**, 439-446, doi:10.1038/nature13193 (2014).
- 69 Ahmed, A. S., Sheng, M. H., Wasnik, S., Baylink, D. J. & Lau, K. W. Effect of aging on stem cells. *World J Exp Med* **7**, 1-10, doi:10.5493/wjem.v7.i1.1 (2017).
- 70 Chakkalakal, J. V., Jones, K. M., Basson, M. A. & Brack, A. S. The aged niche disrupts muscle stem cell quiescence. *Nature* **490**, 355-360, doi:10.1038/nature11438 (2012).
- 71 Thorley, M. *et al.* Changes in Communication between Muscle Stem Cells and their Environment with Aging. *J Neuromuscul Dis* **2**, 205-217, doi:10.3233/JND-150097 (2015).
- 72 Anderson, R. H., Razavi, R. & Taylor, A. M. Cardiac anatomy revisited. *J Anat* **205**, 159-177, doi:10.1111/j.0021-8782.2004.00330.x (2004).
- 73 Xin, M., Olson, E. N. & Bassel-Duby, R. Mending broken hearts: cardiac development as a basis for adult heart regeneration and repair. *Nat Rev Mol Cell Biol* **14**, 529-541, doi:10.1038/nrm3619 (2013).
- 74 Golob, M., Moss, R. L. & Chesler, N. C. Cardiac tissue structure, properties, and performance: a materials science perspective. *Ann Biomed Eng* **42**, 2003-2013, doi:10.1007/s10439-014-1071-z (2014).
- 75 Medical gallery of Blausen Medical 2014. *WikiJournal of Medicine* **1**, doi:10.15347/wjm/2014.010 (2014).

- 76 Burchfield, J. S., Xie, M. & Hill, J. A. Pathological ventricular remodeling: mechanisms: part 1 of 2. *Circulation* **128**, 388-400, doi:10.1161/CIRCULATIONAHA.113.001878 (2013).
- 77 Suboc, T. <<https://www.merckmanuals.com/en-pr/professional/cardiovascular-disorders/cardiomyopathies/overview-of-cardiomyopathies>> (2019).
- 78 Thygesen, K. *et al.* Fourth universal definition of myocardial infarction (2018). *Eur Heart J* **40**, 237-269, doi:10.1093/eurheartj/ehy462 (2019).
- 79 Gui, L., Liu, B. & Lv, G. Hypoxia induces autophagy in cardiomyocytes via a hypoxia-inducible factor 1-dependent mechanism. *Exp Ther Med* **11**, 2233-2239, doi:10.3892/etm.2016.3190 (2016).
- 80 Mathiyalagan, P., Keating, S. T., Du, X. J. & El-Osta, A. Chromatin modifications remodel cardiac gene expression. *Cardiovasc Res* **103**, 7-16, doi:10.1093/cvr/cvu122 (2014).
- 81 Richardson, W. J., Clarke, S. A., Quinn, T. A. & Holmes, J. W. Physiological Implications of Myocardial Scar Structure. *Compr Physiol* **5**, 1877-1909, doi:10.1002/cphy.c140067 (2015).
- 82 Bergmann, O. *et al.* Identification of cardiomyocyte nuclei and assessment of ploidy for the analysis of cell turnover. *Exp Cell Res* **317**, 188-194, doi:10.1016/j.yexcr.2010.08.017 (2011).
- 83 Bensley, J. G., De Matteo, R., Harding, R. & Black, M. J. Three-dimensional direct measurement of cardiomyocyte volume, nuclearity, and ploidy in thick histological sections. *Sci Rep* **6**, 23756, doi:10.1038/srep23756 (2016).
- 84 Frontera, W. R. & Ochala, J. Skeletal muscle: a brief review of structure and function. *Calcif Tissue Int* **96**, 183-195, doi:10.1007/s00223-014-9915-y (2015).
- 85 Straka, T. *et al.* Postnatal Development and Distribution of Sympathetic Innervation in Mouse Skeletal Muscle. *Int J Mol Sci* **19**, doi:10.3390/ijms19071935 (2018).
- 86 Braun, T. & Arnold, H. H. Myf-5 and myoD genes are activated in distinct mesenchymal stem cells and determine different skeletal muscle cell lineages. *EMBO J* **15**, 310-318 (1996).
- 87 Gunther, S. *et al.* Myf5-positive satellite cells contribute to Pax7-dependent long-term maintenance of adult muscle stem cells. *Cell Stem Cell* **13**, 590-601, doi:10.1016/j.stem.2013.07.016 (2013).
- 88 Baghdadi, M. B. & Tajbakhsh, S. Regulation and phylogeny of skeletal muscle regeneration. *Dev Biol* **433**, 200-209, doi:10.1016/j.ydbio.2017.07.026 (2018).
- 89 Liu, J. *et al.* Current Methods for Skeletal Muscle Tissue Repair and Regeneration. *Biomed Res Int* **2018**, 1984879, doi:10.1155/2018/1984879 (2018).
- 90 Garcia-Prat, L. & Munoz-Canoves, P. Aging, metabolism and stem cells: Spotlight on muscle stem cells. *Mol Cell Endocrinol* **445**, 109-117, doi:10.1016/j.mce.2016.08.021 (2017).
- 91 Kuang, S., Kuroda, K., Le Grand, F. & Rudnicki, M. A. Asymmetric self-renewal and commitment of satellite stem cells in muscle. *Cell* **129**, 999-1010, doi:10.1016/j.cell.2007.03.044 (2007).
- 92 Conboy, I. M. *et al.* Rejuvenation of aged progenitor cells by exposure to a young systemic environment. *Nature* **433**, 760-764, doi:10.1038/nature03260 (2005).
- 93 Gorbunova, V., Seluanov, A., Mao, Z. & Hine, C. Changes in DNA repair during aging. *Nucleic Acids Res* **35**, 7466-7474, doi:10.1093/nar/gkm756 (2007).

- 94 Rossi, D. J. *et al.* Deficiencies in DNA damage repair limit the function of haematopoietic stem cells with age. *Nature* **447**, 725-729, doi:10.1038/nature05862 (2007).
- 95 Zhou, J. *et al.* Elevated H3K27ac in aged skeletal muscle leads to increase in extracellular matrix and fibrogenic conversion of muscle satellite cells. *Aging Cell* **18**, e12996, doi:10.1111/ace1.12996 (2019).
- 96 Blau, H. M., Cosgrove, B. D. & Ho, A. T. The central role of muscle stem cells in regenerative failure with aging. *Nat Med* **21**, 854-862, doi:10.1038/nm.3918 (2015).
- 97 Lukjanenko, L. *et al.* Aging Disrupts Muscle Stem Cell Function by Impairing Matricellular WISP1 Secretion from Fibro-Adipogenic Progenitors. *Cell Stem Cell* **24**, 433-446 e437, doi:10.1016/j.stem.2018.12.014 (2019).
- 98 Shea, K. L. *et al.* Sprouty1 regulates reversible quiescence of a self-renewing adult muscle stem cell pool during regeneration. *Cell Stem Cell* **6**, 117-129, doi:10.1016/j.stem.2009.12.015 (2010).
- 99 Sousa-Victor, P., Perdiguero, E. & Munoz-Canoves, P. Geroconversion of aged muscle stem cells under regenerative pressure. *Cell Cycle* **13**, 3183-3190, doi:10.4161/15384101.2014.965072 (2014).
- 100 Preussner, J. *et al.* Oncogenic Amplification of Zygotic Dux Factors in Regenerating p53-Deficient Muscle Stem Cells Defines a Molecular Cancer Subtype. *Cell Stem Cell* **23**, 794-805 e794, doi:10.1016/j.stem.2018.10.011 (2018).
- 101 Wynick, D. *et al.* Galanin regulates prolactin release and lactotroph proliferation. *Proc Natl Acad Sci U S A* **95**, 12671-12676, doi:10.1073/pnas.95.21.12671 (1998).
- 102 Pope, R. J., Holmes, F. E., Kerr, N. C. & Wynick, D. Characterisation of the nociceptive phenotype of suppressible galanin overexpressing transgenic mice. *Mol Pain* **6**, 67, doi:10.1186/1744-8069-6-67 (2010).
- 103 Lepper, C. & Fan, C. M. Inducible lineage tracing of Pax7-descendant cells reveals embryonic origin of adult satellite cells. *Genesis* **48**, 424-436, doi:10.1002/dvg.20630 (2010).
- 104 Buenrostro, J. D., Wu, B., Chang, H. Y. & Greenleaf, W. J. ATAC-seq: A Method for Assaying Chromatin Accessibility Genome-Wide. *Curr Protoc Mol Biol* **109**, 21 29 21-21 29 29, doi:10.1002/0471142727.mb2129s109 (2015).
- 105 Chen, X., Miragaia, R. J., Natarajan, K. N. & Teichmann, S. A. A rapid and robust method for single cell chromatin accessibility profiling. *Nat Commun* **9**, 5345, doi:10.1038/s41467-018-07771-0 (2018).
- 106 Meadows, E., Cho, J. H., Flynn, J. M. & Klein, W. H. Myogenin regulates a distinct genetic program in adult muscle stem cells. *Dev Biol* **322**, 406-414, doi:10.1016/j.ydbio.2008.07.024 (2008).
- 107 Dobin, A. & Gingeras, T. R. Mapping RNA-seq Reads with STAR. *Curr Protoc Bioinformatics* **51**, 11 14 11-19, doi:10.1002/0471250953.bi1114s51 (2015).
- 108 Lun, A. T., Bach, K. & Marioni, J. C. Pooling across cells to normalize single-cell RNA sequencing data with many zero counts. *Genome Biol* **17**, 75, doi:10.1186/s13059-016-0947-7 (2016).
- 109 Costa-Silva, J., Domingues, D. & Lopes, F. M. RNA-Seq differential expression analysis: An extended review and a software tool. *Plos One* **12**, e0190152, doi:10.1371/journal.pone.0190152 (2017).
- 110 Conesa, A. *et al.* A survey of best practices for RNA-seq data analysis. *Genome Biol* **17**, 13, doi:10.1186/s13059-016-0881-8 (2016).

- 111 Kim, H. Y. Statistical notes for clinical researchers: Type I and type II errors in statistical decision. *Restor Dent Endod* **40**, 249-252, doi:10.5395/rde.2015.40.3.249 (2015).
- 112 Xie, C. *et al.* KOBAS 2.0: a web server for annotation and identification of enriched pathways and diseases. *Nucleic Acids Res* **39**, W316-322, doi:10.1093/nar/gkr483 (2011).
- 113 Becht, E. *et al.* Dimensionality reduction for visualizing single-cell data using UMAP. *Nat Biotechnol*, doi:10.1038/nbt.4314 (2018).
- 114 Finak, G. *et al.* MAST: a flexible statistical framework for assessing transcriptional changes and characterizing heterogeneity in single-cell RNA sequencing data. *Genome Biol* **16**, 278, doi:10.1186/s13059-015-0844-5 (2015).
- 115 Zheng, X. *et al.* A Notch-independent mechanism contributes to the induction of Hes1 gene expression in response to hypoxia in P19 cells. *Exp Cell Res* **358**, 129-139, doi:10.1016/j.yexcr.2017.06.006 (2017).
- 116 Sperandio, S. *et al.* The transcription factor Egr1 regulates the HIF-1alpha gene during hypoxia. *Mol Carcinog* **48**, 38-44, doi:10.1002/mc.20454 (2009).
- 117 Ramskold, D. *et al.* Full-length mRNA-Seq from single-cell levels of RNA and individual circulating tumor cells. *Nat Biotechnol* **30**, 777-782, doi:10.1038/nbt.2282 (2012).
- 118 Senyo, S. E. *et al.* Mammalian heart renewal by pre-existing cardiomyocytes. *Nature* **493**, 433-436, doi:10.1038/nature11682 (2013).
- 119 deAlmeida, A. C., van Oort, R. J. & Wehrens, X. H. Transverse aortic constriction in mice. *J Vis Exp*, doi:10.3791/1729 (2010).
- 120 Semenza, G. L. Hypoxia-inducible factor 1 and cardiovascular disease. *Annu Rev Physiol* **76**, 39-56, doi:10.1146/annurev-physiol-021113-170322 (2014).
- 121 Tarpey, T. Linear Transformations and the k-Means Clustering Algorithm: Applications to Clustering Curves. *Am Stat* **61**, 34-40, doi:10.1198/000313007X171016 (2007).
- 122 Thomas, A. *et al.* Hypoxia-inducible factor prolyl hydroxylase 1 (PHD1) deficiency promotes hepatic steatosis and liver-specific insulin resistance in mice. *Sci Rep* **6**, 24618, doi:10.1038/srep24618 (2016).
- 123 Shibuya, M. Vascular Endothelial Growth Factor (VEGF) and Its Receptor (VEGFR) Signaling in Angiogenesis: A Crucial Target for Anti- and Pro-Angiogenic Therapies. *Genes Cancer* **2**, 1097-1105, doi:10.1177/1947601911423031 (2011).
- 124 Hernando-Herraez, I. *et al.* Ageing affects DNA methylation drift and transcriptional cell-to-cell variability in mouse muscle stem cells. *Nat Commun* **10**, 4361, doi:10.1038/s41467-019-12293-4 (2019).
- 125 Lagha, M. *et al.* Itm2a Is a Pax3 Target Gene, Expressed at Sites of Skeletal Muscle Formation In Vivo. *Plos One* **8**, doi:ARTN e6314310.1371/journal.pone.0063143 (2013).
- 126 Jorgensen, L. H. *et al.* SPARC Interacts with Actin in Skeletal Muscle in Vitro and in Vivo. *Am J Pathol* **187**, 457-474, doi:10.1016/j.ajpath.2016.10.013 (2017).
- 127 Galaviz-Hernandez, C. *et al.* Plac8 and Plac9, novel placental-enriched genes identified through microarray analysis. *Gene* **309**, 81-89, doi:10.1016/s0378-1119(03)00508-0 (2003).
- 128 Ouyang, C. *et al.* Placenta-specific 9, a putative secretory protein, induces G2/M arrest and inhibits the proliferation of human embryonic hepatic cells. *Biosci Rep* **38**, doi:10.1042/BSR20180820 (2018).

- 129 Lang, R. *et al.* Physiology, signaling, and pharmacology of galanin peptides and receptors: three decades of emerging diversity. *Pharmacol Rev* **67**, 118-175, doi:10.1124/pr.112.006536 (2015).
- 130 Fang, P. *et al.* Regulatory effects of galanin system on development of several age-related chronic diseases. *Exp Gerontol* **95**, 88-97, doi:10.1016/j.exger.2017.04.009 (2017).
- 131 Xu, X. F. *et al.* Galanin and its receptor system promote the repair of injured sciatic nerves in diabetic rats. *Neural Regen Res* **11**, 1517-1526, doi:10.4103/1673-5374.191228 (2016).
- 132 Tong, M. *et al.* ANXA3/JNK Signaling Promotes Self-Renewal and Tumor Growth, and Its Blockade Provides a Therapeutic Target for Hepatocellular Carcinoma. *Stem Cell Reports* **5**, 45-59, doi:10.1016/j.stemcr.2015.05.013 (2015).
- 133 Pan, Q. Z. *et al.* Annexin A3 as a Potential Target for Immunotherapy of Liver Cancer Stem-Like Cells. *Stem Cells* **33**, 354-366, doi:10.1002/stem.1850 (2015).
- 134 Wang, K. & Li, J. S. Overexpression of ANXA3 is an independent prognostic indicator in gastric cancer and its depletion suppresses cell proliferation and tumor growth. *Oncotarget* **7**, 86972-86984, doi:10.18632/oncotarget.13493 (2016).
- 135 Liu, Y. F., Liu, Q. Q., Zhang, Y. H. & Qiu, J. H. Annexin A3 Knockdown Suppresses Lung Adenocarcinoma. *Anal Cell Pathol (Amst)* **2016**, 4131403, doi:10.1155/2016/4131403 (2016).
- 136 Du, R. *et al.* Downregulation of annexin A3 inhibits tumor metastasis and decreases drug resistance in breast cancer. *Cell Death Dis* **9**, 126, doi:10.1038/s41419-017-0143-z (2018).
- 137 Giordani, L. *et al.* High-Dimensional Single-Cell Cartography Reveals Novel Skeletal Muscle-Resident Cell Populations. *Mol Cell* **74**, 609-621 e606, doi:10.1016/j.molcel.2019.02.026 (2019).
- 138 Wang, J., Chen, W., Wei, W. & Lou, J. Oncogene TUBA1C promotes migration and proliferation in hepatocellular carcinoma and predicts a poor prognosis. *Oncotarget* **8**, 96215-96224, doi:10.18632/oncotarget.21894 (2017).
- 139 Salameh, A. *et al.* PRUNE2 is a human prostate cancer suppressor regulated by the intronic long noncoding RNA PCA3. *Proc Natl Acad Sci U S A* **112**, 8403-8408, doi:10.1073/pnas.1507882112 (2015).
- 140 Chen, C., Zhang, J., Ling, J., Du, Y. & Hou, Y. Nkd2 promotes the differentiation of dental follicle stem/progenitor cells into osteoblasts. *Int J Mol Med* **42**, 2403-2414, doi:10.3892/ijmm.2018.3822 (2018).
- 141 Varga, A. *et al.* RAF1/BRAF dimerization integrates the signal from RAS to ERK and ROKalpha. *Sci Signal* **10**, doi:10.1126/scisignal.aai8482 (2017).
- 142 Wang, D. *et al.* BIRC3 is a novel driver of therapeutic resistance in Glioblastoma. *Sci Rep* **6**, 21710, doi:10.1038/srep21710 (2016).
- 143 Ghil, S., McCoy, K. L. & Hepler, J. R. Regulator of G protein signaling 2 (RGS2) and RGS4 form distinct G protein-dependent complexes with protease activated-receptor 1 (PAR1) in live cells. *Plos One* **9**, e95355, doi:10.1371/journal.pone.0095355 (2014).
- 144 Ma, G. *et al.* MiR-206, a key modulator of skeletal muscle development and disease. *Int J Biol Sci* **11**, 345-352, doi:10.7150/ijbs.10921 (2015).
- 145 Fujita, M. *et al.* Filamin C plays an essential role in the maintenance of the structural integrity of cardiac and skeletal muscles, revealed by the medaka mutant zacro. *Dev Biol* **361**, 79-89, doi:10.1016/j.ydbio.2011.10.008 (2012).

- 146 Bennett, R. D. & Strehler, E. E. Calmodulin-like protein enhances myosin-10 translation. *Biochem Biophys Res Commun* **369**, 654-659, doi:10.1016/j.bbrc.2008.02.056 (2008).
- 147 Liu, L. & Pilch, P. F. PTRF/Cavin-1 promotes efficient ribosomal RNA transcription in response to metabolic challenges. *Elife* **5**, doi:10.7554/eLife.17508 (2016).
- 148 Monticone, M. *et al.* The nuclear genes Mtf1 and Dufd1 regulate mitochondrial dynamic and cellular respiration. *J Cell Physiol* **225**, 767-776, doi:10.1002/jcp.22279 (2010).
- 149 Covelo-Molares, H., Bartosovic, M. & Vanacova, S. RNA methylation in nuclear pre-mRNA processing. *Wiley Interdiscip Rev RNA* **9**, e1489, doi:10.1002/wrna.1489 (2018).
- 150 John, K., Alla, V., Meier, C. & Putzer, B. M. GRAMD4 mimics p53 and mediates the apoptotic function of p73 at mitochondria. *Cell Death Differ* **18**, 874-886, doi:10.1038/cdd.2010.153 (2011).
- 151 Yang, L. *et al.* Histone demethylase KDM6B has an anti-tumorigenic function in neuroblastoma by promoting differentiation. *Oncogenesis* **8**, 3, doi:10.1038/s41389-018-0112-0 (2019).
- 152 Guo, G. *et al.* FRAT1 expression and its correlation with pathologic grade, proliferation, and apoptosis in human astrocytomas. *Med Oncol* **28**, 1-6, doi:10.1007/s12032-009-9402-x (2011).
- 153 Bauer, R. *et al.* Inhibition of collagen XVI expression reduces glioma cell invasiveness. *Cell Physiol Biochem* **27**, 217-226, doi:10.1159/000327947 (2011).
- 154 Feng, X. *et al.* Dual function of VGLL4 in muscle regeneration. *EMBO J* **38**, e101051, doi:10.15252/embj.2018101051 (2019).
- 155 MacNeil, A. J. *et al.* MAPK kinase 3 is a tumor suppressor with reduced copy number in breast cancer. *Cancer Res* **74**, 162-172, doi:10.1158/0008-5472.CAN-13-1310 (2014).
- 156 Komuro, A. *et al.* The AHNAs are a class of giant propeller-like proteins that associate with calcium channel proteins of cardiomyocytes and other cells. *Proc Natl Acad Sci U S A* **101**, 4053-4058, doi:10.1073/pnas.0308619101 (2004).
- 157 Yeter, D. & Deth, R. ITPKC susceptibility in Kawasaki syndrome as a sensitizing factor for autoimmunity and coronary arterial wall relaxation induced by thimerosal's effects on calcium signaling via IP3. *Autoimmun Rev* **11**, 903-908, doi:10.1016/j.autrev.2012.03.006 (2012).
- 158 Sarria, I., Ling, J., Zhu, M. X. & Gu, J. G. TRPM8 acute desensitization is mediated by calmodulin and requires PIP(2): distinction from tachyphylaxis. *J Neurophysiol* **106**, 3056-3066, doi:10.1152/jn.00544.2011 (2011).
- 159 Felisiak-Golabek, A. *et al.* p19(INK4d) mRNA and protein expression as new prognostic factors in ovarian cancer patients. *Cancer Biol Ther* **14**, 973-981, doi:10.4161/cbt.25966 (2013).
- 160 Yu, C. *et al.* FAF1 mediates necrosis through JNK1-mediated mitochondrial dysfunction leading to retinal degeneration in the ganglion cell layer upon ischemic insult. *Cell Commun Signal* **16**, 56, doi:10.1186/s12964-018-0265-7 (2018).
- 161 Zhu, Y. *et al.* MicroRNA-26a/b and their host genes cooperate to inhibit the G1/S transition by activating the pRb protein. *Nucleic Acids Res* **40**, 4615-4625, doi:10.1093/nar/gkr1278 (2012).
- 162 Moore, S. *et al.* The CHD6 chromatin remodeler is an oxidative DNA damage response factor. *Nat Commun* **10**, 241, doi:10.1038/s41467-018-08111-y (2019).

- 163 Jang, H., Choi, S. Y., Cho, E. J. & Youn, H. D. Cabin1 restrains p53 activity on chromatin. *Nat Struct Mol Biol* **16**, 910-915, doi:10.1038/nsmb.1657 (2009).
- 164 Jaiswal, A. S. *et al.* The splicing component ISY1 regulates APE1 in base excision repair. *DNA Repair (Amst)* **86**, 102769, doi:10.1016/j.dnarep.2019.102769 (2020).
- 165 Loftus, K. M. *et al.* Mechanism for G2 phase-specific nuclear export of the kinetochore protein CENP-F. *Cell Cycle* **16**, 1414-1429, doi:10.1080/15384101.2017.1338218 (2017).
- 166 Yang, C. *et al.* NRBF2 is involved in the autophagic degradation process of APP-CTFs in Alzheimer disease models. *Autophagy* **13**, 2028-2040, doi:10.1080/15548627.2017.1379633 (2017).
- 167 Knackmuss, U. *et al.* MAP3K11 is a tumor suppressor targeted by the oncomiR miR-125b in early B cells. *Cell Death Differ* **23**, 242-252, doi:10.1038/cdd.2015.87 (2016).
- 168 Zhang, X. *et al.* LAMA5 promotes human umbilical vein endothelial cells migration, proliferation, and angiogenesis and is decreased in preeclampsia. *J Matern Fetal Neonatal Med*, 1-11, doi:10.1080/14767058.2018.1514597 (2018).
- 169 Khanna, K. *et al.* Secretory Inositol Polyphosphate 4-Phosphatase Protects against Airway Inflammation and Remodeling. *Am J Respir Cell Mol Biol* **60**, 399-412, doi:10.1165/rcmb.2017-0353OC (2019).
- 170 Yoon, D., Bae, K., Lee, M. K., Kim, J. H. & Yoon, K. A. Galanin is an epigenetically silenced tumor suppressor gene in gastric cancer cells. *Plos One* **13**, e0193275, doi:10.1371/journal.pone.0193275 (2018).
- 171 Kitajima, Y. & Ono, Y. Estrogens maintain skeletal muscle and satellite cell functions. *J Endocrinol* **229**, 267-275, doi:10.1530/JOE-15-0476 (2016).
- 172 Kitajima, Y. *et al.* Estrogen deficiency heterogeneously affects tissue specific stem cells in mice. *Sci Rep* **5**, 12861, doi:10.1038/srep12861 (2015).
- 173 Horstman, A. M., Dillon, E. L., Urban, R. J. & Sheffield-Moore, M. The role of androgens and estrogens on healthy aging and longevity. *J Gerontol A Biol Sci Med Sci* **67**, 1140-1152, doi:10.1093/gerona/gls068 (2012).
- 174 Mei, Z. *et al.* Galanin suppresses proliferation of human U251 and T98G glioma cells via its subtype 1 receptor. *Biol Chem* **398**, 1127-1139, doi:10.1515/hsz-2016-0320 (2017).
- 175 Garcia-Prat, L., Munoz-Canoves, P. & Martinez-Vicente, M. Dysfunctional autophagy is a driver of muscle stem cell functional decline with aging. *Autophagy* **12**, 612-613, doi:10.1080/15548627.2016.1143211 (2016).
- 176 Scott, R. W., Arostegui, M., Schweitzer, R., Rossi, F. M. V. & Underhill, T. M. Hic1 Defines Quiescent Mesenchymal Progenitor Subpopulations with Distinct Functions and Fates in Skeletal Muscle Regeneration. *Cell Stem Cell* **25**, 797-813 e799, doi:10.1016/j.stem.2019.11.004 (2019).
- 177 Uezumi, A. *et al.* Fibrosis and adipogenesis originate from a common mesenchymal progenitor in skeletal muscle. *J Cell Sci* **124**, 3654-3664, doi:10.1242/jcs.086629 (2011).
- 178 Morales, M. G., Acuna, M. J., Cabrera, D., Goldschmeding, R. & Brandan, E. The pro-fibrotic connective tissue growth factor (CTGF/CCN2) correlates with the number of necrotic-regenerative foci in dystrophic muscle. *J Cell Commun Signal* **12**, 413-421, doi:10.1007/s12079-017-0409-3 (2018).
- 179 Meng, X. M., Nikolic-Paterson, D. J. & Lan, H. Y. TGF-beta: the master regulator of fibrosis. *Nat Rev Nephrol* **12**, 325-338, doi:10.1038/nrneph.2016.48 (2016).

- 180 Taneera, J. *et al.* Expression profiling of cell cycle genes in human pancreatic islets with and without type 2 diabetes. *Mol Cell Endocrinol* **375**, 35-42, doi:10.1016/j.mce.2013.05.003 (2013).
- 181 Carroll, P. A., Freie, B. W., Mathsyaraja, H. & Eisenman, R. N. The MYC transcription factor network: balancing metabolism, proliferation and oncogenesis. *Front Med* **12**, 412-425, doi:10.1007/s11684-018-0650-z (2018).
- 182 Quezada-Ramirez, M. A., Castaneda-Arellano, R., Perez-Sanchez, G., Hernandez-Soto, J. & Segovia, J. The Growth arrest specific 1 (Gas1) gene is transcriptionally regulated by NeuroD1 via two distal E-boxes. *Exp Cell Res* **363**, 332-341, doi:10.1016/j.yexcr.2018.01.034 (2018).
- 183 Gopinath, S. D., Webb, A. E., Brunet, A. & Rando, T. A. FOXO3 promotes quiescence in adult muscle stem cells during the process of self-renewal. *Stem Cell Reports* **2**, 414-426, doi:10.1016/j.stemcr.2014.02.002 (2014).
- 184 Tonami, K. *et al.* Calpain-6 deficiency promotes skeletal muscle development and regeneration. *PLoS Genet* **9**, e1003668, doi:10.1371/journal.pgen.1003668 (2013).
- 185 Jorgensen, L. H., Jensen, C. H., Wewer, U. M. & Schroder, H. D. Transgenic overexpression of ADAM12 suppresses muscle regeneration and aggravates dystrophy in aged mdx mice. *Am J Pathol* **171**, 1599-1607, doi:10.2353/ajpath.2007.070435 (2007).
- 186 Judson, R. N., Low, M., Eisner, C. & Rossi, F. M. Isolation, Culture, and Differentiation of Fibro/Adipogenic Progenitors (FAPs) from Skeletal Muscle. *Methods Mol Biol* **1668**, 93-103, doi:10.1007/978-1-4939-7283-8_7 (2017).
- 187 Lahnemann, D. *et al.* Eleven grand challenges in single-cell data science. *Genome Biol* **21**, 31, doi:10.1186/s13059-020-1926-6 (2020).
- 188 Bergmann, O. *et al.* Evidence for cardiomyocyte renewal in humans. *Science* **324**, 98-102, doi:10.1126/science.1164680 (2009).
- 189 Koudstaal, S. *et al.* Concise review: heart regeneration and the role of cardiac stem cells. *Stem Cells Transl Med* **2**, 434-443, doi:10.5966/sctm.2013-0001 (2013).
- 190 Claydon, A. J. & Beynon, R. Proteome dynamics: revisiting turnover with a global perspective. *Mol Cell Proteomics* **11**, 1551-1565, doi:10.1074/mcp.O112.022186 (2012).
- 191 Shiojima, I. *et al.* Disruption of coordinated cardiac hypertrophy and angiogenesis contributes to the transition to heart failure. *J Clin Invest* **115**, 2108-2118, doi:10.1172/JCI24682 (2005).
- 192 Nakamura, K., Yamanouchi, K. & Nishihara, M. Secreted protein acidic and rich in cysteine internalization and its age-related alterations in skeletal muscle progenitor cells. *Aging Cell* **13**, 175-184, doi:10.1111/acer.12168 (2014).
- 193 Ravi, R. *et al.* Regulation of tumor angiogenesis by p53-induced degradation of hypoxia-inducible factor 1alpha. *Genes Dev* **14**, 34-44 (2000).
- 194 Sano, M. *et al.* p53-induced inhibition of Hif-1 causes cardiac dysfunction during pressure overload. *Nature* **446**, 444-448, doi:10.1038/nature05602 (2007).
- 195 Nakada, Y. *et al.* Hypoxia induces heart regeneration in adult mice. *Nature* **541**, 222-227, doi:10.1038/nature20173 (2017).
- 196 Orr-Weaver, T. L. When bigger is better: the role of polyploidy in organogenesis. *Trends Genet* **31**, 307-315, doi:10.1016/j.tig.2015.03.011 (2015).
- 197 Pandit, S. K., Westendorp, B. & de Bruin, A. Physiological significance of polyploidization in mammalian cells. *Trends Cell Biol* **23**, 556-566, doi:10.1016/j.tcb.2013.06.002 (2013).

- 198 Windmueller, R. *et al.* Direct Comparison of Mononucleated and Binucleated Cardiomyocytes Reveals Molecular Mechanisms Underlying Distinct Proliferative Competencies. *Cell Rep* **30**, 3105-3116 e3104, doi:10.1016/j.celrep.2020.02.034 (2020).
- 199 Zigmond, R. E. Cytokines that promote nerve regeneration. *Exp Neurol* **238**, 101-106, doi:10.1016/j.expneurol.2012.08.017 (2012).
- 200 Kiecker, C., Bates, T. & Bell, E. Molecular specification of germ layers in vertebrate embryos. *Cell Mol Life Sci* **73**, 923-947, doi:10.1007/s00018-015-2092-y (2016).
- 201 Sipkova, J., Kramarikova, I., Hynie, S. & Klenerova, V. The galanin and galanin receptor subtypes, its regulatory role in the biological and pathological functions. *Physiol Res* **66**, 729-740 (2017).
- 202 Gonzalez-Freire, M., de Cabo, R., Studenski, S. A. & Ferrucci, L. The neuromuscular junction: aging at the crossroad between nerves and muscle. *Front Aging Neurosci* **6**, doi:ARTN 20810.3389/fnagi.2014.00208 (2014).
- 203 Valenzuela, D. M. *et al.* Receptor tyrosine kinase specific for the skeletal muscle lineage: Expression in embryonic muscle, at the neuromuscular junction, and after injury. *Neuron* **15**, 573-584, doi:10.1016/0896-6273(95)90146-9 (1995).
- 204 Glass, D. J. *et al.* Agrin Acts via a MuSK Receptor Complex. *Cell* **85**, 513-523, doi:10.1016/s0092-8674(00)81252-0 (1996).
- 205 Liu, W. *et al.* Loss of adult skeletal muscle stem cells drives age-related neuromuscular junction degeneration. *Elife* **6**, doi:10.7554/eLife.26464 (2017).
- 206 Liu, W., Wei-LaPierre, L., Klose, A., Dirksen, R. T. & Chakkalakal, J. V. Inducible depletion of adult skeletal muscle stem cells impairs the regeneration of neuromuscular junctions. *Elife* **4**, doi:10.7554/eLife.09221 (2015).
- 207 Rodgers, J. T. *et al.* mTORC1 controls the adaptive transition of quiescent stem cells from G0 to G(Alert). *Nature* **510**, 393-396, doi:10.1038/nature13255 (2014).
- 208 Rodgers, J. T., Schroeder, M. D., Ma, C. & Rando, T. A. HGFA Is an Injury-Regulated Systemic Factor that Induces the Transition of Stem Cells into GAlert. *Cell Rep* **19**, 479-486, doi:10.1016/j.celrep.2017.03.066 (2017).
- 209 Low, S., Barnes, J. L., Zammit, P. S. & Beauchamp, J. R. Delta-Like 4 Activates Notch 3 to Regulate Self-Renewal in Skeletal Muscle Stem Cells. *Stem Cells* **36**, 458-466, doi:10.1002/stem.2757 (2018).
- 210 Zammit, P. S. *et al.* Muscle satellite cells adopt divergent fates: a mechanism for self-renewal? *J Cell Biol* **166**, 347-357, doi:10.1083/jcb.200312007 (2004).
- 211 Scaramozza, A. *et al.* Lineage Tracing Reveals a Subset of Reserve Muscle Stem Cells Capable of Clonal Expansion under Stress. *Cell Stem Cell* **24**, 944-957 e945, doi:10.1016/j.stem.2019.03.020 (2019).
- 212 Evano, B. & Tajbakhsh, S. Skeletal muscle stem cells in comfort and stress. *NPJ Regen Med* **3**, 24, doi:10.1038/s41536-018-0062-3 (2018).
- 213 Conboy, I. M. & Rando, T. A. Heterochronic parabiosis for the study of the effects of aging on stem cells and their niches. *Cell Cycle* **11**, 2260-2267, doi:10.4161/cc.20437 (2012).
- 214 Hall, J. K., Banks, G. B., Chamberlain, J. S. & Olwin, B. B. Prevention of muscle aging by myofiber-associated satellite cell transplantation. *Sci Transl Med* **2**, 57ra83, doi:10.1126/scitranslmed.3001081 (2010).
- 215 Wang, D. *et al.* Immunohistochemistry in the evaluation of neovascularization in tumor xenografts. *Biotech Histochem* **83**, 179-189, doi:10.1080/10520290802451085 (2008).

- 216 Parente, L. & Solito, E. Annexin 1: more than an anti-phospholipase protein. *Inflammation Research* **53**, 125-132, doi:10.1007/s00011-003-1235-z (2004).
- 217 Brglez, V., Lambeau, G. & Petan, T. Secreted phospholipases A2 in cancer: diverse mechanisms of action. *Biochimie* **107 Pt A**, 114-123, doi:10.1016/j.biochi.2014.09.023 (2014).
- 218 Boye, T. L. *et al.* Annexins induce curvature on free-edge membranes displaying distinct morphologies. *Sci Rep* **8**, 10309, doi:10.1038/s41598-018-28481-z (2018).
- 219 Mahdy, M. A. A. Skeletal muscle fibrosis: an overview. *Cell Tissue Res* **375**, 575-588, doi:10.1007/s00441-018-2955-2 (2019).
- 220 Bena, S., Brancaleone, V., Wang, J. M., Perretti, M. & Flower, R. J. Annexin A1 interaction with the FPR2/ALX receptor: identification of distinct domains and downstream associated signaling. *J Biol Chem* **287**, 24690-24697, doi:10.1074/jbc.M112.377101 (2012).
- 221 Olfert, I. M., Baum, O., Hellsten, Y. & Egginton, S. Advances and challenges in skeletal muscle angiogenesis. *Am J Physiol Heart Circ Physiol* **310**, H326-336, doi:10.1152/ajpheart.00635.2015 (2016).
- 222 Rozhok, A. I. & DeGregori, J. The evolution of lifespan and age-dependent cancer risk. *Trends Cancer* **2**, 552-560, doi:10.1016/j.trecan.2016.09.004 (2016).
- 223 Zilfou, J. T. & Lowe, S. W. Tumor suppressive functions of p53. *Cold Spring Harb Perspect Biol* **1**, a001883, doi:10.1101/cshperspect.a001883 (2009).

7. ACKNOWLEDGEMENTS

Any of my projects would not have been possible without the constant help of my supervisor, **Prof. Dr. Dr. Thomas Braun**. I am deeply grateful for accepting me as a PhD student and for his wise guidance and fruitful suggestions during my doctoral studies. I am very grateful to **Dr. Stefan Guenther** for his daily support and for teaching me everything I know about Next Generation Sequencing. I am also grateful a lot to **Dr. Johnny Kim**, who, firstly, selected me for my interview for the IMPRS graduate program, and secondly, thoroughly discussed all aspects of my projects in recent years. It is important to mention **Dr. Jens Preussner**, **Dr. Johannes Graumann**, **Dr. Carsten Kuenne** and **Mette Bentsen**, who advised me on bioinformatics and programming languages. Working with mice, especially with transgenic strains and legal regulations, would not have been possible without the generous help of **Dr. Andre Schneider**, **Susanne Kreutzer**, **Katja Kolditz**, **Birgit Spitznagel**, and **Jennifer Behm**. FACS would never have been so straightforward without the help of **Ann Atzberger**, **Kerstin Richter** and **Kikhi Khrievono**. Cardiomyocytes isolation and TAC and Sham surgeries were performed by **Marion Wiesnet**. MRI data were provided by **Dr. Claudia Garcia Gonzales** and **Dr. Astrid Wietelmann**. I highly appreciate the work of all animal caretakers, especially **Annette Loeffler** and **Carina Frank**. I would like to thank **Dr. Bilge Reischauer** for her help in managing the IMPRS graduate school, and **Franziska Hainer** for her help with the legal aspects of being a PhD Student in Germany.

In addition, I thank **Prof. Thomas Braun**, as well as **Prof. Norbert Weissmann** for reviewing my dissertation, as well as the PhD defense committee, which also included **Prof. Albrecht Bindereif** and **Prof. Alexander Goesmann**.

I would like to thank all my colleagues from the Max Planck Institute for Heart and Lung Research for making my doctoral studies an incredible and exciting part of my life.

Finally, I am very grateful to my family – **Prof. Dr. Alexandra Pozniak**, **Dzmitry Yekelchik**, **Darya Yekelchik** and **Vanessa Vera** for their sincere support and love.

Michail Yekelchik